# Synthesis, structural characterization, electrochemical properties, and thermal stability of Al-substituted $\text{LiMn}_{1.5}\text{Ni}_{0.5}\text{O}_4$

Amund Midtgard Raniseth

Thesis submitted for the degree of
Master in Materials Science for Energy and Nanotechnology
60 credits

Department of Chemistry
Faculty of mathematics and natural sciences

UNIVERSITY OF OSLO

Spring 2022

# Synthesis, structural characterization, electrochemical properties, and thermal stability of Al-substituted $LiMn_{1.5}Ni_{0.5}O_4$

Amund Midtgard Raniseth

Synthesis, structural characterization, electrochemical properties, and thermal stability of Al-substituted $LiMn_{1.5}Ni_{0.5}O_4$

http://www.duo.uio.no/

Printed: Reprosentralen, University of Oslo

## Abstract

One of the interesting lithium-ion battery cathode materials which have been developed over the last 20 years is the lithium manganese nickel oxide (LMNO). However, problems with lifetime remain. Increasing the lifetime of LMNO is crucial to its commercial adoption, and one of the promising techniques to do this is substituting different elements of the structure.

In this thesis, the structure, electrochemistry, and thermal stability of LMNO have been investigated with different amounts of aluminum substitution attempted to replace either manganese, nickel, or both elements evenly. The findings suggest that substituting manganese is not easily done, as impurities form. However, by replacing mainly nickel, aluminum is successfully incorporated into the structure at a stoichiometric amount of 0.2. This type of substitution was also found to change the electrochemical voltage plateau of the material, in addition to prolonging its cycle life. The aluminum substituted material also exhibited better thermal stability above 100°C.

## Preface

The last two years have gone by very fast, doing something that I have learned to love. During this time, I have been extremely lucky to have supervisors dedicated to help in almost every aspect, both in my research group NAnostructural and FUnctional MAterials(NAFUMA) (Department of Chemistry, UiO), and externally. I would like to give a big thanks to my closest supervisor, Ph.D. fellow Halvor Høen Hval. In addition to being a parent, working 40% outside the university, and having his own Ph.D. to write, he has spent a good amount of time developing my skills, both experimentally and theoretically. With his continuous supervision, discussions, and feedback, I have progressed faster than I could ever have done alone. Working on something close to his project has also given me opportunities for my thesis which not many master's students get. He has arranged for getting synchrotron data, getting me in touch with the Norwegian Defense Research Establishment (FFI), and purchasing chemicals and equipment a master's student rarely gets the freedom to choose. All these opportunities have also been facilitated by my main supervisor and head of NAFUMA, Professor Helmer Fjellvåg. Thanks, Helmer, and thanks for giving me the opportunity to write my thesis in this research group. Last of my supervisors is the knowledgeable and always-helpful Pushpaka Samarasingha (Researcher, NAFUMA). Thank you for offering your time and expertise during this work.

In addition to my direct supervisors, many people in the group have assisted quite a bit. I would like to thank Carmen Cavallo for her excellent guidance and supervision in the laboratory as well as for always being available and interested in finding the best solution to every problem. Also, thanks to David Wragg for help with the analysis of diffraction data, and Salah Bra Amedi for always being available when I break something in the lab. I must also mention that my co-students have given me both mental support, and valuable academic discussions during my time in the research group. Our student fellowship has been very important to me and I would like to thank you for this, Casper, Ina, Mats, Erlend, Odd, Hallvard, and Abilash.

I have been lucky to be gaining experience outside NAFUMA as well. I would especially like to thank scientist Torleif Lian for allowing me to come and do ARC measurements at the FFI, and for the excellent training and supervision, in addition to always being available and accessible for discussions and feedback. Also, thanks to Niels Højmark Andersen, senior engineer at Environmental Sciences (Department of Chemistry, UiO), for taking the time to do Raman spectroscopy with me.

A last thank you goes to my wife, Maria Sjøvik. Without your ever-strong support, I would never have had the energy or ability to arrive at this point.

The thesis was written using MDoc by Knut Magnus Aasrud [1].

# Contents

## List of abbreviations

Table 1: Abbreviations

| **Abbreviation** | **Long name** |
|---|---|
| ARC | Accelerate Rate Calorimetry |
| BMS | Battery Management System |
| CA | Citric acid |
| CE | Coulombic Efficiency |
| CSP | Carbon Super P |
| CV | Cyclic Voltammetry |
| DEC | diethyl carbonate |
| DTBP | Di-tert-butyl peroxide |
| EC | Ethylene carbonate |
| EDX/EDS | Energy Dispersive X-Ray Spectroscopy |
| EG | Ethylene Glycol |
| et al. | et alia (Latin for “with others”) |
| FFI | Norwegian Defense Research Establishment (Forsvarets Forskingsinstitutt) |
| FWHM | Full width half maximum |
| GCPL | Galvanostatic cycling with potential limitation |
| HOMO | Highest occupied molecular orbital |
| ICP-MS | Inductively Coupled Plasma Mass Spectroscopy |
| IPCC | Intergovernmental Panel on Climate Change |
| IR drop | Internal Resistance drop |
| LFP | Lithium Iron Phosphate |
| LIB | Lithium-ion battery |
| LMO | Lithium Manganese Oxide (spinel) |
| LMNO | Lithium Manganese Nickel Oxide (spinel) |
| LTO | Lithium Titanium Oxide |
| LUMO | Lowest unoccupied molecular orbital |
| MoZEES | Mobility Zero Emission Energy Systems (consortium) |
| NAFUMA | NAnostructural and FUnctoinal MAterials (Research group at UiO) |
| NMC | Lithium Nickel Manganese Cobalt Oxide |
| PTFE | Polytetrafluoroethylene |
| PXRD | Powder X-Ray Diffraction |
| SEI | Solid Electrolyte Interphase |
| SEM | Scanning Electron Microscope / Microscopy |
| SOP | Standard Operating Procedure |
| SoC | State of Charge |
| UiO | University of Oslo |

# List of Figures

# List of Tables

# Chapter 1

# Introduction

## 1.1 Background and Motivation

In the most recent report from the Intergovernmental Panel on Climate Change (IPCC) on global warming, they state that the estimated human-caused global warming is in the likely range of 0.8-1.2°C above pre-industrial levels [2]. The goal is to limit this global warming to 1.5°C for the foreseeable future. However, if global warming rises above 2°C, 1.5 billion more people would be exposed to deadly heatwaves, twice as many will face water scarcity and vector-borne diseases such as malaria would reach hundreds of millions of individuals more [3]. The biggest cause of global warming is the release of greenhouse gasses [4], which traps heat from the sun in the atmosphere. Although some of these are naturally occurring, anthropogenic emissions have contributed a significant amount. IPCC suggests that anthropogenic emissions are unlikely to cause global warming of more than 0.5°C alone within the next 2-3 decades, however, this would get us to right on the breakpoint of the goal [2].

Of anthropogenic greenhouse gas emissions, 76% originate from the Energy sector, where electricity/heat and transportation are the largest contributors with 42% and 22% respectively (2018 data from CAIT [5]). In order to reduce these emissions, transitioning to clean renewable energy sources and electrifying the transport sector is seen as our only option. Electrification of the transport sector depends on the range and convenience of the electric solutions to be comparable to that of fossil fuels. With electric motors outperforming internal combustion engines in almost every aspect, a lot of focus is put on energy storage. Appealing choices are hydrogen and batteries, however, batteries have already taken the lead due to their simplicity.

While battery-electric personal vehicles are becoming the norm in countries subsidizing them, cheaper and more sustainable batteries need to be developed for this progress to continue in countries without subsidization and also for larger vehicles like trailers. Commercial lithium-ion battery (LIB) chemistries include mostly lithium nickel manganese cobalt oxide (NMC), which has troubles both with cost and sustainability. Cobalt is known to be unethically produced, especially connected to child labor in Congolese mines, and is also expensive [6]. In similarity to cobalt, nickel has also become expensive in recent years, which is especially concerning for nickel-rich cathodes [7].

A cathode material containing no cobalt, and with a gravimetric energy density 80% of nickel-rich cathodes is LMNO. This cathode also uses less nickel, with only 0.26 kg nickel per kWh versus 0.64 $\text{kg}_{\text{nickel}}$/kWh of the high nickel cathode (calculated in appendix section A.1). However, it must be noted that a material without both nickel and manganese does exist, namely lithium iron phosphate (LFP). With a gravimetric energy density 72% of nickel-rich cathodes, LFP is a very viable option for applications accepting lower energy density, and is today in commercial use both in electric vehicles and stationary storage. However, LFP has a low operating potential (3.2 V) compared to that of LMNO (4.7 V), leading to an increased need for battery management system (BMS) components.

Although LMNO seems like a viable cathode material for commercialization, issues with capacity retention and degradation of electrolyte at high potentials remain as research topics. Several possibilities have been explored, like coating the particles [8], controlling the morphology [9], or substituting some of the elements [10]–[13]. One type of substitution that has not been extensively researched is aluminum substitution, where only five papers were found in the literature to this date [8], [14]–[17].

The reason aluminum substitution is interesting is because Al is light, increasing the gravimetric energy density of the material, it is non-toxic, less expensive, and also has strong bonds to oxygen, which could lead to better structural stability. In addition, if substituted correctly, it could lead to a scenario where all redox-active species are in their highest oxidation state, while some lithium is still present in the structure. From a fundamental scientific standpoint, it is then interesting to see whether it is possible to extract that lithium, and what happens to the structure, which is a part of this thesis.

LMNO is also the model cathode material of Mobility Zero Emission Energy Systems (MoZEES), a consortium within the research center for environmental energy (FME), which my research group NAFUMA at UiO is a part of. Although this M.Sc. thesis is not officially linked with MoZEES, it is an adjacent part of Halvor Høen Hval's work on LMNO cathodes in the consortium.

This master of science thesis will dive into how various types of aluminum substitution in the LMNO crystal lattice affect its electrochemical properties, in addition to thermal stability. The thesis is built with an introduction - a basic explanation of the most important concepts, followed by theory and methods, results and discussion, conclusion, and lastly the appendices.

## 1.2 History of lithium-ion batteries

The history of lithium-ion batteries starts with the first electrochemical cell. This cell was not a lithium-ion cell, but rather a copper-zinc cell and was named the voltaic pile after its inventor, the Italian physicist Alessandro Volta. This was published in 1799 and was called a pile due to the stacking (as series connection) of electrochemical cells in order to build up voltage. The voltaic pile is believed to be the first battery composed of electrochemical cells and can be viewed in figure 1.1 below.

Figure 1.1: Alessandro Volta's electric battery (Tempio Voltiano in Como, Italy) by GuidoB. CC Attribution Alike 3.0 Unported license

The voltaic pile consisted of zinc and copper electrodes, which were ionically connected through a cloth soaked in brine acting as the electrolyte. This cell, however, dissolved zinc into the electrolyte and made hydrogen gas out of protons in the electrolyte. Due to these processes being very hard to reverse, this cell could not recharge and is thus called a primary cell. Another primary cell that is still around is the Leclancé cell developed in 1866. This cell had a positive electrode (cathode) of manganese oxide and a negative electrode (anode) of zinc, with an electrolyte consisting of ammonium chloride. The Leclancé cell was the first alkaline cell, which we to this day use as primary cells for smaller gadgets and appliances.

The first electrochemical cell which could change the direction of the oxidation and reduction reactions could be found in the Planté battery, invented by French physicist Gaston Planté in 1859 [18]. The Planté battery consisted of nine cells, each with a potential of 2 V for a total of 18 V. The chemistry of these cells consisted of a lead oxide cathode and a metallic lead anode which was soaked in sulfuric acid. During discharge, the cathode would consume protons and sulfate ions to create lead-sulfate and water, while the anode would consume sulfate ions to create lead-sulfate and protons. During a charge of the cell, these reactions would reverse, turning the lead sulfate back to its original lead oxide and metallic lead. Although it has been heavily developed for efficiency and longevity, the core chemistry still remains the same to this day, and can be found in most 12 V car batteries [19].

In addition to the lead-acid battery, several more chemistries have been explored. For instance, nickel cadmium was developed in 1899, although due to the restriction of toxic cadmium in the 1990s it is not often seen anymore. The nickel metal hydride battery developed from 1967 was used in modern EV-hybrids with the use in the first Toyota Prius hybrid cars, however, they have a history of patent wars limiting the market uptake [20].

Today's modern electric battery contains so-called lithium-ion chemistry. Although the first lithium-ion cell was developed in 1965 by NASA in the form of a copper fluoride - lithium cell, the invention by Stanley Whittingham in 1974 is seen as the first modern example. Whittingham was the first to use titanium disulfide as a cathode material, which with its layered structure could *absorb* lithium ions using the same mechanism as most modern cathode materials. However, due to its reactions with water creating toxic gasses and the metallic lithium in the cell being a fire hazard, the cell never saw commercialization. Koichi Mizushima and John B. Goodenough's lithium cobalt oxide cathode material did not have the same unsafe side reactions and were commercialized by Sony in 1991. The invention of Akira Yoshino on soft carbon anodes was also used in the first Sony cells, which eliminated the need for a hazardous lithium metal anode [21].

After Sony's first commercial lithium-ion battery (LIB) in 1991, many incremental advancements have been made. Especially widespread is the use of higher potential cathodes, which are more energy-dense than lithium cobalt oxide and has a longer lifetime but have the same crystal structure. These cathodes are usually called NMC, owing the name to their nickel and manganese cations which have partially substituted cobalt. The anode has also been significantly improved from soft carbon to graphite, where lithium is "absorbed" between the layers.

## 1.3 Introduction to lithium-ion batteries

A basic electrochemical cell works by transporting ions between a domain of high potential and a domain of low potential through a medium that only supports the conduction of the ions themselves, without electronic conduction. The domains of high and low potential are called the cathode and anode respectively or are collectively described as the electrodes. In fact, the wording *cathode* and *anode* comes from the description of chemical reactions meaning where the reduction process and oxidation process happen respectively. This terminology was established in the battery scene when only primary batteries existed, and the reduction always happened at the cathode. However, for secondary (rechargeable) batteries, the redox reaction changes direction depending on if the cell is charging or discharging, meaning that the cathode becomes the anode and vice versa. In practice, the names are not changed, and whatever is the negative electrode is called the anode, and the positive electrode is called the cathode regardless of the reactions happening on the electrode. Truls Norby proposed the use of negatrode and positrode instead of the misleading terms anode and cathode, which has not gained too much traction in literature but is an option for those interested in accurate descriptive wording [22].

While the electrodes and electrolyte are what is needed in a basic electrochemical cell, in a LIB, a plethora of other parts are also needed. Starting with the electrodes, they usually consist of a current collector, often made of a thin sheet of either aluminum (for the cathode) or copper (for the anode), where the so-called *black mass* is coated on top. The black mass consists of a binder, conductive additive, and active material. The binder is used to hold the powders together and to the current-collector, while the conductive additive is there to improve electrical conductivity and the active material is what stores the charge/energy. In addition, between the electrodes, a separator can be found, whose task is to physically separate the electrodes to avoid them touching and establishing an electronic path leading to an internal short circuit. This separator and the electrodes are then soaked in the electrolyte, giving ionic conductivity between the electrodes. For LIBs, this electrolyte most often consists of an organic liquid as a solvent, with a lithium salt dissolved in it for better ionic conductivity.

In figure 1.2 below, a simple lithium-ion electrochemical cell is shown, where the cathode (or positrode) is a layered manganese oxide and the anode (or negatrode) is graphite. The sheet in between illustrates the separator, and everything except the external circuit is soaked in electrolyte which is not shown in the figure.

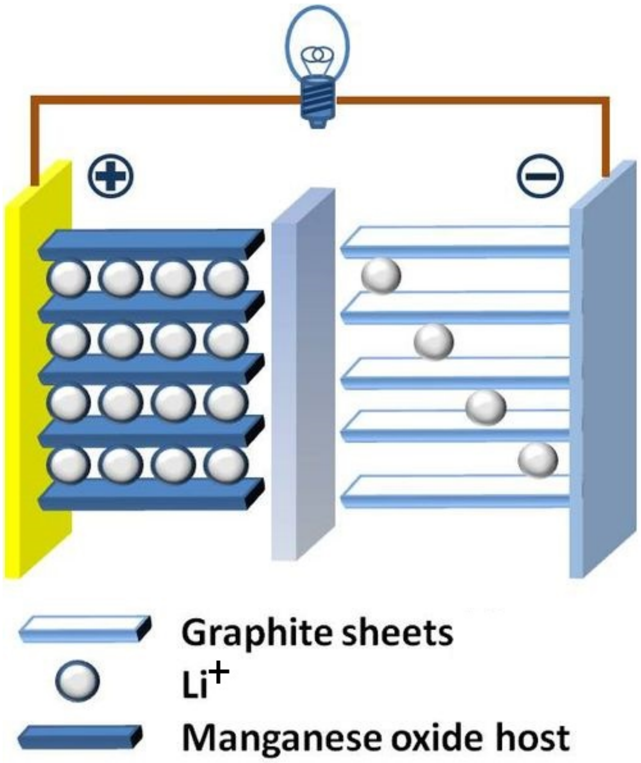

Figure 1.2: Basic battery charging cell by Chem511grpThinLiBat (modified), Date: 02.12.2010. Public Domain. (from Wikimedia Commons)

While the basic setup of a LIB holds true for most batteries, the active materials of the electrodes can change quite a bit. An overview of the most used active materials and their potentials and capacities (further explained in the next sections) can be found in figure 1.3 below.

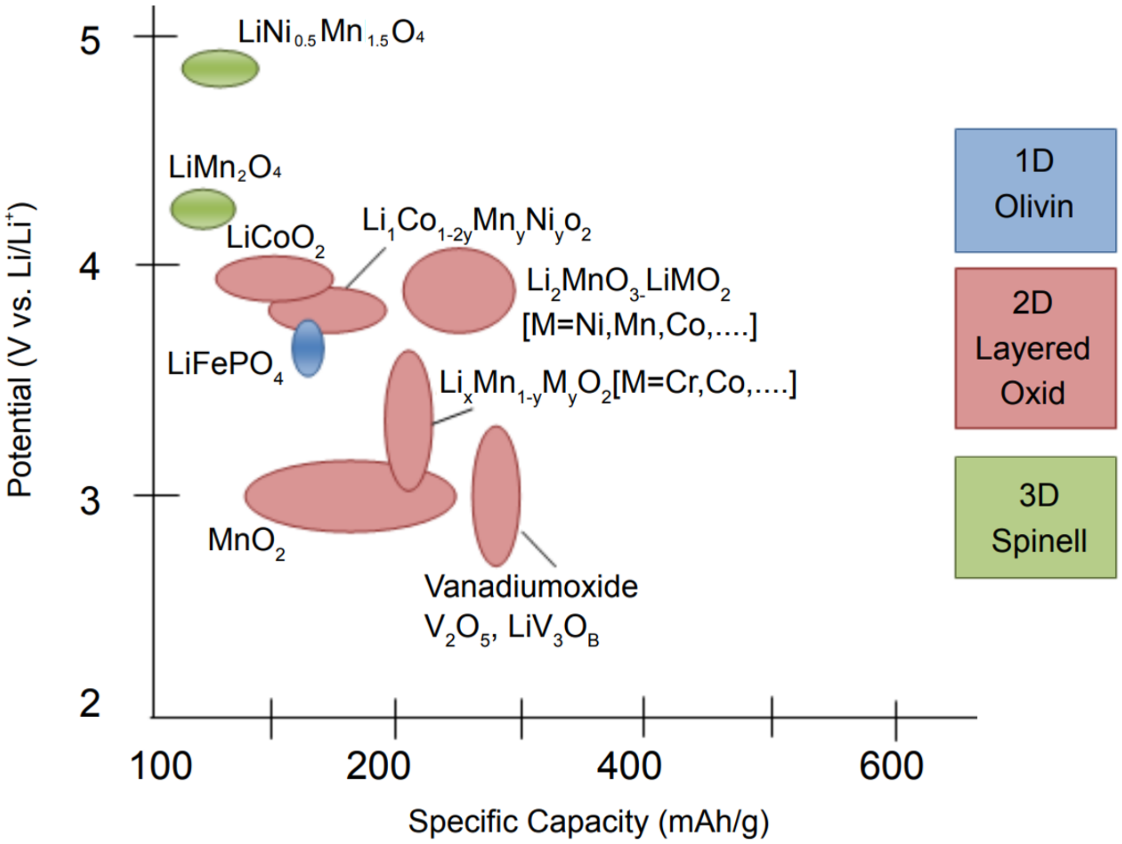

Figure 1.3: Potentials and capacities of the most common cathode materials. Modified from [23]

### 1.3.1 Lithium-ion battery potentials

The electrical potential of a reaction describes the potential needed for a reaction to happen. Since the potential of a reaction can only be measured against another reaction, a reference electrode has been established. In aqueous electrochemistry, the standard hydrogen electrode is often used. However, in LIBs, which do not have an aqueous electrolyte, the standard has become to write the potentials of the active materials in reference to the redox reaction of lithium:

$$Li(s) \leftrightarrow Li^+ + e^-$$

However, although this reaction is usually defined as the zero-potential in LIBs, it actually measures $-3.03$ V versus the standard hydrogen electrode which means that the potential is very low. Reaction potentials of the most common materials versus the standard hydrogen electrode can be found in the *galvanic series*. The potential of popular active materials in LIBs ranges all the way from very close to lithium, usually given the label "anode materials" (silicon, graphite $< 100$ mV), through the mid-range (most notably lithium titanium oxide (LTO) at 1.6 V) which can be both anodes and cathodes, to the cathode materials (Layered oxides $3.5 - 4.2$ V and the spinel oxide LMNO at 4.7 V).

However, due to the change in materials during their charging cycle, the reaction potential versus Li/Li$^+$ can change. Some of these materials and their potential change during a discharge are visualized in figure 1.4 below.

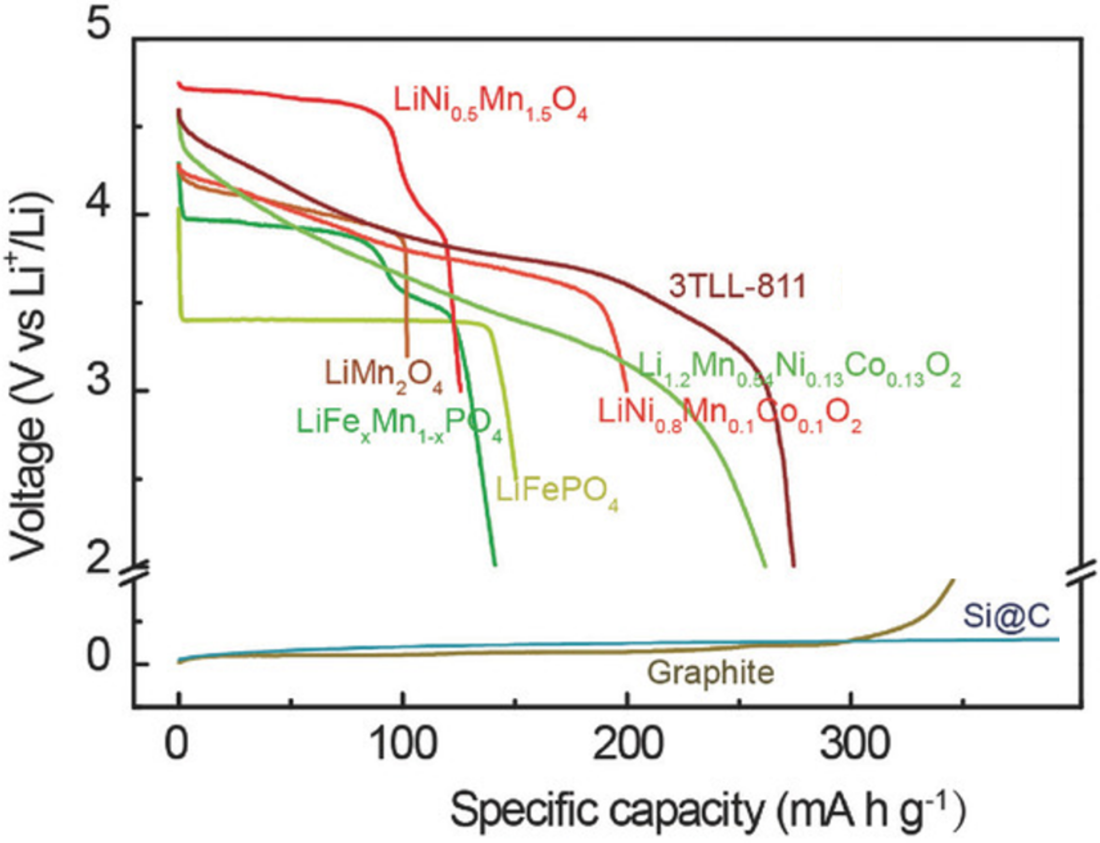

Figure 1.4: Potential profiles starting from the lithiated state of the most common cathode and anode materials. Modified from [24]

### 1.3.2 Lithium-ion battery capacities

The capacity of an electrochemical cell is directly proportional to the number of ions able to transfer between the electrodes which can be understood from Faraday's first law of electrolysis:

From Encyclopedia Britannica: *Faraday's laws of electrolysis*, accessed 29th of March 2022 (2021) [25]:

> The amount of chemical change produced by a current at an electrode-electrolyte boundary is proportional to the quantity of electricity used.

Where if seen from the perspective of lithium-ion batteries, it says that the quantity of electricity (charge) is indeed proportional to the chemical change (transferred lithium ions) in the cell. The number of transferable lithium ions $M_{Li}$ can be related to the electric capacity (or charge) $C$ through the Faraday constant $F$ by equation 1.1 below. The units are written out in equation 1.2 where $x$ is the molar amount of transferable lithium ions.

$$C = F \cdot M_{Li} \tag{1.1}$$

$$C = \frac{26.801Ah}{mol} \cdot x \quad mol \tag{1.2}$$

Two terms usually used to describe LIB capacity are *specific capacity* which on a material level means the electrical capacity of the active material per unit mass (usually in $\frac{mAh}{g}$) and the *capacity density* (or volumetric capacity) which is the electrical capacity per unit volume (usually in $\frac{Ah}{L}$). These measures can also be used for the energy (specific energy and energy density) when the voltage is integrated over the capacity as explained in equation 1.3 below. Note that the specific capacity and capacity density measures decrease substantially going from an active material level to cell, pack, module, and battery level due to the added packaging which is electrochemically inactive but adds weight and volume.

### 1.3.3 Lithium-ion battery energy

While specific capacity and capacity density is used for describing the maximum or nominal capacity of a battery, the State of Charge (SoC) indicates the remaining charge (as a percentage of the maximum capacity) during use of the battery. In fact, during use the potential (as seen in figure 1.4 above or explained in theory section 2.1.1) also changes as a function of SoC. By knowing this, it is clear that in order to calculate the total energy capacity of a cell, the maximum potential cannot simply be multiplied by the maximum charge capacity, they must be integrated over the capacity itself as shown in equation 1.3 below.

$$E_{tot} = \int_{min}^{max} V(C)dC \tag{1.3}$$

Where $E_{tot}$ is the maximum energy stored, $V(C)$ is the function of potential versus capacity, and $C$ is the capacity from minimum to maximum charge.

### 1.3.4 Lithium-ion battery electrolytes

The conduction of lithium ions from the cathode to the anode and back is facilitated by the electrolyte. For commercial LIBs and most experimental research, this consists of an organic liquid and a lithium salt. The organic liquid often consists of a mix of linear and cyclic carbonates, for instance, dimethyl carbonate (DMC) and ethylene carbonate (EC) respectively. The lithium salt which is dissolved in the organic liquid adds lithium ions to the solution, aiding in ionic conductivity. The salt often used is $LiPF_6$. When these substances are mixed in a ratio of 1M $LiPF_6$ in a solution of EC:DMC with a 1:1 ratio by volume, it is called LP30. Where LP describes the salt (Lithium hexafluoroPhosphate), and the number describes the electrolyte solution. Similarly, if the linear carbonate DMC is replaced by diethyl carbonate (DEC), the electrolyte is called LP40. A schematic of the organic molecules and the $LiPF_6$ salt is found in figure 1.5 below.

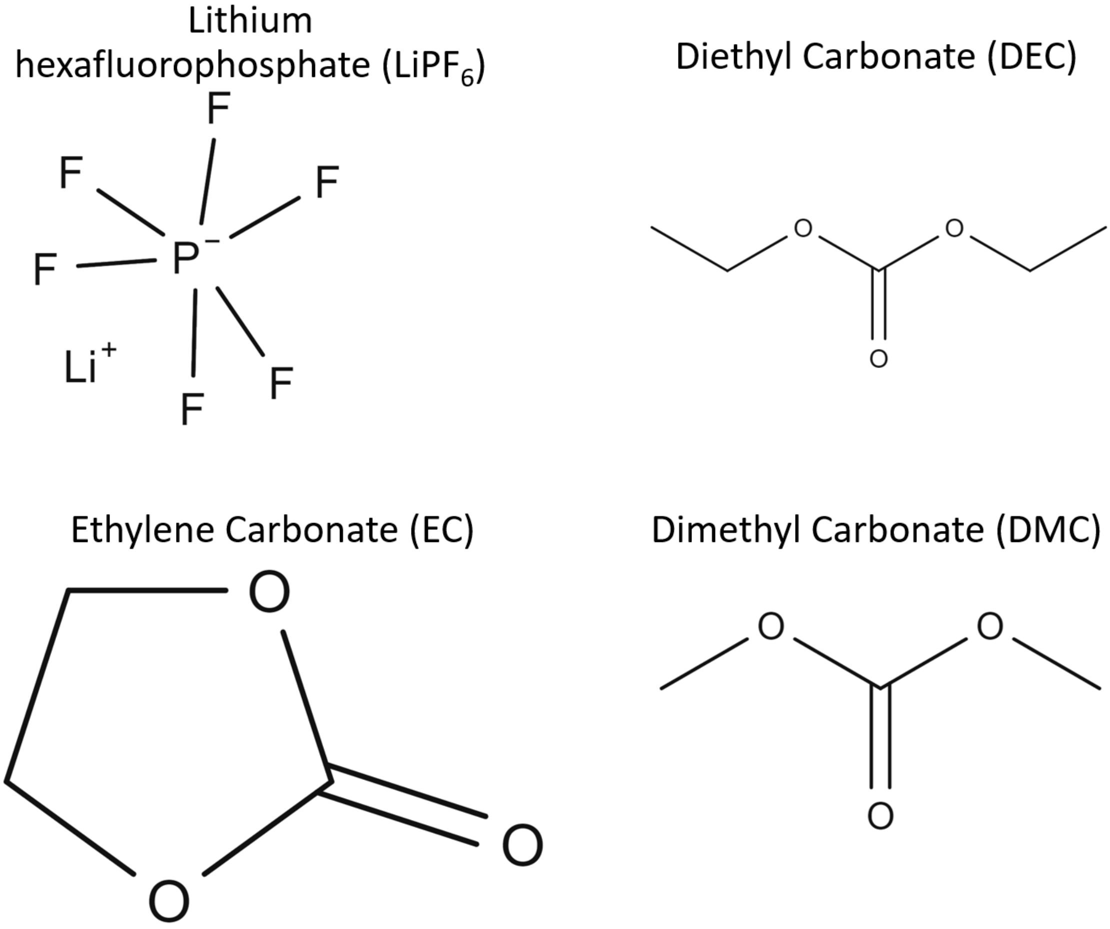

Figure 1.5: Schematic of components of common lithium ion battery electrolytes.

For many different compositions of solvent mixtures, the salt concentration has been optimized for maximum ionic conductivity. Although the concentration of maximum conductivity increases with temperature, this change is very slight and around 1M for $LiPF_6$ in PC:EC:DMC 1:1:1 [26]. Many additives are usually used for various purposes in these electrolytes. For instance, fluoroethylene carbonate (FEC) can be added in small amounts to increase the stability at high voltages, or vinylene carbonate (VC) is used to form a more effective SEI layer on the anode [27].

Other electrolytes used in LIBs are primarily experimental and include ionic liquids and solid-state electrolytes. Ionic liquids consist of organic cations such as pyrrolidinium(PYR) or ammonium, and inorganic or organic anions like $BF_4^-$ or bis(trifluoromethanesulfonyl imide) (TFSI) [28] and are generally considered molten salts. Solid-state electrolytes, often made out of polymer or inorganic/ceramic materials, still have issues with ionic conductivity at room temperatures, as well as having reliable contact with the active materials. However, solid-state electrolytes are invested heavily in and seen as the holy grail of electrolytes due to their supposed safety and the fact that it also works as a separator, eliminating one part from the cell.

## 1.4 Previous work

The LMNO material has previously been researched by Dr. Pushpaka B. Samarasingha here at NAFUMA [29], [30]. He showed by powder neutron diffraction how impurity phases and crystal structure can be tuned through correct post-synthesis heat treatment [29]. Through operando synchrotron studies, he also showed how the variants of LMNO behave during electrochemical cycling [30]. More on what he found in theory section 2.2.4.

When it comes to aluminum substitution, this has been investigated for a wide range of substitution amounts by Zhong et al. [17]. However, they only focused on one type of substitution (Al substituted on both Mn and Ni sites). Aluminum substitution on different sites has been investigated, although with a mol% of less than 5 [14], [16]. In addition, Al-substituted LMNO in the form of hollow microspheres has been investigated [15]. LMNO has also been alumina coated and by sintering of the coated particles doped with aluminum[8].

Personally, I have also worked two-thirds of a semester with this material as the main focus of my bachelor thesis.

## 1.5 Naming of the oxide

In the literature, the compound is referred to by different trivial names, but mostly LNMO or LMNO. Although this material has been around for at least 25 years[31], the literature has not been able to unify and decide on one way to write it. Many articles also refer to this material by the more complicated, yet describing name *high voltage spinel cathode material*, which indicates both its main benefit, crystal structure, and its application.

When it comes to the chemical nomenclature of the material, the book Nomenclature of Inorganic Chemistry in IUPAC Recommendations 2005, frequently called the Red Book [32], delivers some clear rules. First of all, the order of the compounds is first sorted into two categories: electropositive and electronegative. After this, the elements within each category are ordered alphabetically (IR-5.4.1 [32]). For LMNO, this means that the manganese should be in front of the nickel. In addition, the compound should be named with a level of detail satisfying the needs, meaning that a general notation such as ~LiMnNiO (read: circa lithium manganese nickel oxide) can be used (IR-11.3.1 [32]) if the composition is unknown or not of interest. However, if the stoichiometry is known and of interest, this can simply be added, like $\mathrm{LiMn_{1.5}Ni_{0.5}O_4}$, although the convention is to use only small integers like $\mathrm{Li_2Mn_3NiO_8}$ (read: dilithium trimanganese nickel octoxide). For substitutions, the substituent is placed before the substituted atom and can be written in varying compositions like the following (IR-11.3.2 [32]): $\mathrm{LiAl_xMn_{1.5-x}Ni_{0.5}O_4}$ which indicates a substitution of manganese for aluminum with $x$ stoichiometric amount. On this basis, it can also be argued that Ni should be written in front of Mn because Ni is a substituent for Mn in the original compound $\mathrm{LiMn_2O_4}$. For this thesis I have decided to not do this since difficulties in naming will arise when substituting $\mathrm{LiMn_2O_4}$ with both Ni and Al, and rather treat LMNO as a compound worthy of its own name.

# Chapter 2

# Theory and Methods

In this chapter, more advanced electrochemistry is presented, followed by LMNOs material properties, synthesis and safety before the methods of characterization are explained.

## 2.1 Basic concepts of the electrochemical cell

As explained in the introduction, the electrochemical cell consists of mainly three parts: The cathode, electrolyte, and anode, where it is the potentials in the cathode and anode which is the driving force for any reactions. These potentials, what their reactions do, and their kinetics are described in this section.

### 2.1.1 Driving force and potentials

The reason for some materials having higher potentials is that the lithium has lower energy sitting in that structure than what it has when in a low-potential structure. This energy difference is also what is the *driving force* for a battery discharge, where the lithium ion travels from the anode to a cathode (e.g. a graphite anode to a layered oxide cathode). This energy is described by equation 2.1 below, where $\Delta G^0$ is the standard Gibbs energy, $n$ is the charge (number of moles of electrons) involved in the stoichiometric reaction, $F$ is the Faraday constant and $E^0$ is the *standard* cell potential (*standard* means standard conditions, i.e. concentration 1 mol/L, at a pressure of 1 atmosphere, with a temperature of 298.15 K).

$$\Delta G^0 = -nFE^0 \tag{2.1}$$

However, when not in the standard state, the potential can change, and is in that case given by the Nernst equation:

$$E = E^0 - \frac{RT}{nF} ln \frac{a_C^c a_D^d}{a_A a b_B^b} \tag{2.2}$$

where $R$ is the universal gas constant, $T$ is absolute temperature, $nF$ as described above, and $a_i$ the activity of species $i$. The activity of a species is a measure of the effective concentration of a species under non-ideal conditions, and can for an ideal case be swapped with the concentrations. This means that the potential of a LIB changes during its discharge as shown in the introduction section 1.3.1. Note that the above conditions only hold true for steady-state or infinitesimal currents. They do not apply to systems under load where kinetic effects become important.

One of the hot research topics of LIBs is also the potential stability of the LIB parts. J.B. Goodenough explained [33] how the electrolyte is reduced if the electrochemical potential ($\mu_A$) of the anode is above the electrolyte's lowest unoccupied molecular orbital (LUMO). Similarly, if the cathode has an electrochemical potential below that of the highest occupied molecular orbital (HOMO), the electrolyte will be oxidized. A schematic of this is seen in figure 2.1 below.

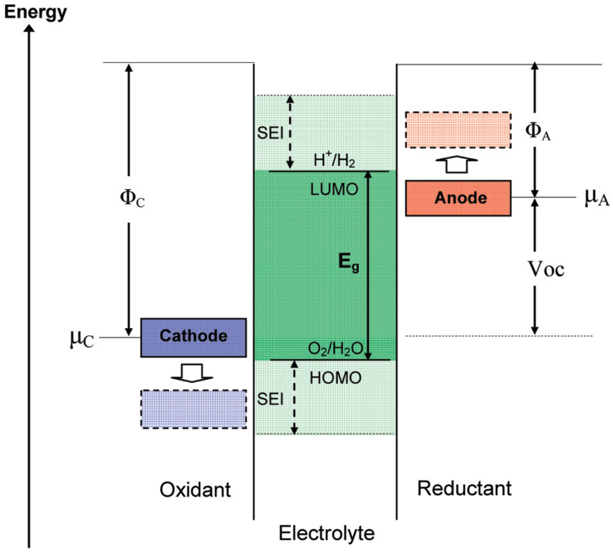

Figure 2.1: Energy diagram of anode, cathode and electrolyte. Reused from [33].

From figure 2.1 above it is also visible how the open circuit cell potential $V_{oc}$ is constituted from the electrochemical potentials of the electrodes $\mu$. This open circuit potential $V_{oc}$ is the same as the cell potential $E$ mentioned above, where $E$ is normally used in electrochemistry, and $V_{oc}$ is used in batteries. The electrochemical electrode potentials can be written in terms of chemical potential $\mu_{chem}$, and the electrostatic potential per mole of species:

$$\mu = \mu_{chem} + zF\Phi \tag{2.3}$$

where $z$ is the number of moles electrons per mole reaction, $F$ is the Faraday constant and $\Phi$ is the work function of the material shown in figure 2.1 above.

The region between the LUMO and HOMO of the electrolyte is called its *electrochemical window*, which for organic electrolytes is usually in the region of 1-4.7 V versus Li/Li$^+$ [33]. Within this region, the electrolyte is thermodynamically stable. However, most anode materials have a higher electrochemical potential ($\mu_A$) than the LUMO of the electrolyte, while still being stable. This is due to a passivation layer that kinetically stabilizes the electrolyte. This passivation layer has been named solid electrolyte interphase (SEI) and is necessary for using today's commercial anode materials. Some cathode materials can also move outside the electrochemical window of the electrolyte, for instance, LMNO at 4.7 V. Some call this cathode electrolyte interphase (CEI)[34] since it differs in material composition from an anode electrolyte interphase, however, I will use SEI for both of these interphases throughout the thesis.

### 2.1.2 Charging, lithiation, and capacity

For the capacity to accumulate, ions and electrons must move. In normal LIBs, the cell is usually assembled with the lithium in the cathode material, and the initial charge state is discharged.

When a current, or a higher voltage, is applied over the two electrodes, the cell is *charged* and the cathode is *delithiated* as the lithium ion moves out, travels through the electrolyte, and lithiates the anode, while the charge neutrality is maintained by the electron flowing in the external circuit.

*Intercalation* is one of the lithiation mechanisms of active materials, and describes the insertion of lithium into an existing structure without changing (restructure, recrystallizing) the structure significantly (ref IR-11.6.6 in the Red Book[32]). Examples of intercalation materials encompass the most used cathode materials, namely layered oxides like $LiCoO_2$ and $Li_3NiMnCoO_6$(NMC). Even though other popular cathode materials like the olivine oxide $LiFePO_4$(LFP) and the spinel oxides $LiMn_2O_4$ and $LiNi_{0.5}Mn_{1.5}O_4$(LMNO) strictly speaking are insertion materials, the word intercalation is often used for these as well. The most used anode material, graphite, also has the intercalation mechanism where the lithium inserts between the layers of graphite. The two other most common lithiation mechanisms are *alloying* and *conversion.* Alloying is when lithium reacts with the electrode to form an alloy. The silicon anode is the most popular alloying electrode we have, and it is still under heavy development due to the large volume changes happening when alloying large amounts of lithium. Conversion electrodes completely change structure when lithiated. Many binary transition metal oxides can undergo a conversion reaction with lithium, although the reversibility of the reaction can be difficult to achieve due to the morphology and structural changes induced by such a conversion. In the reaction equations below these three lithiation mechanisms are exemplified.

**Intercalation (Graphite anode):**

$$Li^+(\text{solv}) + C_6(\text{layered}) + e^- \rightarrow LiC_6(\text{layered})$$

**Alloying (Silicon anode):**

$$Li^+(\text{solv}) + Si(\text{amorphous}) + e^- \rightarrow LiSi(\text{amorphous alloy})$$

**Conversion (CoO anode):** [35]

$$2Li^+(\text{solv}) + CoO(\text{rock salt}) + 2e^- \rightarrow Li_2O(\text{antifluorite}) + Co(\text{hcp or fcc})$$

Keep in mind that the reactions above are simplified and do not directly represent the actual lithiation pathway. Also, note how the electrons in the equations are needed for lithiation to occur. These electrons travel through the external circuit which can be measured and is the whole purpose of electrochemical cells for energy storage. Through these reactions, it is also made clear that the capacity of an electrochemical cell comes from the amount of lithium, and room for it in the electrode.

#### 2.1.2.1 Conductivity and kinetics

There are two main conductivities that are important for a LIB. Electrical conductivity is important in order to efficiently get the electrons from the external circuit and into the active material. In addition, it is equally important that the electrical conductivity is close to non-existent through the electrolyte and separator to minimize internal- or self-discharge. The second conductivity is the ionic conductivity between the electrodes of the cell and through the electrolyte and separator.

The bottleneck in the electronic conductivity will always be between the metallic current collector and the active material particles, and for some materials, this is a bigger problem than for others. For instance, graphite is relatively conductive and can transport its electrons just fine, but many oxide cathodes are semiconductors and need to be of small particle size and have a conductive additive to aid in electron conduction. When electrons reach the areas where metallic electrical conductivity is not an option, several effects like tunneling, activation transport, or hopping transport come into play and significantly increase the total electrical resistance.

The ionic conductivity is often the most troublesome, as lithium is much larger than an electron and generally has lower conductivity. The ionic conductivity of an active material is usually described by its diffusion constant which for a simple concentration gradient can be modeled through Fick's first law in equation 2.4.

$$J = -D\frac{\partial \phi}{\partial x} \tag{2.4}$$

Where $J$ is the diffusion flux, $D$ is the diffusion coefficient (diffusivity), $\phi$ is the concentration and $x$ is the position. However, this law breaks down whenever there are additional electric fields or asymmetry.

The diffusion of lithium ions through the electrolyte (often called the *uncompensated electrolyte resistance*) is also important and has been optimized through systematic studies of electrolytes. Another important factor is the *tortuosity* which describes the effective diffusion length. For instance, if the lithium ion needs to diffuse in between flaked particles, then the diffusion length can change significantly depending on the orientation of the particles, and thus increase the total resistance. These ohmic resistances are called *ohmic polarization*, or *Internal Resistance drop (IR drop)* due to their direct proportionality with the current.

In addition to the ohmic resistances in all the substances, the electrode interface also induces some kinetic barriers. These are referred to as *electrode polarization* and consist of *activation-* and *concentration polarization.* Activation polarization is essentially the overpotential needed to transfer charge from the electrolyte to the active material and is denoted with $\eta_{ct}$ for charge transfer, while concentration polarization $\eta_c$ arises from the mass transport leading to different concentrations of species at the electrode surface than in the bulk.

All these impedances and overpotentials induce an artificial voltage change depending on the direction and magnitude of the current through the electrochemical cell. This voltage deviation is called the overpotential $\eta$, which is then constituted from the following terms:

$$\eta = \eta_{ct} + \eta_c + IR_i \tag{2.5}$$

where the current constituting the overpotentials of electrode polarization ($\eta_{ct}$ and $\eta_c$) has been left out due to its complexity, while the ohmic internal resistance $R_i$ has the simple proportionality to current due to Ohm's law. This total overpotential is then lost as heat (by Joule heating) during operation, as described by:

$$P_{loss} = \eta \cdot I$$

where $\eta$ is the overpotential and $I$ is the total current through the cell. The power is lost as heat through Joule heating.

For conventional aqueous electrochemistry, the Butler-Volmer equation relates overpotential to electrical current shown in equation 2.6 below.

$$j = j_0 \cdot \left\{ \exp\left[\frac{\alpha_a zF\eta}{RT}\right] - \exp\left[-\frac{\alpha_c zF\eta}{RT}\right] \right\} \tag{2.6}$$

Where $j$ is the electrode current density, $j_0$ the exchange current density, $\alpha_a$ and $\alpha_c$ the anodic and cathodic charge transfer coefficients, $\eta$ is the overpotential, $F$ the Faraday constant, $R$ the universal gas constant and $T$ the absolute temperature. Unfortunately, while conventional Butler-Volmer kinetics works well for dilute solutions with single reaction kinetics, it must be modified for analytical use in concentrated solutions and LIBs [36].

## 2.2 Cathode materials

Cathode materials for LIBs can be found in many different structures with many different elements. However, the most commercially evolved today are the layered cathodes.

### 2.2.1 Layered cathodes

The layered cathodes are a group of cathodes where lithium is stored in layers between metal-oxide. Common layered cathodes are: LCO ($LiCoO_2$), NCA ($LiNi_{0.8}Co_{0.15}Al_{0.05}O_2$) and NMC. NMC, or $LiNi_xMn_yCo_zO_2$ is maybe the most ubiquitous cathode, with many variations in transition metal stoichiometry, where $x + y + z = 1$. NMC cathode material has a practical specific capacity of around 200mAh/g when going to 4.2 V versus $Li/Li^+$, which results in a remaining lithium content of around 0.3 in the material when charged [37]. This of course changes depending on the voltage limit of the charge cycle, as it is possible to extract more lithium. However, when this is done, the cathode material gets quite unstable, as there is less and less positive charge between the transition-metal-oxide layers to keep them apart. This instability results in degradation where it is believed that the oxygen oxidizes the electrolyte, and rock salt type structures of the individual transition metals remain.

### 2.2.2 Spinel cathodes

For the spinel cathodes, on the other hand, the structure can be completely delithiated without instant destruction. Most known spinel cathode materials today are variations of LMO ($LiMn_2O_4$). In this material, the capacity is found around 4 V due to the $Mn^{3+}/Mn^{4+}$ redox reaction (more info in section 2.2.5). A variant of this, where 0.5 mol of manganese is substituted with nickel is the LMNO ($LiMn_{1.5}Ni_{0.5}O_4$) this thesis is about.

The biggest reason to use LMNO over LMO is the increased operating potential. The $LiMn_2O_4$ spinel structure has an operating potential of around 4 V, while LMNO is at 4.7 V. The reason for this is that in LMNO, the oxidation of $Ni^{2+}$ and $Ni^{3+}$ happens when lithium is removed. This redox reaction has a higher potential than the oxidation of $Mn^{3+}$ in the LMO. Actually, in most LMNO materials there is some $Mn^{3+}$, which means that some 4 V capacity can be seen. $Mn^{3+}$ mostly occurs due to oxygen vacancies as explained below.

In addition to this, the structural stability of LMNO is higher. This is because of the shortening of the transition metal-oxygen bond, which increases the bond strength and thus the stability of LMNO. This effect has been modeled through DFT [38] and is also found experimentally as can be seen by the lattice parameter difference between the two structures [39]–[43]. This also affects the cycling performance, where it is proposed by Amatucci et al. that due to the lower unit cell size, it is more energetically unfavorable to dissociate transition metals into the electrolyte.

However, even though LMNO is very promising, there are some downsides. One of those is the thermal stability problems, which have been seen to be worse for LMNO [44]. Although, it must be mentioned that it is not completely clear whether this is due to an increased SEI layer due to its high potential, or due to its crystal structure.

### 2.2.3 LMNO - The structure

$LiNi_{0.5}Mn_{1.5}O_4$ (LMNO) has a spinel structure, and according to the ordering of the transition metal cations, can be in two different space groups. The *ordered* material is in space group $P4_332$ with manganese occupying the 12d Wyckoff sites, and nickel occupying the 4a sites. This structure has lithium at the 8c sites and oxygen at 8c and 24e sites. The *disordered* material is in $Fd\bar{3}m$ where manganese and nickel is randomly distributed on the 16d sites. Lithium sits at the 8a sites while oxygen sits at the 32e sites in the disordered structure [45]. For both of these structures, the nickel and manganese sites are octahedrally coordinated.

The ordering of the nickel and manganese on their respective sites makes some planes in the structure different from what they were when the Ni and Mn were randomized. These new planes give rise to what are called superstructure peaks in diffraction data which is a common indicator to use when looking for ordering in the LMNO spinel.

The ordered spinel phase is shown below in figure 2.2. In an idealized LMNO structure, the oxidation states are as follows: $Li^{1+}$, $Ni^{2+}$, $Mn^{4+}$, and $O^{2-}$.

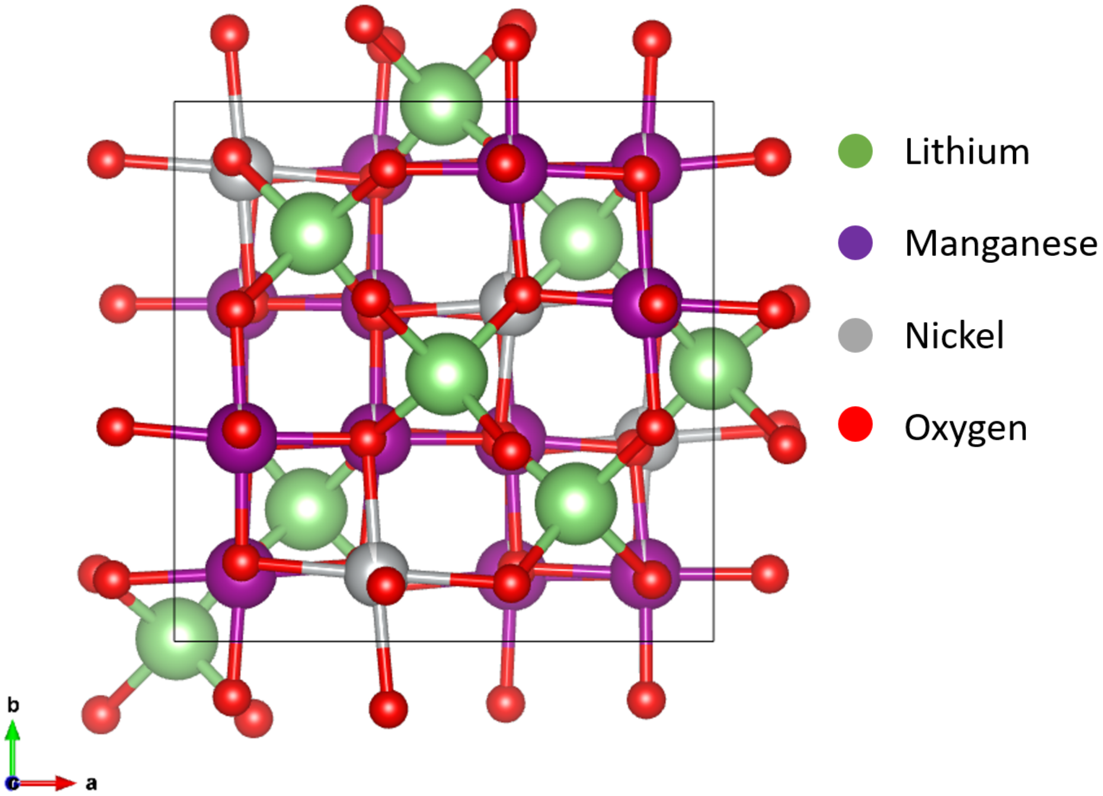

Figure 2.2: Ordered LMNO structure viewed down the c axis. Lithium is green, nickel is gray, manganese is purple and oxygen is red.

To visualize the three-dimensional diffusion paths in the spinel, an off-axis supercell of ordered LMNO is shown in figure 2.3. The diffusion pathways are directly into the figure through the tetrahedral lithium sites. Due to the cubic symmetry of this material, these pathways are found in three directions orthogonal to each other.

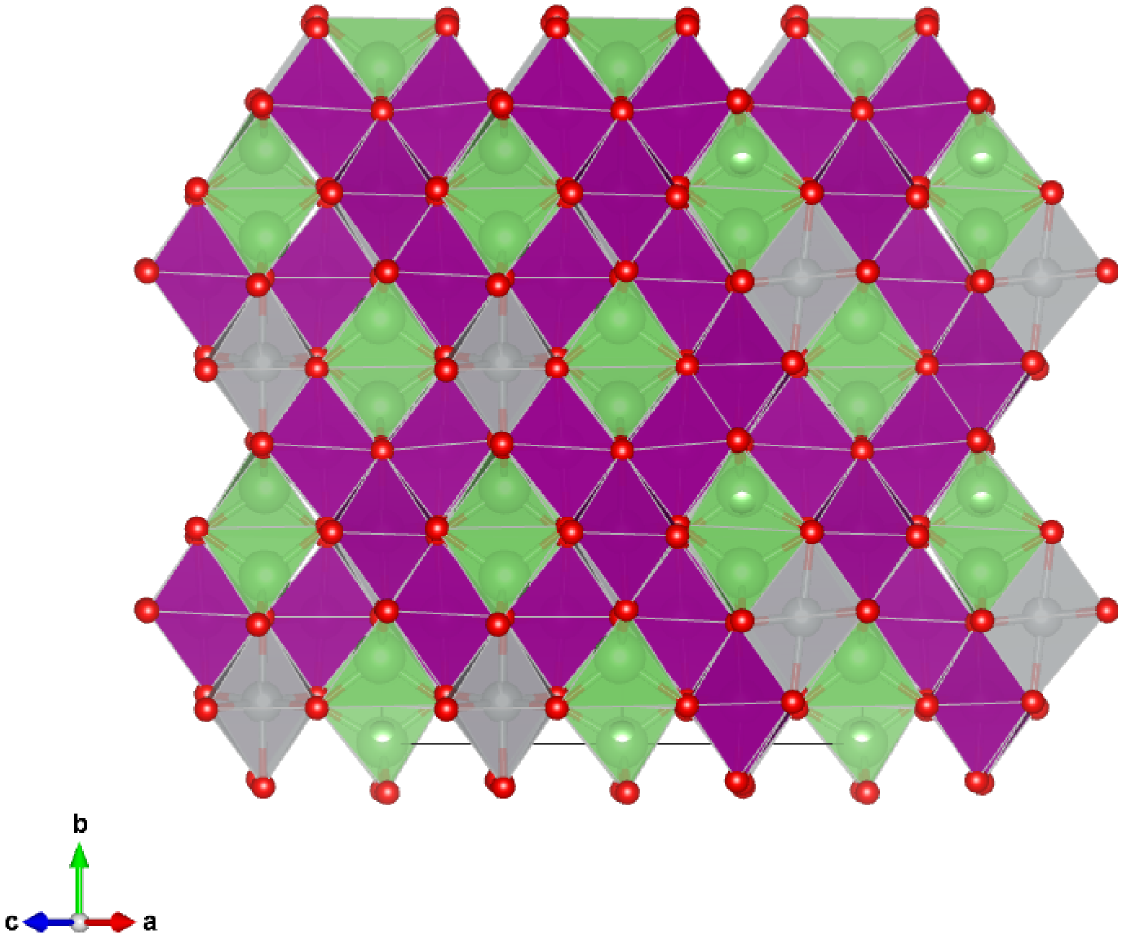

Figure 2.3: Ordered LMNO with polyhedrons in a 2x2x2 supercell. Lithium is green, nickel is gray, manganese is purple and oxygen is red.

### 2.2.4 LMNO - Structural tuning

Samarasingha et al. showed through neutron diffraction and Raman studies that when doing post-synthesis heat treatment of LMNO, some parameters could be tuned. He showed that when sintered at 900°C, the rock salt type impurity phase $Li_xNi_{1-x}O$ is formed, but that this reverses when lowering the temperature [29]. Manganese can also occur in this rock salt type impurity, and then an ordering of manganese and nickel can occur, which would show superstructure peaks in an XRD pattern.

The ordering of the nickel and manganese cations in the LMNO phase can also be tuned by annealing at specific temperatures, where he showed that by sintering at 900°C for 10 hours followed by 700°C for 10 hours, the annealing yielded an ordered structure. However, a fully disordered material could be obtained by only doing heat treatment at 600°C or eliminating the heating step at 700°C [29].

In addition to impurity phases and Mn/Ni ordering, oxygen deficiency has also been studied in the LMNO crystal. For instance, Aktekin et al. [46] showed by thermogravimetric analysis that oxygen release from the spinel material happens at approximately 730°C when under oxygen flow (1bar), while if heated in air it starts at around 695°C. It must be kept in mind that this was for slightly manganese-rich samples ($Mn_{1.56}Ni_{0.44}$) and it has been shown that increasing the nickel content increases the oxygen release temperature [47]. This oxygen release is believed to be charge compensated by some $Mn^{4+}$ reducing to $Mn^{3+}$ [12], [48], [49].

Lithium interstitials can also exist if the material has been prepared with an excess of lithium [50]. However, it is unclear whether the lithium sits on octahedral sites in the regular cubic LMNO structure, or is present in the form of a separate $Li_2$NMO-phase mentioned in section 2.2.5 below.

#### 2.2.4.1 Trivalent transition metal substitution

When substituting any element in a structure, size matters. For instance, when substituting aluminum in place of nickel, the $Al^{3+}$ cation will have a different ionic radius than $Ni^{2+}$, which affects the crystal structure. Vegard's law states that the lattice parameter of a solid solution with two constituents is approximately the weighted mean of the two constituents' lattice parameters [51]. For reference, a table of the relevant ionic radii has been included in table 2.1 below.

Table 2.1: Ionic radii of relevant ions

| Element | Charge | Coordination | Radius (pm) |
|---|---|---|---|
| **Aluminum** | 3+ | Octahedral | 67.5 |
| | 3+ | Tetrahedral | 53 |
| **Manganese** | 2+ (low spin) | Octahedral | 81 |
| | 2+ (high spin) | Octahedral | 97 |
| | 3+ (low spin) | Octahedral | 72 |
| | 3+ (high spin) | Octahedral | 78.5 |
| | 4+ | Octahedral | 67 |
| | 5+ | Octahedral | 60 |
| **Nickel** | 2+ | Octahedral | 83 |
| | 3+ (low spin) | Octahedral | 70 |
| | 3+ (high spin) | Octahedral | 74 |
| | 4+ | Octahedral | 62 |

In addition to the change in unit cell size, the oxidation states of the elements can change. For instance, if a trivalent cation is inserted in place of a tetravalent cation (e.g. $Mn^{4+}$) the charge must be compensated somehow. Examples of charge compensation in LMNO are oxygen deficiency, lithium interstitials, or an increased average oxidation state of nickel. If a trivalent cation is inserted in place of a divalent cation ($Ni^{2+}$), the charge compensation can be made by lowering the average oxidation state of manganese or by having lithium vacancies.

The literature also suggests the same type of charge compensation mechanisms, however, it is believed that the main compensation mechanisms are partial reduction of manganese to 3+ or partial oxidation of nickel to 3+ respective of whether the nickel or manganese was substituted by the trivalent cation [52].

Reports which investigate trivalent doping suggest that trivalent cations segregate to the surface, creating a more stable cathode-electrolyte interface [52], [53]. Other studies suggest that doping, especially with cobalt or iron, could also suppress the Jahn-Teller lattice distortion[54]. Both of these effects are believed to improve the cycle life of the material due to a stronger particle surface and less movement in the crystal lattice respectively.

Previous work on aluminum substitution in the LMNO lattice shows that with the introduction of $Al^{3+}$ ions, the structure tends to be more disordered [8], [16], [17]. In addition to this, there is a trend where the lattice parameter decreases with increased doping, presumably because of the smaller ionic radii of $Al^{3+}$. On solubility limits of aluminum in the structure, no work has been found for LMNO, however, for LMO, Amatucci et al. reported that this was with a molar amount of 0.2 Al [55].

### 2.2.5 LMNO - The electrochemistry

When deintercalating lithium, starting from $x = 1$ in $Li_xNi_{0.5}Mn_{1.5}O_4$ and increasing in voltage, the first capacity plateau is located at 4 V vs $Li/Li^+$. This originates from the redox reaction $Mn^{3+}/Mn^{4+}$ and is only present due to the previously mentioned (section 2.2.4) defects in the structure which is charge compensated by some tetravalent manganese being trivalent. When all the $Mn^{3+}$ has been consumed, nickel is oxidized from 2+ to 4+ at a potential of 4.7 V vs $Li/Li^+$. An example of this can be seen in figure 2.4 below. The voltage plateau at 4.7 V can also be split in two depending on the ordering of the material. These two plateaus then represent the $Ni^{2+}/Ni^{3+}$ and $Ni^{3+}/Ni^{4+}$ redox reactions separately [30]. If the material has been made with a slightly adjusted synthesis procedure, e.g. with excess lithium, $Li_2Ni_{0.5}Mn_{1.5}O_4$ can have been introduced, the delithiation of which usually results in capacity at 3 V [50].

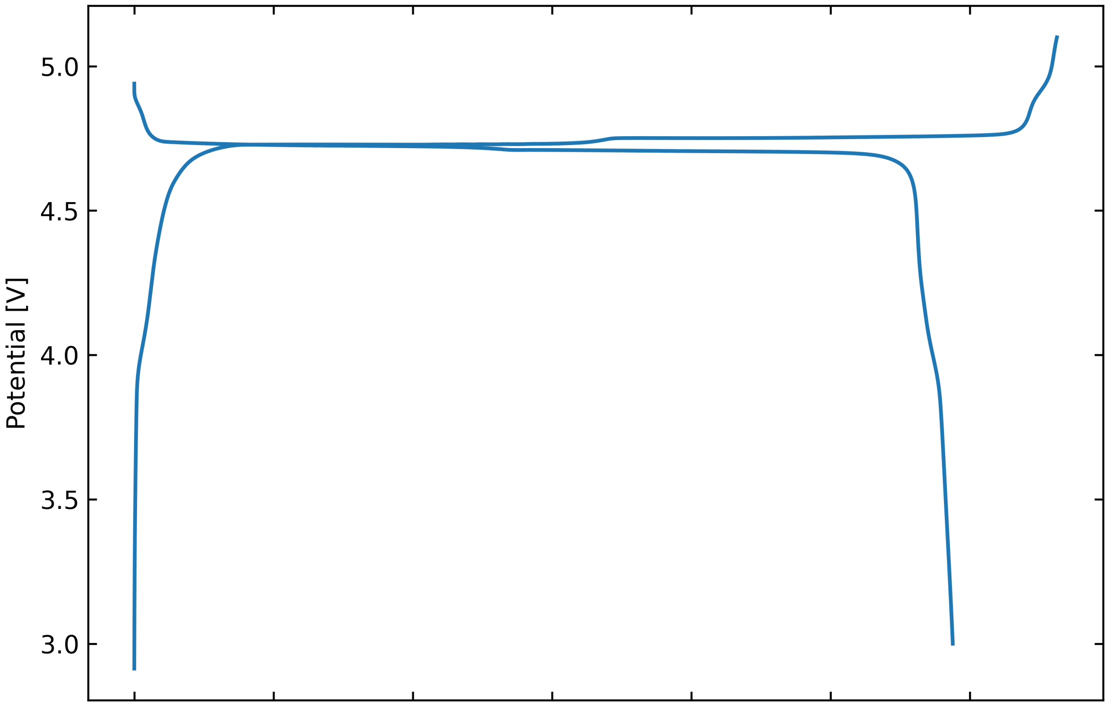

Figure 2.4: Potential versus capacity for an LMNO material with very little $Mn^{+3}$ cycled galvanostatically with a C-rate of C/10.

For LMO, when crossing below 3 V it is believed that the cubic $Li_1Mn_2O_4$ structure transitions to the tetragonal $Li_2Mn_2O_4$, and during this transition Jahn-Teller deformation occurs due to the increase in $Mn^{3+}$. This has been given the blame for the bad cycling stability of the full $0 \leq x \leq 2$

range in $Li_xMn_2O_4$ [56]. This is also seen for LMNO, where X-Ray diffraction shows the expansion of the crystal lattice in one direction and shrinkage in the two others, making a transition from cubic to tetragonal where all lithium over one stoichiometry unit sits on octahedral sites [57], [58].

The literature shows that with trivalent doping generally the conductivity and stability of the material increase [52]. Some theorize that this could be due to the doping lowering the Jahn-Teller distortion and thus reducing $Mn^{3+}$ disproportionation[54].

### 2.2.6 LMNO - Degradation mechanisms

The cycling stability of LMNO is believed to be worse than the most used commercial cathode materials today because of the disproportionation reaction of $Mn^{3+} \rightarrow Mn^{2+} + Mn^{4+}$ where $Mn^{2+}$ is dissolved into the electrolyte. This is believed to happen mostly when the lattice undergoes Jahn-Teller distortion during lithiation and delithiation [54] and also accompanies the protonation of surface oxygen in LMNO [59], [60].

In addition to the manganese dissolution, Sun et al. found through synchrotron X-ray fluorescence microscopy that the fraction of nickel to manganese on the lithium metal anode was higher than the spinel itself (around 0.5) [59]. This indicates that nickel also does dissolve into the electrolyte during the degradation of LMNO, but that it quickly moves to the anode, while manganese can be found in the electrolyte.

It has also been reported that fluorine from the electrolyte could react with trace water in the cell to form hydrofluoric acid (HF). This HF will then dissolve LMNO through equation 2.7 below [61]:

$$\begin{aligned} 2\mathrm{LiNi0.5Mn_{1.5}O_4} + 4\mathrm{HF} \rightarrow \quad & 3\mathrm{Ni_{0.25}Mn_{0.75}O_2} + 0.25\mathrm{NiF_2} \\ & +0.75\mathrm{MnF_2} + 2\mathrm{LiF} + 2\mathrm{H_2O} \end{aligned} \tag{2.7}$$

On the mechanical degradation of LMNO particles, it is believed to happen mostly due to cracks arising from the high crystal stress arising when the structure is delithiated [62].

### 2.2.7 Electrochemical stability of electrolyte

The electrochemical potential of LMNO is right outside of that of normal organic electrolytes used in LIBs (4.7 V) and is thus kinetically stabilized by an SEI. Duncan et al. found this SEI film to be composed of polycarbonates, polyether, LiF, and $Li_xPO_yF_z$ salts [63]. He also found that the thickness of the SEI grows on cycling, but that the composition was the same regardless of the capacity fade. Others have also shown that normal organic electrolyte is unstable above this potential [64], which means that if there is a wish to eliminate the cathode SEI, other electrolytes have to be used. One of the electrolytes promised to be stable above this potential is ionic liquids.

Ionic liquids (introduced in section 1.3.4) have been shown to be stable up to $5.5V$ vs $Li/Li^+$[28]. While the main problem with ionic liquids is the low ionic diffusion rate, the passivation of aluminum is not as good. This is because as salt, the conventional $LiPF_6$ salt is usually not used, and other salts like LiTFSI are used instead [28]. However, unlike more unstable salts like $LiPF_6$ and $LiBF_4$ [65], LiTFSI has good compatibility with moisture and does not react to form HF. The same goes for salts without fluorine, like $LiClO_4$ [66]. This means that with the use of ionic liquids, it is probable that the metallic aluminum of the current collector is not passivated by the HF, and will thus degrade more.

### 2.2.8 Electrochemical stability of mechanical parts

When increasing the potential of the cathode in a cell, the potential often exceeds the electrochemically stable window of the parts on the cathode side [67]. The normal stainless steel used, SS304, shows instability above 4 V. This is believed to be due to the relatively stable $Fe_3O_4$ and $Cr_2O_3$ oxide layers on the surface being corroded by the trace amounts of HF from water residues reacting with the $LiPF_6$ in standard electrolytes [68]. SS316L is more stable and is suitable up to 5.1V, however, there are still small side reactions happening at higher voltages [67]. When going higher than this, aluminum coated parts are used [67], [68].

Myung et al. suggest that aluminum reacts with HF to form $AlF_3$, which works as a passivation layer and prevents further reaction with the material. This should happen at a voltage of around 4 V vs $Li/Li^+$ and hinders further reactions between HF and the aluminum [69]. This is also supported by others [65], [66], [70].

## 2.3 Synthesis of LMNO

LMNO is most often produced through conventional synthesis methods like the solid state[57], [71], co-precipitation[24], [57], [72], and sol-gel[29], [30], [42], [44], [57] methods, however other synthesis routes like thermopolymerization[16], [17] or hydrothermal synthesis[54], [57] can also be used.

While the solid-state synthesis relies on diffusion for homogeneous cation mixing, in the sol-gel method, the cations are already mixed before nucleation and growth, significantly decreasing the time needed for sintering. In addition, because the precursors of the sol-gel synthesis can be in solutions, they can be as dilute as needed for control during the weigh-in, leading to very good stoichiometric control. Another benefit of the sol-gel synthesis versus the co-precipitation synthesis is that the solubility product does not need to be well-controlled, as it is much easier for the cation to stay in solution when in the form of a chelate. These factors make the sol-gel method the preferred choice for easy synthesis of ceramic oxides where high stoichiometric control is needed.

### 2.3.1 The sol-gel synthesis

The sol-gel synthesis starts by mixing a solution (or sol) out of soluble precursors like nitrates, acetates, or oxides. Oxides especially can be hard to dissolve in aqueous solutions, but this can be solved by adding nitric acid. After dissolving cation precursors, a chelating agent is added. The cations stick to the chelating agent's negative hydroxy group by borrowing an electron lone pair and creates a chelate [73]. A very common chelating agent is citric acid, however, others like glycine [74], urea [75], and tartaric acid [76] are also used. When the water is then boiled off, the sol turns to a gel while the cations are still homogeneously mixed and stuck to the chelating agent. When in a gel state, the rest of the water bound in the gel can be evaporated, and a xerogel is formed. This is then followed by a calcination for removal of the organics (e.g. acetate precursor or citric acid) and then sintering for crystallization and growth of the product.

### 2.3.2 The Pechini synthesis and combustion

A twist to this synthesis made by Pechini in 1967 [77] was to use ethylene glycol to bind the chelates together to form a network. This method has been named the sol-gel Pechini method. Further, using the ethylene glycol as an oxidizer to burn off the organics has been used to create the sol-gel Pechini combustion synthesis, where the gel combusts after the evaporation of water, skipping the step with the xerogel and moving straight to partial calcination. This combustion usually results in a homogeneous amorphous mix of cations and left-over organics in the powder, meaning it still needs to be properly calcined and sintered. The working principle of how the sol-gel Pechini synthesis network formation and gelating process happens can be found in figure 2.5 below which has been reused from my bachelor thesis.

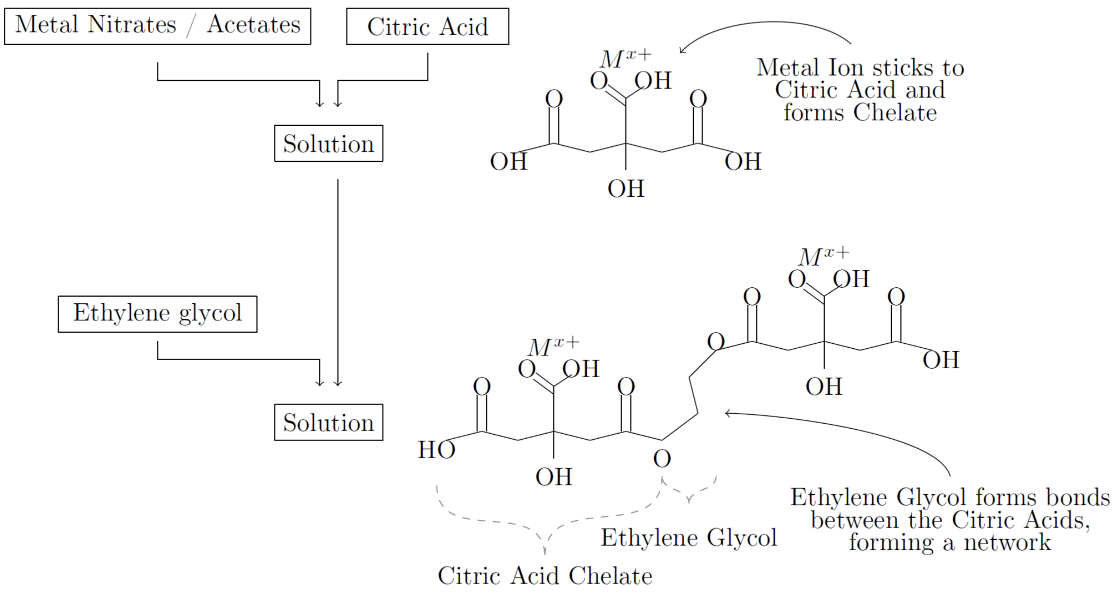

Figure 2.5: Practical and functional principle of the Pechini synthesis. Reused from my bachelor thesis.

### 2.3.3 Other synthesis methods

Here, other synthesis methods used for LMNO preparation are briefly mentioned.

#### Solid-state synthesis

Solid-state synthesis is done by stoichiometric mixing of solid-state precursors, often in the form of oxides, however, other compounds like acetates or nitrates can also be used. This is then either mortared or ball-milled for the best possible mixing of precursors before being calcined and sintered. However, often the kinetics of cation diffusion is too low to create homogeneous products. The kinetics can be increased by increasing the sintering temperature or increasing the surface of diffusion through more thorough precursor mixing. A method often applied is the *shake and bake* which means to mix precursors, calcine and sinter, and then go back to mixing (e.g. mortaring or ball-milling) before sintering again. This is then done as many times as needed to obtain a pure product. Surface contact between precursor particles can also be increased by pellet-pressing.

#### Co-precipitation synthesis

During co-precipitation synthesis, cation precursors can be introduced at two different points, either before or after the co-precipitation. Usually for LMNO, nickel, and manganese solutions are prepared with the correct concentration and added to a coprecipitation reactor in the correct stoichiometric amount to be able to form a metal carbonate with the right Mn/Ni ratio. The concentration is important since the cations need to co-precipitate when the precipitation agent(e.g. an aqueous solution of sodium carbonate) is added. This creates the metal carbonate which can then be filtered out and washed before being sintered with lithium carbonate or eventual substituents like aluminum oxide [78].

## 2.4 Safety

The most prominent threat of today's LIBs is internal short-circuiting. At the pace batteries are being produced, no manufacturer can guarantee flawless manufacturing for each cell. The largest threat during production is loose particles. An internal short circuit, depending on the impedance, can heat a cell to over 1000°C in less than 5 ms leading to decomposition and ignition of the cell materials [79]. An eventual fault does not need to happen straight after manufacturing either. During the cycling of the battery, the electrodes contract and expand which can physically move parts within the cell. This means that LIBs can start self-heating for no apparent reason down the road. Because of this, it is rather important that the chemistry is stable to allow for as much leeway as possible during an eventual thermal scenario.

The different stages of a thermal scenario start with the heating of the battery. This can come from external heat sources, or internally from an internal short, high load, or overcharge. The battery can then continue self-heating which might look slow at the start but which also increases in heating rate. During this process, ignitable gasses can form and if ignited lead to a fire or explosion. When the heating rate comes above 10°C/min regardless of eventual gassing, the battery is said to go into thermal runaway, as this is considered uncontrollable heat output. This scenario will often increase the temperature so high that autoignition of any combustible compounds takes place, which can result in fire or explosion. An overview of how a hazardous event can start and evolve can be found in figure 2.6 below.

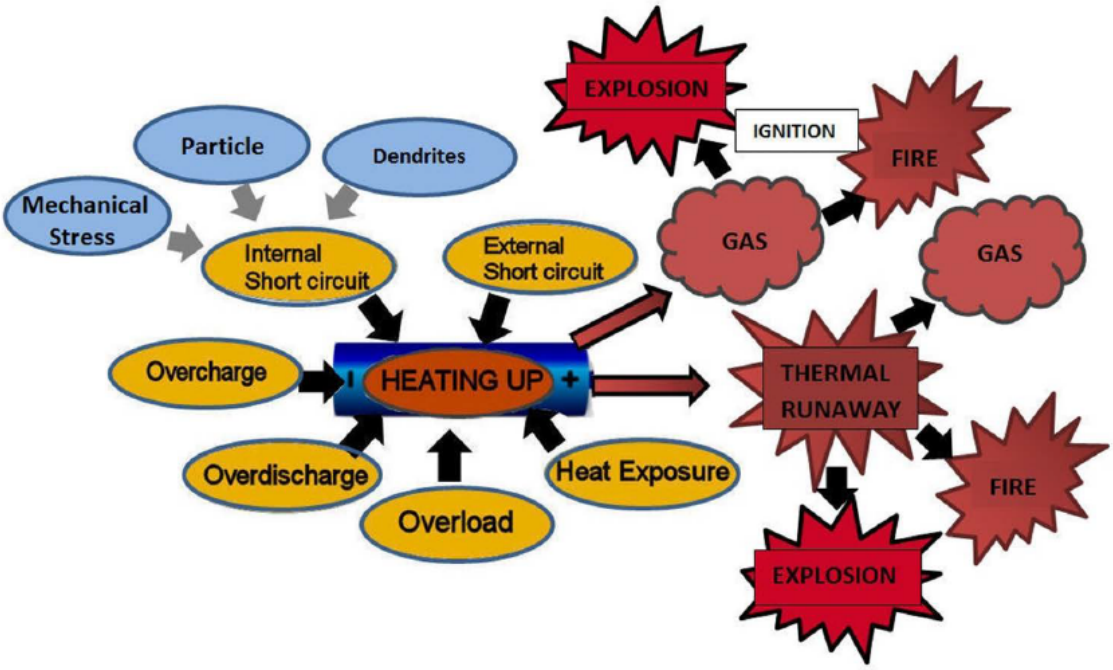

Figure 2.6: Overview of lithium-ion battery hazards. Credit: Torleif Lian, Norwegian Defense Research Establishment (FFI).

Different factors affect the severity of a battery fire. An estimate of the available energy in a battery is a good place to start, but it is also important to evaluate how fast this energy is released. For instance, an explosion or detonation is usually much more harmful than a battery fire. When looking at the available energy, compared to other materials, the one of a lithium-ion battery is very low as can be seen in table 2.2 below.

Table 2.2: Table showing the potential chemical energy in different materials [20].

| **Substance** | TNT | Advanced LIBs | Chocolate |
|---|---|---|---|
| **Energy Density [kWh/L]** | 1.86 | 0.35 | 6.10 |
| **Reaction speed on ignition** | Instant | Seconds - Hours | - |
| **Damage potential** | High | Medium | Low |

However, these numbers are not a good comparison, since the energy from the chocolate is the energy you can get out of eating it, the energy of the TNT of an explosion, and the energy of the battery is only the electrical energy stored in the battery. In reality, the potential energy of a LIB is substantially higher when the energy of burning electrolyte and electrodes are taken into account. This was shown by Brian Barnett in his presentation at the Battery Safety seminar in Boston in 2010 by figure 2.7 below.

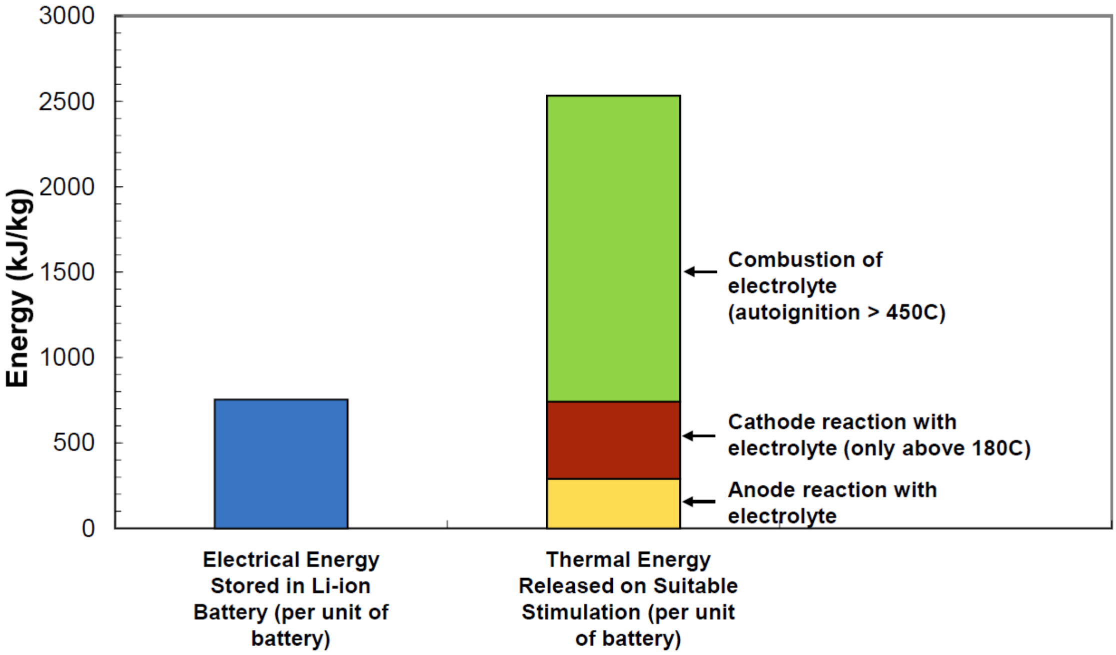

Figure 2.7: Available energy in different parts of a LIB cell. Reused from [80]

### 2.4.1 Thermal stability

The thermal stability of a lithium-ion cell is heavily influenced by the materials used in the cell. This includes the active materials, binders, conductive additives, and electrolyte. Even though the reason for reaching thermal instability is often a mechanical or electrical failure of systems external to the cell, the actual stability is mostly determined by the materials internal to the cell.

Starting with the *anode*, it has been seen that exothermic reactions can start at a temperature around 70°C due to the metastable phases of the SEI which form on the anode. These metastable phases include $ROCO_2Li$, $(CH_2OCO_2Li)_2$, ROLi and polymers, while the stable phases of the SEI includes LiF and $Li_2CO_3$. An example of the reactions can be described as follows [81]:

$$(CH_2OCO_2Li)_2 \rightarrow Li_2CO_3 + C_2H_4 + CO_2 + \frac{1}{2}O_2 \tag{2.8}$$

In addition to this, lithium which has been intercalated in the graphite can be freed by the temperature increase from the exothermic reaction in equation 2.8 (or another heat source), and react with the different organic solvents to form very flammable gasses such as ethylene and ethane from the two most common electrolyte solvents, ethylene carbonate (EC) and dimethyl carbonate (DMC) [81]:

$$2Li + C_3H_4O_3(EC) \rightarrow Li_2CO_3 + C_2H_4 \tag{2.9}$$

$$2Li + C_3H_6O_3(DMC) \rightarrow Li_2CO_3 + C_2H_6 \tag{2.10}$$

These reactions usually start at 100°C.

For the *Electrolytes* it has been shown that the solvents, EC and DMC both show exotherms (at 200°C and 230°C respectively) when heated individually in a C80 micro-calorimeter[82]. These exotherms are believed to be their respective decomposition temperature. These organic solvents also have their respective boiling points (EC at 238°C and DMC at 90°C) which are endothermic [83]. The vaporization enthalpies for these materials are 60kJ/mol for EC while for DMC it is only 37.7kJ/mol.

On the *cathode* side, the SEI layer is most often not as thick as it is on the anode due to the potential of the cathodes being within the electrochemically stable window of the electrolyte. This means that cathode reactions usually happen at higher temperatures, where it is the material itself that undergoes exothermic reactions. In the case of $LiCoO_2$, this happens at around 200°C where oxygen is developed[84]:

$$\mathrm{Li}_y\mathrm{CoO}_2 \to y\mathrm{LiCoO}_2 + \frac{1}{3}(1-y)\mathrm{Co}_3\mathrm{O}_4 + \frac{1}{3}(1-y)\mathrm{O}_2 \tag{2.11}$$

For more modern cathode materials like NMC, the proposed mechanism is[85]:

$$\mathrm{Li}_{0.35}(\mathrm{NiCoMn})_{1/3}\mathrm{O}_2 \to \mathrm{Li}_{0.36}(\mathrm{NiCoMn})_{1/3}\mathrm{O}_{2-y} + \frac{y}{2}\mathrm{O}_2 \tag{2.12}$$

whereas the reaction for delithiated LMO can be described by reduction of the manganese to a lower-valence oxide [86]:

$$2\mathrm{Mn}_2\mathrm{O}_4 \to 2\mathrm{Mn}_2\mathrm{O}_3 + \mathrm{O}_2 \tag{2.13}$$

The decomposition pathways for LMNO have been thoroughly studied and described by Hu et al.[71] by the use of in-situ XRD coupled with mass spectroscopy and XAS, where they found that delithiated LMNO has oxygen-releasing reactions happening already at 300°C whereas the LMO material has no oxygen release before hitting 375°C in heating experiments without the presence of an electrolyte. They propose this to be because of the highly reductive behavior of $Ni^{4+}$. By the use of this setup, they also found that the ordered LMNO phase has the oxygen release peak at a higher temperature (300°C) than the disordered LMNO (250°C), and suggests two different pathways for oxygen release depending on the material Mn/Ni ordering.

$$\begin{aligned}\mathrm{Ni}_{0.5}\mathrm{Mn}_{1.5}\mathrm{O}_4 &\overset{\text{heating}}{\longrightarrow} \frac{1}{2}\mathrm{NiMnO}_3 + \frac{1}{2}\mathrm{Mn}_2\mathrm{O}_3 + \frac{1}{2}\mathrm{O}_2 \uparrow \\ &\overset{\text{heating}}{\longrightarrow} \frac{2}{3}\mathrm{Mn}\left(\mathrm{Ni}_{0.75}\mathrm{Mn}_{1.25}\right)\mathrm{O}_4 + \frac{1}{6}\mathrm{O}_2\end{aligned} \tag{2.14}$$

$$\begin{aligned}\mathrm{Ni}_{0.5}\mathrm{Mn}_{1.5}\mathrm{O}_4 &\overset{\text{heating}}{\longrightarrow} \square_{1-x}\mathrm{Mn}_x\left(\mathrm{Ni}_{0.5}\mathrm{Mn}_{1.5-x}\right)\mathrm{O}_{4-2x} + x\mathrm{O}_2 \uparrow \\ &\overset{\text{heating}}{\longrightarrow} \frac{2}{3}\mathrm{Mn}\left(\mathrm{Ni}_{0.75}\mathrm{Mn}_{1.25}\right)\mathrm{O}_4 + \frac{2}{3}\mathrm{O}_2 \uparrow\end{aligned} \tag{2.15}$$

where the first reaction 2.14 is the most dominant for the disordered type spinel and happens when the delithiated LMNO decomposes to ilmenite $NiMnO_3$ and $\alpha$-$Mn_2O_3$ where most of the oxygen is released, before the formation of the $NiMn_2O_4$ spinel. The second reaction path (eq 2.15) was attributed to the ordered spinel with a migration of the manganese ions from octahedral sites to the empty Li tetrahedral sites (denoted with $\square$ in the equation). Due to this migration process without a significant change in the crystal structure, the oxygen is released over a larger temperature window.

To summarize the findings on the thermal stability of different parts of a lithium-ion cell, figure 2.8 below has been compiled from the literature. The same findings have been tabulated in table (2.3) with references. The *Method* column denotes which type of characterization was used, where ARC is Accelerating Rate Calorimetry (further explained in section 2.5.5) and DSC is Differential Scanning Calorimetry.

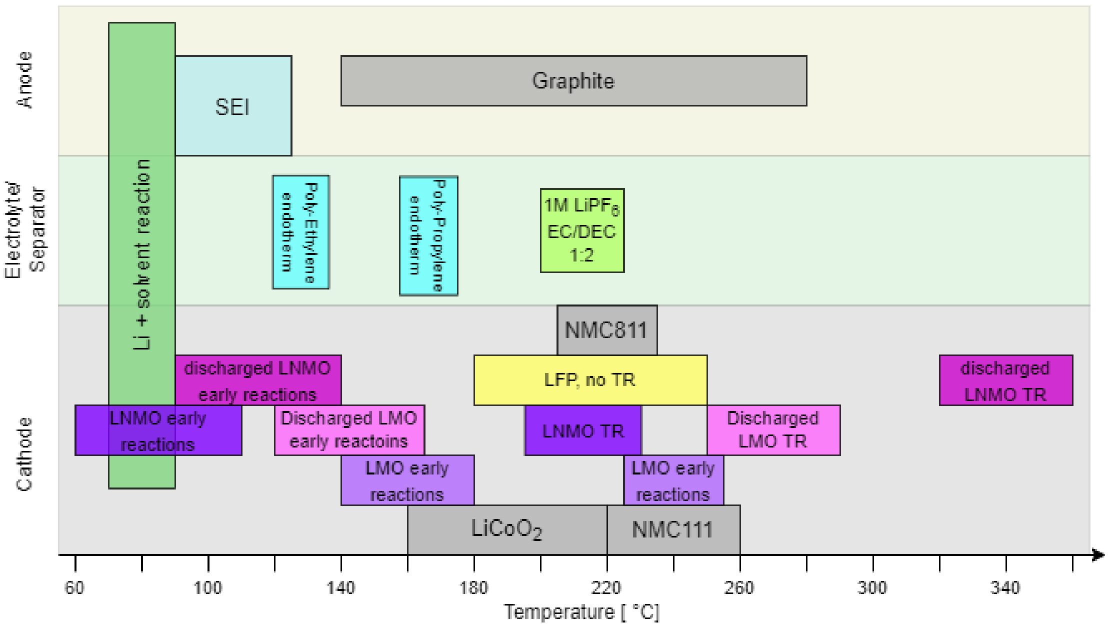

Figure 2.8: Overview of thermal reactions in a LIB at different temperatures. TR means thermal runaway. All materials are in delithiated form unless specified otherwise.

Table 2.3: Thermal stability of different materials in a LIB as reported from experimental studies. Chg denotes if the material is fully charged, and Ele denotes if it was measured together with electrolyte. For ARC experiments, the temperature given for $T_{peak}$ is the temperature when crossing over to thermal runaway(>10°C/min), while for DSC it is the center of the temperature rate peak.

| **Material** | **Chg Ele** | $\mathbf{T_{onset}}$ | $\mathbf{T_{peak}}$ | **Method** | **Ref** |
|---|---|---|---|---|---|
| SEI | – ✓ | 70 | ? | | [81] |
| Graphite | ✓ ✓ | 140 | 260 | DSC | [87] |
| PolyEthylene | – $x$ | – | melt 133 | DSC | [87] |
| PolyPropylene | – $x$ | – | melt 163 | DSC | [87] |
| (1M LiPF$_6$ EC/DEC 1:2) | – ✓ | 205 | 210 | ARC | [44] |
| LCO | ✓ ✓ | 160 | 210 | ARC | [88] |
| NMC111 | ✓ ✓ | 220 | 260 | DSC | [87] |
| NMC442 | ✓ ✓ | 175 | 250 | ARC | [89] |
| NMC811 | ✓ ✓ | 210 | 230 | DSC | [90] |
| LMNO | – ✓ | 80 | 350 | ARC | [44] |
| LMO | – ✓ | 120 | 275 | ARC | [44] |
| LMNO | ✓ ✓ | 60 | 215 | ARC | [44] |
| LMO | ✓ ✓ | 140 | 244 | ARC | [44] |
| LFP | ✓ ✓ | 180 | – | ARC | [91] |

Although the values in table 2.3 identify the onset and thermal runaway temperatures of the materials, it must be noted that the heat rates beyond the thermal runaway can vary from material to material, and has not been included in this comparison due to instrumental uncertainties at these high heat-rates.

### 2.4.2 Thermal stability of LMNO

Khakani et al. [44] conducted ARC experiments on LMNO synthesized by the sol-gel method and commercial solid-state synthesized LMO. The ARC material was prepared by mixing 80% active material, 10% conductive carbon (TIMCAL EBN1010), and 10% PVdF with NMP before drying, mortaring, and sieving through a 300$\mu$m sieve, and pellet pressing. The pellet was then used either in the uncharged state or placed in a 2032 coin cell for delithiation with electrolyte (1 M $LiPF_6$ in EC:DEC 1:2 by volume) to 4.2 V (LMO) or 4.9 V (LMNO) versus $Li/Li^+$ with a C-rate of C/20 at 60°C. The pellet was then ground and rinsed with DMC before being dried in the glovebox antechamber. Their ARC experiment was conducted in a TIG (Tungsten Inert Gas) welded stainless steel tube, meaning high pressure after initial reactions.

They found that LMO performs worse than LMNO in the uncharged state, by going into a thermal runaway at 275°C versus LMNO's 350°C. However, for the LMNO, there are some unsustained exotherms already at 90°C. For the charged sample, however, the LMNO performs much worse, with unsustained exotherms as low as 60°C, and thermal runaway at 215°C, whereas the LMO has its first exotherm at 140°C and thermal runaway at 244°C. By performing post-ARC XRD analysis at different temperatures they found out that the reactions below 100°C were most probably attributed to surface reactions since the structure seemed unchanged before and after the reaction.

They also conducted experiments to differentiate between the dry cathode material, the addition of solvent, and the addition of electrolyte (solvent with salt) for uncharged materials. They found that for LMO, the changes were minuscule with some unsustained exothermic reaction at 140°C for the one with electrolyte, whereas the dry one starts at 175°C. Although for all these three variations in the testing, the thermal runaway for LMO is at roughly the same temperature (250°C). For LMNO however, the thermal signature is significantly worsened when adding solvent, where the thermal runaway starts at 190°C versus the dry one at 270°C. For the one with added electrolyte, a significant unsustained exotherm occurs as low as 70°C, with a thermal runaway at 220°C.

## 2.5 Methods

The methods of characterization used in this thesis are briefly described in this section.

### 2.5.1 Powder X-Ray diffraction

X-Ray Diffraction (XRD) arises from the Bragg diffraction phenomena and can give information on the crystal structure of a material. Bragg diffraction is when the incident photon beam is partially transmitted and reflected through atomic planes, leading to the extinction of the reflected beam at angles which creates perfect destructive interference between the electromagnetic waves reflected by the planes. In figure 2.9 below it is visible how the condition for Bragg diffraction is only satisfied when equation 2.16 holds true. Equation 2.16 is called the Bragg condition and describes how the diffraction order $n$, radiation wavelength $\lambda$, lattice planar distance $d$, and diffraction angle $\theta$ must couple for Bragg diffraction to occur. Note that the rightmost scenario in the figure below happens for all angles and wavelengths where equation 2.16 is invalid because there are several thousand planes below, and at some depth, there will be a plane with the correct distance to the first plane to have perfect extinction.

$$n\lambda = 2dsin\theta \tag{2.16}$$

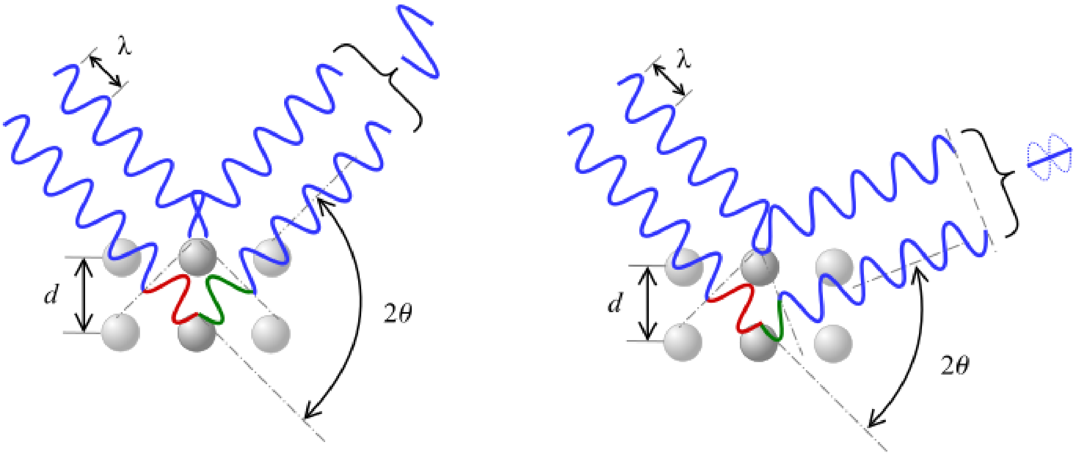

Figure 2.9: Bragg's law by Gregors, Date: 11.03.2011. Creative Commons Attribution-Share Alike 3.0 Unported. (from Wikimedia Commons)

On a higher level, the characterization method works by irradiating a sample with X-rays and measuring the intensity of the scattered beam over an angular range. This range is called the $2\theta$ range and is often represented in Q-range to be wavelength agnostic. The conversion from $2\theta$ to Q is done by equation 2.17.

$$Q = \frac{4\pi}{\lambda} sin\left(\frac{2\theta}{2}\right) \tag{2.17}$$

Where $\lambda$ is the wavelength of the X-Ray radiation and $2\theta$ is the scattering angle. Q is also the length of the reciprocal lattice vector which is not described here. The $2\theta$ values can be converted into lattice spacings $d$ by using Bragg's law 2.16.

For a cubic crystal, the lattice spacing $d$ for a specific atomic plane can be calculated from the miller-indices of that atomic plane, and the lattice parameter $\alpha$ by:

$$d = \frac{\alpha}{\sqrt{h^2 + k^2 + l^2}} \tag{2.18}$$

In conventional XRD a somewhat large area ($> 0.1\text{mm}^2$) of the sample is irradiated, meaning that the characterization technique gives the average for an area of the sample.

### 2.5.1.1 Instrumental setup

The X-Ray Diffraction instrument, the diffractometer, consists of an X-Ray source, the sample to be measured, and a movable detector. There are primarily two types of XRD instrument geometries, the reflection geometry (Bragg-Brentano) and the transmission geometry (Debye-Scherrer). Where the reflection geometry diffractometers irradiate a flat sample, the transmission geometry diffractometers measure the diffracted beams coming through the sample and out the other side. This means that height adjustment is critical for accurate d-spacing estimates in reflection geometry, however for transmission measurements, the height error is less critical. An illustration of a reflection geometry diffractometer is depicted below in figure 2.10.

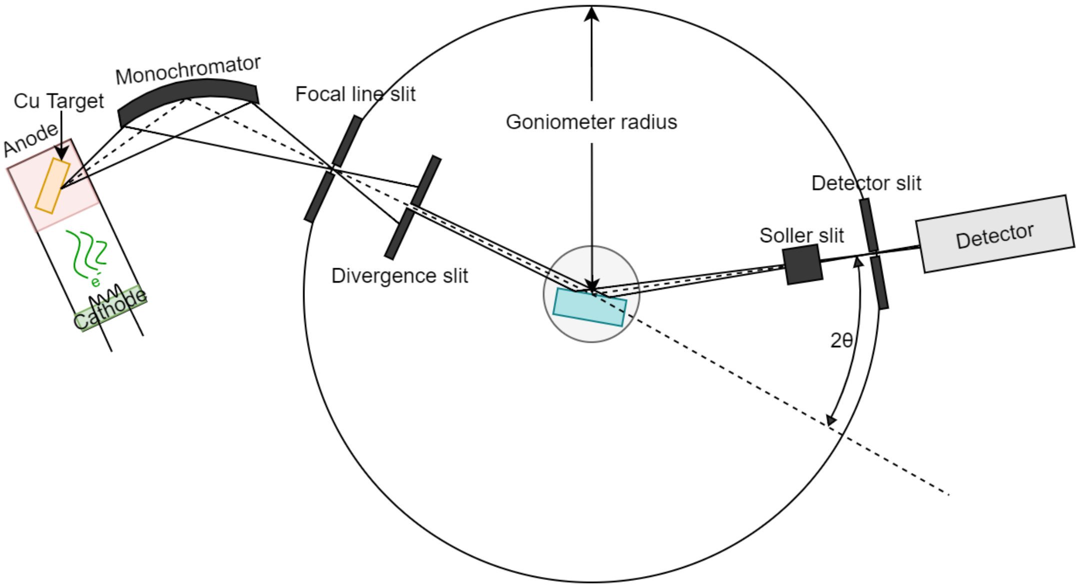

Figure 2.10: Bragg-Brentano geometry diffractometer schematic

The X-Rays are generated in the X-Ray tube depicted on the very left side of figure 2.10. The X-Ray tube consists of a wolfram filament that generates electrons. These electrons are then accelerated towards the target by a high potential ($\sim$ 48kV) cathode and anode, which can be the filament and target itself. To not lose electron intensity, the entire tube is under vacuum. When the electrons hit the target, which can be copper, molybdenum, or other metals, they excite electrons in the metal. When these electrons then relax, characteristic X-rays are generated. For copper, the electrons are usually accelerated to excite electrons from the K orbital to the L orbital. The L orbital has two different, but quite similar energy levels, which is the origin of the two wavelengths generated by a copper target. These two wavelengths of radiation are called Cu-K$\alpha_1$ and Cu-K$\alpha_2$ and exit the tube through a transparent window, usually made of boron.

Even though many diffractometers use both these radiations, many also filter them. Filtering can be done by for example a single crystal monochromator. A single crystal monochromator works by the principle of Bragg diffraction, where one wavelength can be selected by choosing the correct diffraction angle. For a germanium (111) monochromator, the 111-plane of the germanium crystal is exposed. This plane has a d-spacing of 2.353Å calculated by equation 2.18, and germaniums lattice parameter $\alpha$. By using Bragg's law (2.16) and the wavelengths of Cu-K$\alpha_1$ and Cu-K$\alpha_2$, it is evident that the crystal scatters the different radiations with a difference in angle by roughly 0.05°, which can then be removed by a focusing slit.

For both diffractometer geometries, different slits are used. As seen in figure 2.10, there is a focal line slit to remove unfocused rays(wavelengths not wanted), and a divergence slit to remove rays that diverge too much. Some instruments also have beam masks to limit the beam area. On the scattered side of the sample, a Soller slit is used to remove non-collimated beams, which means that mostly parallel beams can pass. The degree of filtration through a Soller slit is determined by the slit spacing, however, it is important to note that with lower slit spacing the transmission intensity decreases.

#### 2.5.1.2 Synchrotron radiation

A synchrotron consists of a ring where electrons are sent around and around, in addition to other parts like a linear accelerator and a booster ring as shown in figure 2.11 below. This ring often consists of straight lines with bends, and in these bends, *bremsstrahlung* is generated when the electrons are bent (or accelerated) by a magnetic field created by the *bending magnets*. On the straights of the electron flow, *insertion devices* can be placed, which wiggle the electrons back and forth to achieve the same effect, and thus X-Ray radiation can be extracted at several places around the ring. However, due to the increased efficiency of an insertion device over a bending magnet, insertion devices can be found used at the bends as well.

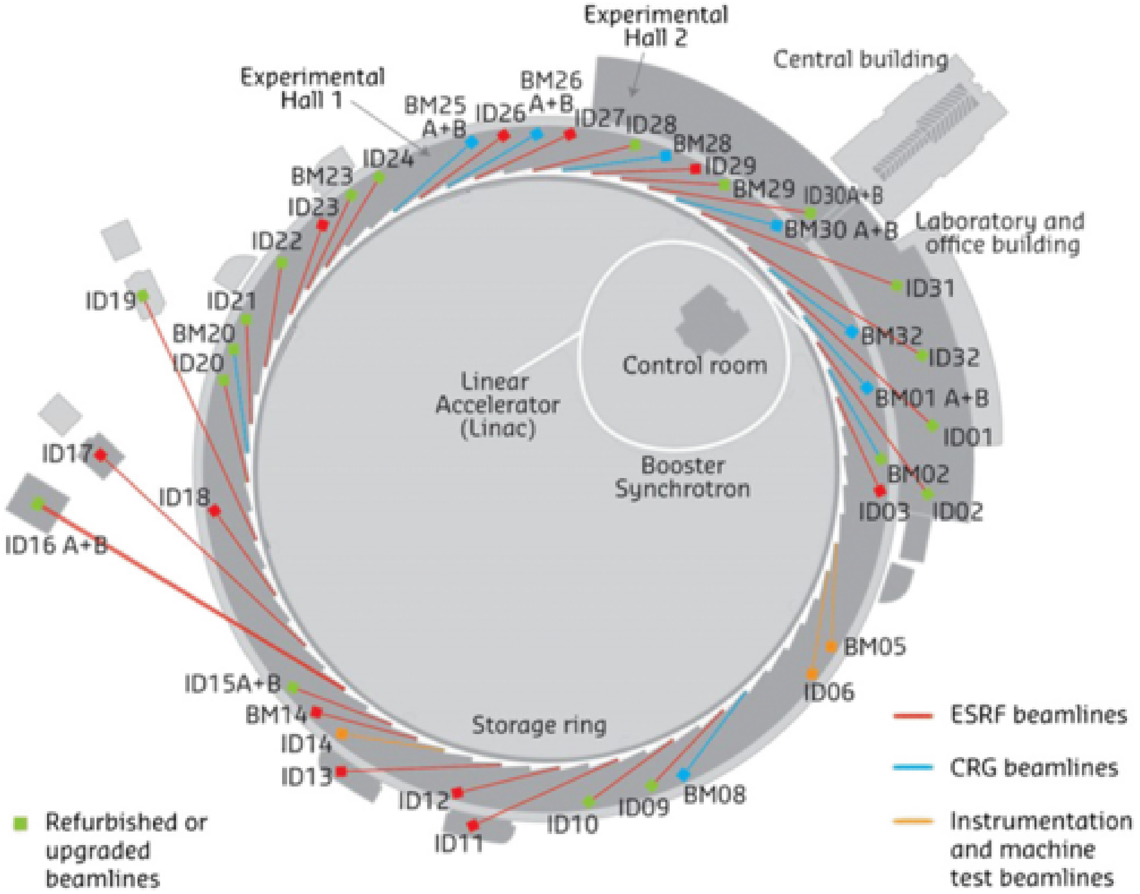

Figure 2.11: A schematic of the European Synchrotron Radiation Facility in Grenoble, France (image courtesy of the ESRF communication group).

After the white bremsstrahlung is created, the beam is monochromatized before going through a series of slits and hitting the sample as explained in the general instrumental setup above. Due to the cost of the synchrotron, a larger and more expensive 2D detector is used, compared to small 2D, 1D, or point detectors used in home labs. This further increases the signal-to-noise ratio.

The quality of an X-Ray beam is often measured by its *brilliance* where the brilliance of radiation in a synchrotron facility can be up to 10 orders of magnitude higher than that of a regular X-ray tube with an anode. [92] The brilliance, $B$ of a beam is calculated by the photon intensity $I$ in photons per second divided by the divergence $d$ in milliradians squared, the area of the source $A$ in square millimeters, and the bandwidth $BW_{0.1\%}$ relative to 0.1%. The equation becomes as in equation (2.19) below.

$$B = \frac{I}{d^2 \cdot A \cdot BW_{0.1\%}} \tag{2.19}$$

#### 2.5.1.3 Peak broadening

Peak broadening arises from two main sources which need to be separated for low error analysis. The instrumental peak broadening which arises from imperfect monochromatization, beam divergence, and bad focus in addition to other instrumental parameters needs to be evaluated before any diffraction data can be analyzed. This instrumental peak broadening can be calculated theoretically or determined experimentally[93]. The other source of broadening is the sample, where strain and crystallite size are the two main factors and are sometimes of direct interest in the research being conducted.

#### 2.5.1.4 Sample absorption

Sample absorption happens when the incident X-Ray beam excites electrons in the sample. This is called photoelectric absorption and can happen to electrons at various energy levels in the sample. If the excited electron was in a lower energy state, an electron from a higher energy level can fall and release the energy difference in the form of fluorescent X-Ray emission. Especially iron, chromium, and manganese fluoresce heavily under Cu-K$\alpha_1$ radiation due to the beam energy being close to electron transition energies of the elements. This gives an increased background to the data but can be suppressed and filtered with slits and monochromators, or by choosing a different wavelength for the beam. Another result of sample absorption can be Auger electron emission. Due to the physical nature of this phenomenon, sample absorption can be calculated and compensated for during data analysis.

#### 2.5.1.5 XRD data analysis

Simple XRD data analysis can give very important information about the crystal structure. For instance, $d$-spacings for the different peaks can be directly calculated from the peak position, and by using equation 2.18, it is possible to figure out which atomic planes these spacings belong to. Using the same formula, it is also possible to find the experimental value for the lattice parameter $\alpha$. However, even though equation 2.18 is limited to cubic structures, other equations exist for all the different Bravais lattices. By using this manual analysis method it is possible to determine the space group as well.

In addition to this crucial information on the basic crystal structure, other parameters like Debye-Waller factors which say something about the thermal motion of the atoms, atomic positions, and site occupancies can be retrieved from peak intensities. From peak broadening, information about crystallite size and strain can be retrieved. In general, crystallite size and strain can be differentiated by their different broadening shapes. Peak broadening because of small crystallites would yield a more Lorentzian peak shape, and in addition, its width would be inversely proportional to $cos(\theta)$. For the strain, the peak broadening would be more Gaussian, with a width proportional to $tan(\theta)$ [94]. The background of the data can be used to say something about the amorphous fraction of the sample, or the local order/disorder.

#### 2.5.1.6 The Rietveld refinement method

An advanced, yet very popular analysis technique is the Rietveld refinement method. It was developed by Hugo Rietveld when working on the HFR reactor in Petten, a small town in the Netherlands [95].

The method itself is only for structure refinement and relies on existing information about the sample, like space-group, lattice parameters, and atom positions. The initial parameters have to be relatively close to perfect for the refinement to work. The refinement is done by calculating a diffraction pattern based on the input data, followed by difference minimization between it and the experimental data by the use of the least-squares method used for the intensity values. This is an iterative process where the parameters are changed to minimize the error function. Guidelines for reporting results from the Rietveld method were given by R. A. Young in 1982 [96].

### 2.5.2 Raman Spectroscopy

#### 2.5.2.1 Vibrational modes and energies

In vibrational spectroscopy, the vibrational modes of a molecule or crystal are stimulated by some type of incident radiation, usually photons. A simple example is the water molecule which has three vibrational modes seen in figure 2.12 below. The number of vibrational modes can be calculated by the formula $3N - 6$ for non-linear molecules where $N$ is the number of atoms.

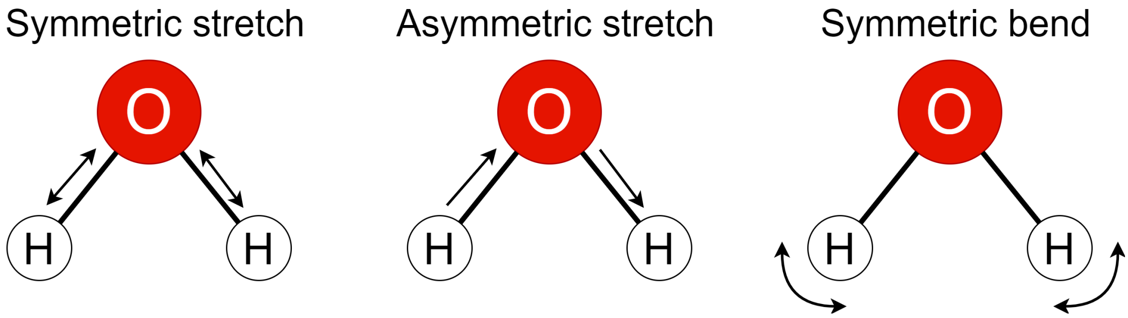

Figure 2.12: Vibrational modes of the water molecule

Each of these vibrational modes can be in different discrete energy states, as described by quantum mechanics. For a single diatomic molecule with only one vibration, the energy can be modeled by a harmonic oscillator potential with simple spring energy in the form $E = \frac{1}{2}kx^2$. The available energy levels can be calculated using the Schrödinger equation, and will not be shown here. A more realistic model for the diatomic molecule is the Morse potential, which shows that there is a dissociation potential for the vibrational mode.

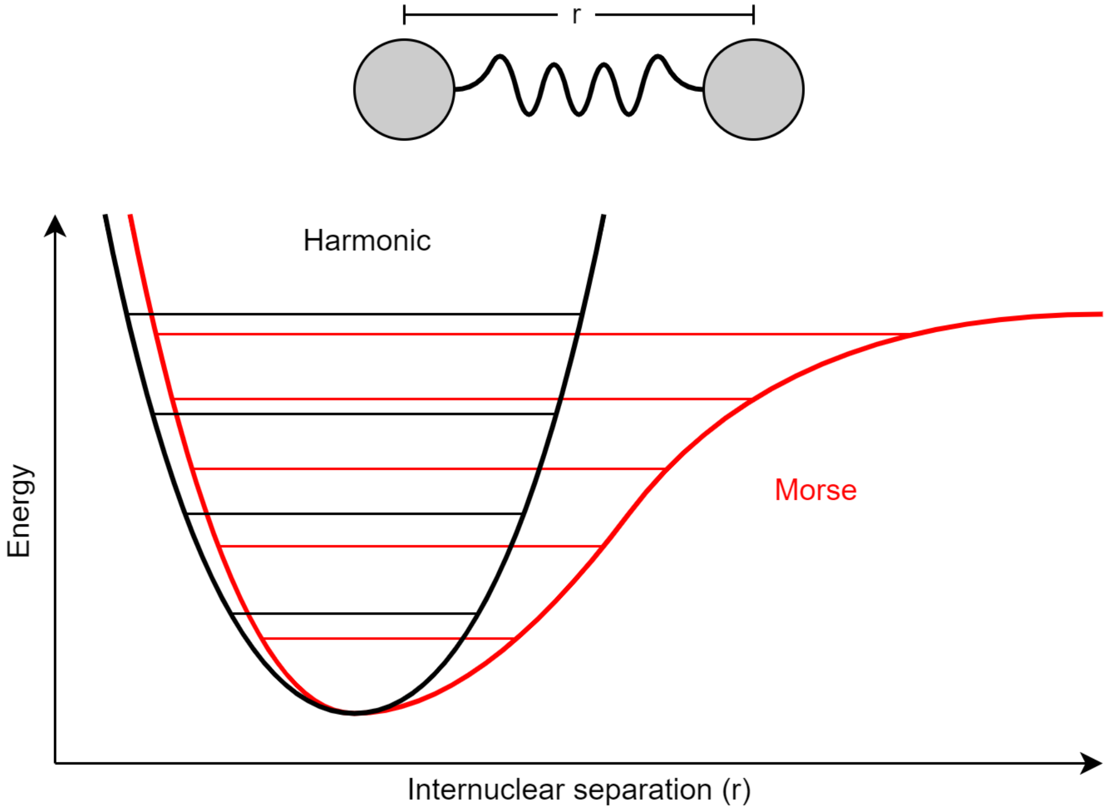

Figure 2.13: Harmonic Oscillator potential and Morse potential for a diatomic molecule vibration

Usually, these vibrations possess the lowest energy level at room temperature, however when they are excited by for example incident radiation, the vibrational energy increases. During the relaxation of the vibration, the radiation is re-emitted, or *scattered*. When the scattered photon has the same energy as the incident photon, it is called an elastic scattering since the energy is preserved. This is also called Rayleigh scattering. However, when the energy is not preserved, the scattering is inelastic. The change in photon energy can be divided into loss or gain, which is called Stokes and anti-Stokes scattering respectively, both of which fall under the term *Raman scattering*. It is important to note that most of the scattering that takes place is Rayleigh scattering, and only around every ten-millionth photon is Raman scattered [97].

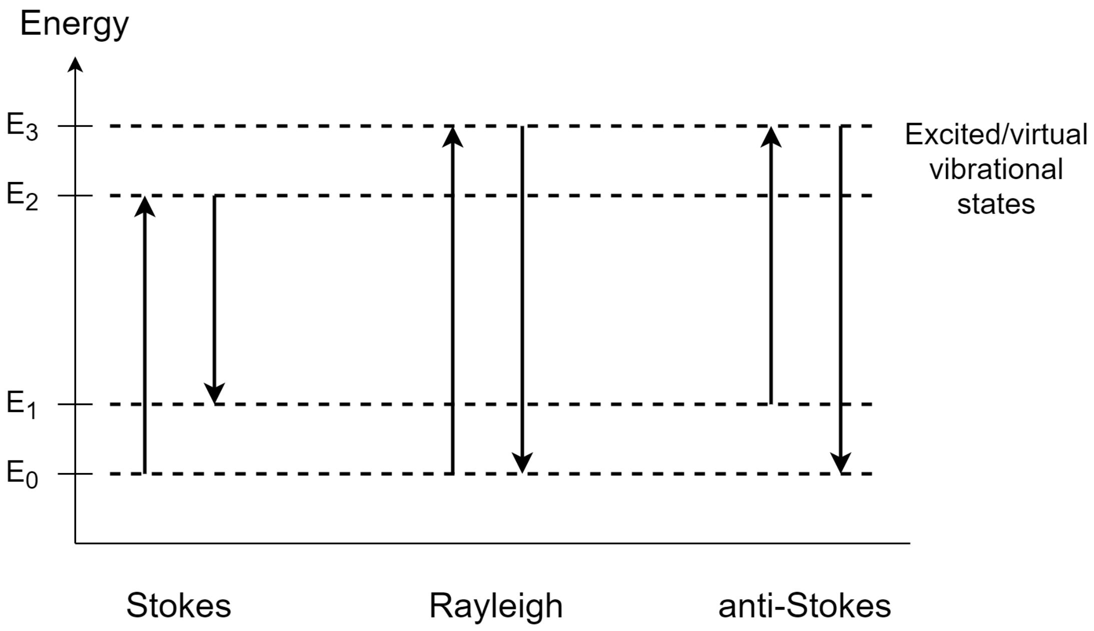

Figure 2.14: Different types of photon scattering by vibrational modes

#### 2.5.2.2 IR and Raman spectroscopy

The most used type of vibrational spectroscopy is Infrared Spectroscopy. With this type of spectroscopy, the sample is irradiated with a light consisting of a broad range of frequencies in the infrared (IR) domain. A detector is then placed on the other side of the sample, and the transmittance is measured. This results in an intensity spectrum over the selected IR range with intensity dips at the wavelengths which are scattered by the molecule. Often, the x-axis is represented by the wavenumber, which is the reciprocal wavelength of the radiation in centimeters ($cm^{-1}$), to better represent the different vibrational modes.

Raman spectroscopy on the other hand uses only a single-wavelength (monochromatic) radiation, usually from a laser. This wavelength must be chosen such that it does not damage the sample, however, it needs enough energy to excite the vibrations sufficiently. The resulting Rayleigh scattering is then filtered out, and the remaining Stokes and anti-Stokes scattered photons can be measured. Because most vibrational modes already are in the lowest energy state, anti-Stokes scattering occurs significantly more seldom than Stokes scattering and is usually discarded. This also allows for cheaper filters, which also filter out radiation higher in energy than the incident beam, and not only the beam itself [98]. The Raman spectrum is represented by intensities of Raman-scattered photons on the y-axis and a Raman shift (unit: $cm^{-1}$) on the x-axis which describes the change in energy from the incident radiation.

#### 2.5.2.3 Previous Raman work on LMNO

As Raman spectroscopy requires analysis and computational understanding and power to theoretically understand, empirical evaluations have been made valuable through previous experimentation on this material. Especially useful is how the ordered and disordered LMNO structure can be discriminated by Raman. This is easiest shown by two bands emerging at 216 cm$^{-1}$ and 235 cm$^{-1}$, and two bands emerging at 578 cm$^{-1}$ and 596 cm$^{-1}$ when the order of the materials increase. For fully disordered materials, the first two peaks (at 216 cm$^{-1}$ and 235 cm$^{-1}$) are invisible and the two latter form a plateau at around 590 cm$^{-1}$ [29].

### 2.5.3 Scanning Electron Microscopy

Scanning electron microscopy is a microscopy technique where electrons are used to form an image of a sample that cannot be seen with light microscopy. A light microscope is generally limited to a resolution of $0.2\mu$m. The resolution can be increased by increasing the light frequency (e.g. ultraviolet instead of visible light) or increasing the refractive index (e.g. by submerging the lens in oil), however, it is still limited to around $0.1\mu$m [99]. A big part of this is that lenses for light must consist of matter, and making perfect matter, both in the sense of shape, surface, impurities, and defects is impossible. In addition to this, the resolution is limited by the wavelength of the radiation. These are just two of the reasons why the Scanning Electron Microscope (SEM) is so popular. By using electrons instead of photons, they can be focused and accelerated in magnetic and electric fields instead. In addition to this, electrons have a much harder time penetrating matter, meaning that they are both safer to work with for the operator, and the surface resolution increases since the signal from within the sample are lost.

The SEM consists of an electron gun, the beam-column, the sample, and a set of detectors. The electron gun is usually in the form of a Schottky, thermionic or field-emission cathode, and an opposing anode [100]. The potential across the cathode and anode is called the acceleration voltage of the electron and determines the wavelength of the electrons. It is usual to have an acceleration voltage in the range of $1 - 30$ kV in a normal home-lab SEM. The electron beam then travels through the beam-column illustrated in figure 2.15 which very simplified consists of a condenser lens, an aperture, and an objective lens. These can be used to increase the resolution by decreasing the spot size which is done by focusing the beam. However, due to the way the column is set up, this also results in less intensity since more of the beam will be blocked by the aperture. This means that there is a tradeoff between resolution and intensity, the latter of which is mainly wanted for generating characteristic X-rays. Not depicted in the illustration are also the scanning coils, which steer the beam to scan the surface of the sample. After completing the journey through the beam-column, the electrons hit the sample. More on sample interaction can be found in section 2.5.3.1 below. The various signals from the sample are then detected by various detectors situated around the sample. The complete setup where electrons travel has to be evacuated since electrons scatter heavily in air.

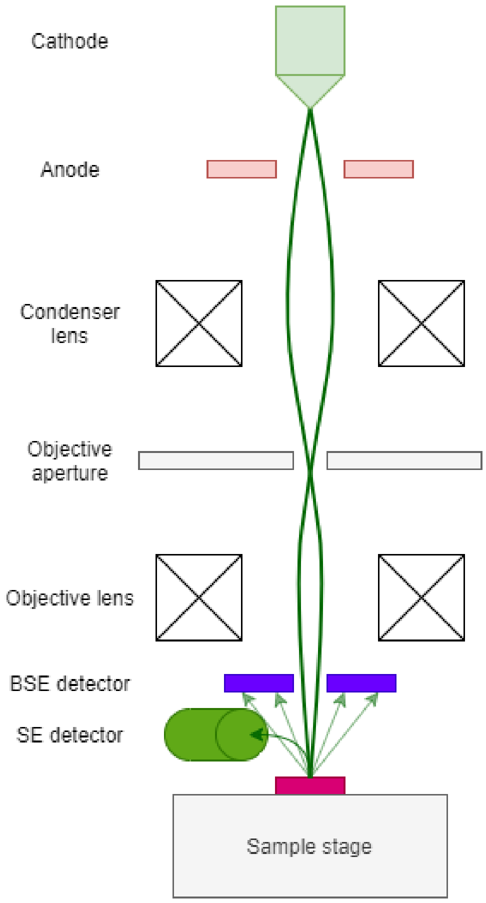

Figure 2.15: Simple schematic of a SEM and its setup

#### 2.5.3.1 Sample interaction

When the electron beam hits the sample, there are a couple of mechanisms happening at the same time. Some of these mechanisms have very weak response signals, and can therefore only signal from the surface sample will be detected. A schematic of the interaction volume can be seen in figure 2.16.

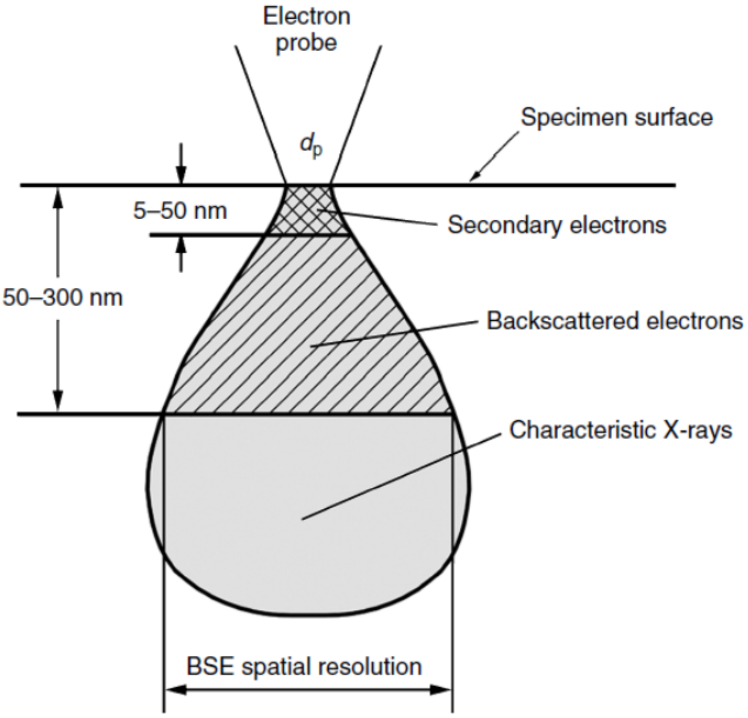

Figure 2.16: Electrons interaction volume in sample. Reused from KJM3120 lecture slides, Dept. of Chemistry, UiO 2020.

From the figure above it is clear that the beam size, $d_p$ has an impact on the resolution. The same goes for all the different interaction volumes. The incoming beam can penetrate deep into the sample, however, the signal response is very dependent on the type and energy of radiation that is created. Starting from the very surface, the Auger electrons (not shown in the figure) have such low energy that the ones generated deep in the sample never reach the detectors. Then, increasing in energy there are the secondary electrons. Already here the interaction volumes start to increase significantly from the beam size. Then there are the backscattered electrons, and lastly the characteristic X-rays.

The *secondary electrons* are made when an incident electron knocks out an electron from an electron orbital. The energy of secondary electrons is usually less than $1-10$ eV [101], which means that the ones generated deep in the sample will not make it out. *Backscattered electrons* on the other hand, are incident electrons that are directly scattered by the nucleus, and thus the mass of the nucleus indicates the intensity of the scattered beam. By knowing this, images that show atomic number contrast can be formed. The energy of a backscattered electron is between $60-80\%$ of the incoming electrons. Both these mechanisms are illustrated in figure 2.17 below.

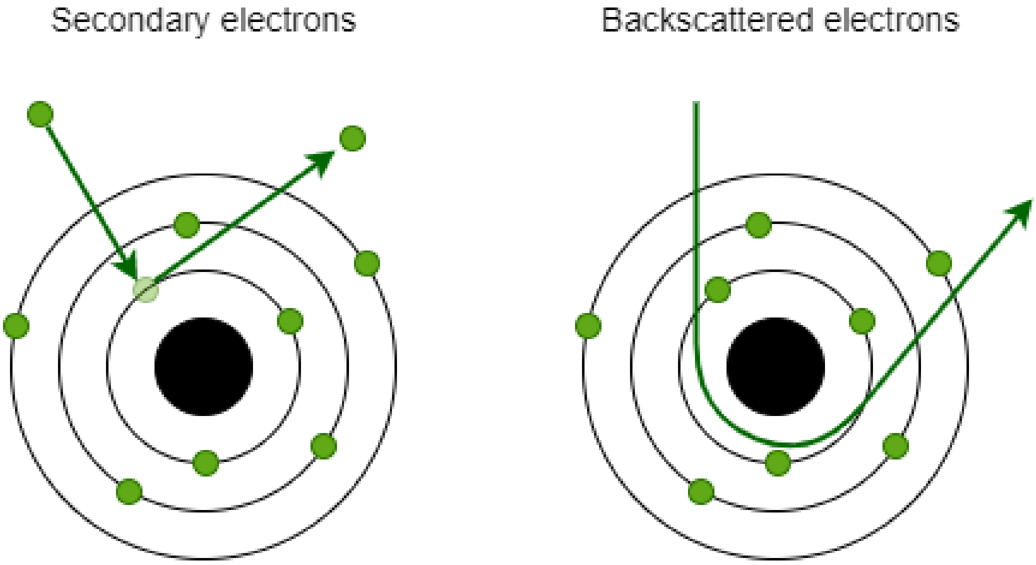

Figure 2.17: The mechanism of secondary electrons and backscattered electrons

The two other signals mentioned come from *Auger electrons* and *characteristic X-rays.* Both these signals are formed when an electron in the inner orbitals is knocked out by the electron beam and the vacant site is occupied by another electron with higher energy. When the electron falls from high energy to the low energy of the inner shell, the energy can be dissipated either by emitting an X-ray or by exciting an outer-shell electron so that it escapes. The latter one is called an Auger electron, and both the processes are depicted in figure 2.18 below.

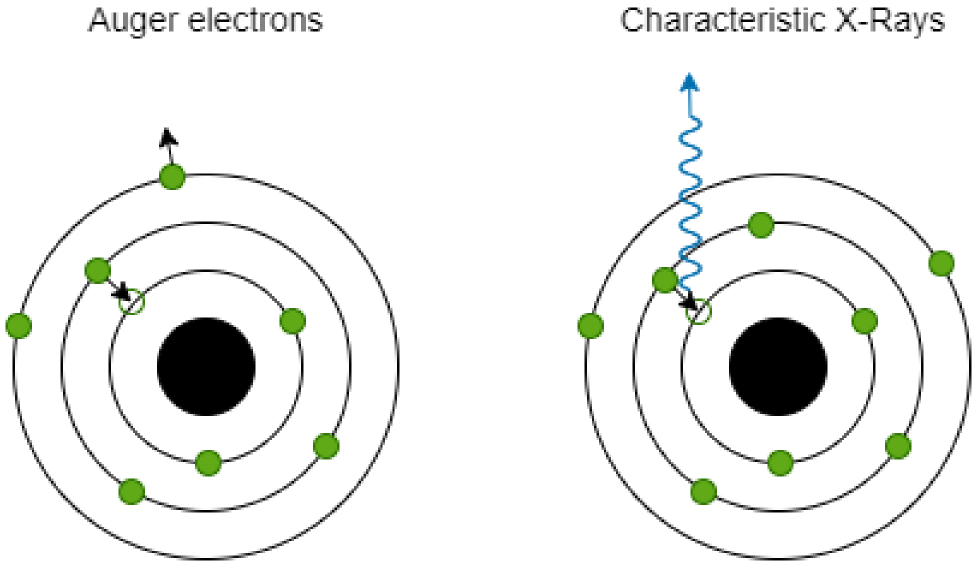

Figure 2.18: The mechanism of characteristic X-rays and Auger electrons

#### 2.5.3.2 Energy Dispersive X-Ray Spectroscopy

Because the X-Rays generated from within the sample under normal operation are very characteristic of the element (the electron transition energies is a fingerprint for an element), the possibility of doing an elemental analysis occurs. By detecting the energies and intensities of the characteristic X-rays, a quantitative analysis of the elemental composition can be done. This is called energy-dispersive X-ray spectroscopy (EDX or EDS) Since this signal is generated while taking a normal image with secondary electrons, a map of elemental analysis can be overlaid on the SEM image as long as there is a detector for it. This EDX map gives very valuable information on for instance impurities in the material, separate impurity phases, core-shell structures, and more.

### 2.5.4 Electrochemical characterization

For testing LIBs and materials in LIBs, there are mainly three different electrochemical characterization methods. These are *galvanostatic cycling*, *cyclic voltammetry*, and *electrochemical impedance spectroscopy (EIS)*. The two first ones are the most basic techniques controlling only the current or a potential sweep rate respectively, whereas the last one is more involved and typically requires more preparation work and analysis to be useful.

#### 2.5.4.1 Galvanostatic cycling

During galvanostatic cycling, a constant current is applied to the electrochemical cell, and the potential response is measured. For LIBs this typically means starting at either a charged or discharged state and applying a current to reach the opposite charge state, before the current is reversed to reach the original charge state again. This is usually done many times in a row and is then called *cycling* a cell. Usually, the potential boundaries are set at the maximum and minimum charge potential of the LIB, in which case the technique is called galvanostatic cycling with potential limitation (GCPL).

When cycling a cell using the GCPL technique there are several interesting effects to look at. The first couple of cycles will give information on any formation reactions or side reactions happening when first charging or discharging the cell. Throughout cycling, one can often see the voltage curves change, which can be used to analyze what type of degradation mechanisms happens in the cell during cycling. GCPL data is often visualized in a two-dimensional plot where the potential is on the y-axis and either capacity or time is on the x-axis. When plotting with capacity on the x-axis, the capacity, $C$ is calculated by integrating the current, $I$ applied over time, $t$ as shown in equation 2.20.

$$C(V) = \int_0^{t(V)} Idt(V) \tag{2.20}$$

Different variations of this plot are shown in figure 2.19 below, where the two first cycles of a new cell are visualized. As can be seen, visualizing overpotentials and the hysteresis of the potential response is easiest in the bottom right plot, whereas the pure data is easiest visualized in the top plots. The bottom right plot becomes more useful with more cycles, to spot trends in the discharge or charge cycles respectively.

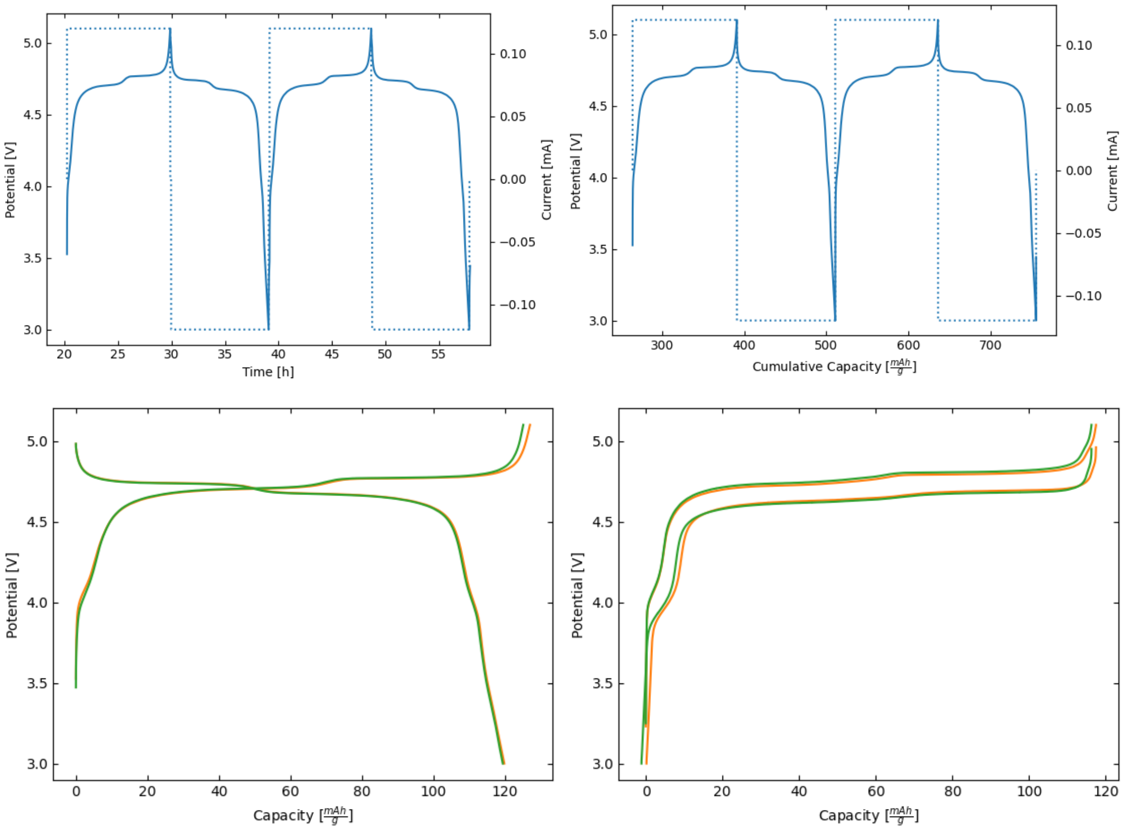

Figure 2.19: Top left shows potential response over time, top right shows potential response over capacity, bottom left shows capacity reset for each charge and discharge, and bottom right shows the potential response without resetting the capacity.

A very important parameter is the *coulombic efficiency* (CE) which is a percentage made by dividing the total discharge capacity by the total charge capacity and tells you the number of irreversible reactions (which are electrochemically active) which happen during each cycle. This data is usually plotted on a twin x-axis with the full charge/discharge capacities of each cycle as shown in figure 2.20 below.

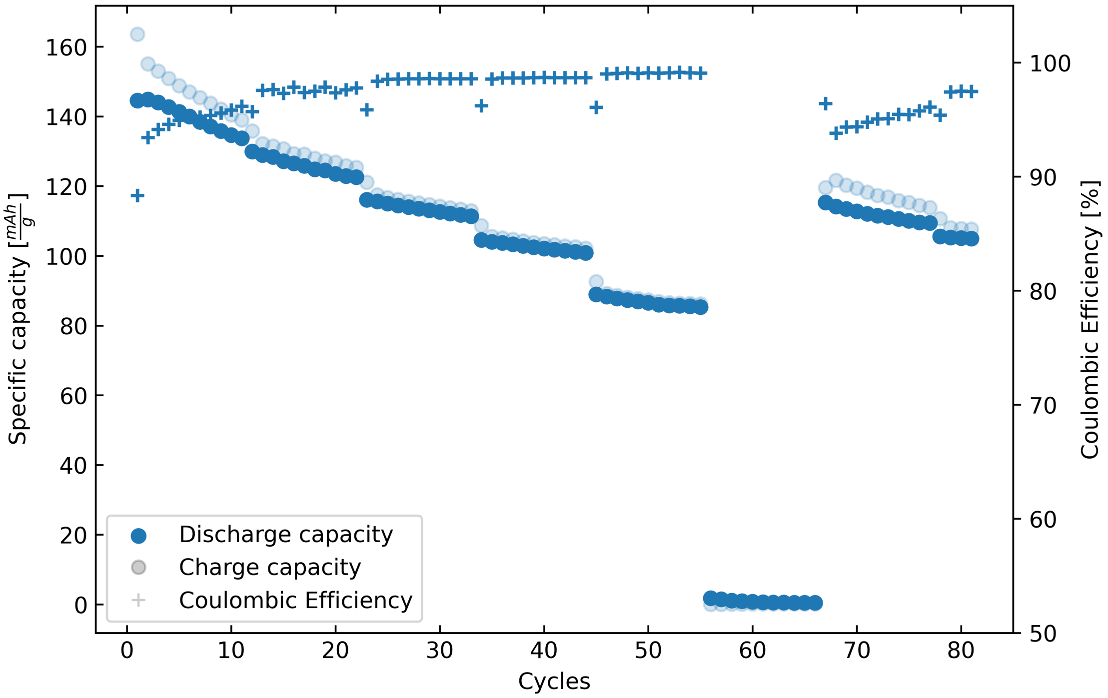

Figure 2.20: Cycle life plot of a cell during rate capability testing, with coulombic efficiency on the right y-axis.

#### 2.5.4.2 Rate Capability

*Rate capability* testing as seen in figure 2.20 above is simply changing the galvanostatic current after some amount of cycles, usually increasing it by some factor each tenth cycle. From this technique, information about kinetics can be extracted. For instance, the internal resistance drop (IR drop), activation energy, and mass transport can be assessed, but additional characterization is necessary to differentiate them. The simple ohmic resistance is simply calculated by Ohms law 2.21 where if the overpotential $\eta$ is inserted for the resistance, will give the IR drop at the given C-rate.

$$V = RI \qquad \rightarrow \qquad R = \frac{V}{I} \tag{2.21}$$

The overpotential measured for a specific current can be used to calculate the internal resistance of the cell, which with a proper data foundation can be used for the analysis of the resistance of the active material in question. Also, by gathering the overpotential at different C-rates, pseudo sweep voltammetry experiment data can be constructed. The data of such an experiment can in theory be used with Butler-Volmer theory (see eq (2.6)) to evaluate electrode kinetics. However, usually for LIBs, this is not done due to the limitations of Butler-Volmer in concentrated solutions as described by Bazant et al [36].

### 2.5.4.3 Differential capacity analysis

Another way of treating the GCPL data is by differentiating the capacity over potential. By doing this, "peaks" will form from the capacity plateaus and might make the visualization of certain effects easier. Many use this as a replacement for conducting separate cyclic voltammetry (see next section) experiments, however since the electrical perturbation of the cell is done differently, it should not be directly compared. To calculate the differential capacity, formula 2.22 below is used.

$$\frac{dQ}{dV} = I \cdot \frac{dt}{dV} \tag{2.22}$$

This visualization is popular amongst data scientists as it makes parameterization of the degradation easier as the peaks usually become broader and lower. This analysis technique requires high precision data gathering or significant data smoothing to work properly.

### 2.5.4.4 Cyclic Voltammetry

Contrary to galvanostatic cycling, *cyclic voltammetry* is performed by applying a potential to the electrochemical cell that changes with time. This change is called a potential sweep, which is usually linear with time and is done cyclically. A cyclic voltammetry plot has the resulting current plotted against the potential as shown in figure 2.21 below.

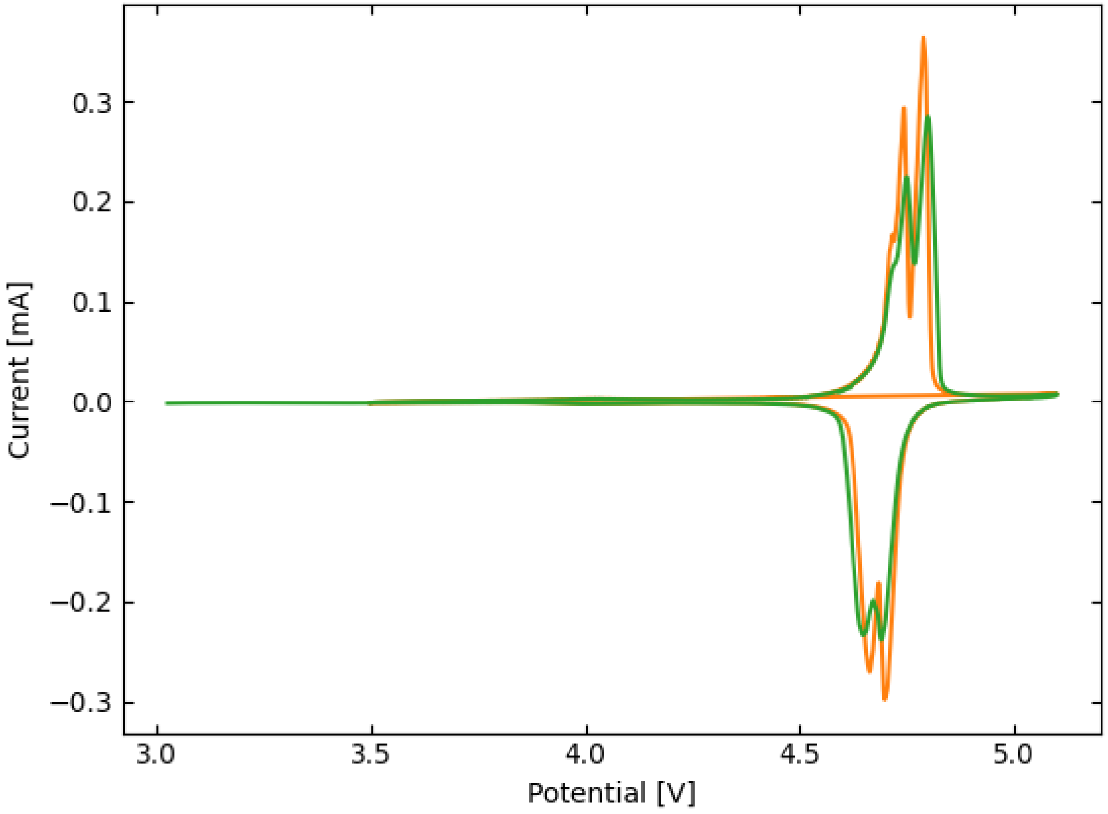

Figure 2.21: Cyclic voltammetry plot

### 2.5.5 Accelerating Rate Calorimetry

Accelerating Rate Calorimetry (ARC) is used as a characterization technique to see heat development over a temperature range when a specific sample is heated. The sample can be a whole battery, a cell (e.g. cylindrical 18650 cell), or the electrode material, just to name a few.

A regular ARC experiment has two different modes, a *heat-wait-seek* mode and an *adiabatic* mode. Initially, in heat-wait-seek mode, the adiabatic chamber is heated in short intervals with a temperature change $\Delta T$, waiting for the temperature transients to relax before measuring the sample's self-heating in the seeking period. This process is repeated until a specified self-heating rate is measured. This specified heating rate is for many battery experiments set to 0.02°C/min. From here, the instrument enters adiabatic mode, which means that it is only monitoring the heating rate[102].

To keep the chamber adiabatic during the adiabatic mode, the temperature is closely monitored by the instrument, and the chamber is heated so that the temperature difference between the sample and the chamber is very low. By having a very low temperature gradient, very little heat flow between the sample and the chamber, and a simulated adiabatic condition can be sustained. However, at high heating rates, the chamber is unable to keep up with the temperature increase, and the adiabatic function of the setup can be lost. For this reason, high heat rates beyond the instrument's limitations are very hard to analyze.

Through a battery test cycle, several events can occur. These are, in chronological order:

1. Preheating to a stable starting temperature
2. Heat-wait-seek mode
3. Self-heat-rate initialization
4. Adiabatic mode
5. Venting temp (for cells)
6. Accelerating heat output
7. Uncontrolled heat output, also called thermal runaway.

#### 2.5.5.1 $\phi$-factor

When doing ARC, most of the heat will be absorbed by the sample and the sample holder since adiabatic conditions are being simulated by the chamber. This means that a thorough description of the sample holder is quite important, however, not many reports do this [103].

A good way of describing the heat lost to the sample holder is by the $\phi$-factor, which relates the total heat capacity of the sample to the total heat capacity of the sample holder, or bomb.

$$\phi = 1 + \frac{m_b c_b}{m_s c_s} \tag{2.23}$$

In equation 2.23, the numerator describes the mass and specific heat capacity of the bomb, while the denominator describes the mass and specific heat capacity of the sample. Any additional parts that will absorb heat should also have their heat capacity added to the numerator. It is discussed whether the electrolyte should be included in the $\phi$-factor, as it is quite volatile and will evaporate and react a lot during the measurement, thus some do not include the electrolyte [89], while some do [91]. To have as realistic tests as possible, the $\phi$-factor should be similar to that of the real cell used for its application. This means that if the application is a large pouch cell with a low $\phi$-factor due to the large active material to packaging ratio it might be as low as 1.5, while if the cell used is a coin cell the *phi*-factor will be much higher, maybe as high as 10. However, when a $\phi$ factor equal to that in a real cell is impossible to attain, the phi factor can also be used to correct the temperature data so it shows what the temperature would be without the container. Because of this, the $\phi$-factor should be taken into account whenever ARC results are compared.

#### 2.5.5.2 Heat capacity of novel oxides

Even though LMNO has been known for a while, many of its properties have yet to be determined. This is especially true when the ratios of the transition metals change, or when new metals are introduced. One of these properties is the specific heat capacity, which is important in ARC testing to properly address the $\phi$-factor.

Several studies suggest that the Neumann-Kopp rule lacks sufficient precision at high and low temperatures, but is fairly reliable around room temperature [104]–[106]. Since the decomposition of electrolytes mostly happens below 150°C, the Neumann-Kopp rule is probably sufficient for this use.

From B.Millards book *Physical Chemistry for Colleges: A Course of Instruction Based Upon the Fundamental Laws of Chemistry*, page 96(1921)[107]:

> Kopp's law states that the molecular heat capacity of a solid compound is the sum of the atomic heat capacities of the elements composing it; the elements having atomic heat capacities lower than those required by the law of Dulong and Petit retain these lower values in their compounds.

Then, the mathematical formula is given by [106] as

$$C = \sum_{i=1}^{N} (C_i \cdot f_i)\,,$$

where $C$ is the total specific heat capacity, $N$ is the number of constituents, $C_i$ is the specific heat capacity of each constituent, and $f_i$ denotes the mass faction of the constituent. For aluminum substituted delithiated LMNO, the equation becomes

$$C = C_{Al} \cdot f_{Al} + C_{Ni} \cdot f_{Ni} + C_{Mn} \cdot f_{Mn} + C_O \cdot f_O. \tag{2.24}$$

Gotcu et al. also used this method [108] and reported that experimental data on this in the literature is inconclusive with reported values varying between 0.7 and 1.3 J/gK. An example demonstrating this is Knyazev et al. who found the heat capacity of Fd$\bar{3}$m $LiMn_2O_4$ to be 0.98 J/gK at 300 K and vary by 2% within a temperature window of 20 K [109].

#### 2.5.5.3 The addition of electrolyte

Most experiments include an electrolyte in the bomb when doing ARC testing[88], [89], [110], while some do not [71]. For the experiments without electrolyte, the reaction is often less intense. This is because the cathode material and electrolyte mix include both oxidizer (oxygen released from the cathode material) and fuel (organic solvent in the electrolyte) meaning that direct combustion reactions can happen, compared to cathode degradation alone [110].

Other thermal stability tests have been done with superfluous amounts of added electrolyte (1-2 times the mass of cathode material) [88], [91], [102], [111], however, this is not representable of a real cell where there is less electrolyte deadweight. A more realistic mass ratio is 2:1 of cathode material to electrolyte as used by the Norwegian Defense Research Establishment in [89] and by MacNeil and Dahn in [110]. The mixing ratio between the active material and electrolyte is also reported by MacNeil [110] to heavily influence the results due to the reaction between the oxygen-release of the cathode material, and the decomposition of the electrolyte. This means that with less cathode material, the oxygen supply is limited compared to the thermal mass of the whole sample, leading to a lower temperature rise rate. MacNeil[110] also showed that for $Li_0Mn_2O_4$ the exothermic onset varied with the concentration of $LiPF_6$ salt in the electrolyte, where reducing the salt concentration from 1.25M to 0.5M changed the average low-temp (below 210°C) self-heating rate from 1 to $0.05^{\circ}C/min$. This is believed to be because increased salt amounts lead to increased amounts of HF, which cleans the cathode particle surface, and thus lets the cathode-electrolyte oxidation reaction start earlier.

#### 2.5.5.4 Pressure conditions

When doing ARC for LIBs, considerations of gas evolution must be made. The Norwegian Defense Research Establishment (FFI) has reported that for NMC, the experiments with an external gas system with a volume of 500mL did not enter thermal runaway, whereas the samples ran in a sealed bomb did. This indicates that gas may leave the system and carry heat away in the process, yielding a lower thermal signature in the experiments. Commercial cells are designed to release the eventual buildup of pressure through various venting mechanisms, which makes testing with an external gas system more realistic than a closed bomb. The most realistic approach would be to have a relief valve that automatically opens at a given pressure, however, this would also induce more irregularities from sample to sample, and make it harder to do gassing amount analysis.

#### 2.5.5.5 Surface area

The eventual reactions between the electrolyte and the cathode material will propagate from the interfacing surface between the two. Therefore, the interface-to-bulk ratio is important to have control over in order to have comparable results. Often, to characterize such a surface, the Brunauer-Emmett-Teller (BET) surface area is used [103]. In fact, it has been seen that an increase in the surface area increases the onset temperature, and at the same time significantly increases the maximum heat rate of the sample [102].

# Chapter 3

# Experimental

The experimental section is written in the order the experiments were done, starting with synthesis and physical characterization (XRD, Raman, and SEM) before continuing with electrochemical coin cell fabrication for electrochemical testing and lastly accelerated rate calorimetry.

## 3.1 Synthesis

The sol-gel Pechini synthesis (introduced in theory section 2.3) with combustion was used in order to get homogeneous crystallite sizes. This synthesis had also been tuned by Pushpaka Samarasingha, a researcher at our research group (NAFUMA) giving me second-hand experience when starting.

The synthesis is split into five parts: (1) weighing, (2) mixing, (3) evaporating, (4) combustion, and (5) sintering. However, before this, the precursors were made.

The precursors were made as concentrated aqueous solutions from metal nitrates of high purity as found in table 3.1 below. These aqueous solutions were mixed so that their total water content was approximately correct for the synthesis. This was done since nitrates often are hygroscopic, and their mass in powder form varies with ambient air moisture whereas a solution is much more resistant to environmental changes. The solutions were calibrated by annealing four crucibles with a carefully weighed amount of solution in each, with a quartz wool layer on top to avoid loss of material due to aggressive boiling. The crucibles and quartz wool were annealed right before weighing in the solution and kept in desiccators when not under weighing to avoid water absorption. The annealing temperatures used were 900°C for manganese and aluminum to create $Mn_2O_3$ and $Al_2O_3$, while the nickel calibration was annealed at 800°C to get NiO. When ramping up to annealing temperatures, all batches had a water evaporation step, going as slow as 1°C/min between 90°C and 120°C. An XRD scan was done to make sure the anticipated product was made after the crucibles had been carefully weighed. The concentration error was calculated by the standard deviation between the four crucibles.

Table 3.1: Precursors and their origins

| **Precursor** | **Starting material** | **Manufacturer** | **Purity** | **Molality [mol/kg]** |
|---|---|---|---|---|
| $MnNO_3$ sol | Mn(II)$NO_3$ sol 50% by volume | Alfa Aesar | - | 3.057 ± 7E-5 |
| $NiNO_3$ sol | $Ni(NO_3)_2 \cdot 6H_2O$ | Sigma Aldrich | 99.997% | 0.989 ± 3E-3 |
| $AlNO_3$ sol | $Al(NO_3)_3 \cdot 9H_2O$ | Sigma Aldrich | 99.999% | 1.161 ± 4E-3 |

| **Precursor** | **Starting material** | **Manufacturer** | **Purity** | **Molality [mol/kg]** |
|---|---|---|---|---|
| $LiNO_3$ powder | Anhydrous $LiNO_3$ handled under Argon | Alfa Aesar | 99% | |

The (1) weighing is done by calculating what amount of the respective element is needed to achieve the specific stoichiometry and was enough to make approximately 9 grams LMNO if the yield was 100%. Anhydrous lithium nitrate (AlfaAesar) stored under argon atmosphere was weighed in directly, while nickel, manganese, and aluminum were added as a concentrated solution (see table 3.1 above). After this was weighed and poured into a 5L beaker, the citric acid (CA, monohydrate, 99.0% pure from Sigma Aldrich) was added and stirred in for 5 minutes with a magnetic stirrer rod. After this, the ethylene glycol (EG, anhydrous, 99.8% pure from Sigma Aldrich) was added. The molar ratio of LMNO to CA to EG was 1:1:4. If needed, small amounts of additional deionized water can be used to flush the precursors into the beaker.

(2) Mixing simply happens in a 5L beaker with a magnetic stirrer at 100 RPM over night as shown in figure 3.1 below.

The (3) evaporation step is started early the next morning by turning the heat on the hotplates up to 90°C. This is then left on until the morning the following day. At this point, the solution has turned to a gel and should be so thick that the magnet can not spin.

As shown in figure 3.1, for the (4) combustion step the magnet is removed from the beaker and a glass plate with holes is placed over the beaker to contain most of the powder from the combustion reaction. The heat is turned up gradually to around 180°C to where it should combust. The combustion temperature depends a bit on the precursors and if it does not combust at 180°C, the temperature can be incremented 10°C every 15 minutes until it does. After the combustion, the heat is turned up to 300 °C where any leftover citric acid will combust. It is left at this temperature for two hours before the hot plate is turned off and left for cooling.

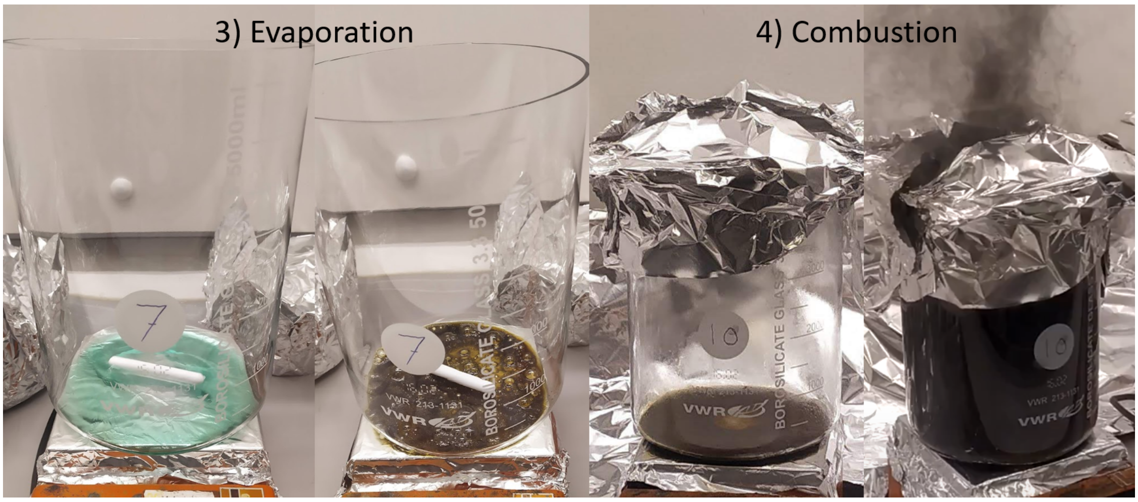

Figure 3.1: Sol-gel combustion synthesis: Evaporation (step 3) before and after and combustion (step 4).

The powder is then scraped out of the beaker and added to a small alumina crucible, which is then placed in a tube furnace under an oxygen flow of 30mL/min. It is sintered for 10 hours at 900°C and then 10 hours at 700°C. All ramp rates are 5°C/min.

The synthesized materials are then mortared by hand in 0.7g batches for 10 minutes.

## 3.2 Powder X-Ray diffraction

In-house XRD was performed at the Norwegian Centre for X-ray Diffraction, Scattering, and Imaging in Oslo using three different instruments. Routine XRD checks were conducted on the DIFF5, a Bruker D8 Discover with CuK$\alpha_1$ radiation selected by a Ge (111) Johanssen monochromator and a Lynxeye detector.

General capillary measurements were done at either the RECX1 which is a Bruker D8-A25 with CuK$\alpha_1$ radiation through Ge (111) Johanssen monochromator with a Lynxeye detector in Debye-Scherrer geometry or RECX2 which is a Bruker D8 A25 with Mo radiation, focusing mirror optics, Eiger2 R 500k 2D area detector and either a capillary or general XYZ stage. The RECX2 with the XYZ stage was used for operando measurements.

For an improved signal-to-noise ratio, synchrotron radiation was used to collect diffraction data on all pristine powders. This was done at Bending Magnet 01(BM01), Swiss-Norwegian BeamLines(SNBL), European Synchrotron Radiation Facility (ESRF), Grenoble, France on the 5th of November 2021 using a simple wiggling capillary stage and their azimuthal integration software to calculate a diffractogram from the 2D Pilatus2M detector data [93].

For all capillary samples of pristine powders, 0.3mm glass capillaries were used. For other powders (post-mortem, electrodes, and post-ARC), 0.5mm glass capillaries were used. Regular disc samples were prepped using the isopropanol method or by dropping powder on a thin layer of grease. The isopropanol method is to simply morter the material in isopropanol before dripping the colloidal solution from the morter on the flat sample holder disc. This is then let dry, and a nice flat layer of the sample is left. With this method, a silicon standard reference material could also be mortared in (NIST SRM 640d was in that case used).

### 3.2.1 Rietveld refinement with TOPAS

Most in-house XRD experiments were conducted to do simple checks and were quickly analyzed using DIFFRAC.EVA version 6 by Bruker without any Rietveld refinement. The synchrotron data was used for extensive analysis and thus had some corrections done to it during the Rietveld refinement (in TOPAS v6 from Bruker). The peak shape of the instrument was withdrawn from a $LaB_6$ sample using D. Chernyshovs function written in the TOPAS input file language. More on the resolution for powder diffraction can be found in his article [112]. Sample absorption was corrected by calculating the capillary absorption through Argonne national laboratory's online X-ray absorption calculator [113] and inserting the absorption $\mu$ into the TOPAS INP file. For instance, the wavelength used for all synchrotron experiments was 0.68925 Å and with this wavelength for the pure LMNO material and a packing density of 0.5, the tool calculated a $\mu$ of 44.01 $cm^{-1}$.

As stated, the INP file feature of TOPASv6 has been extensively used for inserting the wanted parameters and controlling what to refine. The INP file used was constructed as explained in Appendix C section C.2.

TOPAS will allow refinement of many parameters at the time. This can lead to parameter refinement being stuck at false minima created by parameters that do not resemble the real world. To avoid this, all variables were held constant when doing the refinements except the specific variables which was of interest to refine. An example of Rietveld refinement can be found in Appendix A section A.2.

## 3.3 Raman Spectroscopy

Raman Spectroscopy was conducted using the Department of Chemistry, University of Oslo's Horiba T6400, with a laser wavelength of 532.1 nm and a measured power of 1.4 mW at the sample. The grating was 1800 lines/mm, 300 $\mu$m slit, x100 Olympus objective magnification, with a Synapse CCD detector. The spot size on the sample was approximately 2 $\mu$m.

A Raman spectrum of a paracetamol pill was collected each day before starting the data gathering to make sure that the instrument was still working optimally. The measurements were taken with 60 seconds of exposure time, five times in a row, and then averaged. This was done for two regions to fill the whole spectrum of 40-930 $cm^{-1}$.

## 3.4 Scanning Electron Microscopy

SEM micrographs were taken on synthesized powders as well as commercial samples to analyze the morphology of the powder particles. This was done on a Hitachi SU8230 located at the Centre for Materials Science and Nanotechnology at the University of Oslo using the main secondary electron detector at various acceleration voltages below 5 kV with 10 $\mu$A of beam current and a working distance between 8.5 and 12.5 mm.

## 3.5 Inductively Coupled Plasma Mass Spectroscopy

Inductively Coupled Plasma Mass Spectroscopy (ICP-MS) was completed by an external contractor secretive about their methods. The company was Mikroanalytisches Labor Kolbe, c/o Fraunhofer Institut UMSICHT, Gebäude G – Osterfelder Str. 3, D-46047 Oberhausen. Two experiments of the same sample were done in order to verify the results.

From the mass percentages measured, the molar amount per mole LMNO $M_i$ for the specific element $i$ was calculated by the following equation (eq 3.1) under the assumption that the transition metals always added up to 2 moles per mole LMNO.

$$M_i = 2 \cdot \frac{\frac{mp_i}{mm_i}}{\frac{mp_{Mn}}{mm_{Mn}} + \frac{mp_{Ni}}{mm_{Ni}} + \frac{mp_{Al}}{mm_{Al}}} \tag{3.1}$$

where $mp$ is mass percentage from the measurement and $mm$ is the molar mass of the element in g/mol.

## 3.6 Cell fabrication

In order to gather electrochemical data, electrochemical cells first had to be made. This starts with making electrodes of the active material, binder, and conductive additive, before adding a separator, electrolyte, and a casing of some sort. These processes with their variations have been described below.

### 3.6.1 Electrode fabrication

The standard electrode laminate was made by mixing an 8:1:1 mass ratio of LMNO, PVDF (Arkema Kynar HSV1810 BINDER MATERIAL), and Carbon Super P (Timcal) as active material, binder, and conductive additive respectively to a total mass of 300 mg in a small ThinkyMixer box. Then approximately 1.2 grams NMP (Sigma Aldrich) was added to dissolve the PVDF binder and mix the materials. It was mixed in a ThinkyMixer (ARE250) at 2000 RPM for 3 minutes, and then at 700 RPM for 2.3 minutes as a defoaming step. An appropriately sized(7x15 cm) piece of aluminum foil (15 $\mu$m thick) was prepared on the coater (RK K control coater) by sticking it down with ethanol, washing the surface with acetone thoroughly with a tissue, and finishing by wiping with ethanol. It was made sure that the roughest side of the aluminum foil was facing upwards (the roughest side was always the inside when rolled up). The slurry from the ThinkyMixer was poured in a line across the aluminum foil. The doctor blade of the coater (K Control Coater from RK Print Coat) was set to a height of 300 $\mu$m above the foil and then set to smear the slurry across the foil with a speed of 2 m/min. All electrodes were dried at 80°C for at least 4 hours under a dynamic vacuum before being brought into the glovebox.

The following sections **??** to 3.6.1.3 explain deviations from the standard procedure for special scenarios. If not specifically mentioned, the regular procedure described above was used.

#### 3.6.1.1 Accelerated degradation test modifications

For the electrodes used with accelerated degradation testing, smaller amounts of slurries and thinner electrodes were made. In this case, the batch size was 60mg active material with 300mg solvent in the same ratio and with the same materials as explained in section 3.6.1 above. All other steps in the process were identical to the general electrode laminate fabrication described above in 3.6.1.

#### 3.6.1.2 Freestanding electrodes

To make porous free-standing electrodes for use in the Swagelok- (introduced in section 3.6.6 or glass-cell (introduced in section 3.6.7, active material was mortared with 20 wt% conductive additive (Carbon Super P) and 15 wt% binder (PTFE, Alfa Aesar) to a total mass of 1 g. 0.9 mL solvent (NMP) was added and mortared in until the consistency was reminiscent of a putty. This was then applied to an aluminum foil current collector with a spoon before a clean ziplock bag was laid on top and squished gently down under a microscope slide to approximately 5mm thickness. The ziplock bag was then peeled gently off the wet putty before the putty and current collector were punched with a 17 mm diameter punching tool to get a pellet shape. This putty disc was then dried in the büchi oven at 80°C for 4 hours under vacuum. After the vacuum drying, the pellet had shrunk in size and delaminated from the aluminum foil which could be removed.

#### 3.6.1.3 Pouch cell modifications

Modifications of the cathode electrode manufacturing process were done for pouch cells, where the total mass was targeted to 600 mg, using 2.5 g NMP, with an increased coating thickness of 400 $\mu$m.

For the graphite anodes used in the pouch cells, sodium carboxymethyl cellulose (Na-CMC, Sigma Aldrich) was used as a binder with water as solvent. The ratio between active material:Na-CMC:Carbon super P was 93:6:1, with around 2.4 mL water per 30 mg Na-CMC. The batch size was 800 mg. As a current collector, dendritic copper was used instead of aluminum to avoid the lithium alloying reaction with aluminum at 0.3 V[70]. In pouch cells, graphite was used in place of lithium as anode, for safety reasons.

### 3.6.2 Coin cell fabrication

The procedure was done in an argon-filled glovebox (MBraun Labmaster, $H_2O$, and $O_2 < 0.2$ ppm). Standard 2032 coin cells (20 mm diameter, 3.2 mm high by Pi-Kem) made of SS316L steel were used. First, the anode cap with the rubber gasket was placed on a Teflon workboard covered in clean lint-free tissue. Then a 16 mm diameter metallic lithium disc was brushed with a toothbrush to remove the oxide/nitride layer (with the inside of a clean zip-lock bag as a working surface), and placed with the brushed side up in the anode cap of the cell as seen in figure 3.2 below. A Whatman (Grade GF/C, CAT No. 1822-849) separator of 17 mm diameter was placed over it and soaked with 80 $\mu$L LP30 commercial electrolyte (1 M $LiPF_6$ in EC:DMC 1:1 by volume from Sigma Aldrich). After this, the prepared cathode (ø15 mm) cut with a handheld puncher (Nogami) was added, followed by a ø16mm spacer (0.5 mm thick) and a wave spring, before the cathode coin cell cap was placed on top. Lastly, the cell was pressed gently together with a finger before being pressed in a coin cell press (Hohsen corp. Automatic Coin Cell Crimper).

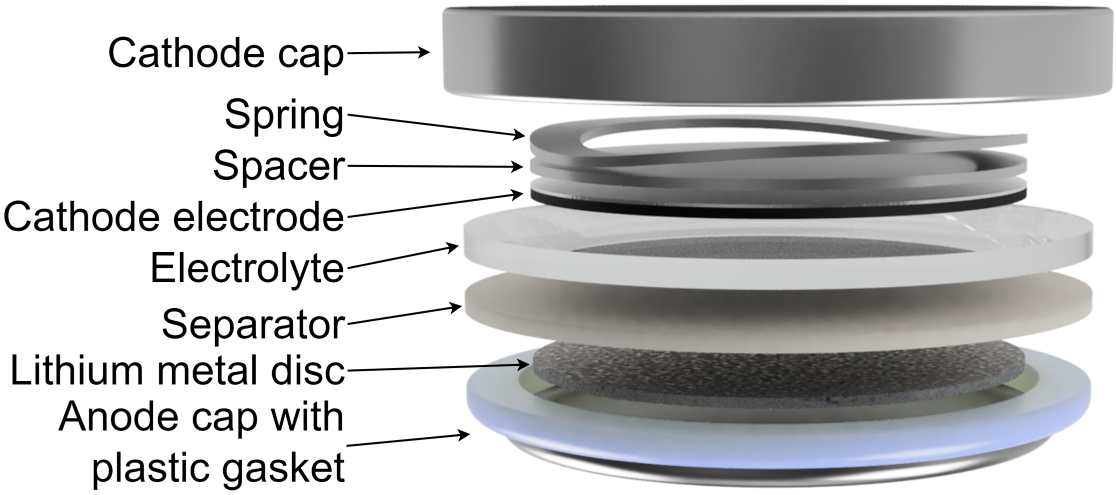

Figure 3.2: Coin cell drawing

### 3.6.3 Coin cells for compatibility testing

For the compatibility testing of the coin cell parts, the spacer and spring had to be moved to the anode side, to avoid reactions between the steel and the electrolyte at the high cathode potentials. Then different cells were made with different cathode cap materials. Two different types of electrolyte were also tested. The experiment with normal LP30 was set up with three different cathode side coin cell materials: SS304, SS316L, and an aluminum claded one (AlClad). For the experiment with Ionic Liquid (IL), the cathode side materials were SS316L, AlClad, or AlClad which had been bathed in LP30 for 24 hours before being washed in DMC and dried before use. The ionic liquid was made by mixing 1.2M LiTFSI in Pyr1333a from solvoionic.

### 3.6.4 Coin cells for accelerated degradation testing

For accelerated degradation testing, the following cell setup was used (The bottom of list is the bottom of the cell, and the first placed component):

- Positive side cap
- SS316 wave spring
- 2x SS316 ø16 mm, 0.5 mm spacers
- Cathode
- 200 $\mu$L LP40 Electrolyte (1M $LiPF_6$ in EC:DEC 1:1v from Sigma Aldrich)
- Separator (WhatMan QMA Quartz Microfiber Filters CAT No. 1851-865)
- 2x ø16 mm, 0.6 mm Lithium metal discs
- Anode cap with plastic gasket

### 3.6.5 Pouch cell fabrication

The pouch cell was made using a standard coffee bag-style aluminum foil with plastic coating (NIP30PE75, PET 12/Al 9/PE 75 from Skultuna). The coffee bag is prepped like an open book, where the top is taped over to eliminate any short-circuiting between the pouch edge and current collector tabs. The cell is stacked in a logical order, with a graphite anode on the bottom, followed by the separator (Whatman Grade GF/C), and lastly the working electrode on top of the separator. The electrodes were prepared as explained in section 3.6.1.3.

This electrode stack is then laid on the coffee bag, and taped with Kapton tape to the inside of the pouch for stability. To properly seal around the current collector tabs, strips of parafilm are placed on both sides of the current collector tabs. This side of the pouch is then heat sealed. The bottom side is also heat-sealed, before being put to vacuum-dry at 60°C for two hours. Then the pouch cell is brought into an argon-filled glovebox. In the glovebox, the pouch is filled with a couple of milliliters of electrolyte (LP30, Sigma Aldrich), in order to soak the separator completely. The last side of the pouch cell is then vacuum-heat-sealed in a VacuChef 40 food sealer on strong evacuation and seal. Preparation of the electrodes was done as explained in section 3.6.1. A picture of the open book pouch cell before sealing can be seen in figure 3.3 below.

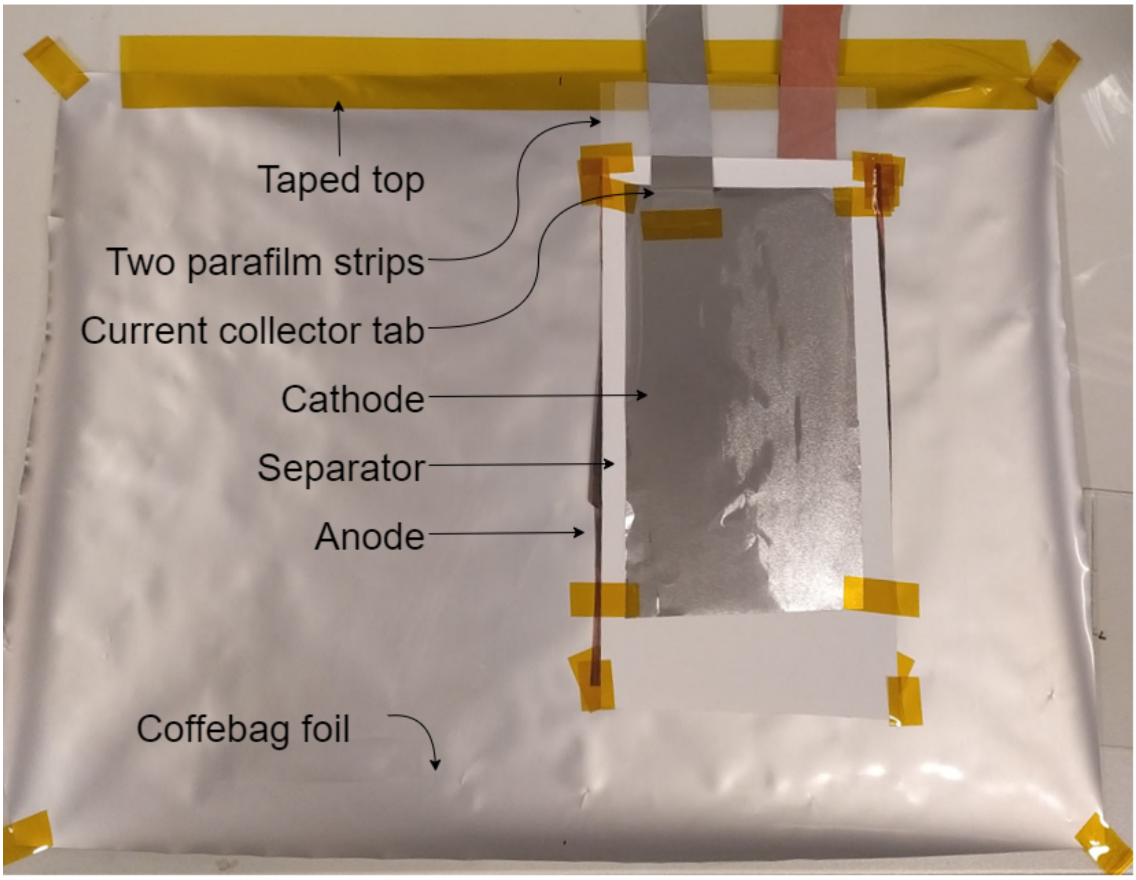

Figure 3.3: Open pouch cell before sealing

The cycling of the cell was done with a C-rate of C/10 and was cycled 2.5 times in the window of 3-5 V. The time spent at 5 V before disassembly was kept between 1-2 days, and a last step to charge to 5V with C/10 was conducted before immediately transporting the pouch into a glovebox for disassembly.

The collection of the delithiated cathode material was done by bringing the pouch cell into a glovebox, carefully cutting open the cell, and removing the cathode. This electrode was then quickly washed with 1mL of diethyl carbonate (DEC) by dripping it all over the electrode with a syringe and letting it run off the side when the electrode was held at an angle. The electrode was then left to dry in the glovebox until visually dry, which takes around 15-20 minutes. The material was then scraped off the aluminum current collector with a spatula and placed in a vial inside a plastic cylinder inside a sealed aluminum coffee bag before being transported over two-three days to an external location where the ARC sample could be prepped.

### 3.6.6 Swagelok cell

The cathode disc prepared as a freestanding electrode as described in section 3.6.1.2 was placed in the Swagelok cell, with a lithium metal anode, separated by a separator (Whatman Grade GF/C, CAT No. 1822-849) and bathed in the electrolyte (1M $LiPF_6$ EC:DMC 1:1 by volume from Sigma

Aldrich). The parts of the Swagelok cell are depicted in figure 3.4 which is a reconstruction of the real part done in Fusion360.

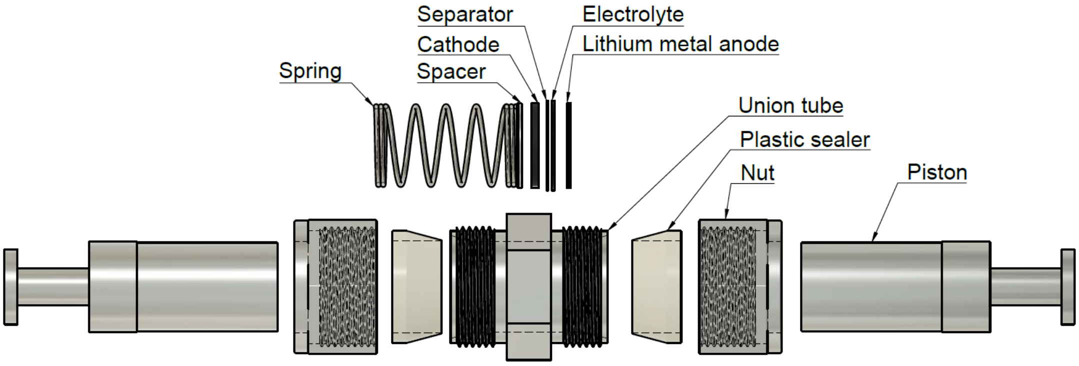

Figure 3.4: Swagelok cell parts

The spring has a spring constant of 640 N/m, and a max elastic force of 13.5 N at 21.4 mm compression. The Union tube has been lined with plastic in order to not be conductive.

### 3.6.7 Glass cell

The glass cell was developed in close collaboration with the workshop at the Department of Physics at UiO. It is sealed by several O-rings and locking nuts. It is 7.1 cm tall when collapsed, and has a piston diameter of 22.5 mm. A schematic can be viewed in figure 3.5 below. The cell was used in the same way as the Swagelok cell, except that the compression of the cell was done by placing a screw clamp across the pistons and tightening it down by hand.

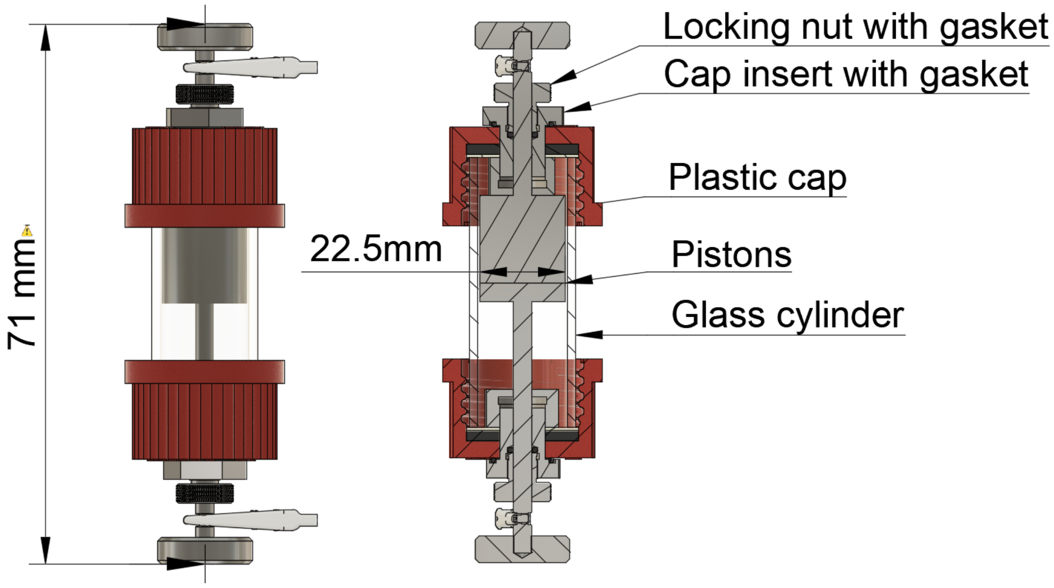

Figure 3.5: Glass cell schematic made by the workshop at Department of Physics, UiO

## 3.7 Electrochemical characterization

Electrochemical characterization was conducted on three different instruments; the Neware CT-4008T-5V10mA-164, Biologic MPG2, and the Astrol Batsmall. The characterization techniques involved were galvanostatic cycling, rate capability, accelerated degradation testing, electrochemical impedance spectroscopy, and cyclic voltammetry. Data is visualized using a self-coded framework for electrochemical data made in Python using the packages Pandas, NumPy and Matplotlib. The package is named *ecdh* for ElectroChemical Data Handling and can be found in [114]. Operando measurements were done using a BioLogic SP-150. Each experiment was conducted twice with two identical cells (twin cells) in order to verify the results.

### 3.7.1 Calculating theoretical capacities and current for C-rates

All currents for use with C-rates were calculated by theorizing how the substitution affects the capacity of the $Ni^{2+} \rightarrow Ni^{4+}$ and $Mn^{3+} \rightarrow Mn^{4+}$ reactions. These equations were created with some assumptions in mind, the reasonability of which was presented in the theory section 2.2.4.1:

- The Al is always in oxidation state 3+ and is not electrochemically active.
- Substituting Al for Ni is charge compensated by an equal amount of Mn being in oxidation state 3+
- Substituting Al for Mn is charge compensated by an equal amount of Ni being in oxidation state 3+

With these assumptions, the capacity is calculated for the Ni and Mn reactions separately as described in equations (3.2) and (3.3).

$$C_{Ni^{2+\to 4+}} = \frac{(2x_{Ni} - 1.5 - x_{Mn})}{M_{tot}} \cdot F \cdot 1000 \tag{3.2}$$

where $x_{Ni}$ is the stoichiometric amount of nickel, $x_{Mn}$ is the stoichiometric amount of manganese, F is the Faraday constant in Ah/mol, the kilo factor is to transform that to mAh/mol, and $M_{tot}$ is the total molar mass (g/mol) of the oxide.

The equation works by finding the relative amount of electrons coming from the $Ni^{2+\to4+}$ reaction ($2M_{Ni}$ because there are two electrons per mole Ni) and subtracting the number of electrons that are bound by the nickel starting in oxidation state 3+. This is then multiplied by a scaled Faraday constant to directly arrive at the maximum theoretical capacity for the nickel redox reaction. The unit becomes $\frac{mAh}{g}$.

Similarly, the equation for the manganese reaction becomes:

$$C_{Mn^{3+\to4+}} = \frac{0.5 - x_{Ni}}{M_{tot}} \cdot F \cdot 1000 \tag{3.3}$$

Which yields the total theoretical capacity for any substitution variation:

$$C_{tot} = C_{Ni^{2+\to4+}} + C_{Mn^{3+\to4+}} \tag{3.4}$$

These capacities are then simply multiplied by the mass of the active material measured for each cell and multiplied by the C-rate to get the current.

$$I = C_{tot} \cdot m_{activematerial} \cdot \text{C-rate}$$

Calculated theoretical capacities can be found in Appendix B, section B.5.5.

### 3.7.2 Rate capability degradation testing

Rate capability degradation testing was conducted on BioLogic MPG2 potentiostats. The experiments were run galvanostatically with 10 cycles for each increasing C-rate, before starting again with the lowest C-rate. The C-rates chosen were C/10, C/5, C/2, C, 2C, and 5C. The currents for the corresponding C-rates were calculated by the theoretical maximum capacity of the specific material as described in section 3.7.1 above. After coin cell assembly as described in section 3.6.2, the cells rested for approximately one hour before the testing program was initiated.

### 3.7.3 Accelerated degradation

To accelerate the degradation, special cells were prepared as explained in 3.6.4 and placed in a 45°C chamber for cycling. The cycling program started with three full cycles with a C-rate of C/10 as formation cycles. This was then followed by 1C cycling with each 20th cycle being C/10, with EIS measurements after the charge and after the discharge. The EIS program was 1kHz-0.1MHz with 10 steps per decade and 5mV perturbation potential.

### 3.7.4 Coin cell parts compatibility experiments

The cells for these experiments were made as explained in experimental section 3.6.3. Cyclic voltammetry was conducted in the range 3.5V-5.1V with a sweep rate of 0.01 mV/s for the cells with LP30. These were cycled at 25°C as usual. The cells with IL only had one single linear sweep from OCV and up to around 8 V while being placed in a temperature chamber at 40°C as the high voltage stability of the ionic liquid was what we wanted to test.

### 3.7.5 Extended potential range experiments

Extended potential range experiments were done in the range of 1-5V for the pure LMNO and LMNO with slight Al substitution on both Ni and Mn sites ($Al_{0.05}$-Mn/Ni).

## 3.8 Accelerating Rate Calorimetry

The instrument used was an esARC from Thermal Hazard Technologies with their ARC-ES v6.3.2 software. The chamber had a 14 cm diameter, and 13 cm depth, where the sample is fastened to the bottom of the lid before being placed in the chamber. There was also 500 mL of external volume for eventual gas evolution to settle in without dramatically increasing the pressure. This external volume was connected with a thin gas line as illustrated in figure 3.6 below. The gas system was tested earlier to have a volume of 38 mL excluding the bottle [89], where the only change to this setup is the removal of a Swagelok quick connector on the bottle.

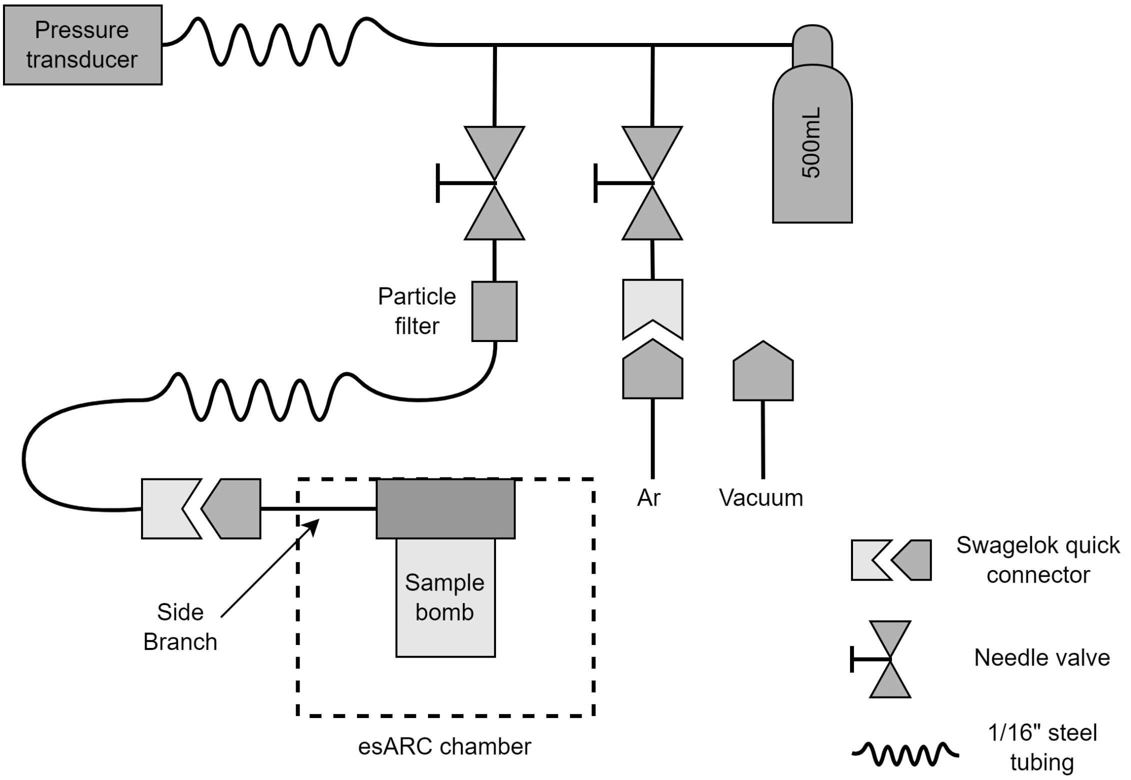

Figure 3.6: ARC setup gas diagram

Further specific settings were an initial temperature of 50°C, heating step of 5°C, wait time of 25 minutes, and a search time determined by the software. The adiabatic mode was triggered on 0.02°C self-heating rate, which was then measured until the sample reached 355°C, or the heat rate was below 0.02°C again. If the heat rate fell below 0.02°C the instrument restarted the heat-search process.

Before the experiments were conducted, the instrument was calibrated and drift-tested in addition to doing a standard reference experiment with 20% di-tert-butyl peroxide (DTBP) in toluene. This data can be found in Appendix B, figure B.19

### 3.8.1 $\phi$-factor

The $\phi$-factor for the experiments was set to be 3 since our collaboration partner FFI had previously carried out experiments at this $\phi$-factor before [89].

The specific heat capacity for the Al-substituted LMNO sample ($Al_{0.2}$-Ni) was calculated by equation 2.24. Then the heat capacity of eventual additives like conductive carbon or binder were added together. The heat capacity of the electrolyte is neglected as advised by our research collaborator FFI. More on this in Appendix A section A.3.

### 3.8.2 Sample preparation

The bomb used was an ARC-ES-1750, $\sim$ 1.32 g, 5.5 cm length, 0.15 mm wall thickness, welded on one side, heat capacity 0.5 J/K which were washed in nitric acid, acetone, and then ethanol before use. The cathode black mass was monitored for 5 minutes before being weighed into the bomb according to the $\phi$-factor. Especially with the LMNO, the mortaring resulted in the particles fusing together again to form flakes, this was combated by crushing and scraping with the edge of a spoon in order to decrease the particle size to the same size as the previous material by visual inspection. Images were taken at the end of each mortering to be able to compare the flake size to previous images. The weighing was followed by a compression stage, where a piston was pressed down in the bomb with a force of 1.25 kgF (resulting in 670 kPa compression pressure) three times before the electrolyte (1M $LiPF_6$ in EC:DMC 1:1 v:v, Sigma Aldrich) were added in the ratio of 2:1 of cathode black mass and electrolyte. The compression setup was modeled using Fusion360 and printed on a Prusa i3 mk3 3D printer. A photograph can be seen in figure 3.7 below.

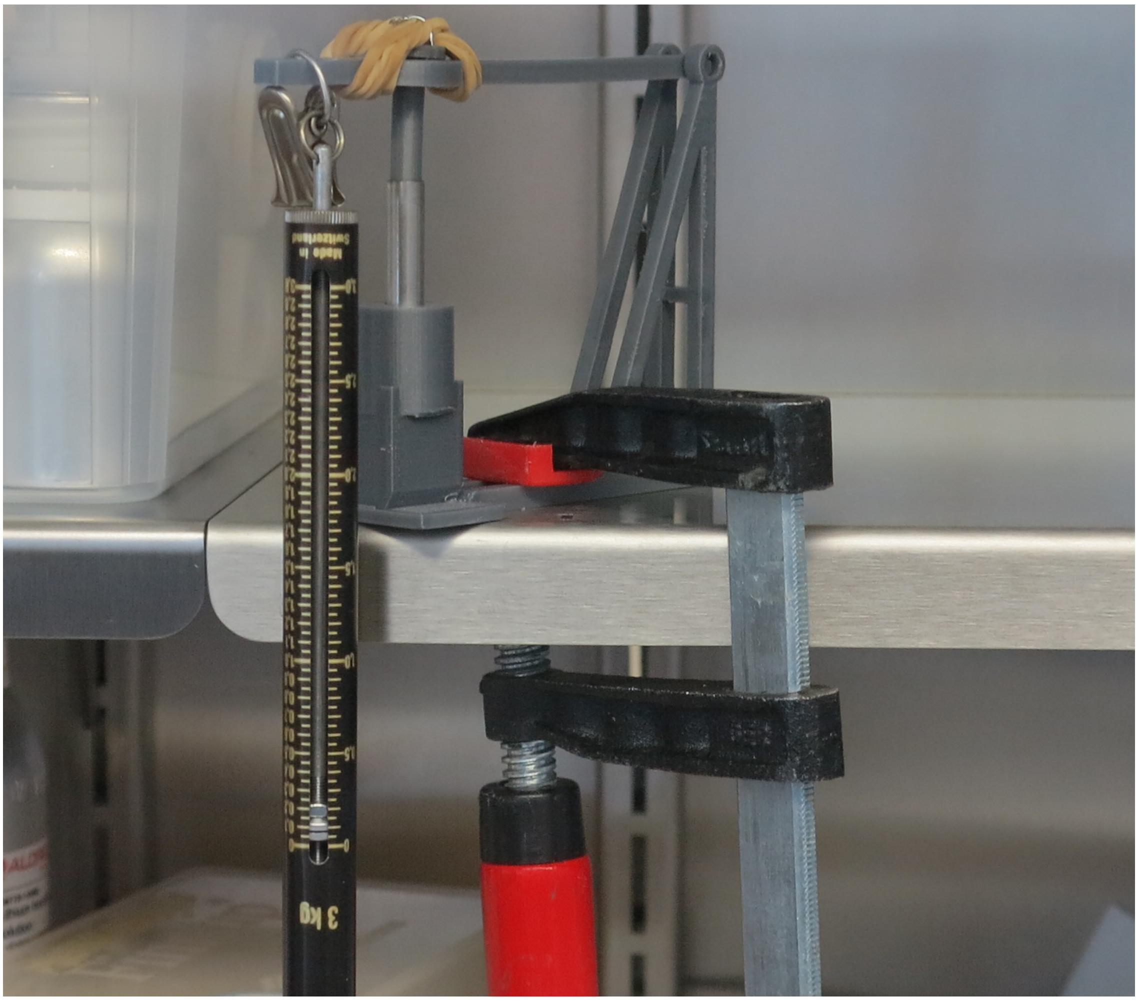

Figure 3.7: Powderpress setup used for ARC sample preparation

After this, the bomb could be fastened to the side branch by using a Swagelok nut, tightening by hand followed by one full rotation with spanners. The side branch consists of a thin tube connecting the bomb volume with an external gas system through a Swagelok quick-connector which holds the material under Argon when transferring from the glovebox to the instrument. The side-branch and bomb assembly were moved over to the instrument and attached to the lid by the bolt-in mechanism. Before bolting in, thermal paste (RS Stock No.:554-311, 0.65 W/mK) was added to the interface between the side-branch head and the lid to help the heat flow between the two. Then, the temperature sensor was mounted at a height of 1.5 cm from the bottom of the bomb and secured with an aluminum clip with a mass of approximately 0.32 g. The setup can be seen in figure 3.8 below.

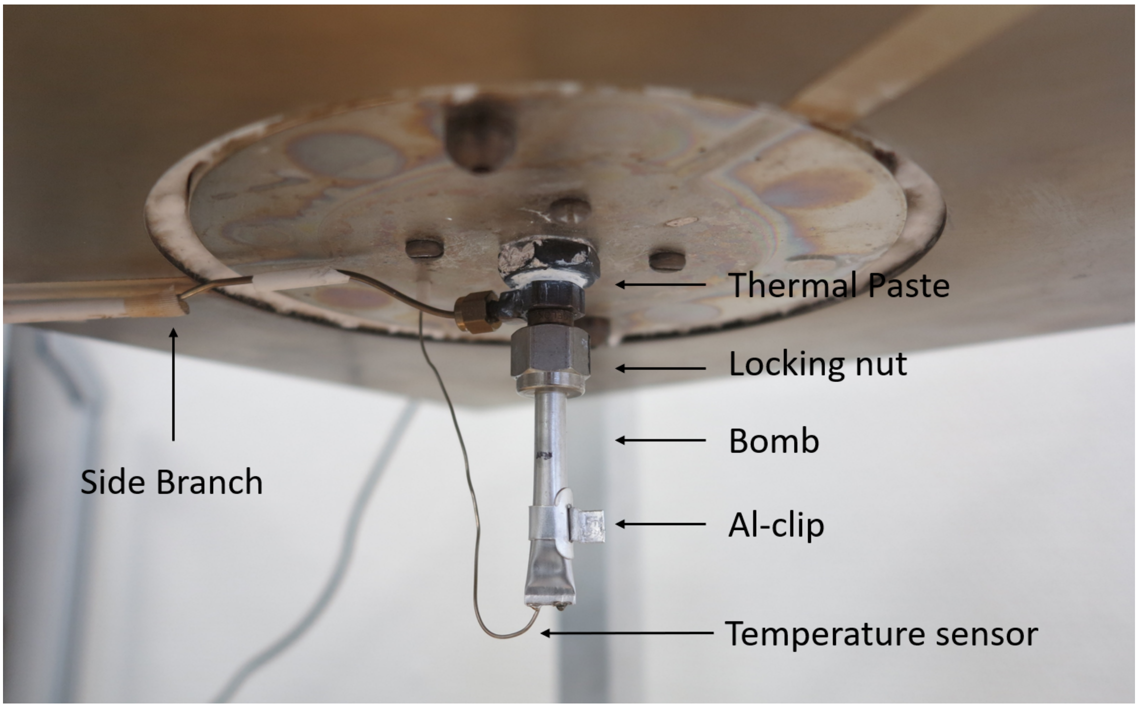

Figure 3.8: The bomb mounted in the ARC lid with the temperature sensor fastened by an aluminum clip. The black line on the tube signifies the top of the sample.

### 3.8.3 Data treatment

From the esARC software that runs the experiment, the .DAT file for the experiment was taken and used for analysis. Data from this file was plotted by using the matplotlib package in Python. The data was also smoothed by using a rolling average. A comparison of smoothed versus not smoothed data can be found in results section 4.8.5.

## 3.9 Sample naming scheme

The sample naming scheme used for the samples throughout the results and discussion is constructed simply from the amount of aluminum substitution, and on which site the substitution was attempted. An example is:

$$Al_{0.2} - Mn/Ni$$

which means that 0.2 Al were attempted substituted on both Mn and Ni site as this: $LiAl_{0.2}Mn_{1.4}Ni_{0.4}O_4$. Pure LMNO is just called LMNO. In table 3.2 below, the names are linked with their attempted formula.

Table 3.2: Sample names and their attempted stoichiometry.

| **Stoichi. subst.** | **Mn subst.** | **Ni subst.** | **50/50** |
|---|---|---|---|
| 0.05 | $LiAl_{0.05}Mn_{1.45}Ni_{0.5}O_4$<br>$Al_{0.05}$-Mn | $LiMn_{1.5}Al_{0.05}Ni_{0.45}O_4$<br>$Al_{0.05}$-Ni | $Al_{0.05}LiMn_{1.475}Ni_{0.475}O_4$<br>$Al_{0.05}$-Mn/Ni |
| 0.1 | $LiAl_{0.1}Mn_{1.4}Ni_{0.5}O_4$<br>$Al_{0.1}$-Mn | $LiMn_{1.5}Al_{0.1}Ni_{0.4}O_4$<br>$Al_{0.1}$-Ni | $Al_{0.1}LiMn_{1.45}Ni_{0.45}O_4$<br>$Al_{0.1}$-Mn/Ni |
| 0.2 | $LiAl_{0.2}Mn_{1.3}Ni_{0.5}O_4$<br>$Al_{0.2}$-Mn | $LiMn_{1.5}Al_{0.2}Ni_{0.3}O_4$<br>$Al_{0.2}$-Ni | $Al_{0.2}LiMn_{1.4}Ni_{0.4}O_4$<br>$Al_{0.2}$-Mn/Ni |

# Chapter 4

# Results

The results are discussed along with the presentation of data, following the same structure as in previous chapters, starting with the synthesis and analysis of the pristine material, followed by electrochemical and ARC measurements.

## 4.1 Synthesis

When synthesizing the samples, the exothermal reaction (combustion) was aimed to proceed slowly and not explosively. When looking at the combustion, it could be seen how the ignition started in one place in the beaker before the reaction front expanded over the entire bottom of the beaker. The Al-substituted samples, namely $Al_{0.2}$-Mn, $Al_{0.2}$-Ni, and $Al_{0.2}$-Mn/Ni, deviated somewhat from the general behavior. They also ignited, however, the fire only puffed the gel up to a very fluffy and crisp aerogel. A picture of this is included in figure 4.1 below. This means that the combustion reaction conditions were not the same for all samples.

Figure 4.1: Sol-Gel combustion synthesis of the $Al_{0.2}$-Mn sample

In addition, a few white spots were found on the side of the beaker after combustion of sample $Al_{0.05}$-Mn. This sample was not subjected to extensive studies, however, a picture of this can be found in Appendix B section B.2.

## 4.2 Powder X-Ray diffraction

XRD was done to identify the crystalline phases present in the samples. This included quantitative analysis of LMNOs spinel structure, as well as the amount of impurities present.

### 4.2.1 Phase identification and analysis

The three following figures, figure 4.2, 4.3, and 4.4, shows a region(1-3.5 $Å^{-1}$) of the diffraction patterns for the series where aluminum was attempted substituted on Mn sites, Ni sites, and both sites respectively. The intensities have been normalized concerning the (331)-peak to avoid normalizing with the increased background at lower Q.

For the LMNO spinel phase and the rock salt type impurity phase (introduced in section 2.2.4), the superstructure peaks from the ordering of nickel and manganese, have been pointed out. The intensity of the rock salt type impurity phase peaks has also been discussed, as these indicate the amount of impurity phase. This is also quantified through Rietveld refinement in the next subsection.

Figure 4.2 below shows two main changes with increased aluminum substitution attempted replacing manganese ($LiAl_xMn_{1.5-x}Ni_{0.5}O_4$). The first one is that the ordering of the spinel material decreases to the point where it is invisible in the XRD data. This can be seen from the fact that the superstructure peaks (annotated with blue stars) lowers in intensity with increased aluminum substitution and seems to be gone already at a substitution of $x = 0.1$. This is a significant change, as the ordering peaks intensity should only decrease by 30% for the maximum aluminum substitution (calculated in Appendix section B.3.3).

The second feature is how the rock salt type phase is changing - both the intensity and the angular peak positions increase with increased aluminum substitution. This can be seen by the two peaks from the (111)- and (200)-planes of the rock salt type impurity phase. At the same time, a slight increase in the intensity of the superstructure peaks (annotated by orange plus signs) for the rock salt type impurity phase is visible. The lowered unit cell size and increased ordering indicate that aluminum might be entering the rock salt type impurity phase.

Also note the anomalous slightly elevated flat plateau at 2.83-2.90 Å$^{-1}$, which is an error in the azimuthal integration where the diffraction ring goes over a border between two silicon chips in the Pilatus detector.

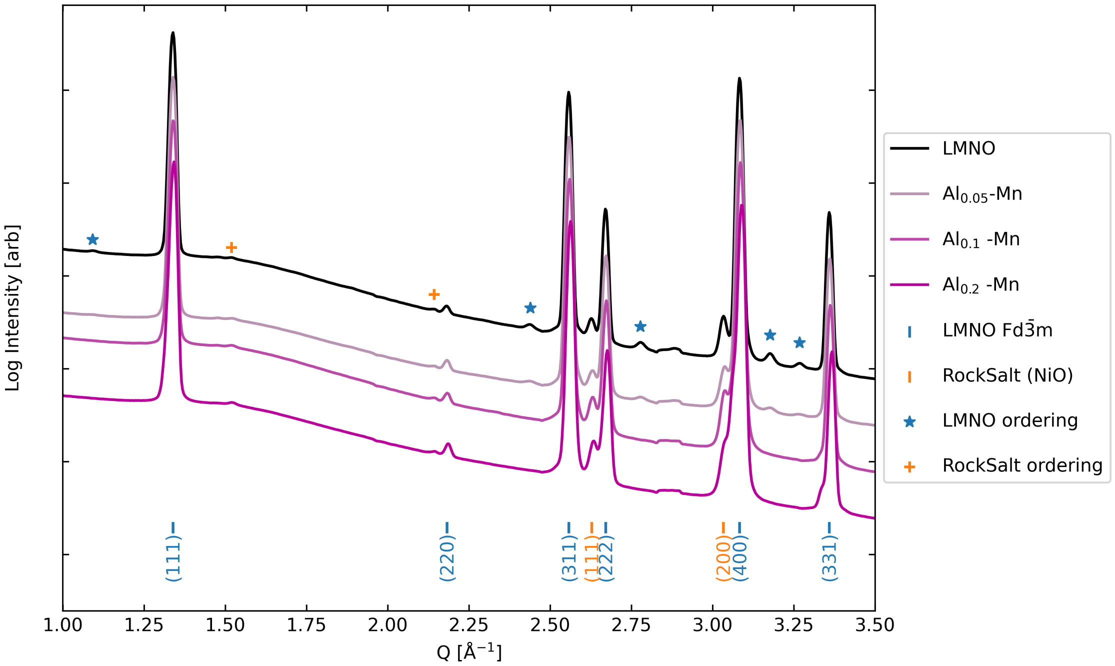

Figure 4.2: Raw synchrotron PXRD data of pristine LMNO where aluminum in the amounts 0, 0.05, 0.1, and 0.2 has been attempted substituted on manganese sites. Intensity normalized on the (331) peak.

For the series with aluminum attempted substituted for nickel ($LiMn_{1.5}Al_xNi_{0.5-x}O_4$) shown in figure 4.3, the spinel Ni/Mn ordering seems to go below the observable amount much faster than for the manganese substituted sample. A small hump can be seen on sample Al$_{0.05}$-Ni for the superstructure peak at 3.177 Å$^{-1}$ which is the last sight of spinel ordering in this series.

For the rock salt type impurity phase, the unit cell size does not seem to decrease as it did for the manganese substituted sample (Al$_x$-Mn). The peak intensity of the impurity phase is also highest for sample Al$_{0.05}$-Ni, and decreases slightly when going to Al$_{0.1}$-Ni before it almost completely vanishes for Al$_{0.2}$-Ni. This indicates that the spinel structure is more thermodynamically favorable compared to the rock salt type impurity phase under synthesis conditions for the $x = 0.2$ substitution amount.

One could suggest that the low amount of rock salt type impurity in the $Al_{0.2}$-Ni sample is because it is completely unordered and have a smaller lattice parameter, thus moving all its peaks into the peaks of the spinel. This is highly unlikely as there is a small peak visible from the (111) plane of the rock salt type impurity, proving that this is not the case.

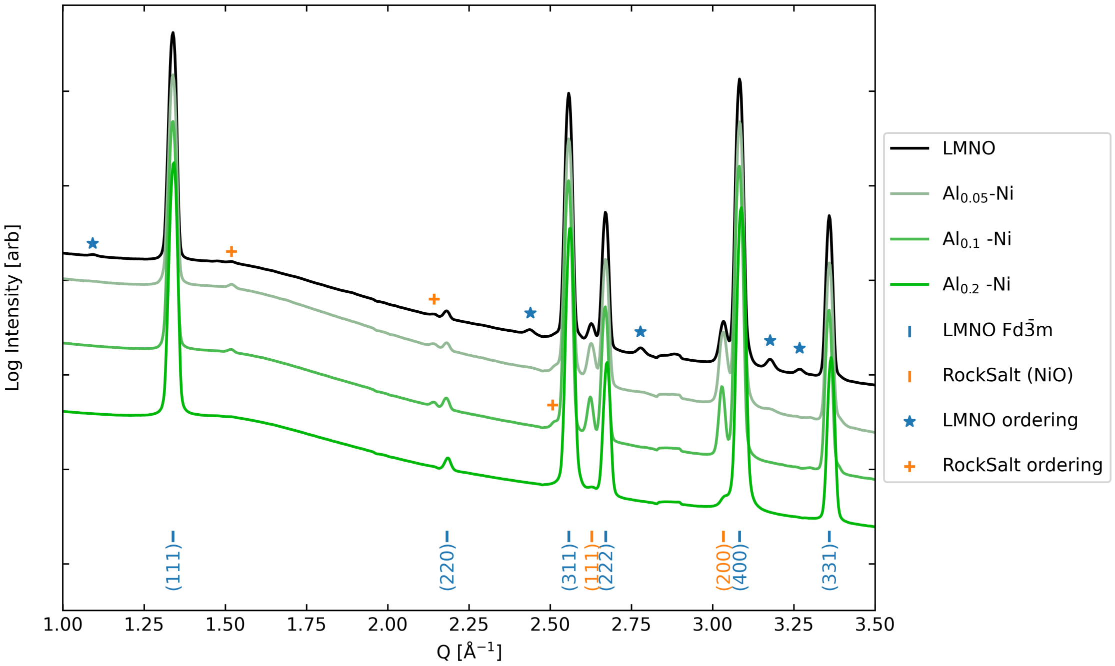

Figure 4.3: PXRD data of pristine LMNO where aluminum in the amounts 0, 0.05, 0.1, and 0.2 has been attempted substituted on nickel sites. Intensity normalized on the (331) peak.

When aluminum is attempted substituted for equal amounts of Mn and Ni ($LiMn_{1.5-x/2}Al_xNi_{0.5-x/2}O_4$ in fig 4.4 below), the effects of nickel substitution and manganese substitution seems to have combined.

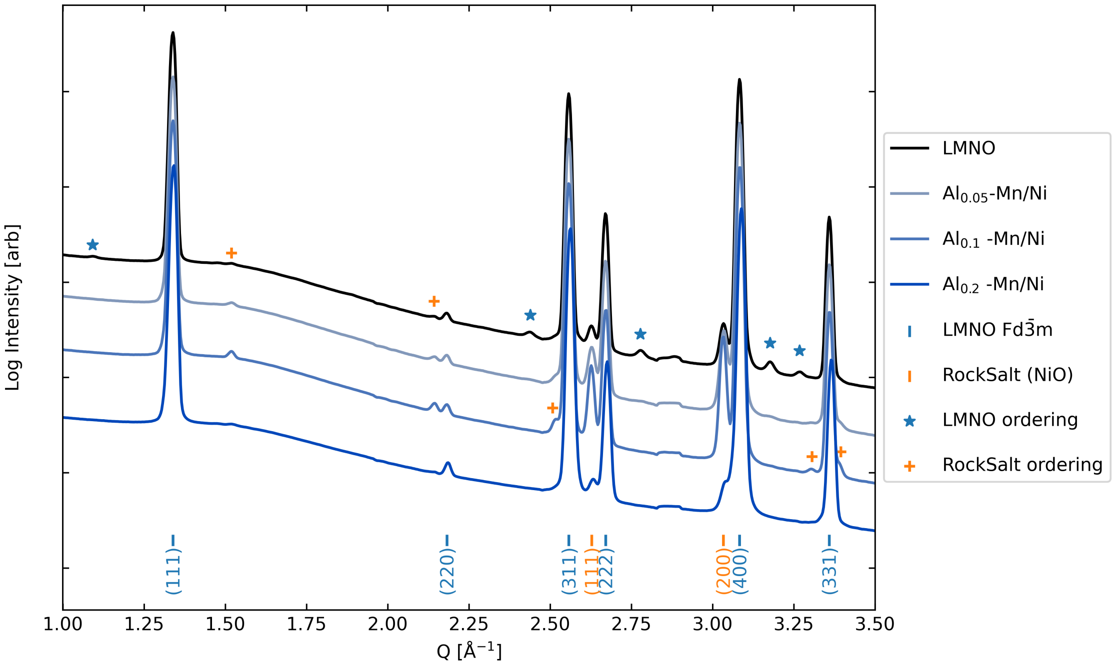

Figure 4.4: Raw synchrotron PXRD data of pristine LMNO where aluminum in the amounts 0, 0.05, 0.1, and 0.2 has been attempted substituted 50/50 on nickel and manganese sites. Intensity normalized on the (331) peak.

A comparison of the samples with the highest aluminum substitution on the different sites with pristine LMNO for reference can be found in figure 4.5 below. The figure shows how the impurity phase of the $Al_{0.2}$-Mn is more prominent than in regular LMNO, and that it is almost gone for the $Al_{0.2}$-Ni sample, while for sample $Al_{0.2}$-Mn/Ni there is an intermediary amount. This indicates that Al substitution for manganese is difficult, but also that Al substitution in the correct amounts for nickel can actually lower the amount of impurities.

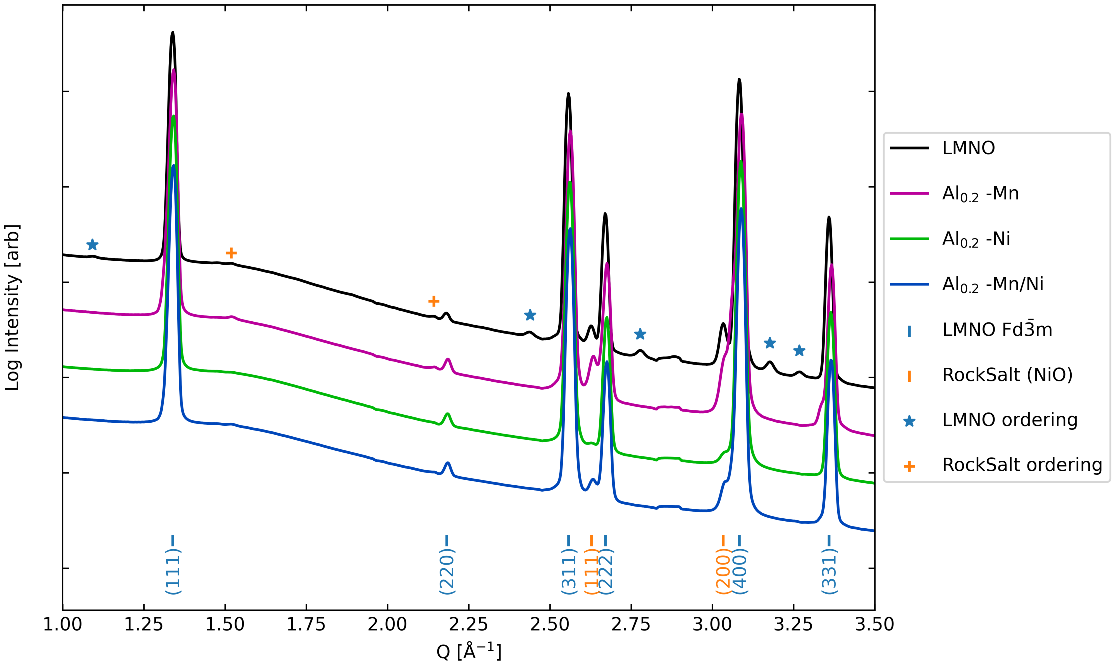

Figure 4.5: Synchrotron PXRD data of the 0.2 Al substituted samples on different sites with pure LMNO for reference. Intensity normalized on the (331) peak.

As to the reason why aluminum easily replaces nickel but not manganese, there are a couple of theories. Firstly, if aluminum is attempted substituted on the manganese sites, this must be charge compensated either by oxygen vacancies, lithium interstitials, or $Ni^{3+}$. Charge compensation with oxygen vacancies would result in an oxygen stoichiometry of 3.9, or a site occupancy of 0.975. This is very possible, but somewhat unlikely due to the synthesis conditions being targeted for full occupancy (10 hour step at 700°C with oxygen flow and slow cooling to room temperature) as discussed in theory section 2.3.

Charge compensation by lithium interstitials would result in a Li stoichiometry of 1.2, or 120% where everything above 1 is believed to be placed on octahedral sites. However, the excess lithium in the synthesis was only 5%, which is not enough, and in addition, there was no 3 V capacity in the electrochemistry data (shown in results section 4.6.2) which is generally attributed to the intercalation of lithium on octahedral sites as described in theory section 2.2.5.

The last option of charge neutrality is that some nickel is in oxidation state 3+. However, $Ni^{3+}$ is hard to form, especially considering the nickel in the precursor was in the 2+ oxidation state. What might have happened then is, as seen in figure 4.5 above that aluminum rather replaces nickel, nickel is pushed out and a Ni-rich rock salt type impurity forms.

By instead substituting 0.2 aluminum for nickel, charge compensation can easily be done by decreasing the oxidation state of manganese from 4+ to 3+ for 0.2 stoichiometric units of manganese. In this way, all the nickel and manganese can stay in the spinel structure, avoiding the formation of the impurity phase as shown in 4.5 above. However, the solid solubility of Al on Ni sites seems to be limited to a specific concentration range as shown in figure 4.3.

### 4.2.2 Lattice parameter and impurity phase analysis

From Rietveld refinements, the spinel lattice parameter of all the samples has been estimated in addition to the amount of impurity phase with a disordered rock salt type phase of nickel oxide. For this, the synchrotron XRD data were used due to their superior signal-to-noise ratio. These are shown in figure 4.6 below, with error bars indicating the mathematical error calculated by TOPAS for the refinement.

As can be seen, for the samples where Mn was substituted (purple), the lattice parameter decreases linearly with increased Al substitution amount. At the same time, the amount of rock salt type impurity increases, which might indicate that some Al occupies the Ni sites, and some Ni goes into the impurity phase.

On the contrary, for the samples where Ni was substituted (green), the impurities start higher before dropping. This is an indication of a structural change in the spinel which increases the solid solubility of aluminum with increased stoichiometric amounts of aluminum.

The strongest deviation in the trends seen in the figure is that the spinel lattice parameter of sample $Al_{0.1}$-Ni is significantly higher than the other samples. It is unclear exactly why this is, but it is a material property as the Rietveld refinements were all visually inspected and accepted in terms of peak intensities and position.

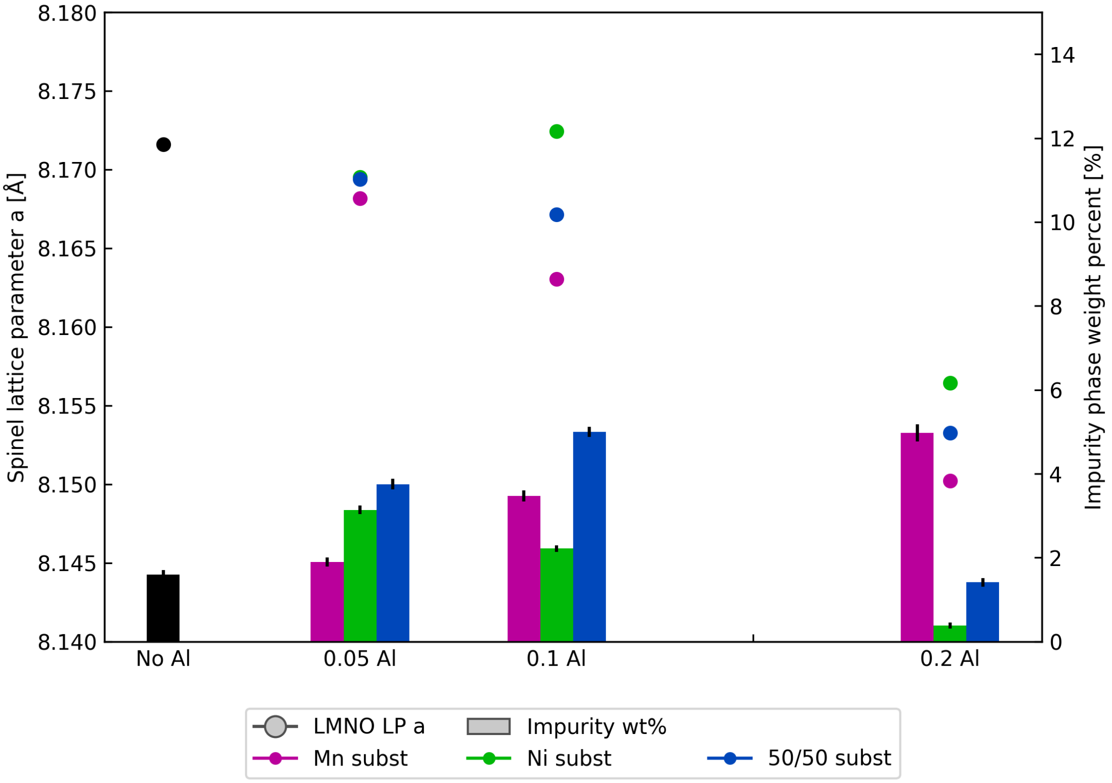

Figure 4.6: Refined spinel lattice parameter $a$, and amount of rock salt type impurity phase in all the LMNO samples. The spinel lattice parameter of the blue and green sample for the $Al_{0.1}$-Ni and $Al_{0.1}$-Mn/Ni is almost identical. $R_{wp} \in [4.5,6.1]$, mathematical error of the lattice parameter is within the extent of the dots, and visualized by a black bar for the impurities.

### 4.2.3 Delithiated materials

Pouch cell post-mortem material was characterized by XRD using the home-lab capillary instrument with a molybdenum ($K\alpha_1$ and $K\alpha_2$) source. Rietveld refinements were done to determine lattice parameters and phase content for these samples. Interestingly, for the pure LMNO sample, when delithiated, two LMNO phases with differing lattice parameter was found. For the $Al_{0.2}$-Ni sample, only one LMNO phase was found. The lattice parameters can be found in table 4.1 below. The outcome from the Rietveld refinements, with observed, calculated and difference intensity profiles, is shown in figure 4.7 below.

Table 4.1: Rietveld refinement of delithiated LMNO and $Al_{0.2}$-Ni from post-mortem pouch cell material.

| **Sample** | **Phase** | **Lattice Parameter a (Å)** | **Amount (%)** | $\mathbf{R}_{wp}$ |
|---|---|---|---|---|
| LMNO | LMNO Fd$\bar{3}$m 1 | 8.089 | 33 | 5.6 |
| | LMNO Fd$\bar{3}$m 2 | 8.001 | 67 | 5.6 |
| $Al_{0.2}$-Ni | LMNO Fd$\bar{3}$m | 8.041 | 100 | 5.9 |

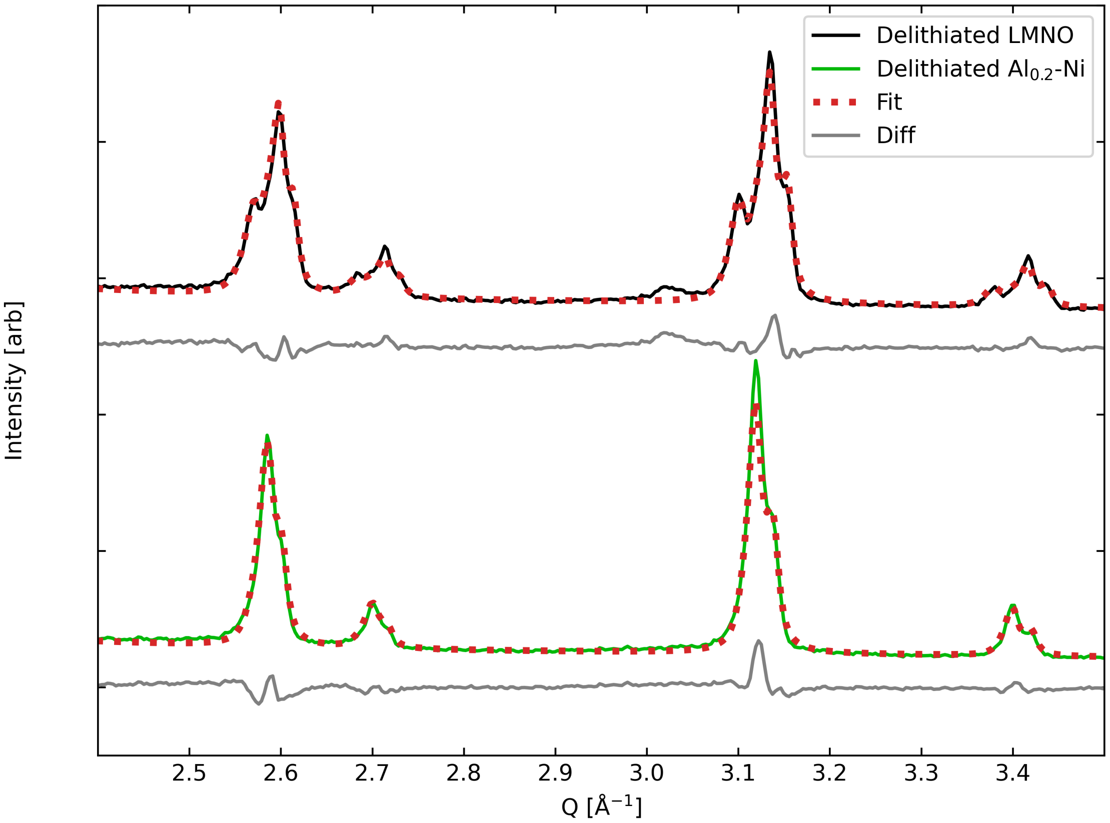

Figure 4.7: Home lab capillary XRD of delithiated LMNO (black) and delithiated $Al_{0.2}$-Ni (green). Red dotted is the calculated diffraction pattern from Rietveld analysis, and grey is the difference between the fit and the measured data. The radiation is molybdenum K$\alpha_1$ and K$\alpha_2$.

The lattice parameters and mass percentages shown in table 4.1 above agree somewhat with Samarasingha et al's operando work [30] (shown in Appendix section B.3.1) and others work [115], [116]. Samarasingha et al's work show that when fully lithiated, the ordered spinel material should have a bit of a phase with a lattice parameter of 8.08 Å (10wt%), and a significant amount of LMNO phase with 8.00 Å lattice parameter (80wt%). Since for my sample I have 33 wt% of LMNO 1 phase, it indicates that my degree of delithiation was less than that Samarasingha et al. reached.

For the delithiated disordered material, Samarasingha showed that there should be a phase of 8.00 Å, however, for the aluminum substituted material ($Al_{0.2}$-Ni), a phase with a lattice parameter of 8.04 Å was found, indicating that the delithiation mechanism for this sample is somewhat different from the pure disordered LMNO structure which he synthesized. While the slightly changed lattice parameter can be from the effects of substitution, this only contributed to a change of 0.02 Å for the pristine material. It is therefore proposed that the lattice parameter of the $Al_{0.1}$-Ni sample is so high because of the remaining lithium in the structure. This is expected, as at some point all manganese and nickel will be in oxidation state 4+, while some lithium is still in the structure.

## 4.3 Scanning Electron Microscopy

SEM micrographs have been taken for all the materials and were taken after combustion and heat treatment but before mortaring. From figure 4.8 it can be seen that for pure LMNO polycrystalline particles have formed in a 3D network where the grain sizes are on the order of 0.2-0.7 $\mu$m. In between these particles, larger single crystals with a diameter of approximately 5 $\mu$m can be found. This shows that the powder morphology is not homogeneous for the pure LMNO sample.

The particle homogeneity for the 0.2 Al substituted samples seems to be a bit better since they have a smaller size difference between the large single crystals and the polycrystalline particle grains. For instance, the $Al_{0.2}$-Mn sample grains sizing (0.2-0.5 $\mu$m) in the same polycrystalline particle, and single large crystallites appear seldom and are below 1 $\mu$m in diameter. This can be seen in figure 4.9 below and also seems to be the case for the two other highly substituted samples, $Al_{0.2}$-Ni and $Al_{0.2}$-Ni/Mn. This means that it seems like an increased aluminum substitution yields a smaller crystallite size.

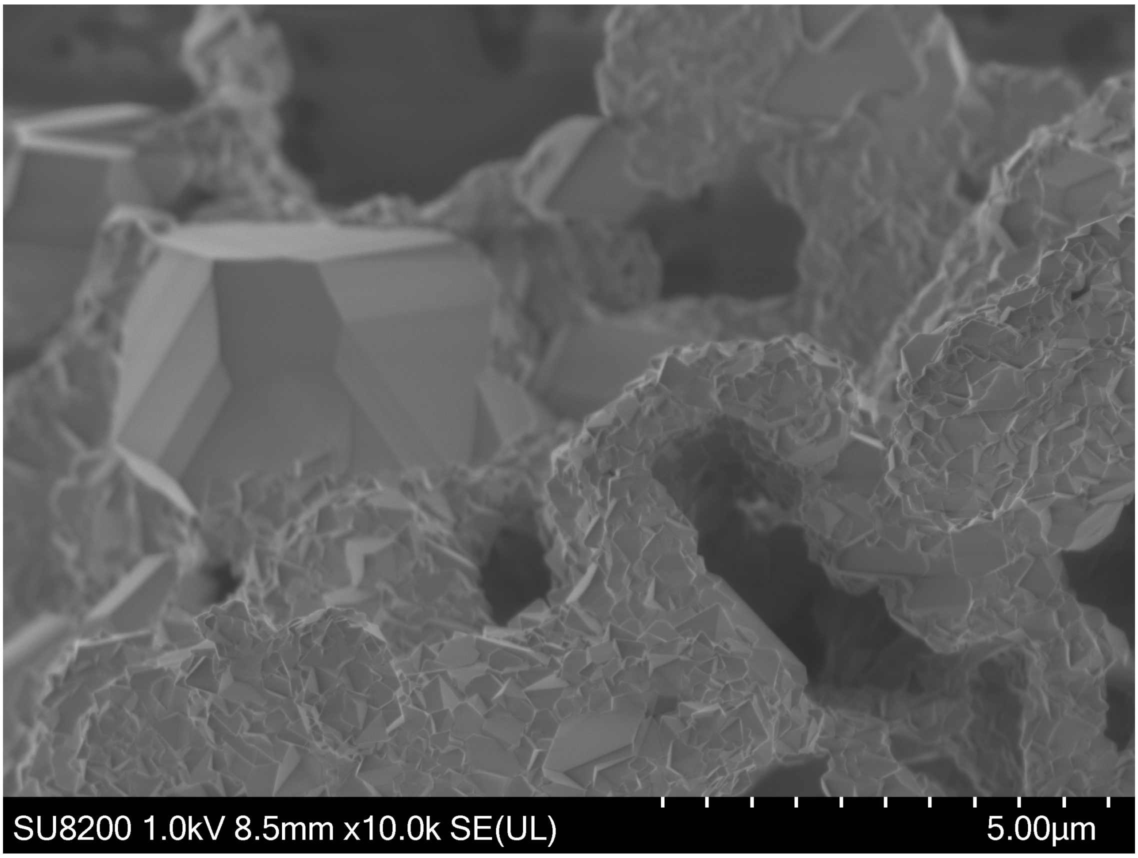

Figure 4.8: SEM micrograph of pure LMNO.

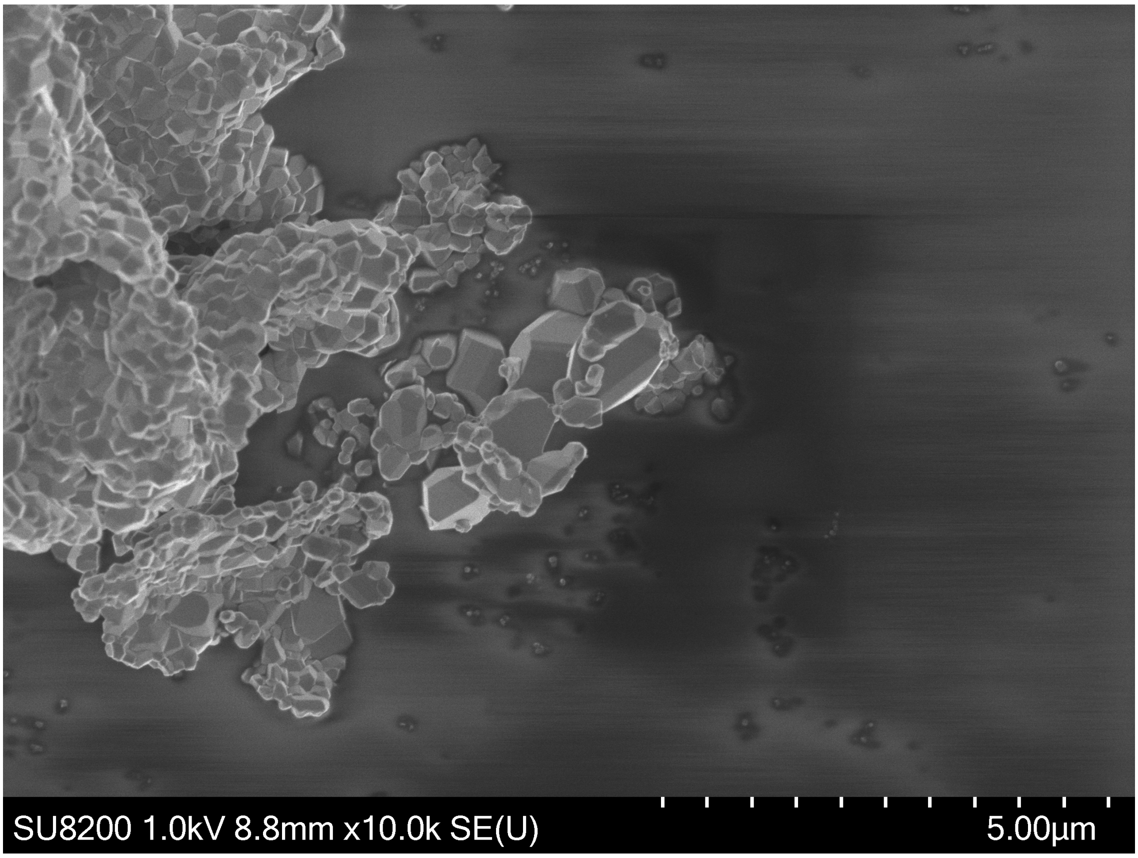

Figure 4.9: SEM micrograph of $Al_{0.2}$-Ni.

The pristine and post-mortem SEM micrographs of a pouch cell electrode of material $Al_{0.2}$-Ni used for ARC measurements were also imaged and are found in figure 4.10 below. In the top-right micrograph in figure 4.10, a huge fiber was observed from what is believed to be the separator. This is evidence that washing with 1 mL of DMC on an electrode of 100 $cm^2$ in size is not sufficient for the complete removal of separator fibers. Mitigation of this can be done by replacing the separator with a plastic alternative, as washing with more DMC or other organic solvents can dissolve the SEI layer formed on the particles to a varying degree. The post-mortem sample was also imaged before and after washing, with the only visible difference that there were fewer separator fibers on the sample after the washing had been completed. However, the difference in fiber concentration was impossible to visualize when taking the micrographs due to the fibers being too small for overview micrographs. Because of this, the micrographs comparing washed and unwashed have been omitted.

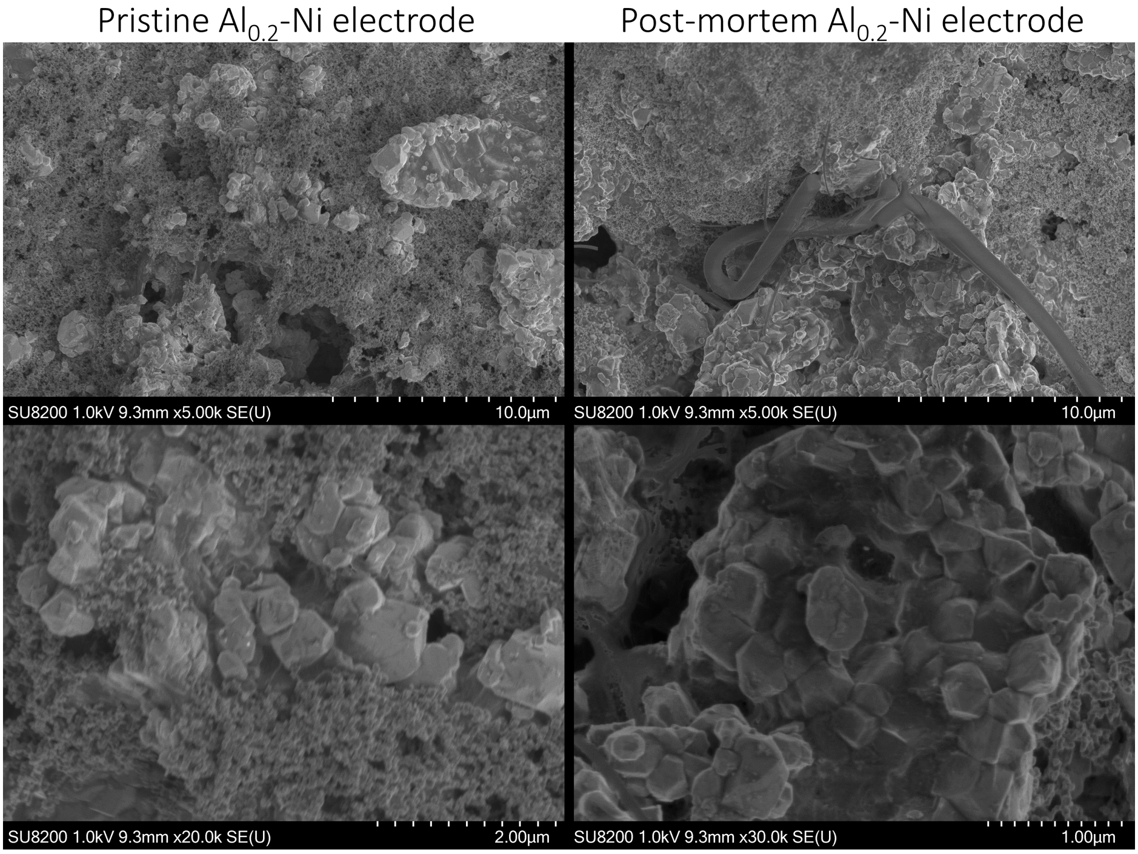

Figure 4.10: Pristine versus post-mortem electrode in $Al_{0.2}$-Ni pouch electrode

## 4.4 Raman Spectroscopy

The Raman experiments showed quite clearly that the quality of the recorded data, and possibly also the crystallographic state of the sample, depended strongly on the positioning of the beam on different bunches of crystallites. Three measurements of the same material are shown in figure 4.11 below. LMNO is extremely absorbant to this radiation, meaning that these measurements can probe as little as 25 nm into the surface of the sample [29]. If this is the case, then the radiation spot size on the sample, and the morphology of the sample is very important.

As seen in the SEM results, there are quite large particles forming three-dimensional networks out of small crystallites (0.25-1 $\mu$m facet diameter) while some larger crystals with a diameter around 5 $\mu$m also can be found separate from the polycrystalline particles. Since the laser spot size on the sample was around 2 $\mu$m, we might be seeing an effect where one facet has been probed, which measures an ordered structure, while at another facet, or at the facet boundaries on the surface of the polycrystalline particles, no ordering is measured. This needs further investigation and a natural next step would be to systematically measure the different facets in a spectrometer with a high-resolution microscope and positioning system.

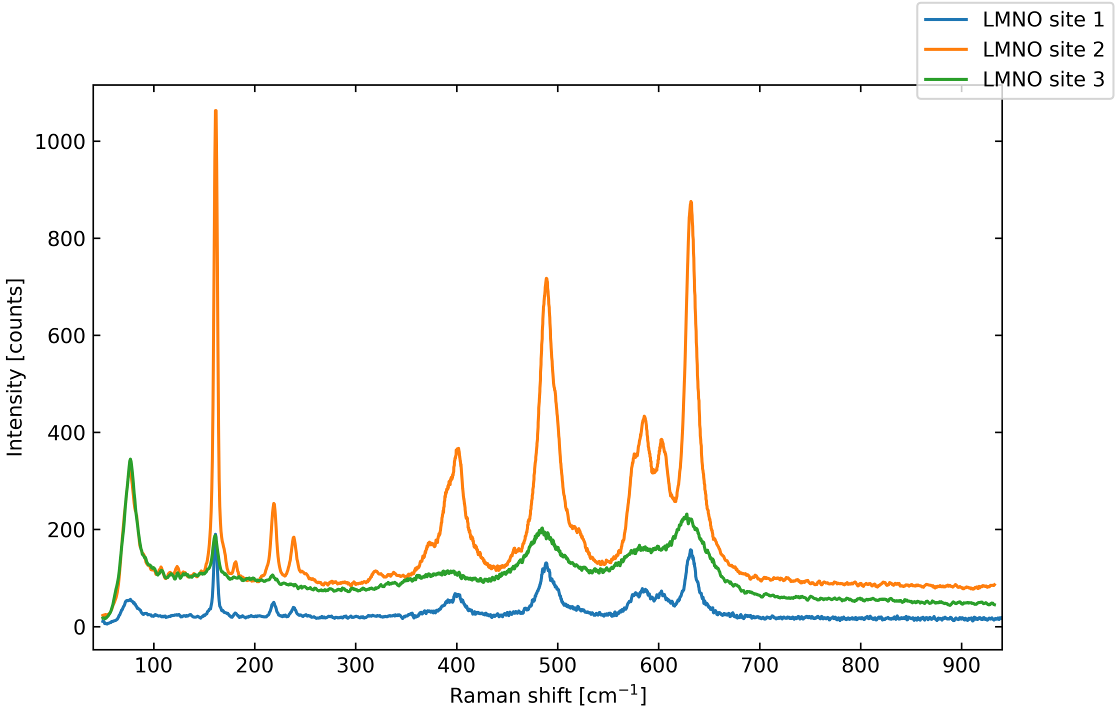

Figure 4.11: Three different Raman specters on the same material

Two days of measurement were done and the paracetamol reference measurement was done before and after the other measurements. Although they vary a bit between the scans, this seems to only be the noise-signal ratio, and not the peaks themselves. This is shown in figure 4.12 below.

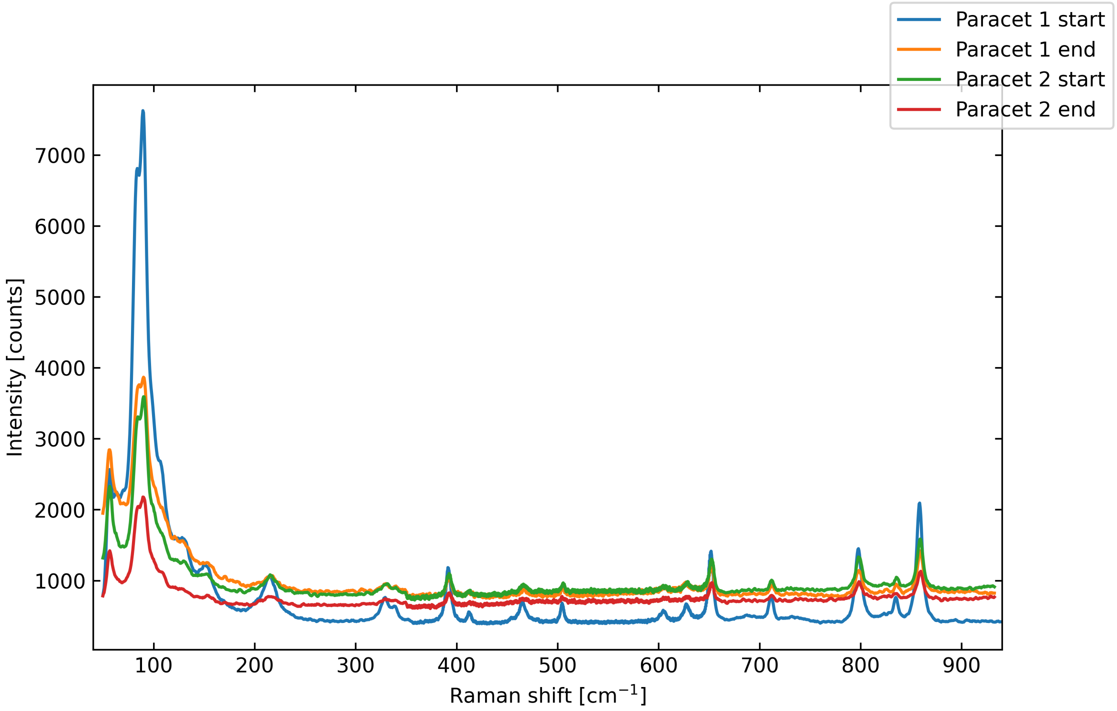

Figure 4.12: Paracet measurement on the start and end of the two days of measurement

Due to the poor reproducibility of these measurements, no further Raman spectra will be shown or discussed.

## 4.5 Inductively Coupled Plasma Mass Spectroscopy

ICP-MS was done for the pure LMNO sample and the $Al_{0.2}$-Ni sample, and verified by a duplicate experiment. This was done to verify that no material was lost during the synthesis, where we were especially interested in the lithium content as lithium can evaporate at high temperatures in the form of lithium hydroxide [117]. The results of ICP-MS shown in table 4.2 and 4.3 shows that the anticipated ratio of metals was found and that very little lithium has escaped. It must also be noted that a 5% excess of lithium was used in the synthesis.

Table 4.2: ICP-MS data for pure and substituted LMNO samples in mass percent.

| **Sample** | **% Li** | **% Mn** | **% Ni** | **% Al** |
|---|---|---|---|---|
| LMNO | 3.53 | 42.19 | 15.07 | - |
| LMNO | 3.55 | 42.21 | 15.05 | - |
| $Al_{0.2}$-Ni | 3.45 | 39.76 | 8.83 | 3.14 |
| $Al_{0.2}$-Ni | 3.41 | 39.81 | 8.81 | 3.17 |

Table 4.3: ICP-MS data for pure and substituted LMNO samples in moles per mole LMNO.

| **Sample** | **Li** | **Mn** | **Ni** | **Al** |
|---|---|---|---|---|
| LMNO | 0.993 | 1.499 | 0.501 | - |
| LMNO | 0.998 | 1.500 | 0.500 | - |
| $Al_{0.2}$-Ni | 1.004 | 1.461 | 0.304 | 0.237 |
| $Al_{0.2}$-Ni | 0.990 | 1.461 | 0.303 | 0.237 |

However, from table 4.3 it is visible that there is more aluminum than what was attempted. According to the weigh-in of the precursors, this stoichiometry should have been $LiMn_{1.481}Al_{0.198}Ni_{0.296}$, only with uncertainties in the third decimal (arising from precursor purities, standard solution, and weigh-in errors). This means either manganese and nickel have escaped, or aluminum must have entered. This material was sintered in an alumina crucible, so an exchange of aluminum and manganese can have happened between the two. However, this crucible had been used many times for LMNO sintering before and should have been saturated with Mn in that case. In addition to this, for Al to transfer to LMNO, it would have to be more thermodynamically stable in LMNO than alumina, which is unlikely. During synthesis, there is also the chance of nickel or manganese carbonyls or hydroxy-variants leaving the beaker together with the evaporation of water and off-gassing of $NO_x$. This matter needs more investigation.

## 4.6 Electrochemical testing

The electrochemical characterization included galvanostatic cycling through rate capability testing, accelerated degradation testing as well as experiments for evaluating the compatibility of parts in a coin cell and the electrochemical window of electrolytes.

For all electrochemical data, the data from a representative cell has been chosen for plotting. The data for the eventual twin cell (explained in [3.7) is shown in Appendix B: Supplementary data (B.5).

For the following sections about galvanostatic cycling and rate capability testing, all data figures are different visualizations of the same experiments collected as rate capability degradation testing.

### 4.6.1 Reproducibility of coin cell experiments

Two identical cells of pure LMNO and $Al_{0.2}$-Mn/Ni are compared in figure 4.13 in order to demonstrate the reproducibility of coin cells. It shows that for lower C-rates, the reproducibility is quite good. However, for C-rates of 2C and above, larger variations occur. This is further discussed in section 4.6.4 below.

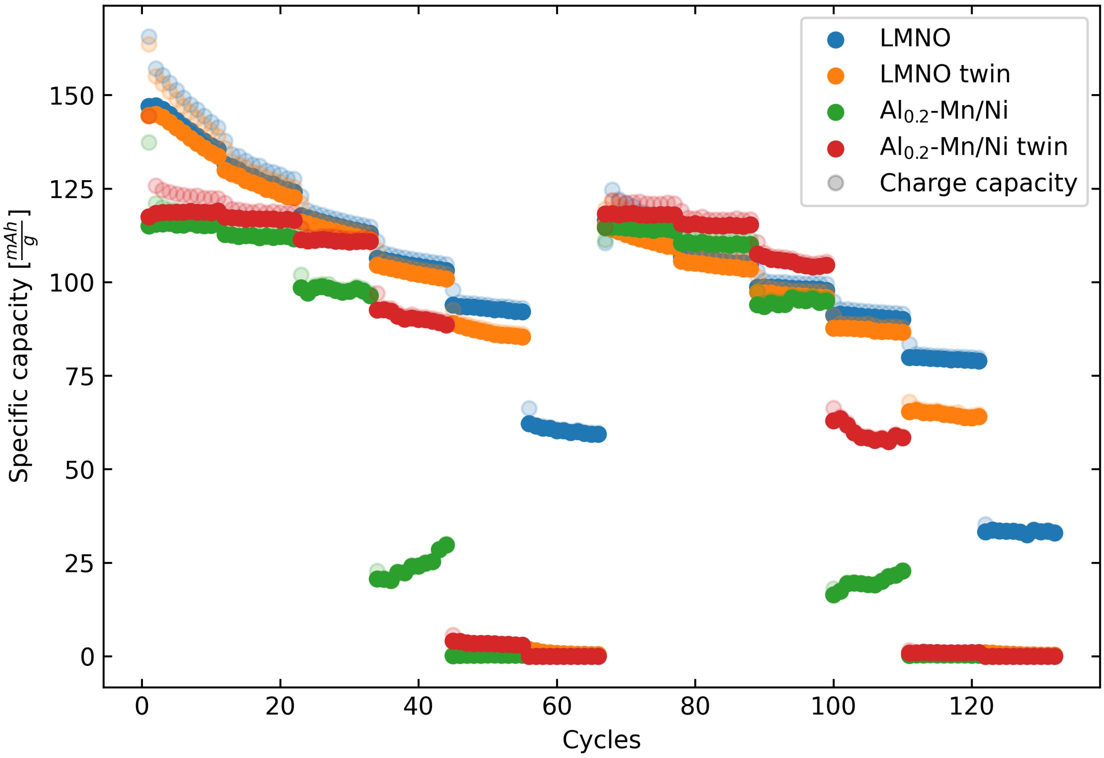

Figure 4.13: Reproducibility of rate capability degradation testing.

The cause of bad reproducibility can be hard to determine, but some suggestions can be made. Firstly, the main source of error is the difficulty of weighing in the small masses of the electrodes. The scale used had a resolution of 0.1 mg, however, in a glovebox where there are ventilation and pressure changes regularly, both the drift and the offset of the scale are hard to control and might lead to some uncertainty in calculated cycling currents, which in turn creates different overpotentials for different current steps and different rate of degradation.

In addition to this, macroscale effects like electrode and separator wetting, electrode stack pressure, and electrode alignment can all affect the measurements. The issues especially arise when parts are changed out without doing an optimization study for each change. For all my electrodes, the cathode looked to be quickly wetted by the electrolyte when dripped on top, however, it is hard to know if this is the case for the micropores below the surface of the coating. The electrode stack pressure should also be the same in all of these cells, as the loading of the cells was roughly the same (around $5-7$mg of active material) and all other parts were the same thickness. Electrode alignment should not be a problem either as the anode lithium metal disc is 1mm larger in diameter than the electrodes, which gives a significant margin when aligning them on top of each other.

Impurities can also introduce errors by leading to unfavorable reactions in the cell. Impurities could have been introduced in any step of the process where the precursors were exposed to air or argon, however, the work environment has been made relatively clean, both inside the glovebox and outside. Water absorption of the electrodes could also be a source of error as they were vacuum-dried and then taken back out into air atmosphere before being quickly inserted into the glovebox antechamber.

### 4.6.2 Galvanostatic cycling curves

The galvanostatic cycling curves for very low C-rates are mostly controlled by thermodynamics rather than kinetics. This means that the reproducibility of potential curves at low C-rates is significantly higher than that of high C-rate cycling. Firstly, the galvanostatic cycling data for one cycle of pure LMNO is compared to that of $Al_{0.2}$-Ni, in order to comment on the change in electrochemistry with a high amount of substitution. This can be seen in figure 4.14 below.

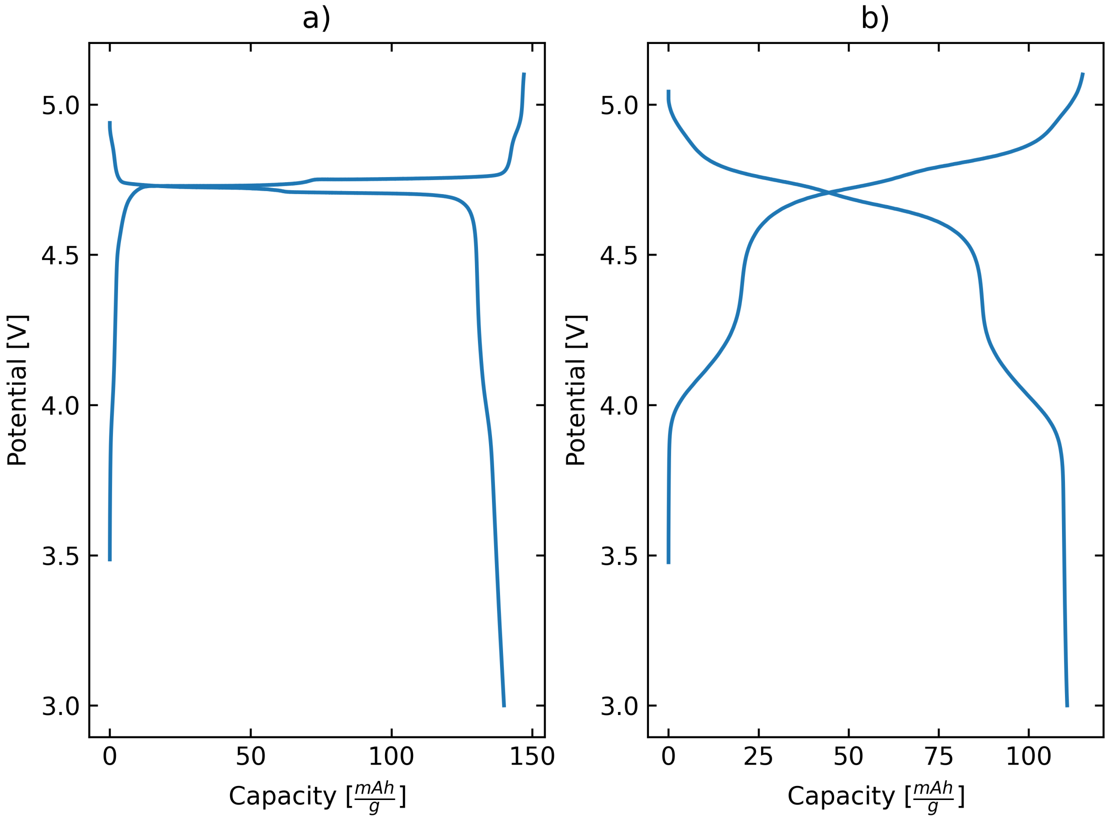

Figure 4.14: Fifth cycle of galvanostatic cycling for a) LMNO and b) $Al_{0.5}$-Ni at C/10.

From figure 4.14 above, the first feature to highlight is the capacity at 4 V for the $Al_{0.2}$-Ni sample. This is most probably due to the charge balance mechanism discussed in theory section 2.2.4.1 which leads to $Mn^{3+}$ being available in the spinel.

Also visible is the two-step plateau at 4.7 V with a separation of 20 mV for the LMNO sample. These different electrochemical potentials are attributed to the $Ni^{2+}/Ni^{3+}$ and $Ni^{3+}/Ni^{4+}$ redox reactions, and their difference is usually below 30 mV for ordered materials [30]. From Samarasingha et al's synchrotron studies, he showed that in the ordered structure, the lithium does not behave as a solid solution in the crystals, but rather as two first-order phase transitions

[30]. His data indicates that there exist three separate phases, perhaps as $Li_1$MNO, $Li_{0.5}$MNO, and $Li_0$MNO, where the amount of the phases changes with the degree of lithiation. If a phase then forms at the surface when a (de)lithiation starts, this phase boundary could travel through the crystal. This also means that at the surface of the crystal, the lithium concentration will be the same throughout the extension of that phase, yielding the same potential. This could be the explanation for the very flat voltage plateaus seen for the LMNO sample above.

For the $Al_{0.2}$-Ni sample shown in figure 4.14 b) however, the potential separation is not nearly as visible and is only 9 mV. In addition, the plateaus slope with the degree of lithiation, indicating that the electrochemical potential at the surface of the particle changes. If it is believed that the lithiation mechanism in this material is a solid solution rather than a phase change, this could make sense as a lithium concentration change at the surface of the particle would affect the potential, much in the same way it does for the conventional layered cathode materials. The proposed theories of lithiation mechanisms can be written out as shown in table 4.4 below.

Table 4.4: Proposed reaction mechanisms for phase transition and solid solution lithiation mechanisms of LMNO.

| **Mechanism** | **Reaction** | **Potential (V)** |
|---|---|---|
| *Three-Phase* | $Li_0M_2O_4 \rightarrow Li_yM_2O_4$ | 4.7 |
| | $Li_yM_2O_4 \rightarrow Li_1M_2O_4$ | 4.7 |
| *Solid Solution* | $Li_xM_2O_4, \quad x \in [0,1]$ | 4.6 - 4.9 |

where y is a phase with an intermediary amount of lithium. It must also be pointed out that it is highly unclear how the potential plateau separation relates to these two proposed mechanisms.

Although the theories suggested in table 4.4 above is supported by Samarasingha et al's data [30], and general lithiation mechanism theory [118], this needs further investigation. A first step would be to do operando X-ray diffraction and see that the crystal changes as expected. This could be followed up by partial lithiation of the two different materials followed by a post-mortem analysis where a particle is cut in two (by e.g. a focused ion beam) and then having the lithium concentration spatially resolved through e.g. spatially resolved secondary ion mass spectroscopy [119].

Following the discussion on electrochemical change with aluminum substitution on nickel sites, the electrochemistry data for substitution on manganese and both sites are shown in figure 4.15 below, with the twin cell data available in Appendix B, figure B.10. The data has been overlaid for easier comparison of capacities at the different plateaus.

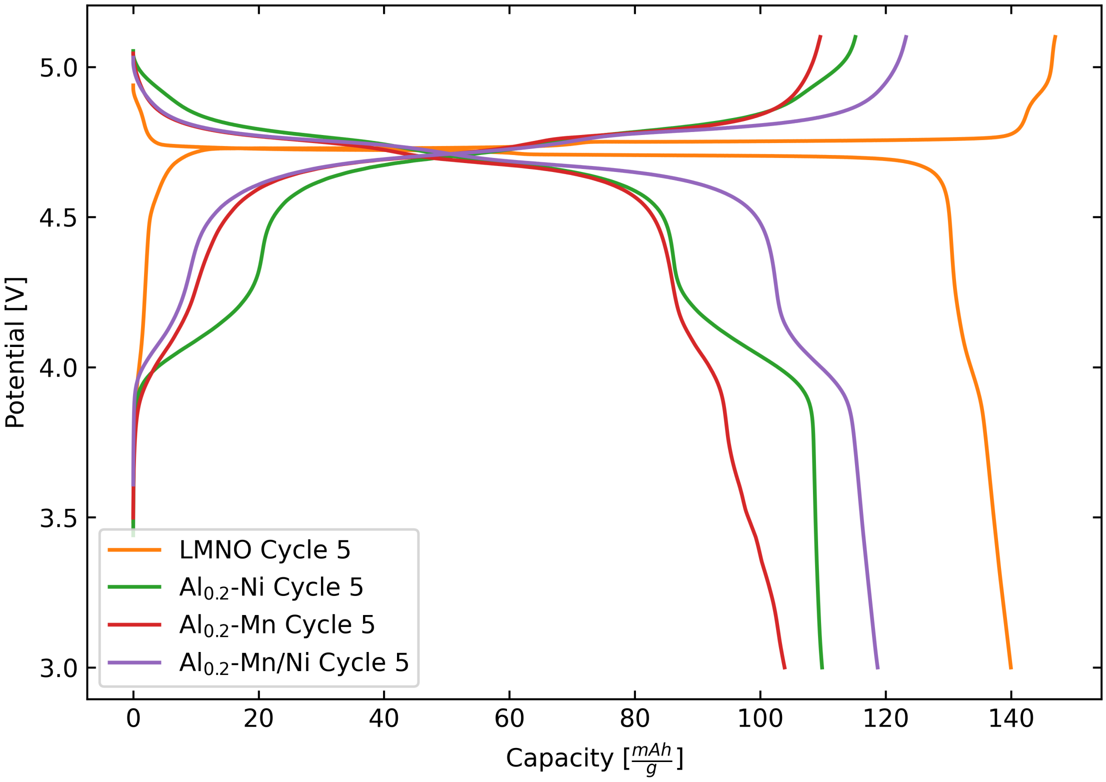

Figure 4.15: Galvanostatic cycling curves of the $5^{th}$ cycle of the pure LMNO (orange) and the substituted samples where 0.2 aluminum is on nickel site (green), manganese side (red), and 50/50 on both sites (purple). C-rate: C/10

The first feature to point out in the figure above is the change of capacity in the 4 V region attributed to the $Mn^{3+} \leftrightarrow Mn^{4+}$ redox reaction. This indicates which site the aluminum ended up on during the synthesis since the different placements of Al results in different charge compensation mechanisms as explained in section 3.7.1. For these cells and their twin, the experimental capacity can be found in table 4.5 below together with their theoretically calculated capacity (see experimental section 3.7.1).

Table 4.5: Experimental charge/discharge capacities of the potential regions 3.5—4.5V ($Mn^{3+} \leftrightarrow Mn^{4+}$) and 4.5—5.0V ($Ni^{2+} \leftrightarrow Ni^{4+}$) for the highest substituted samples. All units are specific capacity in the form of $\frac{mAh}{g}$

| **Cell name** | **Charge** $3.5 - 4.5\mathbf{V}$ | **Discharge** $3.5 - 4.5\mathbf{V}$ | **Charge** $4.5 - 5.0\mathbf{V}$ | **Disharge** $4.5 - 5.0\mathbf{V}$ |
|---|---|---|---|---|
| LMNO calc | 0.0 | 0.0 | 146.9 | 146.9 |
| LMNO | 2.6 | 7.1 | 146.1 | 132.0 |
| LMNO twin | 2.7 | 7.1 | 143.7 | 130.2 |
| $Al_{0.2}$-Mn calc | 0.9 | 0.9 | 117.7 | 117.7 |
| $Al_{0.2}$-Mn | 15.0 | 15.2 | 93.1 | 82.6 |
| $Al_{0.2}$-Mn twin | 14.5 | 14.5 | 94.3 | 84.1 |
| $Al_{0.2}$-Ni calc | 31.2 | 31.2 | 87.9 | 87.9 |
| $Al_{0.2}$-Ni | 21.7 | 25.1 | 89.7 | 84.5 |
| $Al_{0.2}$-Ni twin | 22.4 | 24.3 | 90.1 | 83.9 |
| $Al_{0.2}$-Mn/Ni calc | 16.0 | 16.0 | 102.9 | 102.9 |
| $Al_{0.2}$-Mn/Ni | 8.2 | 17.3 | 108.5 | 95.6 |
| $Al_{0.2}$-Mn/Ni twin | 12.5 | 16.8 | 109.0 | 99.2 |

From table 4.5 above, a couple of assessments can be made. Firstly, it is clear that the pure LMNO has very little manganese redox activity, although there is some. This might come from oxygen vacancies leaving some $Mn^{3+}$ as charge compensation during synthesis.

For the $Al_{0.2}$-Mn sample, a significant and unexpected capacity increase from the manganese reaction can be found, indicating that some of the aluminum might have replaced nickel instead of the attempted manganese.

Moving on to sample $Al_{0.2}$-Ni, there is a significant capacity from the manganese reaction, although it is only 60% of the estimated value. This could be because some Al might have replaced manganese instead of nickel, removing some of the manganese capacity. In addition, the overall capacity of this cell is higher than what was expected, which can be explained by the cathode weighing error discussed in 4.6.1.

For $Al_{0.2}$-Mn/Ni approximately the anticipated capacity is measured from both the redox reactions.

It is also interesting to see the trend of increasing manganese redox activity with an increasing amount of substitution. Unfortunately, data for the medium substituted (0.1) aluminum on nickel site sample ($Al_{0.1}$-Ni) is missing, however, the trend is demonstrated by showing the sample with the least amount of substitution in figure 4.16 below. The fifth cycle of each cell was chosen for visualization as first cycle effects are not in focus.

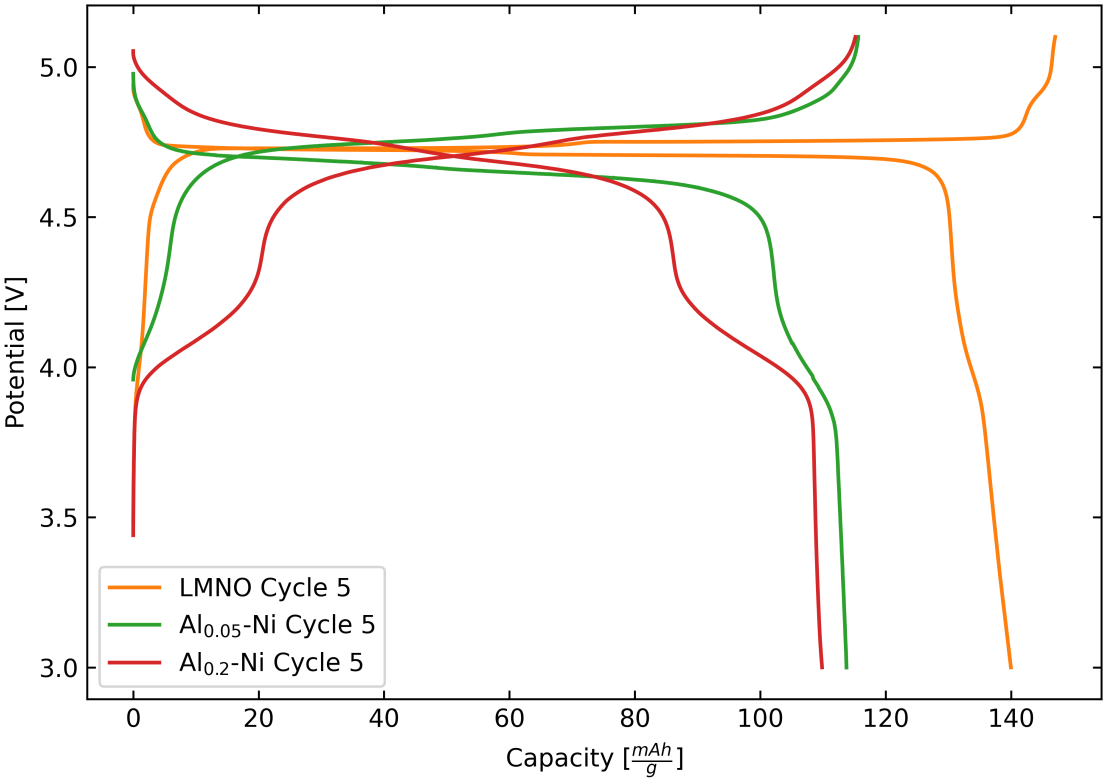

Figure 4.16: Galvanostatic cycling curves of the 5<sup>th</sup> cycle of the pure LMNO (orange) and the nickel-substituted samples with 0.05Al (green) and 0.2Al (red). C-rate: C/10

### 4.6.3 Degradation of cells during cycling and the resulting potential curves

Continuing with the analysis of the cycling curves, it seems like pure LMNO has a more significant change than the $Al_{0.2}$-Ni sample over its cycle life. The significant change consists of three features. Firstly, the capacity degrades faster for LMNO than that of the $Al_{0.2}$-Ni sample. Secondly, the end of the discharge and charge plateaus curves seem to smooth out, meaning that when aged, the lithiation or delitiation is not as abruptly ending as when new. Thirdly, the overpotential increases more rapidly for the pure LMNO, yielding less energy efficiency when aged. The cycling curves over 533 cycles for these materials are shown in figure 4.17 below with twin cells in fig B.11. These cells were cycled using the same rate capability degradation program as explained in the experimental section 3.7.2.

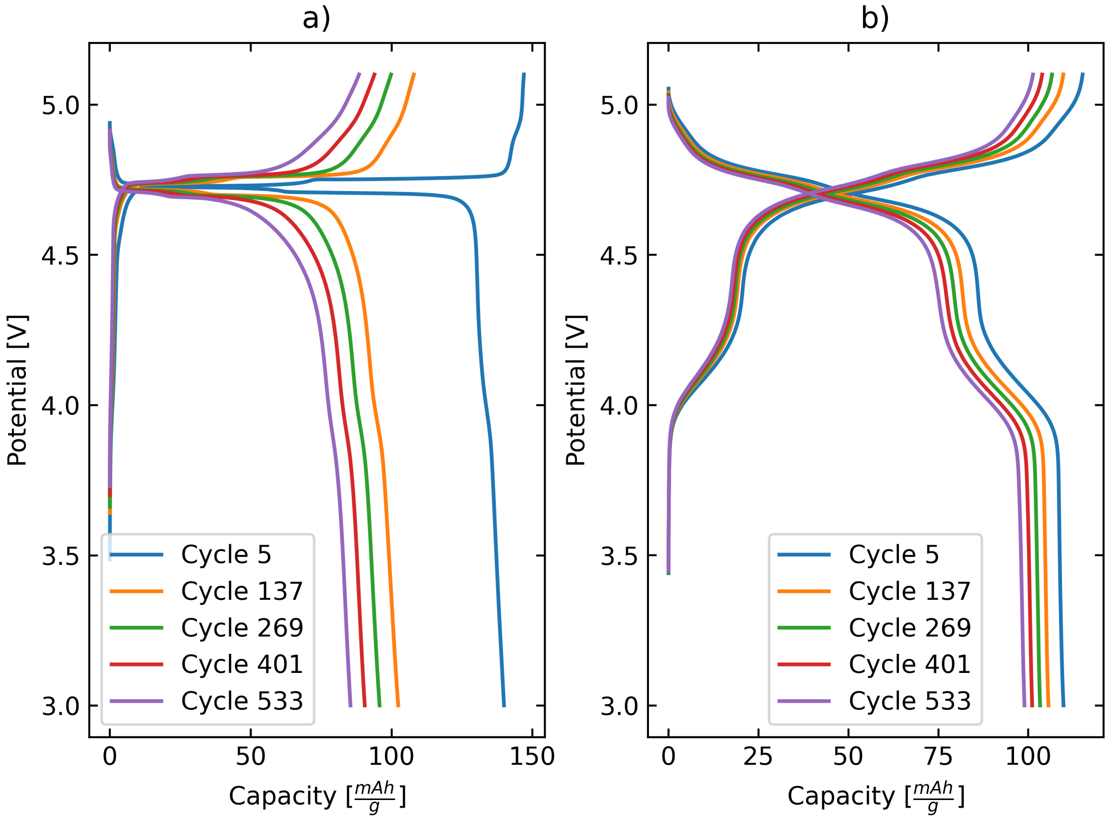

Figure 4.17: Galvanostatic cycling curves during degradation for a) LMNO and b) $Al_{0.2}$-Ni. C-rate: C/10.

The cause for capacity loss is always due to the loss of electrochemically active material, which happens faster for LMNO than $Al_{0.2}$-Ni in these experiments. The smoothing of the end of the charge and discharge plateaus means that at the end of lithiation and delithiation, the electrochemical potential of the reaction changes. This could happen if the surface of an ordered LMNO particle gradually becomes disordered, and the effect of solid solution comes into play (supported by Aktekin et al. [120]). The overpotential change in the plateaus of the LMNO can most probably be attributed to the formation of a thicker SEI layer which induces a higher charge transfer resistance on the surface of the active material particles.

### 4.6.4 Galvanostatic cycling curves at different C-rates

By cycling cells at different C-rates, the C-rate dependence of the redox reactions can be assessed. This is shown for pure LNMO and $Al_{0.2}$-Ni in figure 4.18 below (twin cell data in fig B.12). These cycles are the fifth cycle of their respective C-rate in the rate capability experiment.

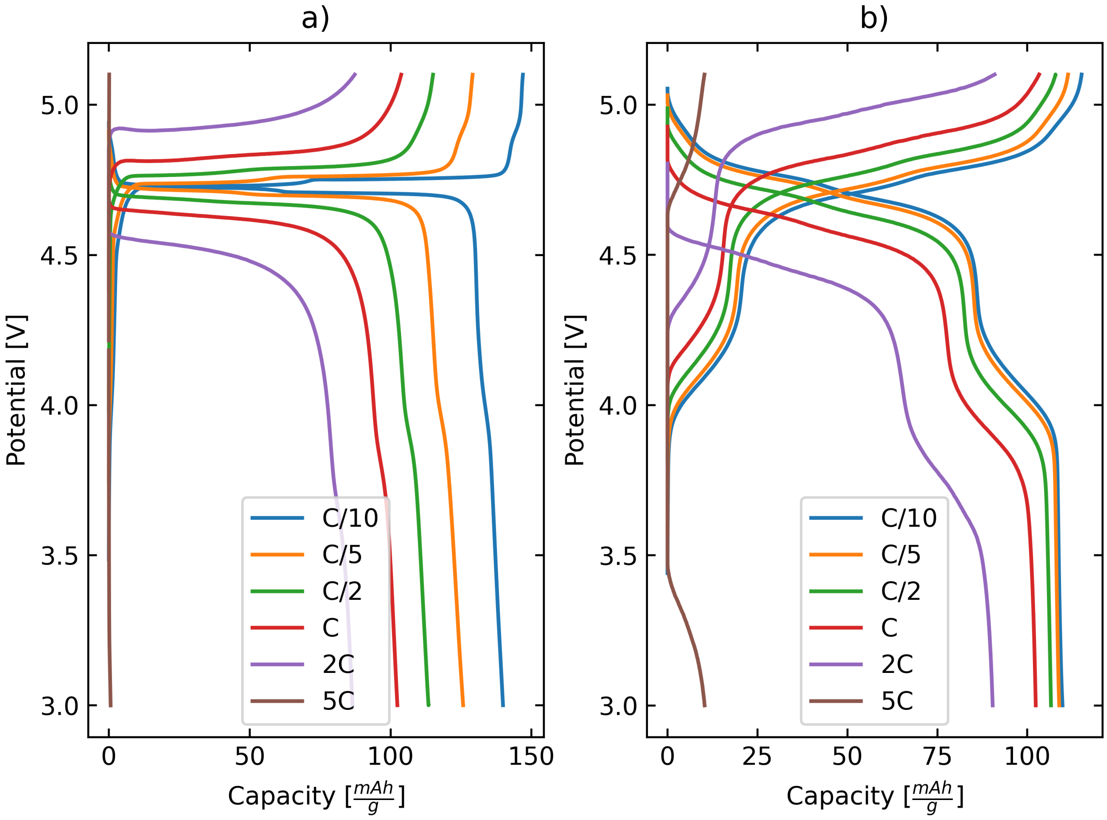

Figure 4.18: Galvanostatic cycling curves at different C-rates for a) LMNO and b) $Al_{0.2}$-Ni.

As can be seen for both samples in figure 4.18 above, the capacity decreases with an increasing C-rate. For the C-rates of 1 and below, this is probably because of the lithium concentration gradient towards the surface of the particle. When the surface has zero concentration of lithium, the cell potential quickly shoots to 5.1 V, and the charge ends, still with some lithium in the structure. This remaining lithium is then a result of steep concentration gradients, which by Fick's law (eq 2.4) is related to the diffusion coefficient of the sample. This means that the capacity loss with increased C-rate indicates the diffusion coefficient, which can be interpreted to be higher for the aluminum substituted sample from the figure above.

However, above 1C the capacity plateau of the $Ni^{2+} \leftrightarrow Ni^{4+}$ redox reaction starts to go outside of the potential range of the experiment, not only due to the lithium concentration gradient in the particle but also due to the other components of overpotential in the cell. This means that the reason for capacity loss at higher C-rates is probably not very crystal structure related, but has more to do with the charge transfer and electrolyte resistance which is affected by the morphology of the particles and the tortuosity of the electrodes and separator, or other mesoscale effects.

If we draw the conclusion that these two kinetic effects (active material lithium diffusion and other resistances) can be somewhat separated in these measurements, the result would be that the aluminum substituted sample has better ionic conductivity, but worse charge transfer kinetics. These effects are hard to quantify and are important to keep in mind in order to not make false crystal structure assessments based on high C-rate potential curves. For LIB chemistries with more sloping potential profiles like NMC[121], these two mechanisms mix more and result in a more gradual decline in capacity over C-rate than the exponential decline seen for all the LMNO samples.

### 4.6.5 Rate capability testing

Rate capability degradation testing as explained in experimental section 3.7 was conducted using BioLogic MPG2 instruments.

Figure 4.19 below shows two rounds of rate capability testing for the pure LMNO and $Al_{0.2}$-Ni. For pure LMNO, the initial capacity loss during the first 50 cycles is high, where it can be seen that regardless of the C-rate increase, the capacity decays. For the $Al_{0.2}$-Ni sample, however, the initial capacity loss is not nearly as bad.

In addition to the capacity decay, it can be seen that the initial capacity of $Al_{0.2}$-Ni (110 $\frac{mAh}{g}$) is 24% lower than that of the pure LMNO (145 $\frac{mAh}{g}$). This does correspond to the theoretically anticipated change described in section 3.7.1 which should be approximately 19% lower for the $Al_{0.2}$-Ni sample than the pure LMNO sample. It must be noted that the specific capacity is calculated by dividing the measured capacity by the mass of active material, which can be inaccurate due to the errors in weighing in of the cathode as mentioned in the reproducibility assessment in section 4.6.1.

Looking at the rate capability itself for this cell is extremely difficult as the reproducibility of the C-rates above 1C was low, and had a significant deviation between the two twin cells. This data can be found in Appendix B, figure B.14.

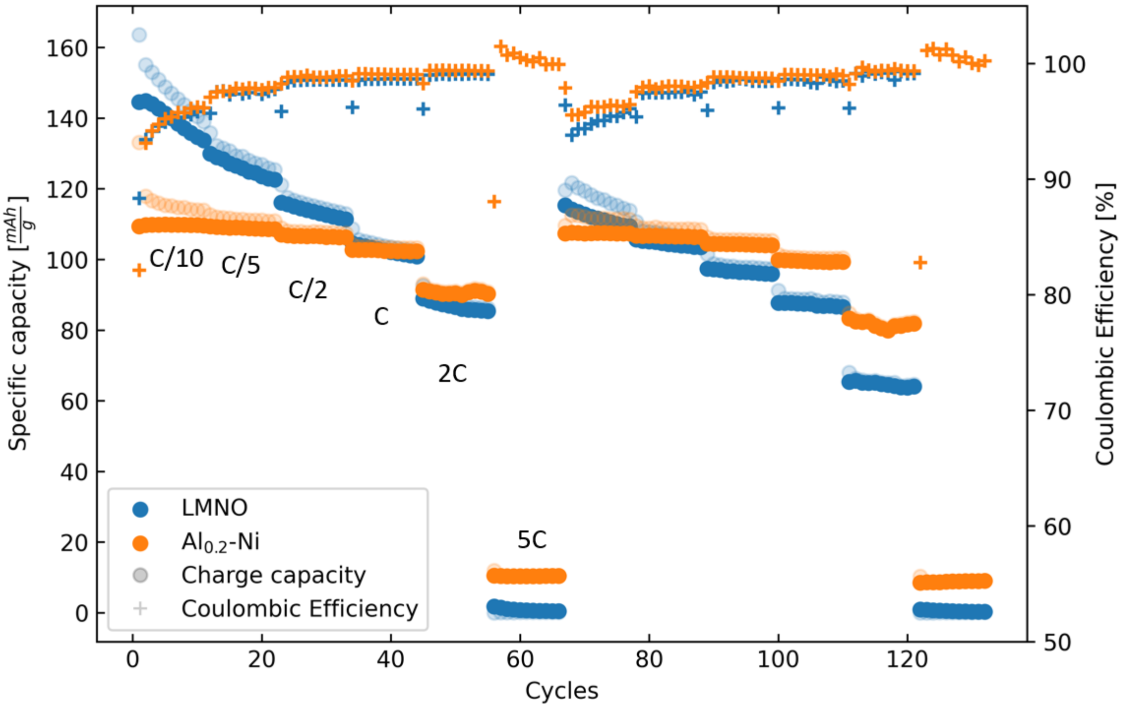

Figure 4.19: Rate capability for the nickel substituted sample compared with the pure LMNO. The lightly colored dots are charge capacities.

Another interesting effect visible in the figure above is the difference in capacity for the charge and discharge cycle, namely the coulombic efficiency (CE). In the first 20 cycles, the reason for higher charge capacity is electroactive irreversible reactions within the electrochemical cell, like the establishment of SEI layer on both the anode and cathode. However, while the low CE diminishes after the first 20 cycles, it reappears when the C-rate comes back to C/10 the second time. This can be due to the surface of the particle cracking when strain is introduced by a steep lithium concentration gradient [62]. These cracks expose fresh surface of the particles which then again will face the irreversible electroactive reactions of SEI formation, and thus the charge capacity is higher than the discharge capacity for a couple more cycles.

The samples where manganese was substituted for aluminum show the same trend. Here, data for three different substitutions are available, namely Al $\in \{0.05, 0.1, 0.2\}$. These samples show that when the amount of aluminum increases, the capacity decrease. This can be seen in figure 4.20 below with the twin cell dataset in Appendix B, fig B.15. It is also interesting that even with just 0.05 Al on the manganese sites, the capacity retention for the first 100 cycles is significantly improved, without the drastic capacity loss as seen for the 0.2 Al substitution in figure 4.20.

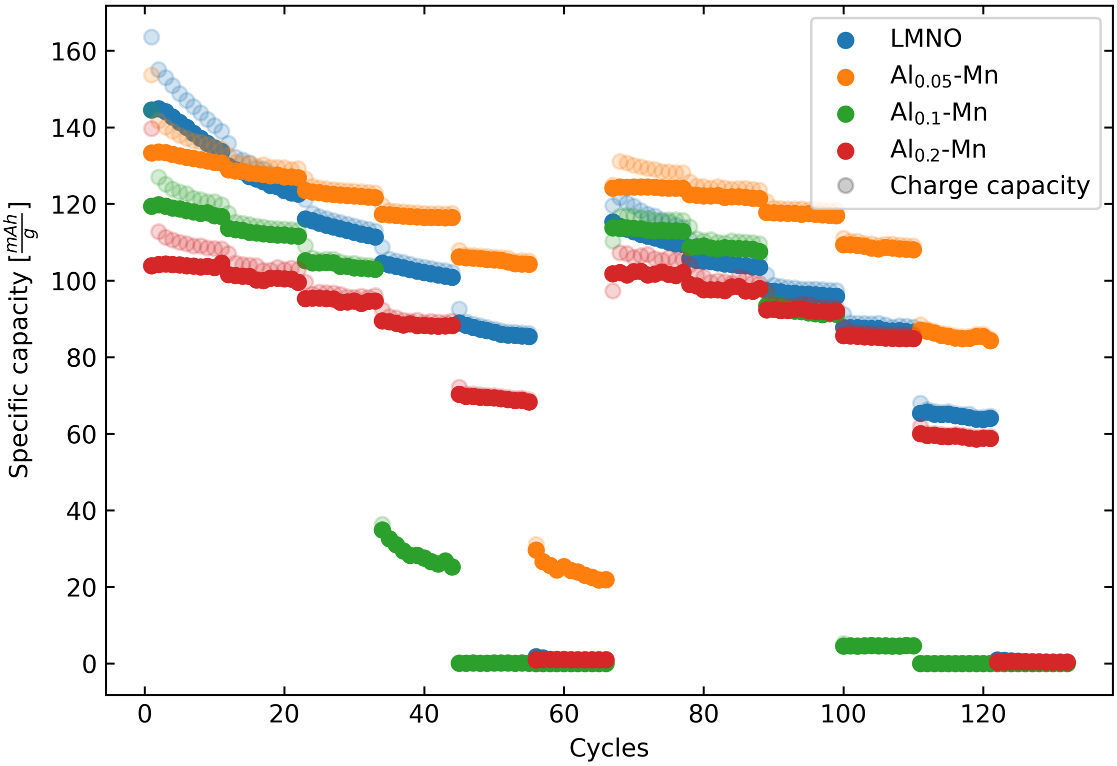

Figure 4.20: Rate capability for the manganese substituted sample compared with the pure LMNO. The lightly colored dots are charge capacities.

#### 4.6.5.1 Rate capability degradation for the nickel substituted sample

Figure 4.21 below shows how the rate capability degradation has evolved over the cycle life of 500 cycles for the pure LMNO, and the $Al_{0.2}$-Ni sample. A figure showing the twin cells is available in Appendix B, figure B.13. It is visible from the plotted data that initially, the capacity of LMNO is higher, however, it quickly degrades to be lower than that of $Al_{0.2}$-Ni, at least for the low C-rate steps (C/10, C/5, C/2, and C). The crossing where the capacity of $Al_{0.2}$-Ni becomes higher than that of the pure LMNO happens after only 130 cycles with this cycling program. When looking at the high C-rate cycles, conclusions are hard to make due to the large variations between cells. However, it does seem that the rate capability degrades similarly for both materials.

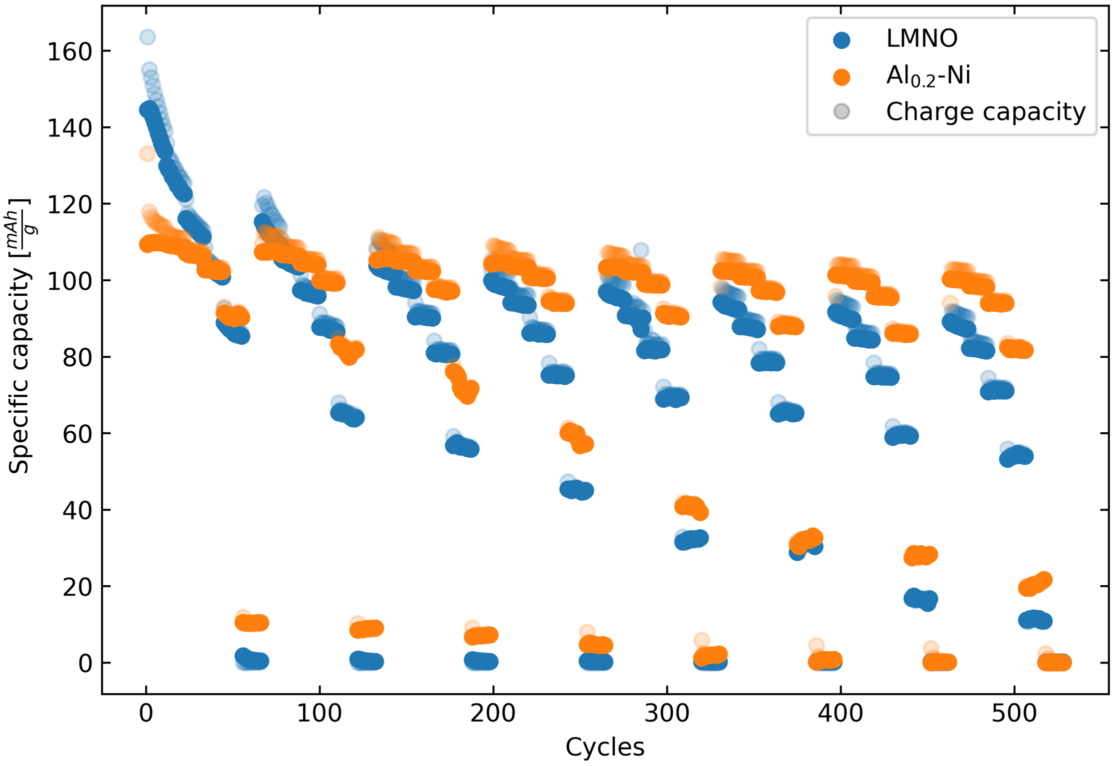

Figure 4.21: Rate capability degradation for the nickel substituted sample compared with the pure LMNO. The steps show 11 cycles at different C-rates where they cycle through C/10, C/5, C/2, C, 2C and 5C eight times.

### 4.6.6 Accelerated degradation

Accelerated degradation were done by cycling between 3.5-5.0V at 1C at 45°C using LP40 as explained in experimental section 3.6.1.1, 3.6.4 and 3.7.3. With this data, it is possible to see how capacity retention changes with substitution amount through the samples pure LMNO, $Al_{0.1}$-Ni and $Al_{0.2}$-Ni. The cell capacity versus cycle life has been plotted in figure 4.22 below and shows that while the initial capacity decreases with increased Al substitution, the lifetime increases.

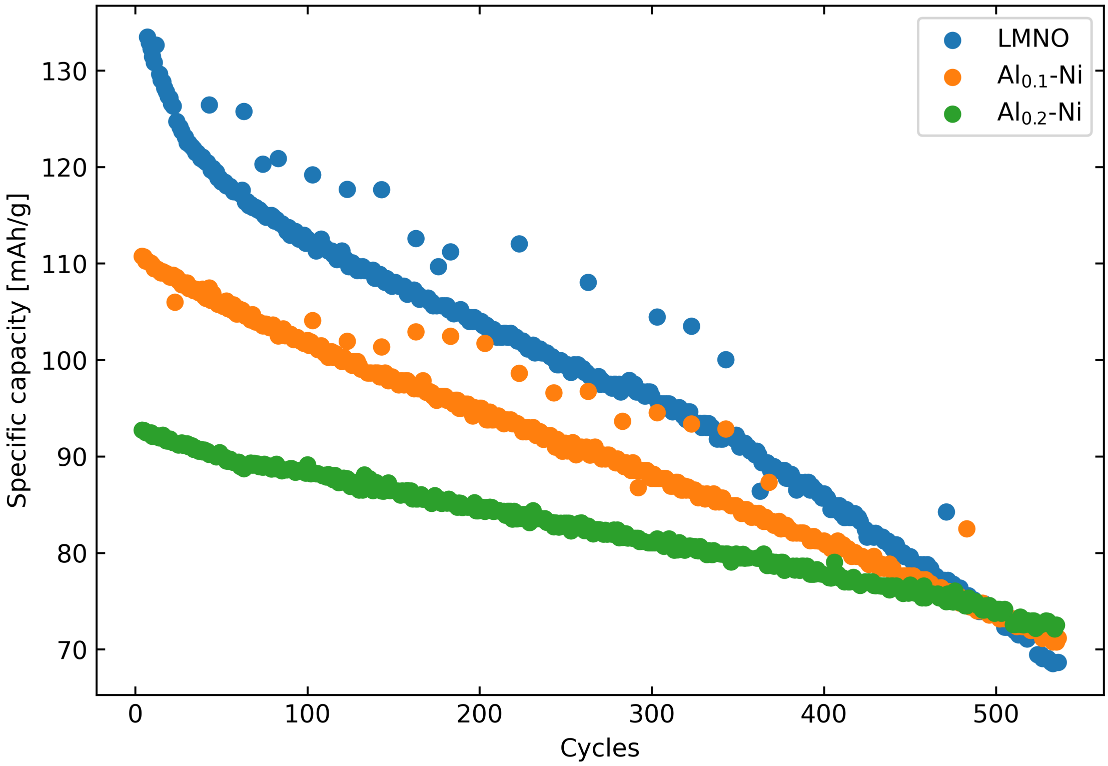

Figure 4.22: Accelerated degradation capacity over cycles for pure LMNO, $Al_{0.1}$-Ni and $Al_{0.2}$-Ni. 3.5-5V, 1C, 45°C in LP40

### 4.6.7 Assessments regarding degradation

Assessing the degradation mechanism differences between the samples is hard, although the literature has deemed manganese dissolution to be one of the most important mechanisms for the loss of active material. In addition, some papers find that trivalent substituents migrate towards the surface of the particles [52], [53], and if that also holds true for aluminum doping, it might form a protective boundary that blocks the dissolution pathways of the $Mn^{2+}$ cation and thus prolongs the lifetime.

Another degradation mechanism hypothesis depends on the suggested lithiation mechanisms being true. If this is the case, then it could make sense that manganese disproportionation (explained in theory section 2.2.6) was more likely to happen at the domain boundary for the three-phase mechanism of ordered LMNO, while for the solid solubility of $Al_{0.2}$-Ni, the gradual lithiation leads to much less stress on the crystal lattice. The literature shows that in LMNO, the strain increases significantly with delithiation [62], exacerbating the strain gradient in an eventual domain boundary.

The proposed particle lithiation mechanisms and probable strain profile have been sketched in figure 4.23 below.

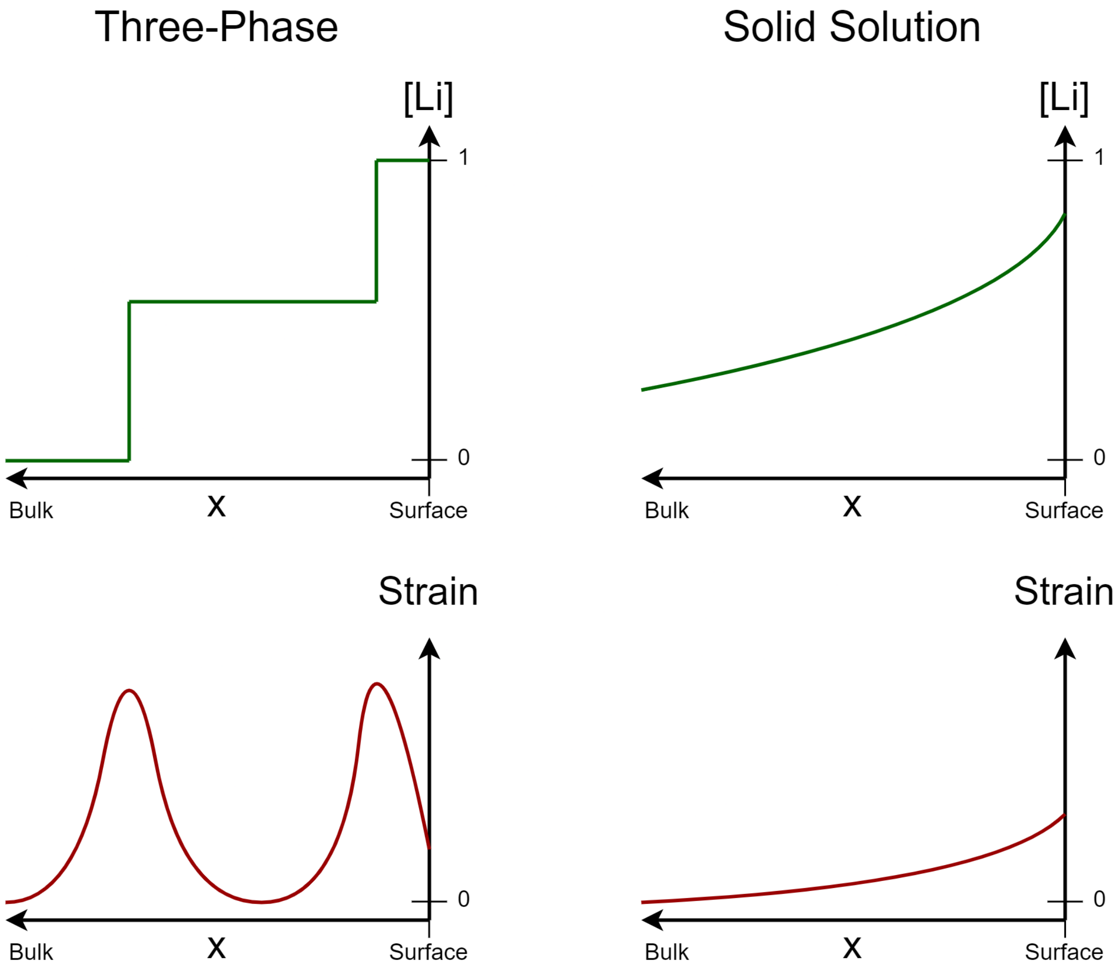

Figure 4.23: Simplistic schematic of suggested lithiation mechanisms (top) and consequent crystal strain (bottom) for the three-phase reaction (left) and solid solution (right). All plots have crystal depth on the x-axis with the surface of the crystallite on the right side and bulk on the left side.

A degradation mechanism that is probably common for the two samples is at the microscale. Expanding and contracting particles induce strain on the electrode network of conductive additive, binder, and active material, and thus might lose entire particles during aging.

### 4.6.8 Coin cell compatibility experiments

The compatibility experiments were conducted with cycling voltammetry as explained in experimental section 3.7.4 and prepared as described in section 3.6.3. This was done to investigate the compatibility of coin cell parts at high potentials (up to 5.1 V).

For the cells with normal LP30 electrolyte, the voltammograms can be seen in figure 4.24 below. There it can be seen in a) that the SS304 cell material has some irreversible reactions with the electrolyte at 4 V (peak ii). For the coin cell of SS316 (fig b)), there is just a small signature from the same potential. For the Al-claded cell, some reactions are happening already at 3.3 V (peak i), which were outside of the scanned potential region on the second cycle. This means that the irreversibility of these reactions can not be guaranteed.

A signature seen in all of these experiments is the small capacity right before the $Al_{0.05}$-Mn capacity at 4.7 V (peak iii) which is believed to be due to the WhatMan glass fiber separator having some irreversible reactions at this potential. The y-axis in the cyclic voltammograms in figure 4.24 has not been converted to active-material specific current for better comparison of the effect of non-active-material related effects.

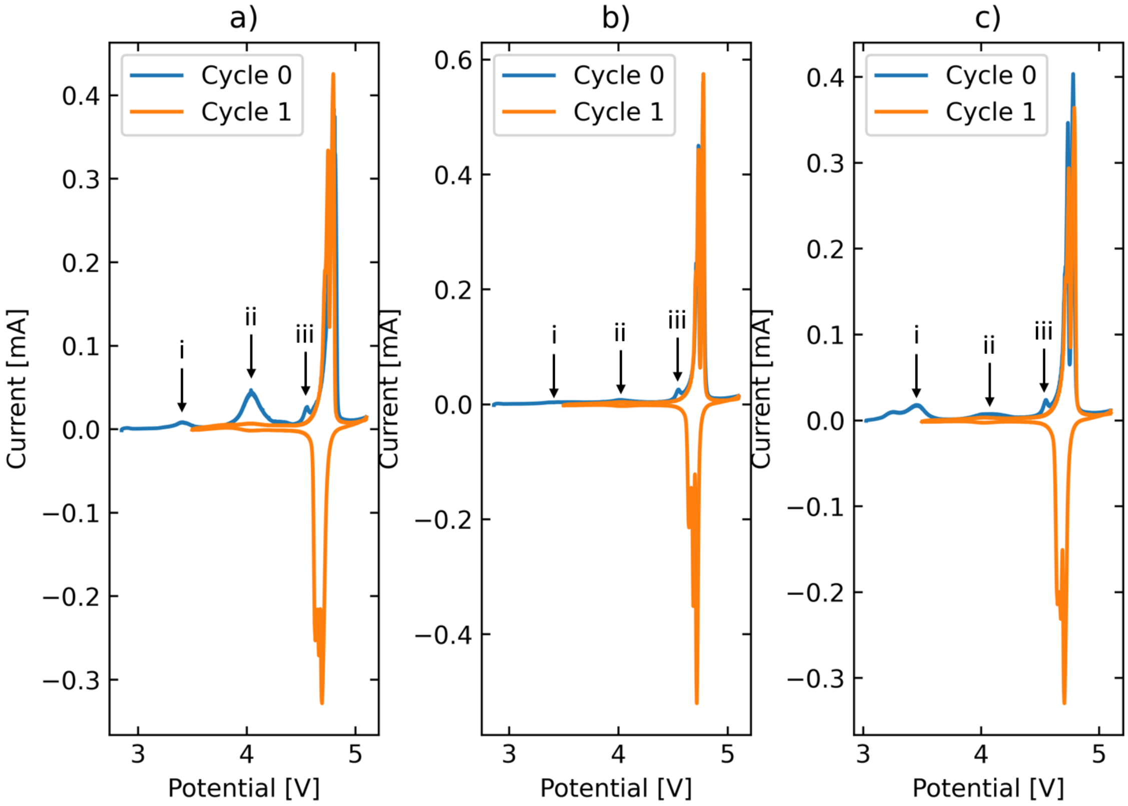

Figure 4.24: Cyclic voltammograms of cathode side cell casing materials a) SS304, b) SS316 and c) Al-Clad, with LP30 electrolyte and LMNO versus $Li/Li^{+}$. 3.5 - 5.1 V, 0.01 mV/s

For the experiment conducted with Ionic Liquid where high voltage compatibility was tested, it is evident that no matter which coin cell parts were used, some part of the cell is not stable above 5.1 V (peak iv). This can be seen in figure 4.25 below. Note that the small currents around 4 V and the spikes above 6.5V are data measurement outliers from electrostatic noise. Determining which parts are unstable requires a systematic study where all parts of the cell are replaced one by one and measured. This includes the caps, plastic gasket, spring, spacer, separator, electrolyte, binder, conductive additive, and current collectors. The main difference between the measurements is the capacity at 6.2V (peak v) which is much higher for the Al-claded cells, indicating that there is some reaction with aluminum at this potential. Although as mentioned, a systematic study is required before making assumptions. For all three experiments, the small peak (peak ii) right before the LMNO capacity (iii) is also visible, strengthening the point made above about this being an effect of the separator.

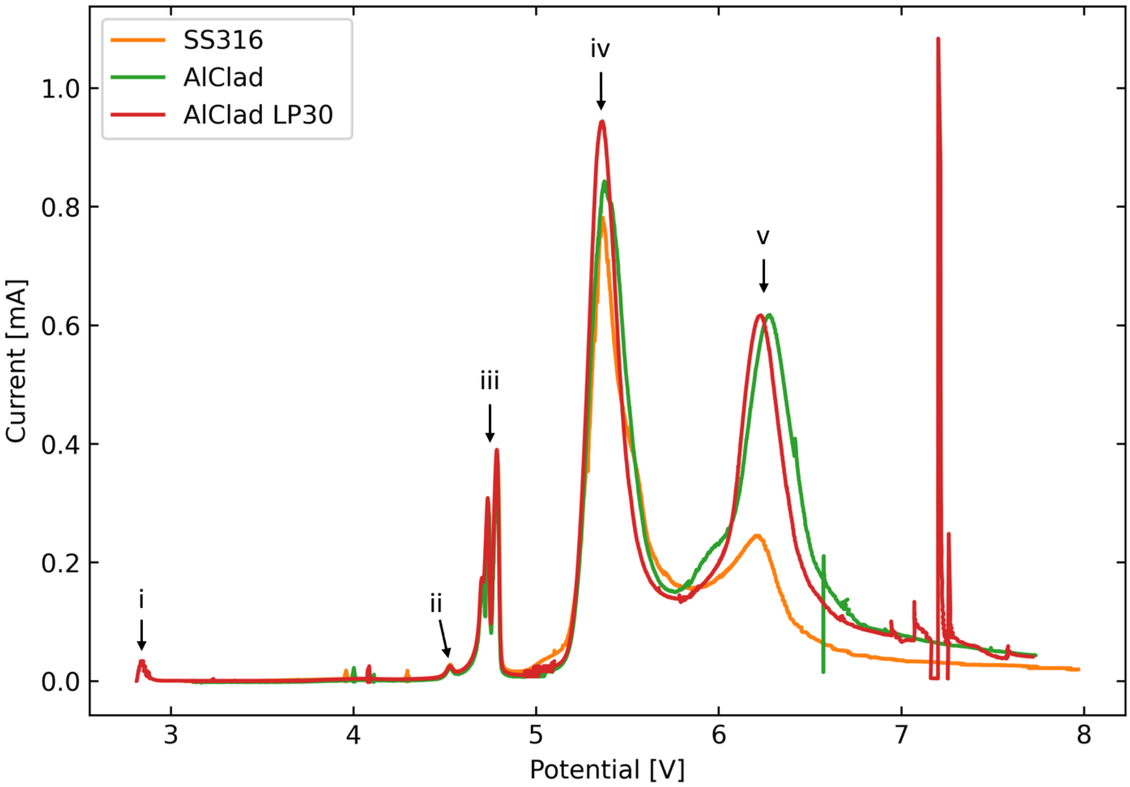

Figure 4.25: Cyclic voltammograms of different cathode side cell materials in Ionic Liquid (1.2M LiTFSI in Pyr1333a). 2.8-8 V, 0.01 mV/s

### 4.6.9 Low potential reactions of LMNO

Low potential cycling was done galvanostatically for pure LMNO and $Al_{0.05}$-Mn/Ni to see if low potential stability can be improved by slight substitution.

Figure 4.26 shows 1-5 V galvanostatic cycling starting with a charge, while figure 4.27 shows the same but starting with a discharge. The capacity plateau at 3 V is believed to be lithium intercalation on the vacant octahedral sites and the capacity below 2 V which seems less reversible can be the formation of a $Li_2Mn_{1.5}Ni_{0.5}O_4$ compound as described in section 2.2.5.

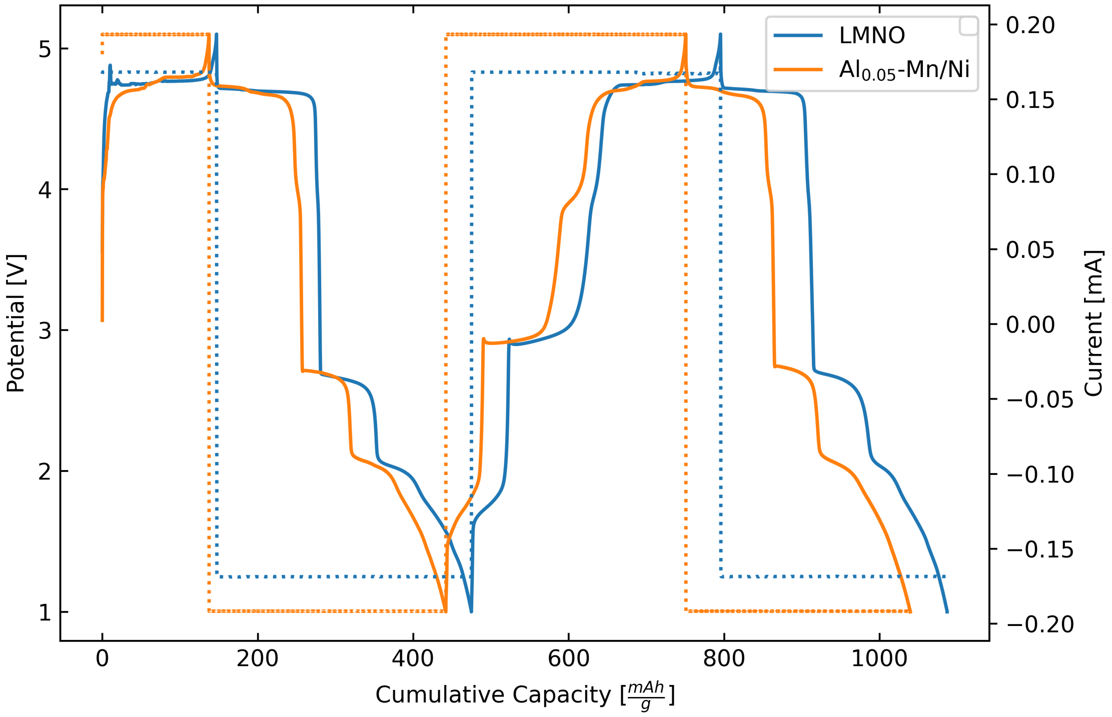

Figure 4.26: Galvanostatic cycling curves of pure LMNO and $Al_{0.05}$-Mn/Ni starting with a charge. C-rate: C/5.

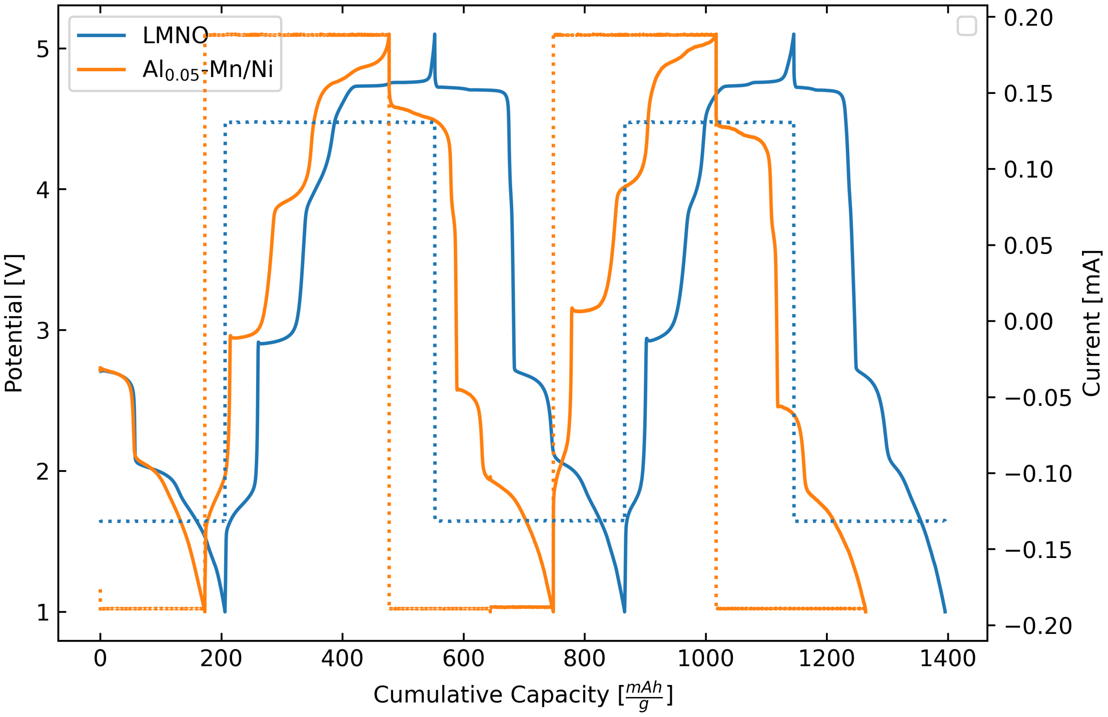

Figure 4.27: Galvanostatic cycling curves of pure LMNO and $Al_{0.05}$-Mn/Ni starting with a discharge. C-rate: C/5.

It is worth noting by comparing fig. 4.26 and 4.27 that LMNO behaves relatively equal whether starting with a charge or a discharge. However, the $Al_{0.05}$-Mn/Ni sample has a steeper potential plateau at 4.9 V with more overpotentials after starting with a discharge. This indicates that something is different with the Al substituted sample. While this is an interesting effect in itself, effort in investigating this has not been spent.

For the degradation within this potential window, the cycling data is shown in figure 4.28 below. The LMNO sample only had 7 cycles due to an instrument error. The main finding from this experiment is that slightly aluminum substituted LMNO does not have an improved cycle life below 3 V.

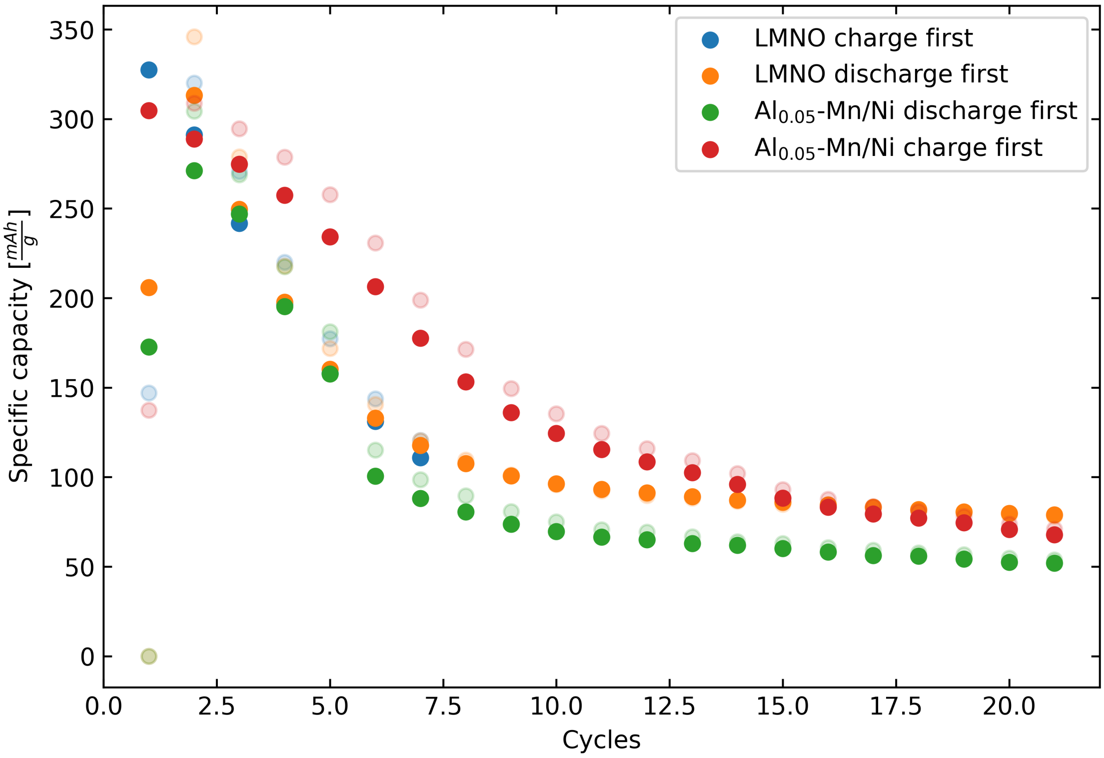

Figure 4.28: Capacity degradation plot of 1-5 V cycled LMNO and $Al_{0.05}$-Mn/Ni with a C-rate of C/5. The lightly colored dots are charge capacities.

## 4.7 Large scale delithiation and full cells

Large scale cells (0.6g black mass) were needed to delithiate enough material for use with Accelerating Rate (ARC) experiments. The development started with bulk charging of material in the form of pressed pellets and thick freestanding electrodes, however, it was found that contact and diffusion issues were too high. What ended up being the best solution was slightly thicker regular electrodes in a pouch cell. When using pouch cells, it was considered unsafe to use a metallic lithium anode, and thus also full cells (active material cathode and anode without lithium metal) were investigated. The following subsections (section 4.7.1 to 4.7.4) present the results of this endeavor.

Because delithiation of the materials for ARC experiments was the goal, the process of arriving there was done in an expedited fashion. This means that in many places, twin experiments for result verification were omitted.

### 4.7.1 Bulk charging

Charging of larger amounts of material in one cell was tested with various methods with the cells shown in sections 3.6.6 and 3.6.7. None of them were found sufficient for use with ARC as the potential change during galvanostatic cycling was not as expected. Some methods were even found to not work at all, as the potential never rose above 4 V. These are listed below.

1. Pouring mixed active material and 20% CSP straight into the Swagelok cell showed very unstable potential when applying current, it might have been caused by CSP floating around the separator, making it internally electrically conductive.
2. 80% LMNO, 10% CSP, and 10% PTFE dry pressed to pellet had better stability on voltage, however on applying current, the voltage never rose above 3 V. PXRD showed a completely uncharged material.
3. 42.5% LMNO, 42.5% CSP, and 15% PTFE dry pressed to pellet showed even better electrochemical stability, but did not make it over 4 V before connectivity issues appeared.

The way which was found to yield the best results was 0.65 g LMNO, 0.2 g CSP, and 0.15 g PTFE mortared together before adding 0.9 mL NMP. After mortaring that in as well, it was possible to form a putty that could be applied by hand onto an aluminum current collector. By stamping out a pellet with a hollow stamping tool, and drying it, the cathode of the cell was ready. Zip-lock bags was found to be a surface sufficiently slippery to handle the putty while working on it. However, this method also showed unstable potential and connection issues where not all the LMNO was delithiated, meaning it was not sufficient for the ARC tests.

### 4.7.2 Graphite cells

Since bulk charging with pellets or free-standing electrodes as described in the section above was unsuccessful, graphite anodes were developed for use in full cells. These fuel cells would then be upscaled to a pouch cell, where a metallic lithium anode could not be used due to safety.

Graphite cells worked best with the Na-CMC + $H_2O$ technique (93:1:6 graphite:CSP:CMC). The PVDF + NMP technique (8:1:1 graphite:CSP:PVDF) did not have a good reversible capacity as can be seen in figure 4.29 below. Thus, the electrode with Na-CMC was used for all large graphite electrodes which were used in pouch cells.

The reason for the PVDF electrode's bad performance is unknown, although it may be attributed to the intercalation of lithium in the CSP (the conductive additive) which increases its size. This could lead to the destruction of the percolating network and thus capacity loss. The same CSP as used in this thesis (TIMCAL Carbon Super P) was used in a study of SEI growth by Attia et al [122] which showed that CSP has up to 200 $\frac{mAh}{g}$ of capacity between 0.01 and 1.2 V. Their data also shows a higher capacity plateau at approximately 0.9 V with a capacity of 200 $\frac{mAh}{g}$ which is probably the same capacity seen at the very start of the first discharge for these samples as well. This indicates that it is the high amount of CSP that was the breaking factor for the PVdF + NMP electrode, and not PVdF itself.

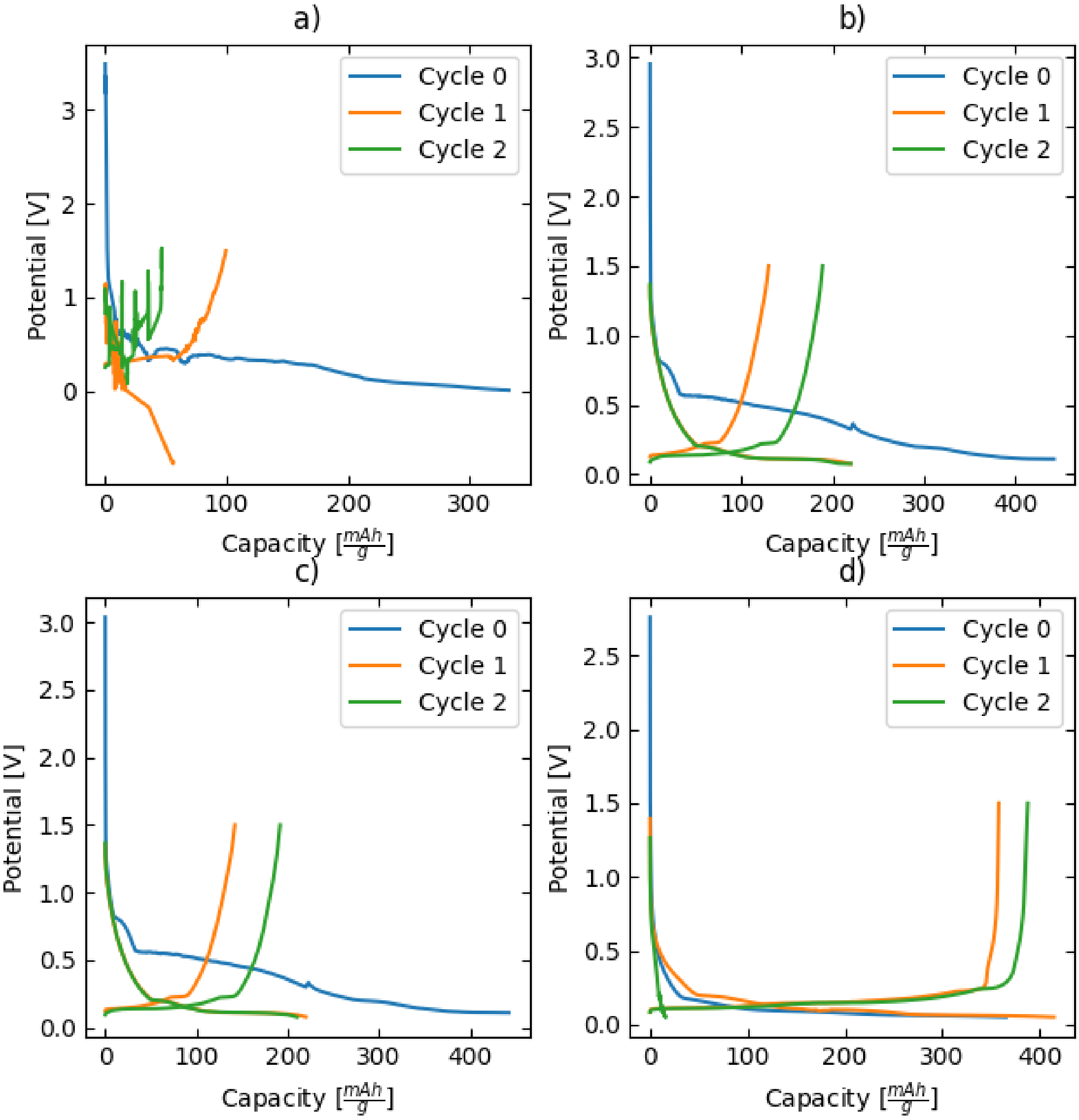

Figure 4.29: First 3 cycles of 8:1:1 graphite:CSP:PVDF (figure a, b and c) and 93:1:6 graphite:CSP:CMC (figure d) electrode composition. 1.5-0.05 V vs Li/Li$^+$, C-rate: C/10

### 4.7.3 Full cells

After the graphite electrodes were ready for use, full coin cells were assembled using the separately tested graphite anodes and LMNO cathodes.

Full cells in the form of coin cells were first tested out with a WhatMan glass fiber separator and regular LP30. In addition, two cells with different types of CellGard separators (2400 and 2021) were tested with LP40. The data for this is shown in figure 4.30 below. Since the first cycle coulombic efficiency for the WhatMan separator was the highest of the three it was decided to use this for the pouch cells as well.

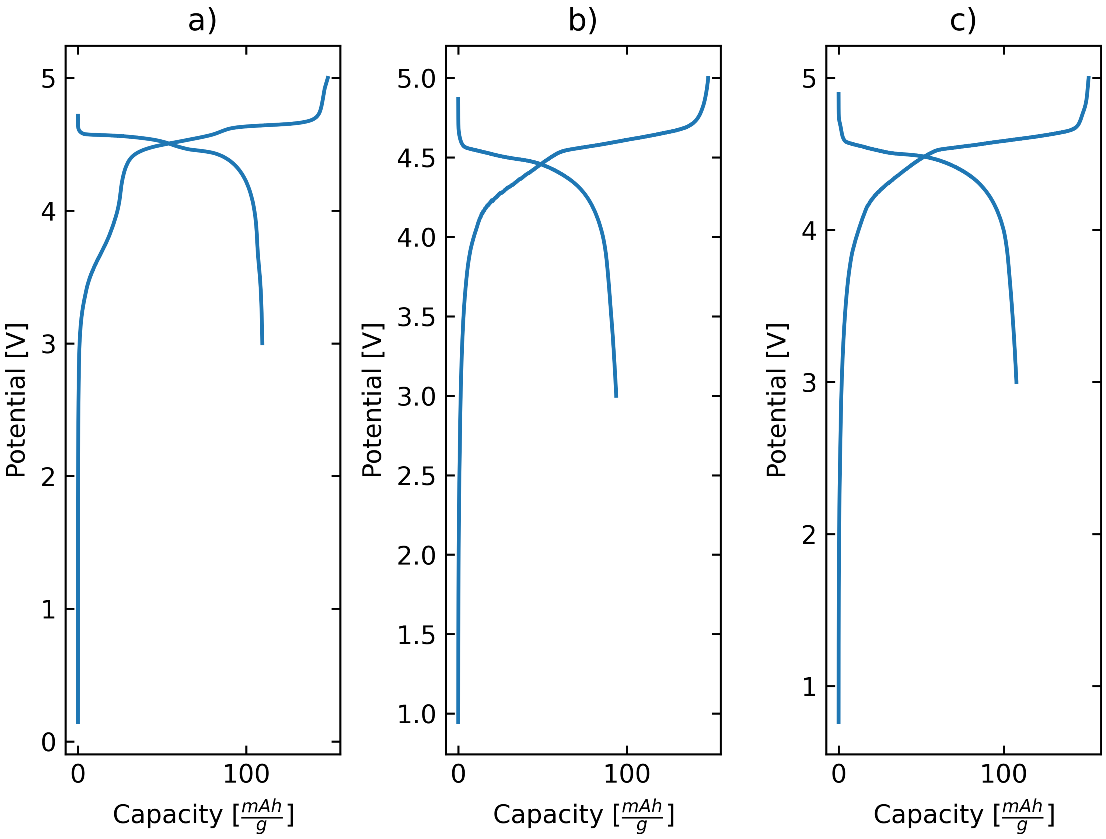

Figure 4.30: First cycle of different separators and electrolyte in full coin cells with Graphite anode and LMNO cathode. a) Whatman separator with LP30, b) CellGard2400 separator with LP40, d) CellGard2021 separator with LP40. 3-5.1 V, C-rate: C/10.

### 4.7.4 Pouch cells

With both electrodes ready, and a sufficient separator and electrolyte were found through testing of full coin cells, the pouch cell development started.

The electrodes were tuned so that the area-specific capacity of the graphite anodes was approximately twice that of the LMNO cathode. However, since the area changed somewhat between the electrodes, the area-specific capacity ratio varied between 1.5 and 2.5. In one of the tests, the anode had changed color to red/yellow after being lithiated and taken apart, which is the color of lithiated graphite. This was an effect of the anode area specific capacity to cathode area specific capacity ratio being very low (1.5), however for all tests used in the ARC measurements, this ratio was increased to approximately 2.3.

Figure 4.31 below shows the color of fully lithiated graphite in the middle, and the regular unlithiated gray color around. This figure also illustrates how the smaller cathode was placed within the edges of the larger anode to eliminate the chance of alignment error. The main results during the development of pouch cells are listed below:

1. For a food vacuum packer, a thin aluminum foil in the coffee bag laminate is crucial. A thick aluminum foil has higher heat transport and makes the plastic hard to fuse.
2. Around the electrode tabs coming out of the pouch, an additional thermoplastic sealant is necessary. Actual LIB pouch cell thermoplastic has too high of a melting point for use with regular food vacuum sealers. Parafilm works as a replacement, although the seal is not as strong.
3. A chamber-style vacuum sealer is beneficial as it can properly remove much more of the gas from the pouch cell. A vacuum sealer where there is only suction on the side will often not remove all the gas, and also suck out the electrolyte.

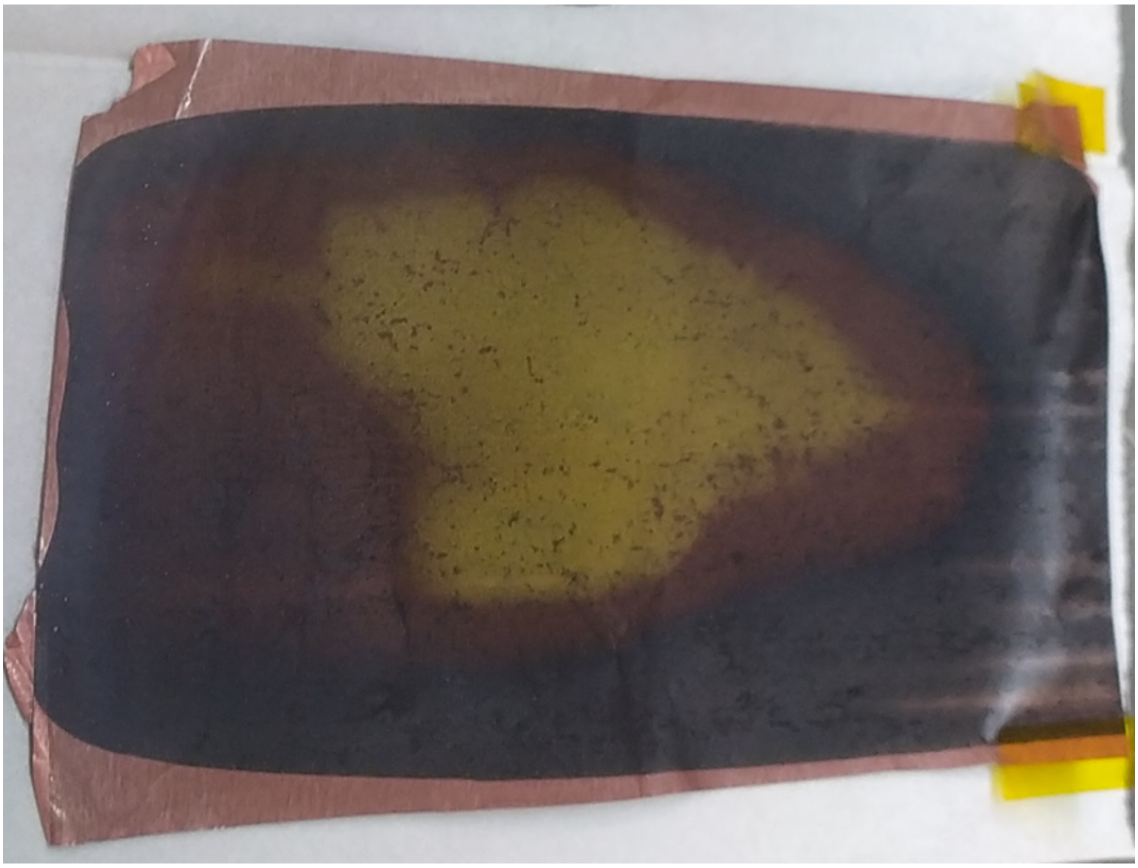

Figure 4.31: A lithiated graphite (yellow) anode after post-mortem of a pouch cell with an LMNO cathode charged to 5.1 V.

The electrochemistry of the pouch cells where the cathode material was used for ARC experiments is shown in figure 4.32 below.

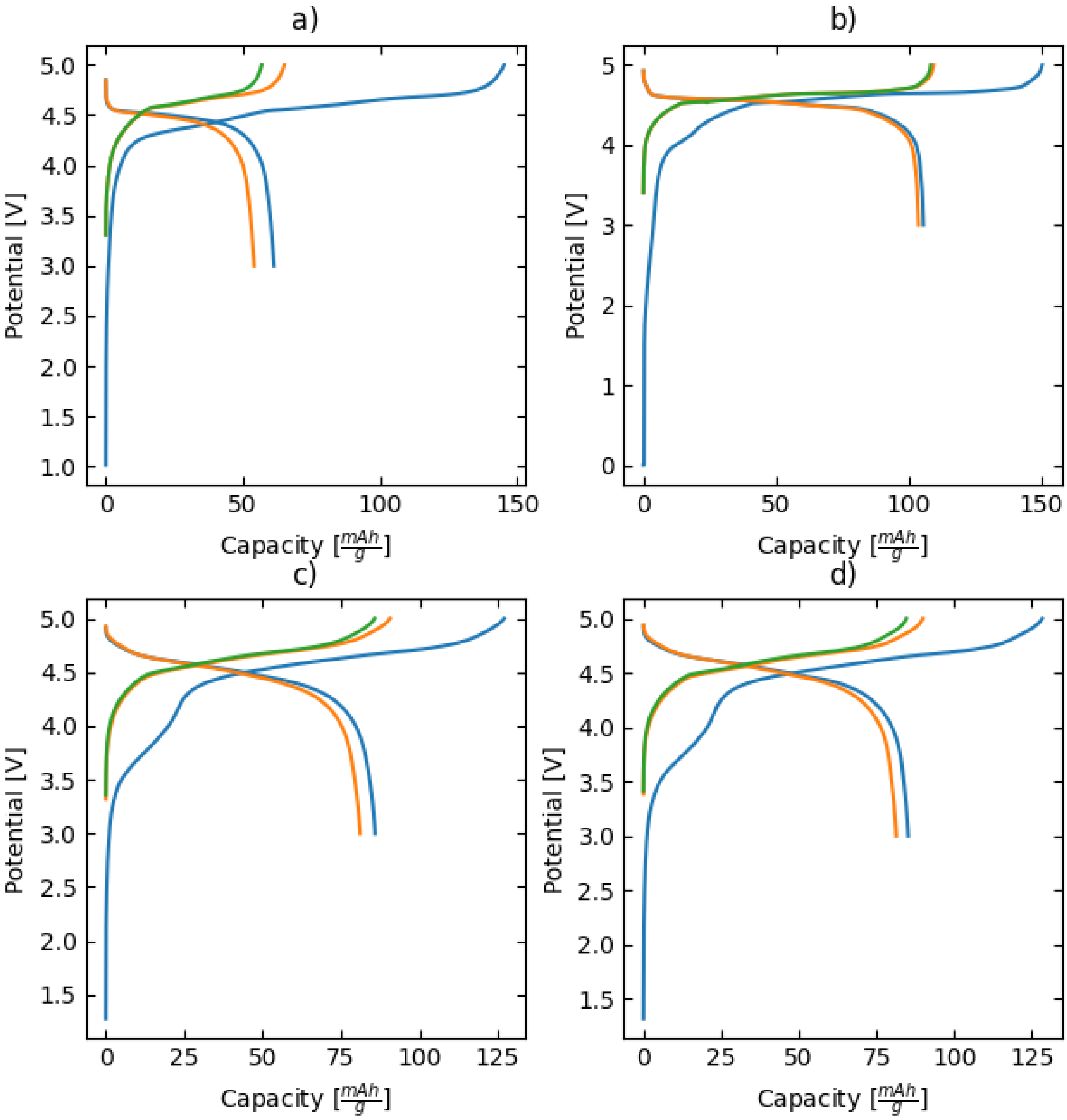

Figure 4.32: Full electrochemistry data for the pouch cells used to delithiate material for the ARC experiments. Three cycles with C-rate C/10 in the potential window 3-5.1 V. a) is for pure LMNO, b) LMNO twin, c) $Al_{0.2}$-Ni and d) $Al_{0.2}$-Ni twin. Blue is 1st cycle, orange is 2nd and green is the 3rd cycle.

## 4.8 Accelerating Rate Calorimetry

Accelerating Rate Calorimetry (ARC) was done using FFI's esARC from Thermal Hazard Technologies as explained in experimental section 3.8. A calibration test was done before starting the experiments, with drift tests done on two occasions to ensure that the instrument was still properly calibrated. Data can be found in Appendix B, figure B.19.

Firstly, pure LMNO and Al substituted LMNO ($Al_{0.2}$-Ni) are compared before they are compared with commercial cathode samples of NMC622 and LMNO. The reproducibility and effect of data smoothing are also shown and discussed.

### 4.8.1 Al substituted and pure LMNO

Figure 4.33 below shows delithiated $Al_{0.2}$-Ni ($Li_0Mn_{1.5}Al_{0.2}Ni_{0.3}O_4$) and pure delithiated LMNO ($Li_0Al_0Mn_{1.5}Ni_{0.5}O_4$). The verification experiment for the aluminum substituted sample yielded identical results and can be found in Appendix B, figure B.19.

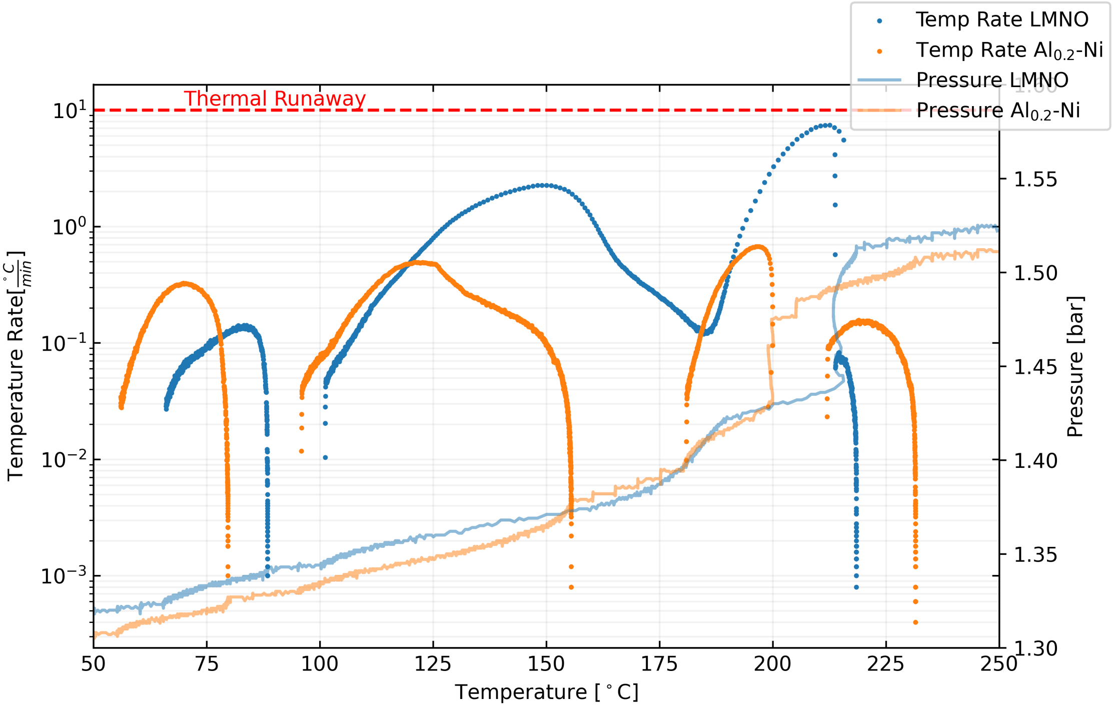

Figure 4.33: Comparison of ARC data from delithiated Al-substituted LMNO and pure LMNO.

Starting with the leftmost exotherm in figure 4.33, it is visible that the first exotherm happens for the Al substituted sample already at 56°C while for the pure LMNO, this does not happen before reaching 66°C. However, it must be noted that the temperature step between searching for exotherms was set to 5°C, meaning that the uncertainty of onset temperature can be as large as negative five degrees.

For the second exotherm between 100°C-160°C, the aluminum substituted sample has a significantly lower maximum heating rate of $0.5\frac{^{\circ}C}{min}$ versus the pure LMNOs $2\frac{^{\circ}C}{min}$. In addition, this exotherm is unsustained for the aluminum substituted sample. For pure LMNO on the other hand, the reaction starting at 100°C was sustained up close to thermal runaway, indicating a higher heat output.

From XRD results of materials taken between the two first exotherms, Khakani et al explained in a paper discussed in theory section 2.4.2 that the reactions below 100°C are most probably only surface reactions since the diffractogram looks unchanged from the pristine delithiated sample [44]. Similar thermal events have been observed for the metastable SEI on graphite anodes as well, as discussed in theory section 2.4.1. This strengthens the hypothesis that the first exotherm is SEI-layer reactions only.

Khakani et al. also did XRD on a sample only heated to 200°C, which is right after the second exotherm for their material. In their data, both $MnO_2$ and NiO can be seen which does indicate that some degradation of the actual LMNO crystallite has taken place, even though the peaks of the normal LMNO were still clearly visible. This shows that the second exotherm is partial degradation of the active material, and thus also affected by the cathode material.

After the third exotherm which started at 180°C it is clear from the post-ARC XRD shown in results section 4.8.3 that structural degradation has played a significant role in the exothermic reactions and that this might be the exotherm most interesting for looking at the structural stability of the active material itself. If this is the case, then the aluminum substituted sample shows a significant improvement over the pure LMNO sample, with a maximum heat rate of $0.6\frac{^\circ C}{min}$ versus pure LMNOs $7.5\frac{^\circ C}{min}$. This might be because of the unknown endothermic reaction happening during the third exotherm which completely overrides the Al substituted samples exotherm at 200°C, 15°C below the pure LMNO sample. Although this requires further investigation, they do align with the boiling points of the organic solvent in the electrolyte used (ref theory section 2.4.1). From the pressure data, it is also evident that there is a rapid pressure increase exactly when the endotherms occur, indicating that some heat might have left the sample bomb with the gas. Further work with different electrolytes would be the first step to look at both this endotherm and the effect it has on the exotherms below 160°C.

### 4.8.2 LMNO, commercial LMNO and NMC

For comparison with commercially available cathodes, a commercial LMNO sample and delithiated CustomCells NMC622 ($Li_{0.3}Ni_{0.6}Mn_{0.2}Co_{0.2}O_2$) samples were also measured. The commercial LMNO sample has unknown stoichiometry but is assumed to be close to $Li_0Al_0Mn_{1.55}Ni_{0.45}O_4$ and was synthesized by a proprietary solid-state method. It must also be noted that this experiment did not have a parallel run and is thus unverified. However, the data has been included in figure 4.34 for reference. The pressure data for these materials can be found in Appendix figure B.21.

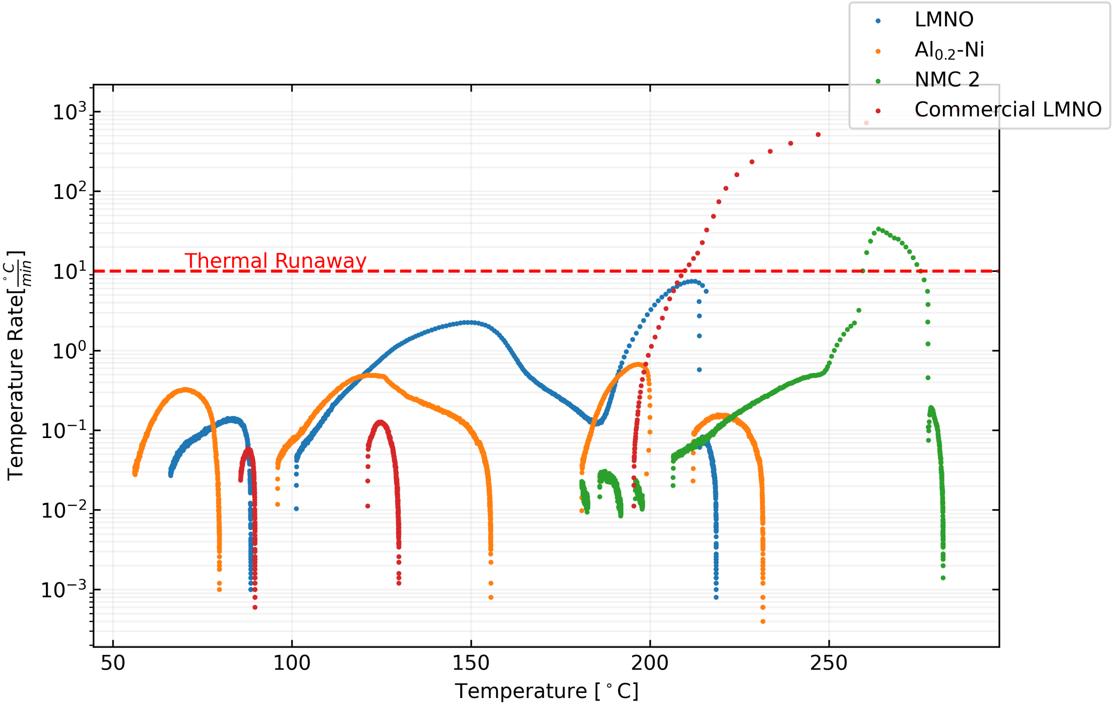

Figure 4.34: Comparison of ARC data from delithiated Al-substituted LMNO, pure LMNO, commercial LMNO, and CustomCells NMC622.

From figure 4.34 above it immediately becomes visible that all LMNO samples do have some unsustained exothermic reactions much lower in temperature (60°C) than the NMC sample (180°C). This is believed to be because of the significant amounts of SEI that forms on the cathode material when going all the way up to 5 V versus graphite (discussed in theory section 2.2.7), which is outside the stability region of the electrolyte (LP30). NMC on the other hand is fully charged at 4.2 V and thus does not trigger the same SEI formation as for the high potential cathodes.

### 4.8.3 X-ray diffraction of measured samples

The XRD done in the home lab of the delithiated material before and after full ARC suggest that LMNO has completely decomposed during the ARC experiment. This is seen by the LMNO (111)-peak at around 1.4 Å$^{-1}$ vanishing in figure 4.35 below.

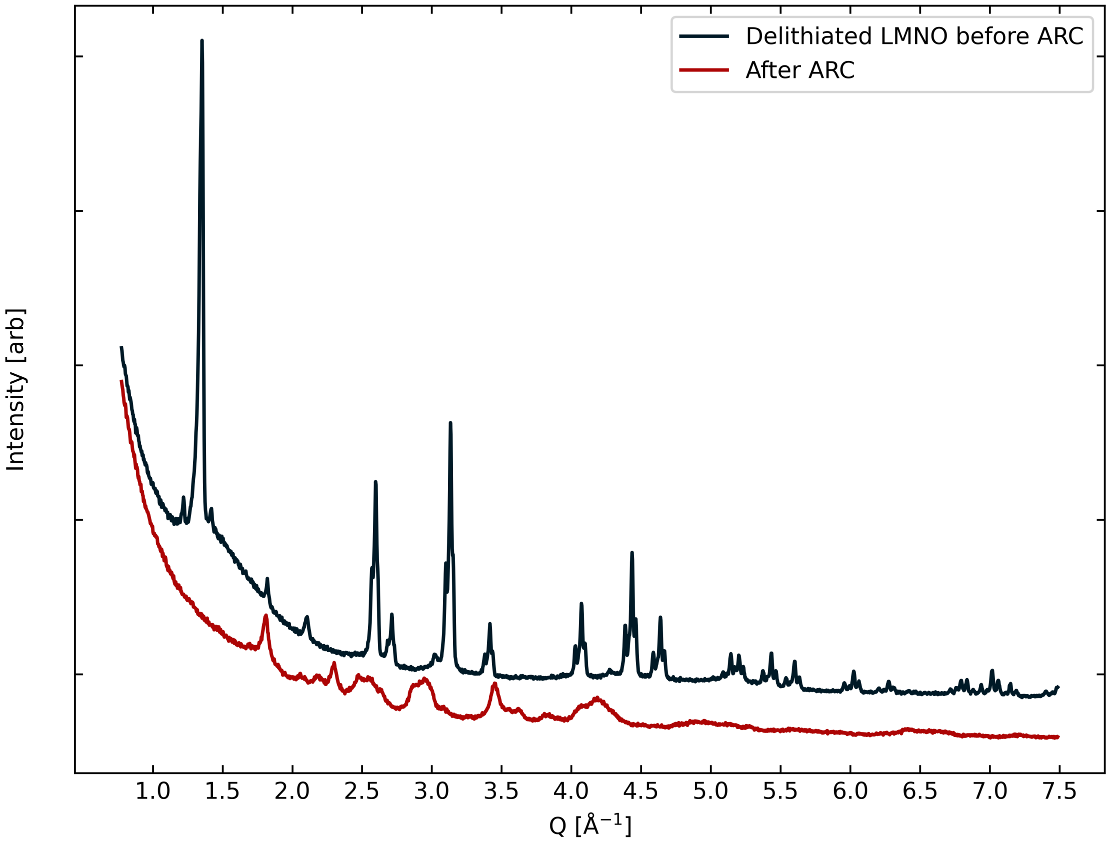

Figure 4.35: Home lab capillary XRD of delithiated LMNO before ARC (black) and after ARC (red). X-ray source: MoK$\alpha_1$ and MoK$\alpha_2$.

### 4.8.4 Reproducibility

Figure 4.36 below shows three different runs for the same material where they have all been prepared in the same way, except for the differences listed in table 4.6 below. The differences include the time between pouch cell disassembly, temperature sensor height from the bottom of the bomb, and material found in the side branch after the experiment. The side branch was cleaned out with acetone and the dirty solution was weighed after the acetone had evaporated. To avoid getting material in the side branch, the glass fiber dot was compacted flat between the thumb and index finger (with clean nitrile gloves) before being inserted into the bomb. No material was found in the side branch for the rest of the experiments after this fix was implemented. It must also be noted that due to a misunderstanding, the NMC 3 sample was heated directly to 185°C, which is 5°C above where the first exotherms for the two other NMC samples started. This might have accelerated the exothermic reactions in the NMC 3 sample.

Table 4.6: Differences affecting reproducibility in ARC tests.

| **Sample name** | **Rest time** | **Temp sensor height (cm)** | **Side branch material weight (mg)** |
|---|---|---|---|
| NMC 1 | 4 weeks | 2.2 | *some* |
| NMC 2 | 3 days | 1.5 | 11 |
| NMC 3 | 5 days | 1.5 | 45.4 |
| Commercial LMNO | 8 weeks | 2.2 | 0 |
| LMNO test | 4 weeks | 2.2 | 0 |

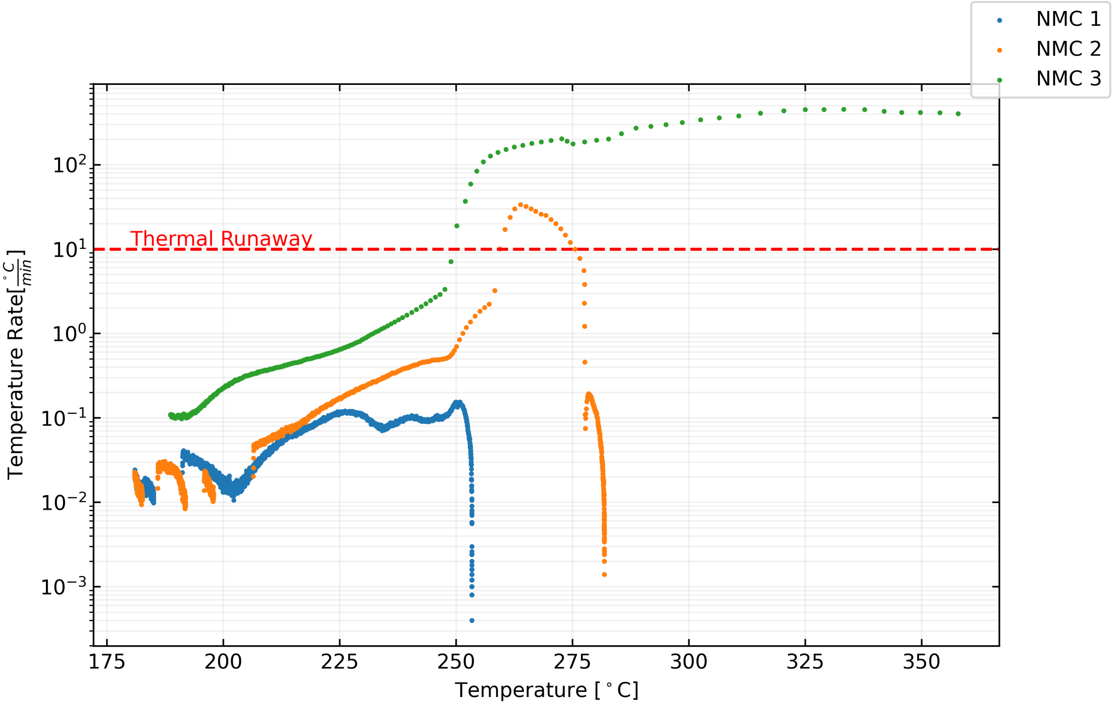

Figure 4.36: Reproducibility of ARC tests, example one.

In figure 4.37 below, all parallel runs for pure LMNO are shown. The LMNO test sample only saw one charge at C/10 up to 5 V whereas the two other samples had two cycles followed by a charge to 5 V. By only charging one time to high potential, and thus being at that potential for a lower amount of time might have yielded less SEI formation on the LMNO test sample. This sample was also stored for four weeks between the post-mortem and the ARC test, whereas the two others were only stored for three days.

This yields three possible answers to why the exotherms below 160°C had a lower temperature rate for the LMNO test sample than the two other samples: 1. the SEI layer was thinner, 2. storing the electrode stabilizes SEI, or 3. oxygen might have entered and already degraded the metastable SEI layer.

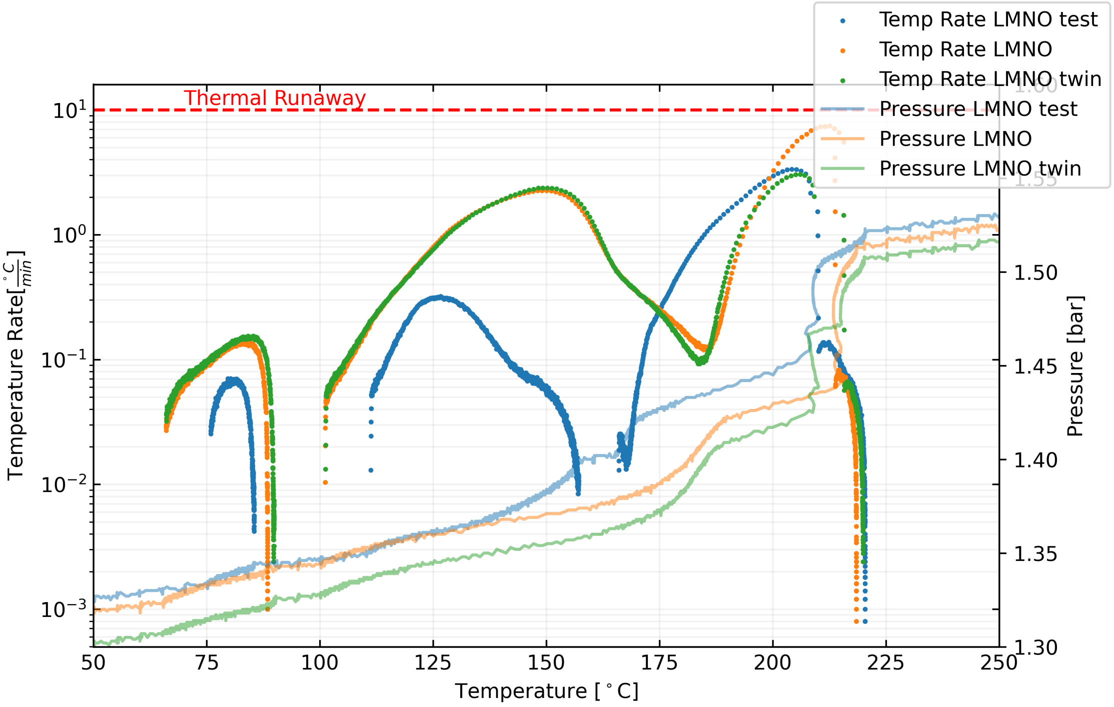

Figure 4.37: Reproducibility of ARC tests, example two.

As shown in the figures above, the reproducibility of an ARC test heavily depends on the ability to recreate the sample and the experimental setup the same every time. Below is a list of pitfalls found to be crucial to avoid for the reproducibility of ARC tests with a material sample in a stainless steel tube bomb.

**Pitfalls for cathode material preparation:**

- Inconsistent electrochemical treatment
- Inconsistent time spent at full charge before post mortem
- Air exposure or prolonged storage in an inert atmosphere
- Inconsistent surface area/particle size of the material before packing in the bomb
- Inconsistent compression/packing of the particles in the bomb

**Pitfalls for instrumental setup:**

- Alterations to anything on the instrument
- Inconsistent temperature sensor placement
- Inconsistent pressure in the gas system

### 4.8.5 Smoothing of data

Data smoothing significantly improves the readability of the temperature rate plots. However, it was found that the simple rolling average might create artifacts when the temperature rate changes rapidly. Adjustments to the rolling average size were done and it can be seen in figure 4.38 below that a good balance between readability and avoiding misrepresentation is struck when the rolling average is done over five points. Smoothing becomes more important for readability when multiple datasets are laid on top of each other.

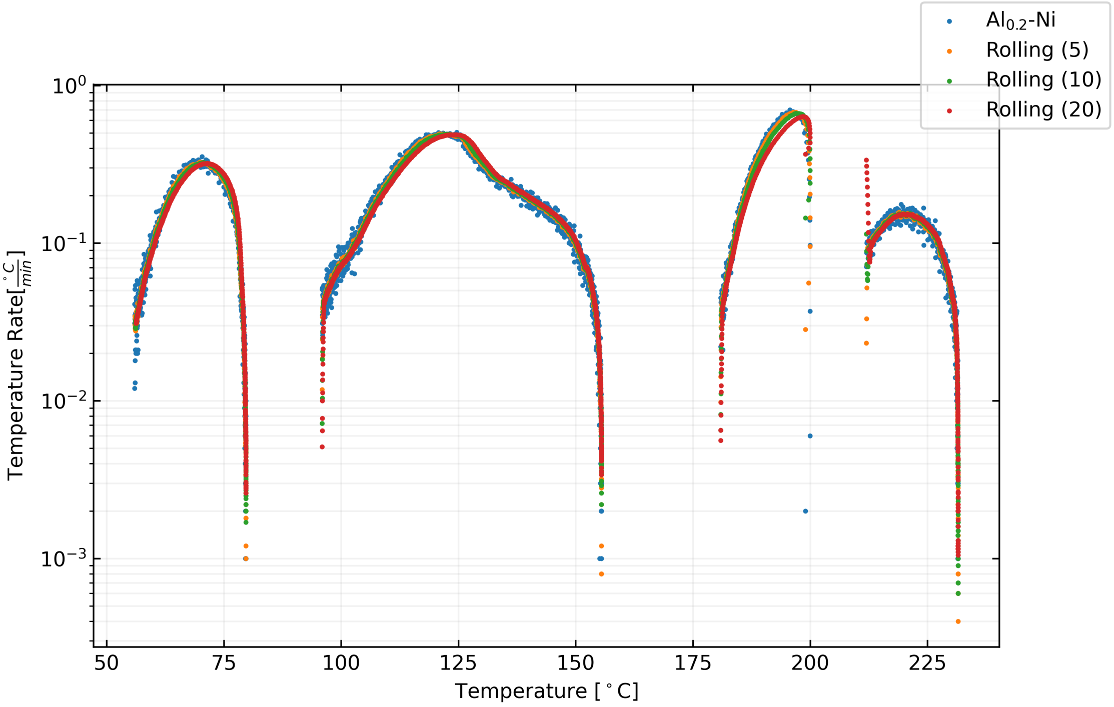

Figure 4.38: Impact on rolling average smoothing of ARC data.

# Chapter 5

# Discussion

In this chapter, the discussions from the separate characterization techniques are seen in conjunction with each other and the success and/or effect of aluminum substitution is seen in the bigger picture

## 5.1 Thermodynamically most favorable composition

The synchrotron PXRD data shown in 4.2 indicates that aluminum is easiest to insert in the LMNO structure when substituted in place of nickel and that a stoichiometry of 0.2 Al is needed to find a thermodynamically stable composition where very little impurities form. However, the electrochemistry does not show a satisfactory increase in the $Mn^{3+} \leftrightarrow Mn^{4+}$ capacity for this sample ($Al_{0.2}$-Ni), indicating that either charge compensation is done by other means, or that 25 mol % of $Mn^{3+}$ is somehow not electrochemically available.

Other charge compensation could have been done by lithium vacancies, as it would only require a 5 mol% lithium deficiency. While this sounds probable from the electrochemistry standpoint, the ICP-MS data shows that the pristine degree of lithiation is above 99% for both samples. If the aluminum were to replace manganese in the structure, this could be done by expelling only 3.3 mol% of manganese, which should form an impurity phase. Due to the low molar percentage of manganese expelled from the structure, this would result in less than 1 wt% impurity phase. This is the most probable mechanism due to the correlation with the Rietveld refinement result showing less than 1 wt% impurity phase for this material ($Al_{0.2}$-Ni).

On this basis, it is believed that the thermodynamically most stable composition is not $Mn_{1.5}Al_{0.2}Ni_{0.3}$, but rather with a bit Al in place of Mn as well (e.g. $Mn_{1.45}Al_{0.2}Ni_{0.35}$). Based on the XRD and electrochemistry results discussed above, this results in an aluminum distribution of 3:1 on the nickel and manganese sites respectively. This also shows that during synthesis, it is likely the Mn-spinel and Mn-rich compositions which represent the more stable situation, owing to the reduced stability of nickel in higher oxidation states (above two).

## 5.2 Lithiation mechanisms

From the voltage curves and post-mortem XRD data of the delithiated LMNO and $Al_{0.2}$ sample, there seems to be significantly different (de)lithiation mechanisms occurring in the two materials. As suggested in the electrochemistry results section 4.6.2, the two different mechanisms may be attributed to a phase change between three different phases for the pure LMNO, whereas for $Al_{0.2}$-Ni there might be more of a solid solution of lithium in the crystal. Although this difference has been shown for ordered and disordered LMNO before [30], [115], [116], the electrochemistry of this aluminum substituted sample ($Al_{0.2}$-Ni) might indicate a fuller solid solution due to the slope of the potential plateau, and that the $Al_{0.2}$-Ni sample only showed one phase when almost delithiated as seen in the XRD results.

The reason for a sloping potential plateau to indicate a fuller solid solution is due to the electrochemical potential of the active material changing with surface concentration. When the potential is constant, on the other hand, the electrochemical potential on the surface of the active material particle must be constant, indicating a constant lithium concentration. For the three-phase mechanism, this can be facilitated by the surface first lithiating to a specific degree, before the phase boundary of this phase travels inwards in the active material particle.

As shown in theory section 2.1.1, the electrochemical potential is the sum of chemical and electrostatic potential. And while the redox reaction with nickel determines the electrostatic potential, the chemical potential is determined by the change of lithiation. One of the commonly accepted hypotheses as to why the LMNO chemical potential does not change with lithiation is that there is very little Li-Li interaction due to the 3D network of lithium in the crystal [20], [123]. My hypothesis contradicts this and says that it is rather because of a constant surface lithium concentration that the chemical potential stays the same.

The electrochemistry data in figure 4.16 also shows how the slope of the potential plateau increases with aluminum concentration. This indicates that possibly, the three phases increase their solid solubility of lithium with an increase in aluminum doping. The data which Samarasingha et al. presented for the disordered spinel (also shown in Appendix B.3.1) also suggest that this might be the case as the lattice parameters for the individual phases change a bit during (de)lithiation.

As a practical consideration when bringing LMNO to commercialization, a sloping voltage plateau is very useful as it can be used as an SoC indicator.

## 5.3 Aging effects

The introduction of aluminum has made the material more disordered (ref XRD data), which by common belief should increase the electrochemical stability of the material [59], [85], [120]. The increased electrochemical stability was also found in the rate capability degradation data and accelerated degradation data to be true. In addition, the ARC data shows increased stability for the Aluminum substituted sample, which further strengthens this point.

A potential cause of the prolonged cycling lifetime of the aluminum substituted sample is the lowered dissolution rate of manganese into the electrolyte. Three suggested mechanisms for this are 1. aluminum blocking the diffusion pathways for manganese in the crystal, 2. that substitution of $Al^{3+}$ reduces the amount of $Mn^{3+}$ which can disproportionate to $Mn^{2+}$ and $Mn^{4+}$, or 3. that aluminum segregates to the surface, making a protective layer around the particles. The last suggestion could be further investigated by XPS or other surface probing techniques. However, if such an aluminum layer did form on the surface, the charge transfer overpotential should be higher, which it does seem to be in the rate capability data in section 4.6.4.

To validate these results, better control of the morphology of the samples is needed. For instance, the surface area of the active material particles will significantly impact the absolute charge transfer resistance. This is impossible to quantify from the SEM micrographs shown in results section 4.3. A first experiment to conduct would be BET surface area measurement of the active material as described in section 2.5.5.5.

Another potential cause of the prolonged lifetime of the $Al_{0.2}$-Ni samples can be tied to the lithiation mechanism. The three-phase transitions (explained above) might result in a harsh structural domain border inducing high structural stress, increasing the possibility of transition metal cation dissolution and thus loss of active material. On the other hand, a continuous change in lattice parameter due to a gradient of lithium concentration would reduce the stress in the crystal, and thus the cation dissolution reactions. This difference is also believed to be the reason for the prolonged cycle life of the disordered LMNO structure [59], [85], [120].

## 5.4 Stability and solid electrolyte interphase

Electrochemically, the cycling stability does improve when aluminum is inserted. As seen in the ARC data, this seems to be the case for the thermal stability of the active material as well. However, it was not only in the high-temperature exotherms of the ARC data that the $Al_{0.2}$-Ni material performed better than pure LMNO, also the medium temperature areas (100-175°C) showed significantly lower heat rate. This could be because less SEI-layer form on the $Al_{0.2}$-Ni sample, maybe due to the aluminum segregating to the surface as previously discussed. The electrochemistry data for the preparation (delithiation) of these materials (shown in section 4.7.4) are inconclusive regarding SEI formation, as the coulombic efficiency for the two pure LMNO parallels is different while the ARC data looks identical.

To conclude on the change in SEI, the possible change in the surface area must also be accounted for as this would change the amount of SEI in the cell. This means that it is unclear whether it is morphological or crystallographic effects that change the thermal behavior between the pure LMNO and the $Al_{0.2}$-Ni sample.

## Chapter 6

# Conclusion

From synchrotron XRD data it was found that a thermodynamically stable solid solution leading to fewer impurities was found for aluminum substituted LMNO; $Li_1Mn_{1.5}Al_{0.2}Ni_{0.3}O_4$. Indication from electrochemistry suggests that even fewer impurities and a more stable solid solution could be achieved in the case of having both manganese and nickel substituted by aluminum, in a 1:3 ratio.

With an increased amount of aluminum substitution, it was found that the potential plateau at 4.7 V becomes less flat and rather more of a slope which indicates a change in the lithiation mechanism. The proposed solution is that the material with 0.2 Al in place of Ni ($Al_{0.2}$-Ni) exhibits more of a solid solution behavior of lithium in the crystal, while ordered pure LMNO exhibit a phase-change type of behavior.

The suggested solid solution (de)lithiation is also supported by degradation data, where it is seen that the cycle life of $Al_{0.2}$-Ni is better than that of pure LMNO. However, it must be noted that at this high substitution, the initial capacity is also 24% lower than for pure LMNO due to replacing redox-active nickel with inactive aluminum. Another explanation for prolonged cycle life could be that aluminum segregates to the surface, making a protective surface barrier that limits the manganese disproportionation reaction.

From ARC experiments, it was shown that the thermal stability of structural degradation significantly improved when going from a pure LMNO material to the $Al_{0.2}$-Ni material. The Al-substituted material also showed a lower heating rate in the medium-temperature section (100-175°C), although it cannot be concluded if this is due to morphological effects or the crystal structure.

# Chapter 7

# Future Prospects

In the future, several investigations regarding both structural topics of LMNO as well as its electrochemical performance in conjunction with electrolytes would be interesting to conduct.

While this thesis found a composition that looks to be thermodynamically stable, a phase diagram of impurities over composition could be developed for mapping the solubility of aluminum in the structure. This would open up for fine-tuning electrochemical performance while still staying within the solubility limits of Al in LMNO.

Further investigations of the electrochemistry of highly Al-substituted samples would also result in a better understanding of the sloping potential plateau of this sample. A simple first experiment would be to do galvanostatic intermittent titration on this material to map its open-circuit voltage over its capacity.

A next step in researching this sloping potential would be to conduct operando XRD of this material. By doing this, one could hopefully characterize the lattice parameter change, and see if any intermediary phases are found. Thereafter, spatially resolved SIMS could be used on a partially delithiated LMNO particle to evaluate lithium concentration with distance from the surface of the particle. SIMS could also be used for mapping the aluminum, nickel, and manganese concentration with distance from the surface to test the theory of aluminum segregating to the surface creating a thinner and more stable SEI.

To test the hypothesis of SEI formation being a key parameter in the exothermic reactions of LMNO below 160°C, ARC experiments with other types of electrolytes could be conducted. With these experiments, it can also be verified if the endotherms in the anticipated material decomposition exotherms are the evaporation of electrolyte. Different morphologies should also be tested to ensure that the result is not an effect of morphology change between my samples. The ARC results of this thesis laid the foundation for further collaboration between FFI, Morrow, UiO, and Baldur in a new project named ARCTIC (Accelerated Rate Calorimetry Towards Ideal Cathodes) in the MOZEES consortium set to start summer of 2022.

More quantitative analysis of ARC results can also be done by starting the experiments at different temperatures. This could be used to determine the activation energy, rate constant, and frequency factor and give more conciseness to the ARC measurements (see appendix section A.4). Also, analysis of the gas escaping from the bomb would be of interest to evaluate the decomposition mechanisms.

# Chapter 8

# References

[1] K. M. Aasrud, “MDoc - the power of LaTeX and simplicity of markdown.” 2022. Available: https://github.com/kmaasrud/mdoc https://kmaasrud.com/mdoc/

[2] I. P. on Climate Change, “GLOBAL WARMING OF 1.5 ºC,” Intergovernmental Panel on Climate Change, Oct. 2018.

[3] Y. Xu, V. Ramanathan, and D. G. Victor, “Global warming will happen faster than we think,” *Nature 2021 564:7734*, vol. 564, pp. 30–32, Dec. 2018, doi: 10.1038/d41586-018-07586-5.

[4] “Causes of climate change,” *European Commission Website*. Available: https://ec.europa.eu/clima/climate-change/causes-climate-change_en

[5] “World | total including LUCF | greenhouse gas (GHG) emissions | climate watch.” 2018. Available: https://www.climatewatchdata.org/ghg-emissions?breakBy=sector&chartType=percentage&source=CAIT

[6] C. Lichner, “The weekend read: Ethical strategies for cobalt supply – pv magazine international,” *PV Magazine*. Jan. 2020. Available: https://www.pv-magazine.com/2020/02/01/the-weekend-read-ethical-strategies-for-cobalt-supply/

[7] R. Backhaus, “Battery raw materials - where from and where to?” *ATZ worldwide*, vol. 123, p. 8, Sep. 2021, doi: 10.1007/S38311-021-0715-5.

[8] P. Sun, Y. Ma, T. Zhai, and H. Li, “High performance LiNi0.5Mn1.5O4 cathode by al-coating and Al3+-doping through a physical vapor deposition method,” *Electrochimica Acta*, vol. 191, pp. 237–246, Feb. 2016, doi: 10.1016/J.ELECTACTA.2016.01.087.

[9] Y. Shu *et al.*, “The effects of a mixed precipitant on the morphology and electrochemical performance of LiNi0.5Mn1.5O4 cathode materials,” *Crystals*, vol. 7, p. 275, 2017, Available: https://doi.org/10.3390/cryst7090275

[10] G. Liu *et al.*, “Study on oxygen deficiency in spinel LiNi0.5Mn1.5O4 and its fe and cr-doped compounds,” *Journal of Alloys and Compounds*, vol. 725, pp. 580–586, 2017.

[11] K. Y. Chung *et al.*, “Comparative studies between oxygen-deficient LiMn2O4 and al-doped LiMn2O4,” in *Journal of Power Sources*, Aug. 2005, vol. 146, pp. 226–231. doi: 10.1016/j.jpowsour.2005.03.033.

[12] J. Lee, N. Dupre, M. Avdeev, and B. Kang, “Understanding the cation ordering transition in high-voltage spinel LiNi0.5Mn1.5O4 by doping li instead of ni,” *Scientific Reports 2017 7:1*, vol. 7, pp. 1–12, Jul. 2017, doi: 10.1038/s41598-017-07139-2.

[13] J. Mao *et al.*, “The effect of cobalt doping on the morphology and electrochemical performance of high-voltage spinel LiNi0.5Mn1.5O4 cathode material,” *Solid State Ionics*, vol. 292, pp. 70–74, 2016, doi: https://doi.org/10.1016/j.ssi.2016.05.008.

[14] A. Chen *et al.*, “Role of al-doping with different sites upon the structure and electrochemical performance of spherical LiNi0.5Mn1.5O4 cathode materials for lithium-ion batteries,” *RSC Adv.*, vol. 9, pp. 12656–12666, 2019, doi: 10.1039/C9RA00374F.

[15] X. Liu *et al.*, “Facile synthesis of aluminum-doped LiNi0.5Mn1.5O4 hollow microspheres and their electrochemical performance for high-voltage li-ion batteries,” *Journal of Alloys and Compounds*, vol. 609, pp. 54–59, Oct. 2014, doi: 10.1016/J.JALLCOM.2014.03.102.

[16] G. B. Zhong, Y. Y. Wang, Z. C. Zhang, and C. H. Chen, “Effects of al substitution for ni and mn on the electrochemical properties of LiNi0.5Mn1.5O4,” *Electrochimica Acta*, vol. 56, pp. 6554–6561, 2011, doi: https://doi.org/10.1016/j.electacta.2011.03.093.

[17] G. B. Zhong, Y. Y. Wang, X. J. Zhao, Q. S. Wang, Y. Yu, and C. H. Chen, “Structural, electrochemical and thermal stability investigations on LiNi0.5-xAl2xMn1.5-xO4 (0 <= 2x <= 1.0) as 5 v cathode materials,” *Journal of Power Sources*, vol. 216, pp. 368–375, 2012, doi: https://doi.org/10.1016/j.jpowsour.2012.05.108.

[18] “Planté battery – 1859 - MagLab.” Available: https://nationalmaglab.org/education/magnet-academy/history-of-electricity-magnetism/museum/plante-battery

[19] P. Kurzweil, “Gaston planté and his invention of the lead–acid battery—the genesis of the first practical rechargeable battery,” *Journal of Power Sources*, vol. 195, pp. 4424–4434, Jul. 2010, doi: 10.1016/J.JPOWSOUR.2009.12.126.

[20] M. Kirkengen, “TEK5320 - battery technology, university of oslo.” University of Oslo, pp. 14–15, 2021.

[21] M. Li, J. Lu, Z. Chen, and K. Amine, “30 years of lithium-ion batteries,” *Advanced Materials*, vol. 30, p. 1800561, Aug. 2018, doi: 10.1002/ADMA.201800561.

[22] X. Sun, S. C. Simonsen, T. Norby, and A. Chatzitakis, “Composite membranes for high temperature PEM fuel cells and electrolysers: A critical review,” *Membranes 2019, Vol. 9, Page 83*, vol. 9, p. 83, Jul. 2019, doi: 10.3390/MEMBRANES9070083.

[23] B. N and D. H, “Review on synthesis, characterizations, and electrochemical properties of cathode materials for lithium ion batteries,” 2016, doi: 10.4172/2169-0022.1000258.

[24] J.-L. Shi *et al.*, “High-capacity cathode material with high voltage for li-ion batteries,” *Advanced Materials*, vol. 30, p. 1705575, Mar. 2018, doi: 10.1002/ADMA.201705575.

[25] T. E. of Encyclopedia Britannica, “Faraday’s laws of electrolysis.” Available: https://www.britannica.com/science/Faradays-laws-of-electrolysis

[26] L. O. Valoen and J. N. Reimers, “Transport properties of LiPF[sub 6]-based li-ion battery electrolytes,” *Journal of The Electrochemical Society*, vol. 152, p. A882, Mar. 2005, doi: 10.1149/1.1872737/XML.

[27] S. J. An, J. Li, C. Daniel, D. Mohanty, S. Nagpure, and D. L. Wood, “The state of understanding of the lithium-ion-battery graphite solid electrolyte interphase (SEI) and its relationship to formation cycling,” *Carbon*, vol. 105, pp. 52–76, Aug. 2016, doi: 10.1016/J.CARBON.2016.04.008.

[28] K. Karuppasamy *et al.*, “Ionic liquid-based electrolytes for energy storage devices: A brief review on their limits and applications,” *Polymers*, vol. 12, Apr. 2020, doi: 10.3390/POLYM12040918.

[29] P. B. Samarasingha, N. H. Andersen, M. H. Sørby, S. Kumar, O. Nilsen, and H. Fjellvåg, "Neutron diffraction and raman analysis of LiMn1.5Ni0.5O4 spinel type oxides for use as lithium ion battery cathode and their capacity enhancements," *Solid State Ionics*, vol. 284, pp. 28–36, Jan. 2016, doi: 10.1016/j.ssi.2015.11.018.

[30] P. B. Samarasingha, J. Sottmann, S. Margadonna, H. Emerich, O. Nilsen, and H. Fjellvåg, "In situ synchrotron study of ordered and disordered LiMn1.5Ni0.5O4 as lithium ion battery positive electrode," *Acta Materialia*, vol. 116, pp. 290–297, Sep. 2016, doi: 10.1016/j.actamat.2016.06.040.

[31] Y. Gao, K. Myrtle, M. Zhang, J. N. Reimers, and J. R. Dahn, "Valence band of LiNi_xMn_2-xO_4 and its effects on the voltage profiles of LiNi_xMn_2-xO_4/li electrochemical cells," *Phys. Rev. B*, vol. 54, pp. 16670–16675, Dec. 1996, doi: 10.1103/PhysRevB.54.16670.

[32] N. G. Connelly, R. S. of Chemistry (Great Britain), I. U. of Pure, and A. Chemistry., "Nomenclature of inorganic chemistry. IUPAC recommendations 2005," p. 366, 2005.

[33] J. B. Goodenough and Y. Kim, "Challenges for rechargeable li batteries," *Chemistry of Materials*, vol. 22, pp. 587–603, Feb. 2010, doi: 10.1021/CM901452Z/ASSET/IMAGES/LARGE/CM-2009-01452Z_0018.JPEG.

[34] H. Wang, X. Li, F. Li, X. Liu, S. Yang, and J. Ma, "Formation and modification of cathode electrolyte interphase: A mini review," *Electrochemistry Communications*, vol. 122, p. 106870, Jan. 2021, doi: 10.1016/J.ELECOM.2020.106870.

[35] P. Poizot, S. Laruelle, S. Grugeon, L. Dupont, and J. M. Tarascon, "Nano-sized transition-metal oxides as negative-electrode materials for lithium-ion batteries," *Nature 2000 407:6803*, vol. 407, pp. 496–499, Sep. 2000, doi: 10.1038/35035045.

[36] M. Z. Bazant, "Theory of chemical kinetics and charge transfer based on nonequilibrium thermodynamics," *Accounts of Chemical Research*, vol. 46, pp. 1144–1160, May 2013, doi: 10.1021/AR300145C/ASSET/IMAGES/AR-2012-00145C_M074.GIF.

[37] K. R. Tallman *et al.*, "Nickel-rich nickel manganese cobalt (NMC622) cathode lithiation mechanism and extended cycling effects using operando x-ray absorption spectroscopy," *Journal of Physical Chemistry C*, vol. 125, pp. 58–73, Jan. 2021, doi: 10.1021/ACS.JPCC.0C08095/SUPPL_FILE/JP0C08095_SI_001.PDF.

[38] J. Shu *et al.*, "Comparison of electronic property and structural stability of LiMn2O4 and LiNi0.5Mn1.5O4 as cathode materials for lithium-ion batteries," *Computational Materials Science*, vol. 50, pp. 776–779, Dec. 2010, doi: 10.1016/J.COMMATSCI.2010.10.010.

[39] Y. M. Hon, S. P. Lin, K. Z. Fung, and M. H. Hon, "Synthesis and characterization of nano-LiMn2O4 powder by tartaric acid gel process," *Journal of the European Ceramic Society*, vol. 22, pp. 653–660, May 2002, doi: 10.1016/S0955-2219(01)00382-X.

[40] L. Tian and A. Yuan, "Electrochemical performance of nanostructured spinel LiMn2O4 in different aqueous electrolytes," *Journal of Power Sources*, vol. 192, pp. 693–697, Jul. 2009, doi: 10.1016/J.JPOWSOUR.2009.03.002.

[41] M. W. Raja, S. Mahanty, and R. N. Basu, "Multi-faceted highly crystalline LiMn2O4 and LiNi0.5Mn1.5O4 cathodes synthesized by a novel carbon exo-templating method," *Solid State Ionics*, vol. 180, pp. 1261–1266, Oct. 2009, doi: 10.1016/J.SSI.2009.06.016.

[42] Y. S. Lee, Y. K. Sun, S. Ota, T. Miyashita, and M. Yoshio, "Preparation and characterization of nano-crystalline LiNi0.5Mn1.5O4 for 5 v cathode material by composite carbonate process," *Electrochemistry Communications*, vol. 4, pp. 989–994, Dec. 2002, doi: 10.1016/S1388-2481(02)00491-5.

[43] S. W. Oh, S. H. Park, J. H. Kim, Y. C. Bae, and Y. K. Sun, "Improvement of electrochemical properties of LiNi0.5Mn1.5O4 spinel material by fluorine substitution," *Journal of Power Sources*, vol. 157, pp. 464–470, Jun. 2006, doi: 10.1016/J.JPOWSOUR.2005.07.056.

[44] S. E. Khakani, D. Rochefort, and D. D. MacNeil, "Thermal stability of high voltage li 1-x mn 1.5 ni 0.5 o 4 cathode material synthesized via a sol-gel method," *Journal of The Electrochemical Society*, vol. 163, pp. A947–A952, Mar. 2016, doi: 10.1149/2.0621606JES/XML.

[45] K. Saravanan, A. Jarry, R. Kostecki, and G. Chen, "A study of room-temperature LixMn1.5Ni0.5O4 solid solutions," *Scientific Reports 2015 5:1*, vol. 5, pp. 1–11, Jan. 2015, doi: 10.1038/srep08027.

[46] B. Aktekin *et al.*, "Cation ordering and oxygen release in LiNi0.5-xMn1.5+xO4-y (LNMO): In-situ neutron diffraction and performance in li-ion full cells," 2019.

[47] H. W. Choi, S. J. Kim, M. Y. Jeong, S. Lee, Y. H. Rim, and Y. S. Yang, "Temperature-dependent oxygen behavior of LixNi0.5Mn1.5O4 cathode material for lithium battery," *APL Materials*, vol. 4, p. 116111, Nov. 2016, doi: 10.1063/1.4968566.

[48] J. Xiao *et al.*, "High-performance LiNi0.5Mn1.5O4 spinel controlled by Mn3+ concentration and site disorder," *Advanced Materials*, vol. 24, pp. 2109–2116, Apr. 2012, doi: 10.1002/ADMA.201104767.

[49] Y. Xia, H. Wang, Q. Zhang, H. Nakamura, H. Noguchi, and M. Yoshio, "Oxygen deficiency, a key factor in controlling the cycle performance of mn-spinel cathode for lithium-ion batteries," *Journal of Power Sources*, vol. 166, pp. 485–491, Apr. 2007, doi: 10.1016/J.JPOWSOUR.2007.01.023.

[50] W. I. F. David, M. M. Thackeray, L. A. D. Picciotto, and J. B. Goodenough, "Structure refinement of the spinel-related phases Li2Mn2O4 and Li0.2Mn2O4," *Journal of Solid State Chemistry*, vol. 67, pp. 316–323, Apr. 1987, doi: 10.1016/0022-4596(87)90369-0.

[51] A. R. Denton and N. W. Ashcroft, "Vegard's law," *Physical Review A*, vol. 43, p. 3161, Mar. 1991, doi: 10.1103/PhysRevA.43.3161.

[52] D. W. Shin, C. A. Bridges, A. Huq, M. P. Paranthaman, and A. Manthiram, "Role of cation ordering and surface segregation in high-voltage spinel LiMn LiMn 1.5Ni 0.5-xM xO 4(m = cr, fe, and ga) cathodes for lithium-ion batteries," *Chemistry of Materials*, vol. 24, pp. 3720–3731, Oct. 2012, doi: 10.1021/CM301844W/SUPPL_FILE/CM301844W_SI_001.PDF.

[53] T. F. Yi, J. Mei, and Y. R. Zhu, "Key strategies for enhancing the cycling stability and rate capacity of LiNi0.5Mn1.5O4 as high-voltage cathode materials for high power lithium-ion batteries," *Journal of Power Sources*, vol. 316, pp. 85–105, Jun. 2016, doi: 10.1016/J.JPOWSOUR.2016.03.070.

[54] M. C. Kim, Y. W. Lee, T. K. Pham, J. I. Sohn, and K. W. Park, "Chemical valence electron-engineered LiNi0.4Mn1.5MtO4 (mt = co and fe) cathode materials with high-performance electrochemical properties," *Applied Surface Science*, vol. 504, p. 144514, Feb. 2020, doi: 10.1016/J.APSUSC.2019.144514.

[55] G. G. Amatucci, N. Pereira, T. Zheng, and J.-M. Tarascon, "Failure mechanism and improvement of the elevated temperature cycling of LiMn2 o 4 compounds through the use of the LiAl x Mn2 − x o 4 − z f z solid solution," *Journal of The Electrochemical Society*, vol. 148, p. A171, Feb. 2001, doi: 10.1149/1.1342168.

[56] G. Amatucci, A. D. Pasquier, A. Blyr, T. Zheng, and J. M. Tarascon, "The elevated temperature performance of the LiMn2O4/c system: Failure and solutions," *Electrochimica Acta*, vol. 45, pp. 255–271, Sep. 1999, doi: 10.1016/S0013-4686(99)00209-1.

[57] R. Amin *et al.*, “Research advances on cobalt-free cathodes for li-ion batteries - the high voltage LiMn1.5Ni0.5O4 as an example,” *Journal of Power Sources*, vol. 467, p. 228318, Aug. 2020, doi: 10.1016/J.JPOWSOUR.2020.228318.

[58] F. Yu *et al.*, “Spinel LiMn2O4 cathode materials in wide voltage window: Single-crystalline versus polycrystalline,” *Crystals 2022, Vol. 12, Page 317*, vol. 12, p. 317, Feb. 2022, doi: 10.3390/CRYST12030317.

[59] H. Sun *et al.*, “Tailoring disordered/ordered phases to revisit the degradation mechanism of high-voltage LiNi0.5Mn1.5O4 spinel cathode materials,” *Advanced Functional Materials*, p. 2112279, 2022, doi: 10.1002/ADFM.202112279.

[60] C. Zhang *et al.*, “Heteroepitaxial oxygen-buffering interface enables a highly stable cobalt-free li-rich layered oxide cathode,” *Nano Energy*, vol. 75, p. 104995, Sep. 2020, doi: 10.1016/J.NANOEN.2020.104995.

[61] X. L. Xu, S. X. Deng, H. Wang, J. B. Liu, and H. Yan, “Research progress in improving the cycling stability of high-voltage LiNi0.5Mn1.5O4 cathode in lithium-ion battery,” *Nano-Micro Letters 2016 9:2*, vol. 9, pp. 1–19, Jan. 2017, doi: 10.1007/S40820-016-0123-3.

[62] S. Kuppan, Y. Xu, Y. Liu, and G. Chen, “Phase transformation mechanism in lithium manganese nickel oxide revealed by single-crystal hard x-ray microscopy,” *Nature Communications 2017 8:1*, vol. 8, pp. 1–10, Feb. 2017, doi: 10.1038/ncomms14309.

[63] H. Duncan, Y. Abu-Lebdeh, and I. J. Davidson, “Study of the cathode–electrolyte interface of LiMn1.5Ni0.5O4 synthesized by a sol–gel method for li-ion batteries,” *Journal of The Electrochemical Society*, vol. 157, p. A528, Mar. 2010, doi: 10.1149/1.3321710.

[64] J. Kasnatscheew, B. Streipert, S. Röser, R. Wagner, I. C. Laskovic, and M. Winter, “Determining oxidative stability of battery electrolytes: Validity of common electrochemical stability window (ESW) data and alternative strategies,” *Physical Chemistry Chemical Physics*, vol. 19, pp. 16078–16086, Jun. 2017, doi: 10.1039/C7CP03072J.

[65] S. S. Zhang, T. R. Jow, S. S. Zhang, and T. R. Jow, “Aluminum corrosion in electrolyte of li-ion battery,” *JPS*, vol. 109, pp. 458–464, Jul. 2002, doi: 10.1016/S0378-7753(02)00110-6.

[66] T. Ma *et al.*, “Revisiting the corrosion of the aluminum current collector in lithium-ion batteries,” *Journal of Physical Chemistry Letters*, vol. 8, pp. 1072–1077, Mar. 2017, doi: 10.1021/ACS.JPCLETT.6B02933.

[67] X. Chen *et al.*, “Effects of cell positive cans and separators on the performance of high-voltage li-ion batteries,” *Journal of Power Sources*, vol. 213, pp. 160–168, Sep. 2012, doi: 10.1016/J.JPOWSOUR.2012.04.009.

[68] N. N. Sinha, J. C. Burns, R. J. Sanderson, and J. Dahn, “Comparative studies of hardware corrosion at high potentials in coin-type cells with non aqueous electrolytes,” *Journal of The Electrochemical Society*, vol. 158, p. A1400, Nov. 2011, doi: 10.1149/2.080112JES.

[69] S. T. Myung, Y. Sasaki, S. Sakurada, Y. K. Sun, and H. Yashiro, “Electrochemical behavior of current collectors for lithium batteries in non-aqueous alkyl carbonate solution and surface analysis by ToF-SIMS,” *Electrochimica Acta*, vol. 55, pp. 288–297, Dec. 2009, doi: 10.1016/J.ELECTACTA.2009.08.051.

[70] S. T. Myung, Y. Hitoshi, and Y. K. Sun, “Electrochemical behavior and passivation of current collectors in lithium-ion batteries,” *Journal of Materials Chemistry*, vol. 21, pp. 9891–9911, Jun. 2011, doi: 10.1039/C0JM04353B.

[71] E. Hu *et al.*, “Oxygen-release-related thermal stability and decomposition pathways of LixNi0.5Mn1.5O4 cathode materials,” *Chemistry of Materials*, vol. 26, pp. 1108–1118, Jan. 2014, doi: 10.1021/CM403400Y/SUPPL_FILE/CM403400Y_SI_001.PDF.

[72] D. Lu, J. Li, J. He, R. Zhao, and Y. Cai, “Relationships between structure, composition, and electrochemical properties in LiNixMn2- xO4 [ x = 0.37, 0.43, 0.49, 0.52, and 0.56] spinel cathodes for lithium ion batteries,” *Journal of Physical Chemistry C*, vol. 123, pp. 8522–8530, Apr. 2019, doi: 10.1021/ACS.JPCC.8B11085/ASSET/IMAGES/MEDIUM/JP-2018-11085Y_0009.GIF.

[73] T. Olav, L. Sunde, T. Grande, and M.-A. Einarsrud, “Modified pechini synthesis of oxide powders and thin films,” Available: https://sintef.brage.unit.no/sintef-xmlui/bitstream/handle/11250/2593090/Modified%2bPechini%2bsynthesis_15_04_16.pdf?sequence=2&isAllowed=y

[74] A. R. L. L. Simon and Kumar, “Synthesis, structural and electrical properties of spinel LiNi0.5Mn1.5O4 synthesized by sol–gel method,” *Journal of Sol-Gel Science and Technology*, vol. 80, pp. 821–826, Dec. 2016, doi: 10.1007/s10971-016-4150-9.

[75] O. Sha *et al.*, “Synthesis of spinel LiNi0.5Mn1.5O4 cathode material with excellent cycle stability using urea-based sol–gel method,” *Materials Letters*, vol. 89, pp. 251–253, 2012, doi: https://doi.org/10.1016/j.matlet.2012.08.126.

[76] A. S. Rahim, N. Aziz, N. A. M. Nor, and Z. Osman, “LiNi0.5Mn1.5O4 cathode material prepared by sol–gel method,” *Molecular Crystals and Liquid Crystals*, vol. 695, pp. 10–18, 2019, doi: 10.1080/15421406.2020.1723901.

[77] M. P. Pechini, “Method of preparing lead and alkaline earth titanates and niobates and coating method using the same to form a capacitor.” 1967. Available: https://patents.google.com/patent/US3330697A/en

[78] Y. Luo, T. Lu, Y. Zhang, L. Yan, S. S. Mao, and J. Xie, “Surface-segregated, high-voltage spinel lithium-ion battery cathode material LiNi0.5Mn1.5O4 cathodes by aluminium doping with improved high-rate cyclability,” *Journal of Alloys and Compounds*, vol. 703, pp. 289–297, 2017, doi: https://doi.org/10.1016/j.jallcom.2017.01.248.

[79] D. P. Finegan *et al.*, “Characterising thermal runaway within lithium-ion cells by inducing and monitoring internal short circuits,” *Energy & Environmental Science*, vol. 10, pp. 1377–1388, Jun. 2017, doi: 10.1039/C7EE00385D.

[80] B. Barnett, “New directions in battery safety: Prospects for fail-safe lithium-ion,” Nov. 2010.

[81] Q. Wang, P. Ping, X. Zhao, G. Chu, J. Sun, and C. Chen, “Thermal runaway caused fire and explosion of lithium ion battery,” *Journal of Power Sources*, vol. 208, pp. 210–224, Jun. 2012, doi: 10.1016/J.JPOWSOUR.2012.02.038.

[82] Q. Wang, J. Sun, and C. Chen, “Effects of solvents and salt on the thermal stability of lithiated graphite used in lithium ion battery,” *Journal of Hazardous Materials*, vol. 167, pp. 1209–1214, Aug. 2009, doi: 10.1016/J.JHAZMAT.2009.01.125.

[83] S. Hess, M. Wohlfahrt-Mehrens, and M. Wachtler, “Flammability of li-ion battery electrolytes: Flash point and self-extinguishing time measurements,” *Journal of The Electrochemical Society*, vol. 162, pp. A3084–A3097, Jan. 2015, doi: 10.1149/2.0121502JES/XML.

[84] M. Kaliaperumal *et al.*, “Cause and mitigation of lithium-ion battery failure—a review,” *Materials 2021, Vol. 14, Page 5676*, vol. 14, p. 5676, Sep. 2021, doi: 10.3390/MA14195676.

[85] S. Feng, X. Kong, H. Sun, B. Wang, T. Luo, and G. Liu, “Effect of zr doping on LiNi0.5Mn1.5O4 with ordered or disordered structures,” *Journal of Alloys and Compounds*, vol. 749, pp. 1009–1018, Jun. 2018, doi: 10.1016/J.JALLCOM.2018.03.177.

[86] R. Spotnitz and J. Franklin, “Abuse behavior of high-power, lithium-ion cells,” *Journal of Power Sources*, vol. 113, pp. 81–100, Jan. 2003, doi: 10.1016/S0378-7753(02)00488-3.

[87] Z. Chen *et al.*, “Multi-scale study of thermal stability of lithiated graphite,” *Energy & Environmental Science*, vol. 4, pp. 4023–4030, Sep. 2011, doi: 10.1039/C1EE01786A.

[88] D. D. Macneil and J. R. Dahn, “Test of reaction kinetics using both differential scanning and accelerating rate calorimetries as applied to the reaction of li x CoO 2 in non-aqueous electrolyte,” 2001, doi: 10.1021/jp001187j.

[89] S. H. Troøyen and T. Lian, “Thermal stability of NMC442 cathode material studied by accelerating rate calorimetry,” Norwegian Defence Research Establishment, 2020.

[90] H. Konishi, M. Yoshikawa, and T. Hirano, “The effect of thermal stability for high-ni-content layer-structured cathode materials, LiNi0.8Mn0.1−xCo0.1MoxO2 (x = 0, 0.02, 0.04),” *Journal of Power Sources*, vol. 244, pp. 23–28, Dec. 2013, doi: 10.1016/J.JPOWSOUR.2013.05.004.

[91] P. Röder, N. Baba, K. A. Friedrich, and H. D. Wiemhöfer, “Impact of delithiated Li0FePO4 on the decomposition of LiPF6-based electrolyte studied by accelerating rate calorimetry,” *Journal of Power Sources*, vol. 236, pp. 151–157, Aug. 2013, doi: 10.1016/J.JPOWSOUR.2013.02.044.

[92] Jens. Als-Nielsen and Des. McMorrow, *Elements of modern x-ray physics*, 2nd edition. Wiley, 2011, pp. 32–35.

[93] V. Dyadkin, P. Pattison, V. Dmitriev, and D. Chernyshov, “A new multipurpose diffractometer PILATUS@SNBL,” *urn:issn:1600-5775*, vol. 23, pp. 825–829, Mar. 2016, doi: 10.1107/S1600577516002411.

[94] G. Will, “Powder diffraction: The rietveld method and the two stage method to determine and refine crystal structures from powder diffraction data,” *Powder Diffraction: The Rietveld Method and the Two Stage Method to Determine and Refine Crystal Structures from Powder Diffraction Data*, pp. 1–224, 2006, doi: 10.1007/3-540-27986-5.

[95] H. M. Rietveld, “The rietveld method,” *Physica Scripta*, vol. 89, p. 098002, Aug. 2014, doi: 10.1088/0031-8949/89/9/098002.

[96] R. A. Young, E. Prince, R. A. Sparks, and IUCr, “Suggested guidelines for the publication of rietveld analyses and pattern decomposition studies,” *urn:issn:0021-8898*, vol. 15, pp. 357–359, Jun. 1982, doi: 10.1107/S0021889882012138.

[97] E. Smith and G. Dent, *Modern raman spectroscopy - a practical approach.* John Wiley; Sons, 2005, pp. 1–210. doi: 10.1002/0470011831.

[98] N. H. Andersen, “Personal communication: Practical course in raman spectroscopy.” Jan. 2022.

[99] A. Ul-Hamid, “A beginners’ guide to scanning electron microscopy,” *A Beginners’ Guide to Scanning Electron Microscopy*, 2018, doi: 10.1007/978-3-319-98482-7.

[100] L. Reimer, “Scanning electron microscopy,” vol. 45, 1998, doi: 10.1007/978-3-540-38967-5.

[101] M. Jensen, “UiO course: KJM3120 - inorganic materials chemistry.” Unpublished, 2020.

[102] M. N. Richard and J. R. Dahn, “Accelerating rate calorimetry study on the thermal stability of lithium intercalated graphite in electrolyte. I. experimental,” *Journal of The Electrochemical Society*, vol. 146, pp. 2068–2077, Jun. 1999, doi: 10.1149/1.1391893/XML.

[103] R. C. Shurtz, Y. Preger, L. Torres-Castro, J. Lamb, J. C. Hewson, and S. Ferreira, “Perspective{—}from calorimetry measurements to furthering mechanistic understanding and control of thermal abuse in lithium-ion cells,” *Journal of The Electrochemical Society*, vol. 166, pp. A2498–A2502, 2019, doi: 10.1149/2.0341912jes.

[104] J. Leitner, P. Voňka, D. Sedmidubský, and P. Svoboda, “Application of neumann–kopp rule for the estimation of heat capacity of mixed oxides,” *Thermochimica Acta*, vol. 497, pp. 7–13, 2010, doi: https://doi.org/10.1016/j.tca.2009.08.002.

[105] J. Leitner, P. Chuchvalec, D. Sedmidubský, A. Strejc, and P. Abrman, “Estimation of heat capacities of solid mixed oxides,” *Thermochimica Acta*, vol. 395, pp. 27–46, 2002, doi: https://doi.org/10.1016/S0040-6031(02)00177-6.

[106] S. K. Kauwe, J. Graser, A. Vazquez, and T. D. Sparks, “Machine learning prediction of heat capacity for solid inorganics,” *Integrating Materials and Manufacturing Innovation*, vol. 7, pp. 43–51, Jun. 2018, doi: 10.1007/s40192-018-0108-9.

[107] B. Millard, *Physical chemistry for colleges: A course of instruction based upon the fundamental laws of chemistry.* McGraw-Hill book Company, Incorporated, 1921, p. 96. Available: https://books.google.no/books?id=oYE6AAAAMAAJ

[108] P. Gotcu and H. J. Seifert, “Thermophysical properties of LiCoO2-LiMn2O4 blended electrode materials for li-ion batteries,” *Physical Chemistry Chemical Physics*, vol. 18, pp. 10550–10562, Apr. 2016, doi: 10.1039/c6cp00887a.

[109] A. V. Knyazev *et al.*, “Study of the phase transition and thermodynamic functions of LiMn2O4,” *Thermochimica Acta*, vol. 593, pp. 58–64, 2014, doi: https://doi.org/10.1016/j.tca.2014.08.020.

[110] D. D. MacNeil and J. R. Dahn, “The reaction of charged cathodes with nonaqueous solvents and electrolytes: II. LiMn[sub 2]o[sub 4] charged to 4.2 v,” *Journal of The Electrochemical Society*, vol. 148, p. A1211, Sep. 2001, doi: 10.1149/1.1407246/XML.

[111] H. F. Xiang *et al.*, “Thermal stability of LiPF6-based electrolyte and effect of contact with various delithiated cathodes of li-ion batteries,” *Journal of Power Sources*, vol. 191, pp. 575–581, Jun. 2009, doi: 10.1016/J.JPOWSOUR.2009.02.045.

[112] D. Chernyshov, V. Dyadkin, H. Emerich, G. Valkovskiy, C. J. Mcmonagle, and W. V. Beek, “On the resolution function for powder diffraction with area detectors,” *research papers Acta Cryst*, vol. 77, pp. 497–505, 2021, doi: 10.1107/S2053273321007506.

[113] R. B. V. Dreele, M. R. Suchomel, and B. H. Toby, “Compute x-ray absorption,” Feb. 2013, Available: https://11bm.xray.aps.anl.gov/absorb/absorb.php?

[114] A. Raniseth and M. Rødne, “Ecdh.” 2022. Available: https://github.com/amundmr/ecdh

[115] K. Ariyoshi, Y. Iwakoshi, N. Nakayama, and T. Ohzuku, “Topotactic two-phase reactions of li [ Ni1 / 2Mn3 / 2 ] o 4 ( P4332 ) in nonaqueous lithium cells,” *Journal of The Electrochemical Society*, vol. 151, p. A296, Jan. 2004, doi: 10.1149/1.1639162.

[116] J. H. Kim, S. T. Myung, C. S. Yoon, S. G. Kang, and Y. K. Sun, “Comparative study of LiNi0.5Mn1.5O 4- and LiNi0.5Mn1.5O4 cathodes having two crystallographic structures: Fd3m and P4332,” *Chemistry of Materials*, vol. 16, pp. 906–914, Mar. 2004, doi: 10.1021/CM035050S/ASSET/IMAGES/LARGE/CM035050SF00015.JPEG.

[117] M. Tetenbaum and C. E. Johnson, “Vaporization behavior of lithium oxide: Effect of water vapor in helium carrier gas,” *Journal of Nuclear Materials*, vol. 120, pp. 213–216, Apr. 1984, doi: 10.1016/0022-3115(84)90058-8.

[118] A. V. D. Ven, J. Bhattacharya, and A. A. Belak, “Understanding li diffusion in li-intercalation compounds,” *Accounts of Chemical Reseach*, 2011, doi: 10.1021/ar200329r.

[119] X. Xu *et al.*, “Application of high-spatial-resolution secondary ion mass spectrometry for nanoscale chemical mapping of lithium in an al-li alloy,” *Materials Characterization*, vol. 181, p. 111442, Nov. 2021, doi: 10.1016/J.MATCHAR.2021.111442.

[120] B. Aktekin *et al.*, “How mn/ni ordering controls electrochemical performance in high-voltage spinel LiNi0.44Mn1.56O4with fixed oxygen content,” *ACS Applied Energy Materials*, vol. 3, pp. 6001–6013, Jun. 2020, doi: 10.1021/ACSAEM.0C01075/ASSET/IMAGES/LARGE/AE0C01075_0007.JPEG.

[121] S. K. Mylavarapu *et al.*, “Effect of TiO xSurface modification on the electrochemical performances of ni-rich (NMC-622) cathode material for lithium-ion batteries,” *ACS Applied Energy Materials*, vol. 4, pp. 10493–10504, Oct. 2021, doi: 10.1021/ACSAEM.1C01309/ASSET/IMAGES/LARGE/AE1C01309_0009.JPEG.

[122] P. M. Attia, S. Das, S. J. Harris, M. Z. Bazant, and W. C. Chueh, “Electrochemical kinetics of SEI growth on carbon black: Part i. experiments,” *Journal of The Electrochemical Society*, vol. 166, pp. 97–106, 2019, doi: 10.1149/2.0231904jes.

[123] C. Liu, Z. G. Neale, and G. Cao, “Understanding electrochemical potentials of cathode materials in rechargeable batteries,” *Materials Today*, vol. 19, pp. 109–123, Mar. 2016, doi: 10.1016/J.MATTOD.2015.10.009.

[124] C. Mao, R. E. Ruther, J. Li, Z. Du, and I. Belharouak, “Identifying the limiting electrode in lithium ion batteries for extreme fast charging,” *Electrochemistry Communications*, vol. 97, pp. 37–41, Dec. 2018, doi: 10.1016/J.ELECOM.2018.10.007.

[125] W. M. Frank, “Characteristics of carbon black dust as a large-scale tropospheric heat source,” *Atmospheric Science*, p. 4, Jan. 1973, Available: https://mountainscholar.org/bitstream/handle/10217/324/0195_Bluebook.pdf?sequence=1

[126] Fluorotherm, “PVDF properties.”

[127] NIST, “1,3-dioxolan-2-one.” NIST. Available: https://webbook.nist.gov/cgi/inchi/InChI=1S/C3H4O3/c4-3-5-1-2-6-3/h1-2H2

[128] Y. Zhou, J. Wu, and E. W. Lemmon, “Thermodynamic properties of dimethyl carbonate *,” 2011, doi: 10.1063/1.3664084.

# Appendix A

# Calculations

## A.1 Energy density and material use in cathode materials

**NMC811** has a reversible capacity of 190mAh/g [124]. With a nickel mass percentage of

$$\frac{0.8 * 58.693}{6.94 + 0.8 * 58.693 + 0.1 * 54.938 + 0.1 * 58.933 + 2 * 15.99} = 48.27$$

this leads to a nickel use of

$$\frac{0.4827}{190Ah/kg} = 2.54e - 3kg_{Ni}/Ah$$

Which with the 4.0 V nominal capacity of NMC leads to a nickel use per energy capacity (kWh) of 0.635 kg/kWh.

**LMNO** has a reversible capacity of 130 mAh/g. With a nickel mass percentage of

$$\frac{0.5 * 58.693}{6.94 + 0.5 * 58.693 + 1.5 * 54.938 + 4 * 15.99} = 16.07$$

this leads to a nickel use of

$$\frac{0.1607}{130Ah/kg} = 1.236e - 3kg_{Ni}/Ah$$

Which with the 4.7V nominal capacity of LMNO leads to a nickel use per energy capacity (kWh) of 0.263 kg/kWh.

## A.2 Rietveld refinements

Figure A.1 below shows the refinement of pristine LMNO where only the disordered spinel and the disordered rocksalt has been included as structural phases. This was done because fitting the perfectly ordered LMNO structure yielded issues with the superstructure peaks not being high enough for the least squares method to evaluate higher than e.g. the background.

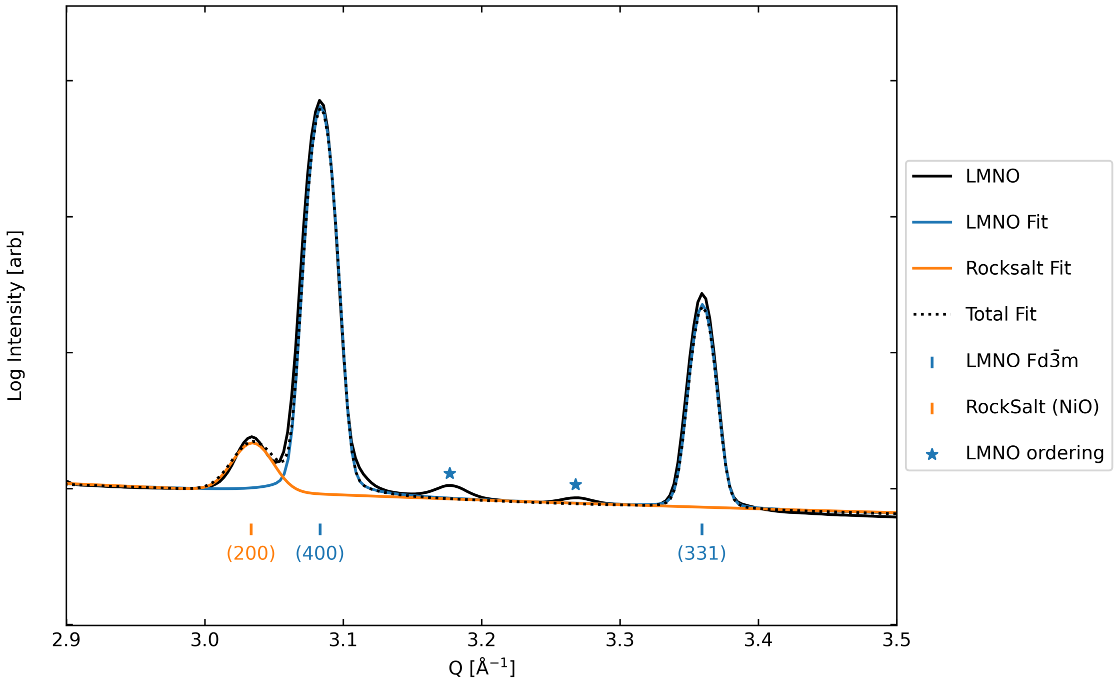

Figure A.1: Fitting of disordered LMNO and rocksalt phase to pristine LMNO synchrotron XRD data.

Rietveld refinements done in TOPASv6 seemed to yield quite accurate results for most samples. This is quality assued by the $R_{wp}$ value and most importantly, visual inspection.

## A.3 Accelerated Rate Calorimetry

The specific heat capacity of a delithiated LANMO sample is calculated by equation 2.24:

$$C = 904 \text{ J/kgK} \cdot f_{Al} + 445 \text{ J/kgK} \cdot f_{Ni} + 479 \text{ J/kgK} \cdot f_{Mn} + 919 \text{ J/kgK} \cdot f_O.$$

For $Li_0Al_0Ni_{0.5}Mn_{1.5}O_4$, the stoichiometry times the atomic mass can serve as the weight ratio, where the denominator is just the normalization factor of the mass ratios:

$$C = \frac{904 \text{ J/kgK} \cdot 0 + 445 \text{ J/kgK} \cdot 0.5 \cdot 58.7u + 479 \text{ J/kgK} \cdot 1.5 \cdot 54.9u + 919 \text{ J/kgK} \cdot 4 \cdot 16u}{0 + 0.5 \cdot 58.7u + 1.5 \cdot 54.9u + 4 \cdot 16u}$$

$$C \approx 633.6J/kgK$$

In addition to this, the powdermix on the cathode includes conductive additive and binder. In this thesis, Carbon Super P (CSP) and PVDF is used, which have heat capacities of 523J/kgK [125] and 1500J/kgK [126] respectively.

With a mass ratio of 8:1:1 of active material, conductive additive and binder, the total heat capacity will be

$$\begin{aligned} C_{tot} &= 0.8 * C_{LANMO} + 0.1 * C_{CSP} + 0.1 * C_{PVDF} \\ &= 0.8 * 633.6 + 0.1 * 532 + 0.1 * 1500 \\ &= 710.1 J/kgK \end{aligned}$$

Electrolyte (LP30) heat capacity: EC(150 J/molK or 1700$J/kgK$ [127]) DMC ( 140J/molK or 1556J/kgK)[128]. For a 1:1 (v:v) mixture of them, the resulting heat capacity, $C_p$ = 1628J/kgK. Although the effect of the 1M $LiPF_6$ salt is unaccounted for. These numbers were not used in the calculations and is purely as reference and insight into how the phi factor changes if electrolyte is included in the calculation.

The mass of needed material for a $\phi$-factor of 3 with the following sample holder: Stainless steel (SS) tubes (ARC-ES-1750, ~ 1.32g, 5.5cm length, 0.15 mm wall thickness, welded on one side, heat capacity 0.5J/K) and an aluminum clip for the temperature sensor (0.32g of 900J/kgK = 0.288J/K). This gives the total sampleholder the heat capacity of 0.788J/K

We can find the mass needed by using equation 2.23:

$$\begin{aligned} m_{s \text{ (cathode material)}} &= \frac{m_b c_b}{(\phi - 1) \cdot c_s} \\ &= \frac{0.788 J/K}{(3-1) 710.1 J/kgK} * 1000g \\ &= 0.554g \end{aligned}$$

If we include electrolyte in the calculation with a 2:1 wt ratio of cathode material to electrolyte, we get:

$$\begin{aligned} m_{s \text{ (cathode material + electrolyte 2:1 by wt)}} &= \frac{m_b c_b}{(\phi - 1) \cdot c_s} \\ &= \frac{0.788 J/K}{(3-1) \cdot \frac{2 \cdot 710.1 J/kgK + 1628 J/kgK}{3}} * 1000g \\ &= 0.388g \end{aligned}$$

## A.4 Quantitative analysis of ARC: the Arrhenius equation

Richard and Dahn [102] demonstrated in 1999 that the thermal triplets, rate constant $k$, activation energy $E_a$ and frequency factor $A$ can be determined for specific reactions by the use of ARC. This was done by heating the sample to different temperatures exceeding the reaction onset before starting the measurements in order to gather rate constants for different temperatures. They showed that the self-heating rate can be written on the form

$$\frac{dT}{dt} = \frac{h}{C} A e^{\frac{-E_a}{k_B T}} x^n \tag{A.1}$$

where $h$ is the heat of reaction, $C$ is the specific heat (together constituting $h/C$, the temperature increase from the reactions of all reactant), $A$ is the frequency factor, $E_a$ is the activation energy, $k_B$ the Boltzmann constant and T the temperature. $x$ is the concentration of the reactant and $n$ is the reaction order. This equation was built from the Arrhenius equation A.2 by inserting it for the rate constant in the equation for consumption of reactant A.3 which is then inserted into the self heating rate described in equation A.4.

$$k = Ae^{\frac{-E_a}{k_B T}} \tag{A.2}$$

$$\frac{dx}{dt} = -kx^n \tag{A.3}$$

$$\frac{dT}{dt} = \frac{h}{C}\left|\frac{dx}{dt}\right| \tag{A.4}$$

By then setting the reactant concentration to 1, taking the logarithm of both sides of equation A.1 and plotting the ARC data on the form $ln\left(\frac{dT}{dt}\right)$ versus the inverse temperature, $\frac{1}{T}$, the activation energy $E_a$ can be found from the slope of the exotherms while the frequency factor can be found from the slope crossing of the y-axis. Although they showed this to work for their graphite anode scenario, there are many complicating factors. Some of them are: Setting the concentration of reactants to 1, the possibility of having multiple overlapping reactions and the reproducibility of an experiment being difficult.

# Appendix B

# Supplementary Data

## B.1 Naming scheme

The naming scheme used in my personal documents are a bit more complex than what has been used in the results and discussion section in order to have full traceability of data. It is constructed from the unique identifier for the synthesis $x$, the amount of aluminum doping $y$ and which element was targeted substituted (by the position of $y$) as shown in equation B.1 below.

$$x\_\mathrm{LA}y\mathrm{MNO} \tag{B.1}$$

For example the pure $LiMn_{1.5}Ni_{0.5}O_4$ is named 6_LMNO, and $LiMn_{1.5}Al_{0.2}Ni_{0.3}O_4$ is named 14_LMA2NO showing that 0.2 formula units of nickel were attempted substituted by aluminum. Table B.1 below shows an overview of the sample names and the attempted stoichiometry.

Table B.1: Naming scheme of synthesized samples

| **Stoichi. subst.** | **Mn subst.** | **Ni subst.** | **50/50** |
|---|---|---|---|
| 0.05 | $LiAl_{0.05}Mn_{1.45}Ni_{0.5}O_4$<br>7_LA05MNO<br>$Al_{0.05}$-Mn | $LiMn_{1.5}Al_{0.05}Ni_{0.45}O_4$<br>8_LMA05NO<br>$Al_{0.05}$-Ni | $Al_{0.05}LiMn_{1.475}Ni_{0.475}O_4$<br>9_A05LMNO<br>$Al_{0.05}$-Mn/Ni |
| 0.1 | $LiAl_{0.1}Mn_{1.4}Ni_{0.5}O_4$<br>10_LA1MNO<br>$Al_{0.1}$-Mn | $LiMn_{1.5}Al_{0.1}Ni_{0.4}O_4$<br>11_LMA1NO<br>$Al_{0.1}$-Ni | $Al_{0.1}LiMn_{1.45}Ni_{0.45}O_4$<br>12_A1LMNO<br>$Al_{0.1}$-Mn/Ni |
| 0.2 | $LiAl_{0.2}Mn_{1.3}Ni_{0.5}O_4$<br>13_LA2MNO<br>$Al_{0.2}$-Mn | $LiMn_{1.5}Al_{0.2}Ni_{0.3}O_4$<br>14_LMA2NO<br>$Al_{0.2}$-Ni | $Al_{0.2}LiMn_{1.4}Ni_{0.4}O_4$<br>15_A2LMNO<br>$Al_{0.2}$-Mn/Ni |

For electrochemistry data, the electrode tape number and cell number is also appended to the sample name in order to have full traceability. An example of a coincell name can be:

$$14\_LMA2NO\_E1\_C3$$

which shows that this was the first usable electrode fabricated and the third cell.

## B.2 Synthesis

Figure B.1 shows the white dots found in the beaker of sample 7_LNA05MO ($Al_{0.05}$-Mn) after combustion.

Figure B.1: White spots in the beaker for the $Al_{0.05}$-sample after combustion.

## B.3 Powder X-Ray Diffraction

Below are plots with all diffractograms inserted.

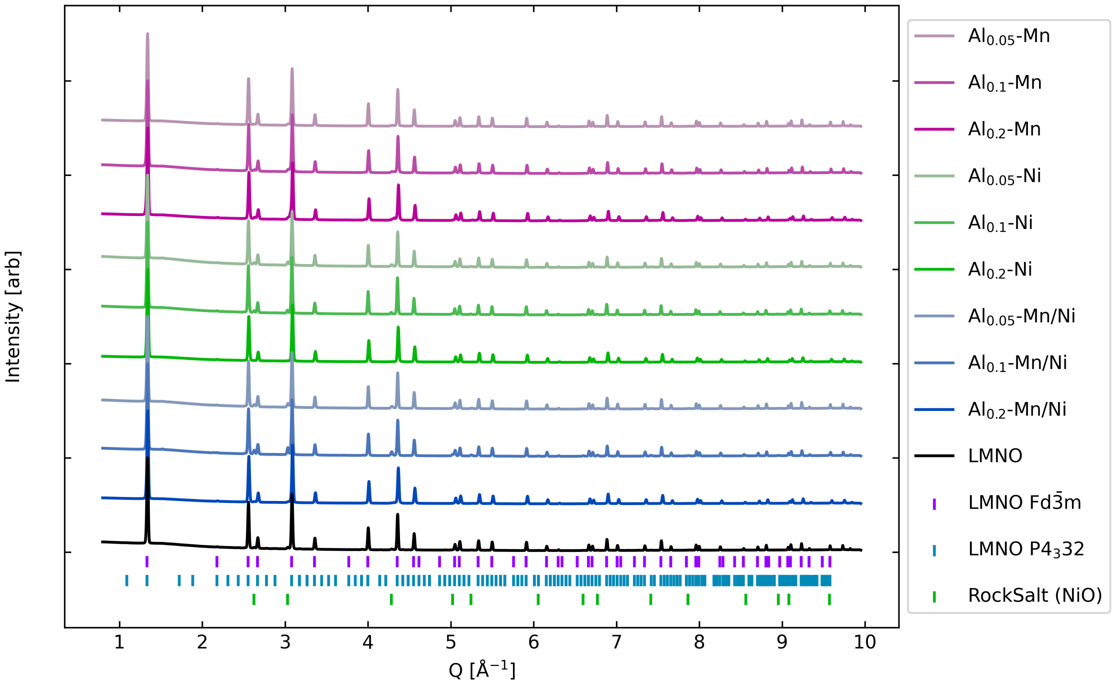

Figure B.2: Synchrotron XRD data for all pristine synthesized samples including hkl ticks for the disordered LMNO, ordered LMNO and the rocksalt impurity NiO.

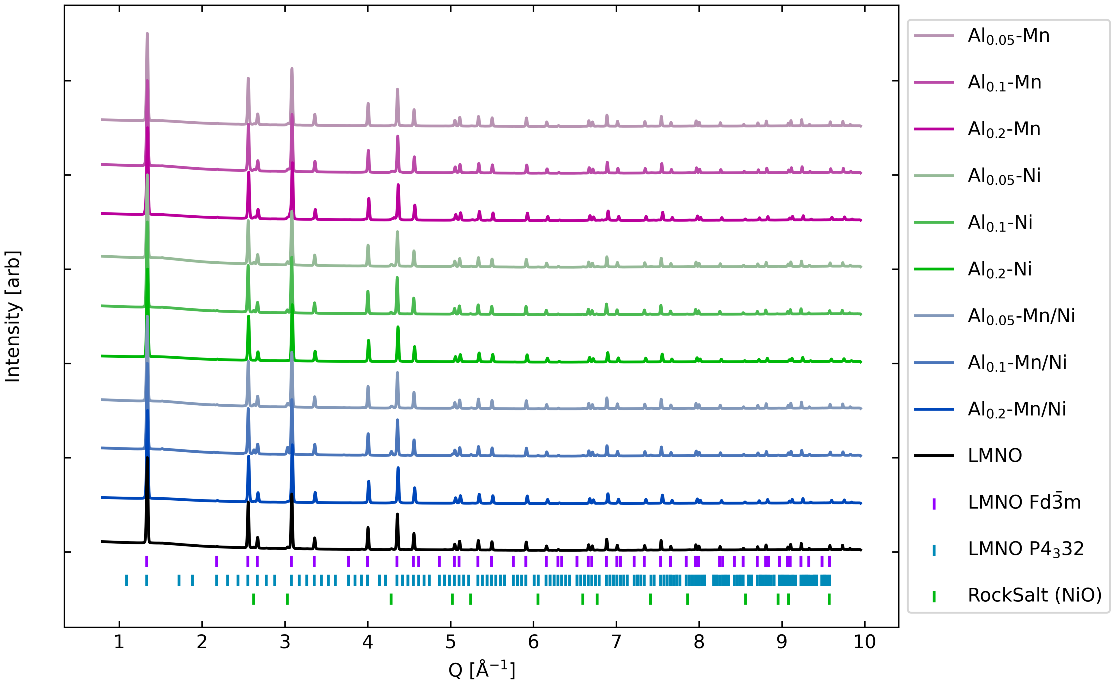

Figure B.3: Synchrotron XRD data for all pristine synthesized samples including hkl ticks for the disordered LMNO, ordered LMNO and the rocksalt impurity NiO zoomed in.

### B.3.1 Previous operando studies by Samarasingha et al.

The plots shown in figure B.4 have been reused from Samarasingha et als operando synchrotron work on LMNO [30] and shows how the disorder phase has more of a solid solution and three phase reaction with lithium intercalation (right side, b)) while the ordered LMNO has almost a pure three phase reaction.

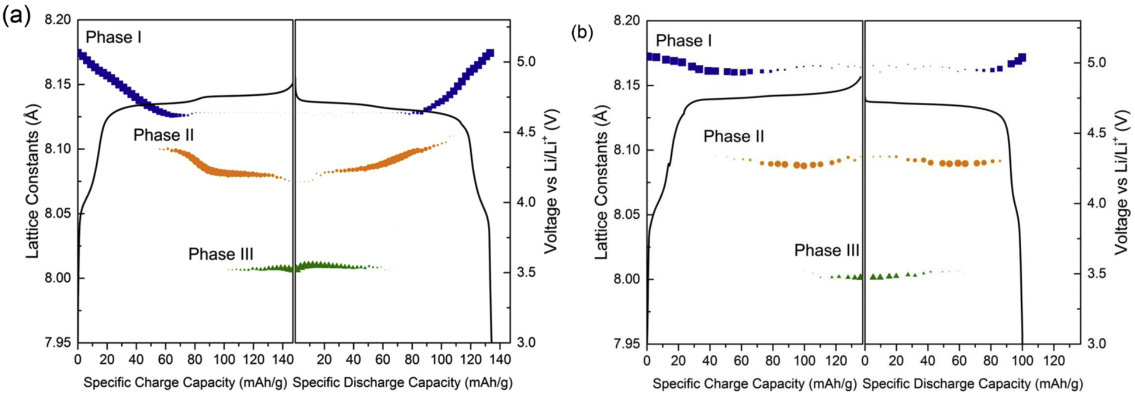

Figure B.4: a) Lattice parameter of disordered LMNO spinel during charge and discharge, and b) lattice parameter of ordered LMNO during charge and discharge.

### B.3.2 Quantification of the Aluminum content

Using TOPASv6, LMNO structure diffractograms were simulated at various aluminum substitution amounts ($\text{Al}_x \in \{0, 0.2, 0.4, 1.0\}$) and on two different sites, the Ni/Mn site (16d) and the Li site (8a). This was done to evaluate the possibility of detecting aluminum substitution using XRD with synchrotron data. This is visualized in figure B.5 below, where also the measurement data for the $\text{Al}_{0.2}$-Ni sample has been included in blue. From the figure, it is clearly evident that a substitution amount of 0.2 aluminium is way too low to be able to detect using Rietveld refinement on synchrotron XRD data.

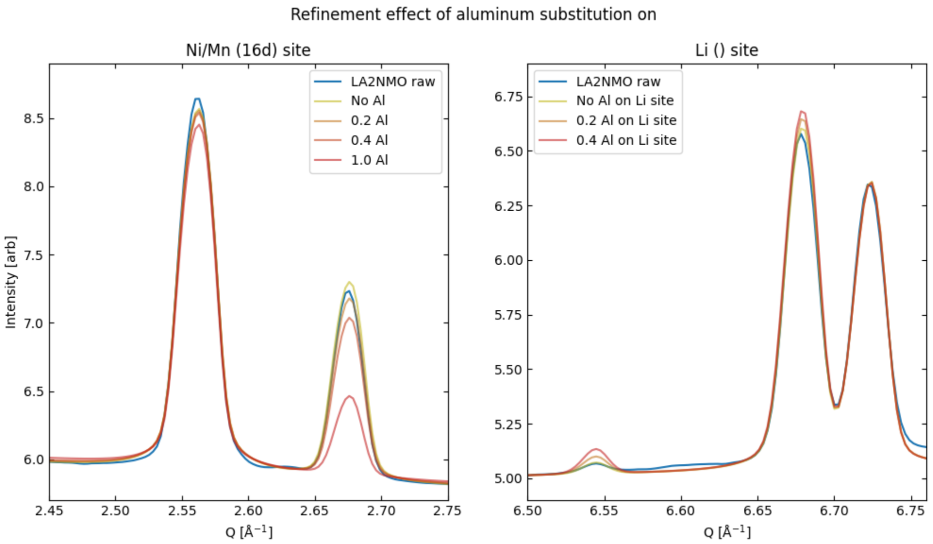

Figure B.5: Effect of Al subst in refinements

### B.3.3 Change in superstructure peaks with Aluminum substitution

Using TOPASv6, the $P4_332$ LMNO (ordered) structure was simulated with various amounts of aluminum substitutions on only nickel sites (4a) and manganese sites (12d). The result shows that the intensity of superstructure peaks should double when 0.2 aluminum is substituted for nickel, and decrease by 70% when substituted for manganese. This is shown in figure B.6 below.

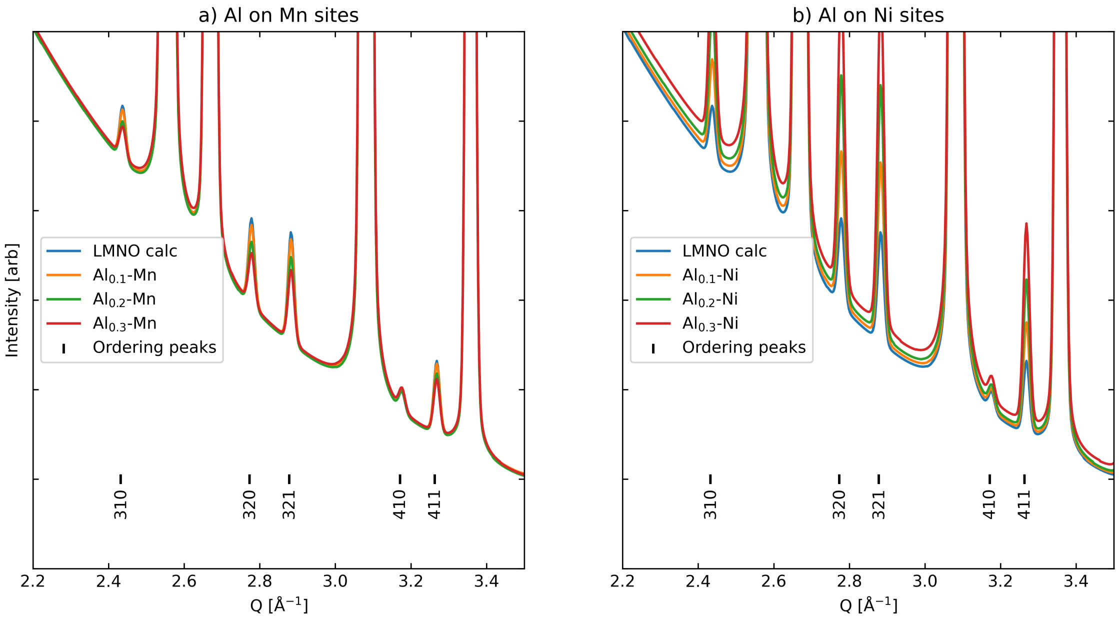

Figure B.6: Change in ordering peaks intensity of LMNO $P4_332$ phase when aluminum is substituted on a) manganese site or b) nickel site. Simulated using TOPASv6.

## B.4 Scanning Electron Microscopy

A grid of the different materials on different magnification levels (3k, 10k and 20k) can be visualized in figure B.7, B.8 and B.8 below. A commercial sample of LMNO and a commercial NMC sample (CustomCells NMC622) has also been included since accelerating rate calorimetry has been conducted on these samples as well.

Figure B.7: SEM micrographs of all pristine materials at 3k magnification

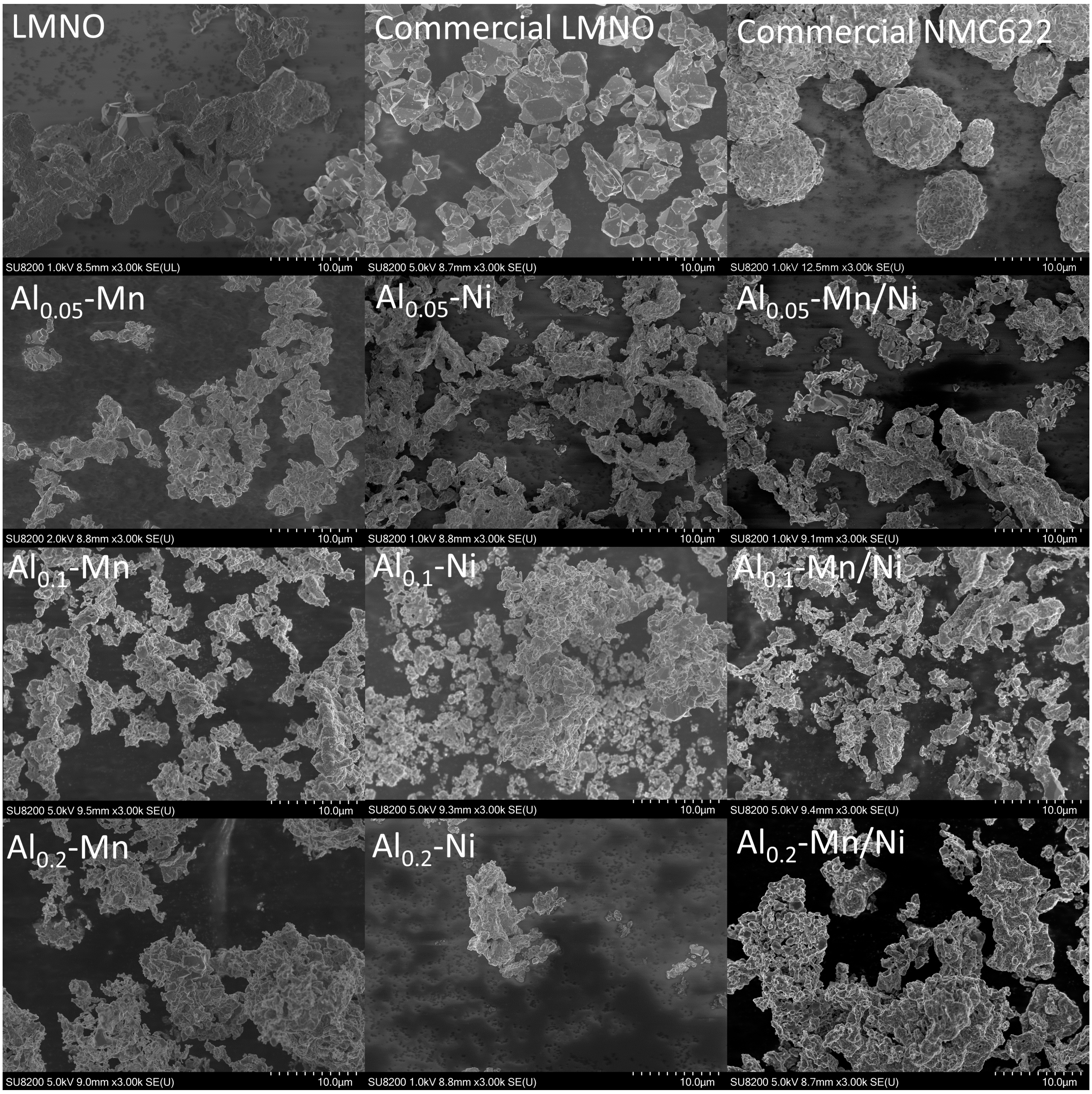

Figure B.8: SEM micrographs of all pristine materials at 10k magnification

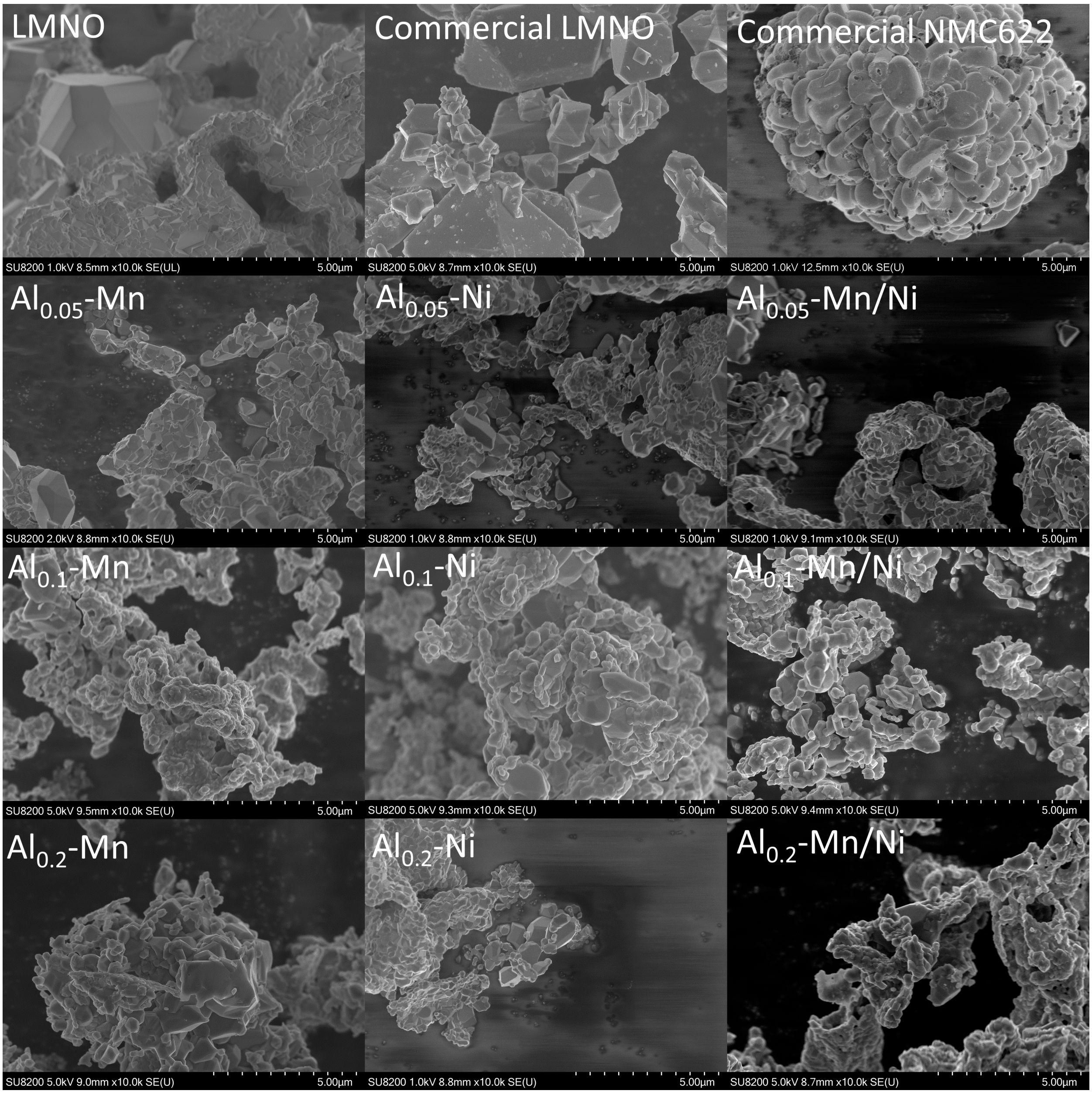

Figure B.9: SEM micrographs of all pristine materials at 20k magnification

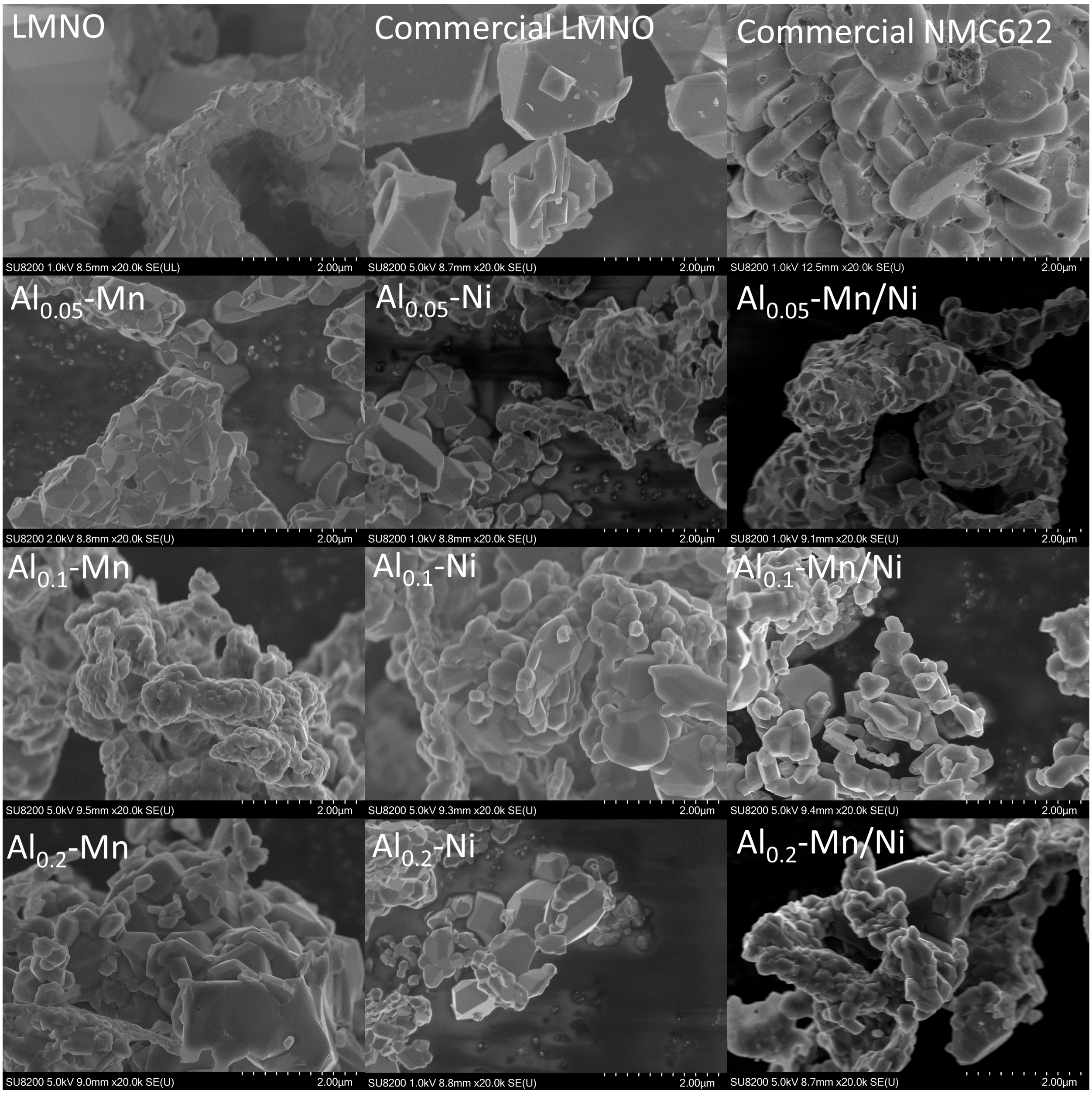

## B.5 Electrochemistry

### B.5.1 Galvanostatic cycling curves

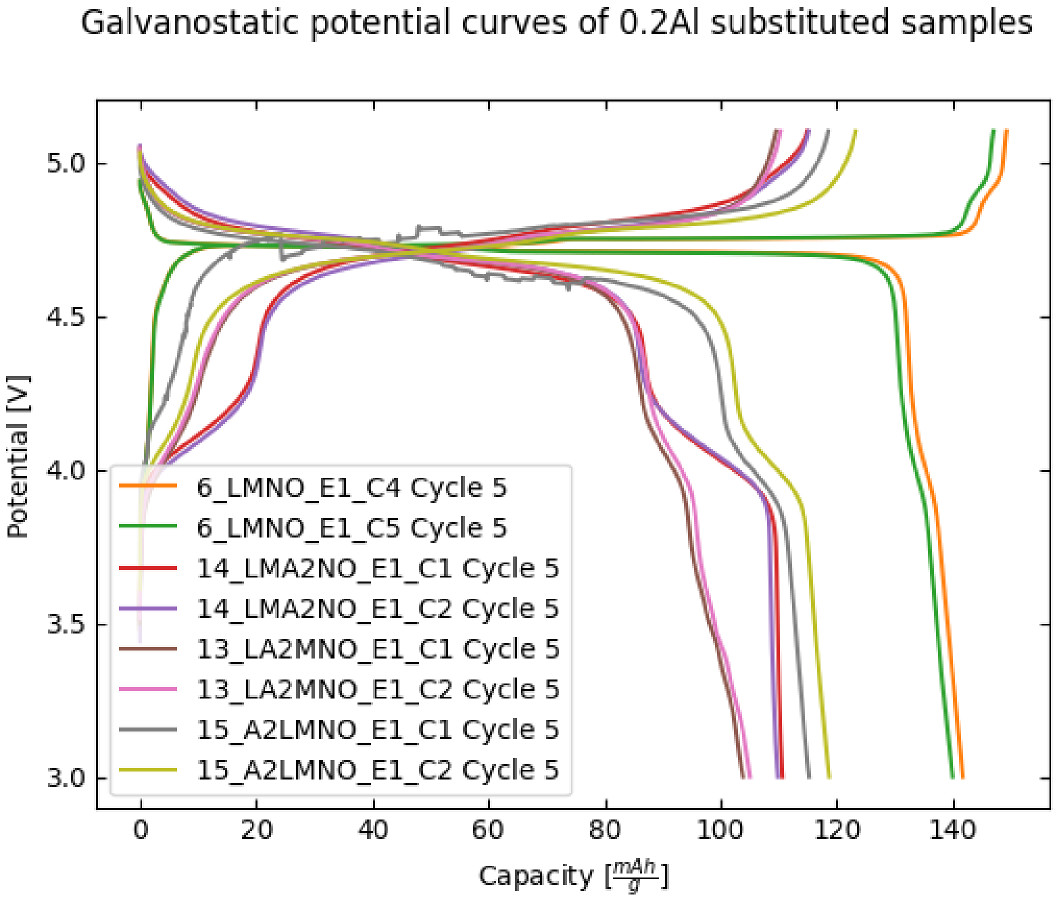

Figure B.10: Galvanostatic cycling curves of all 0.2Al substituted cells, plus pure LNMO at a C-rate of C/10.

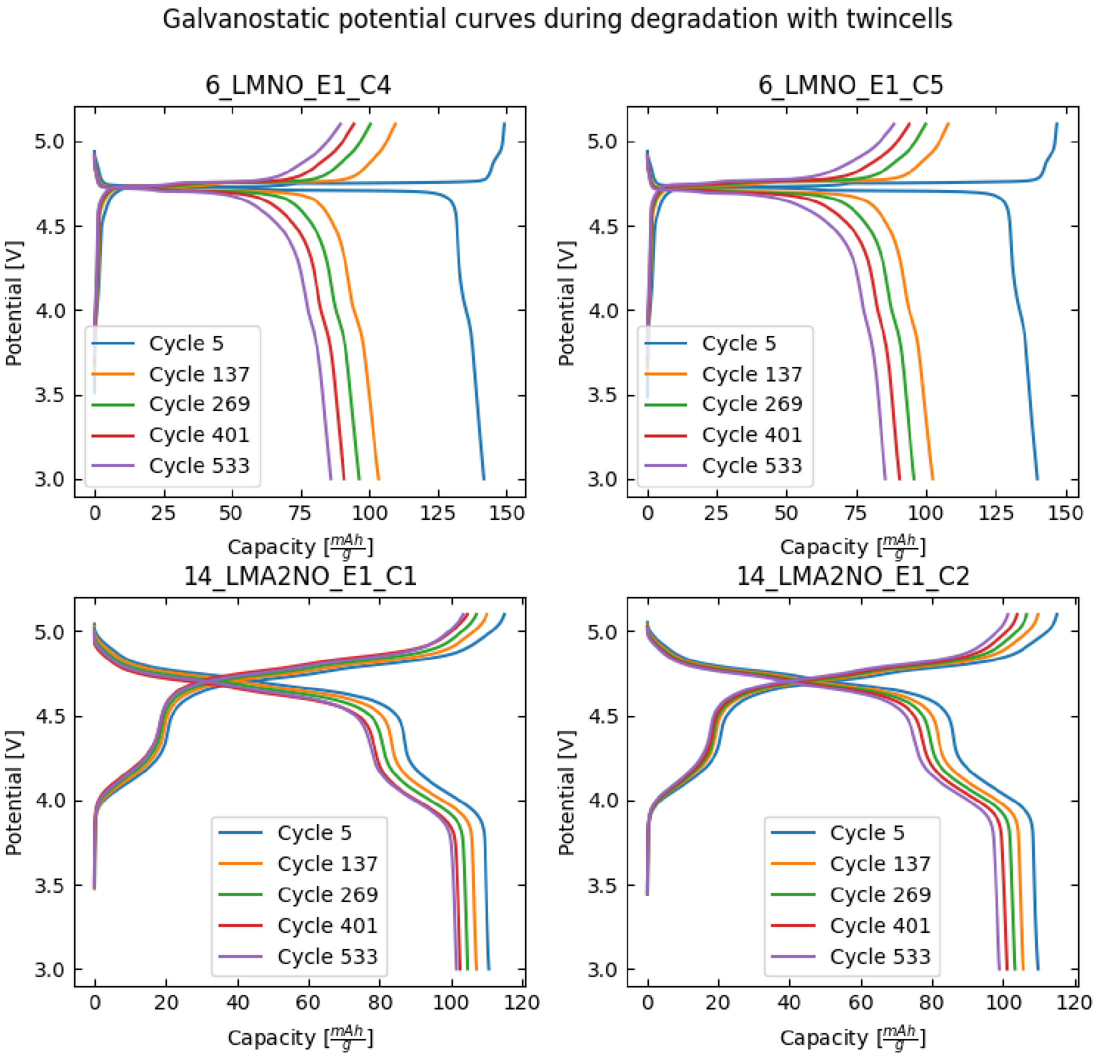

Figure B.11: Galvanostatic cycling curves during degradation with twin cell data. C-rate: C/10

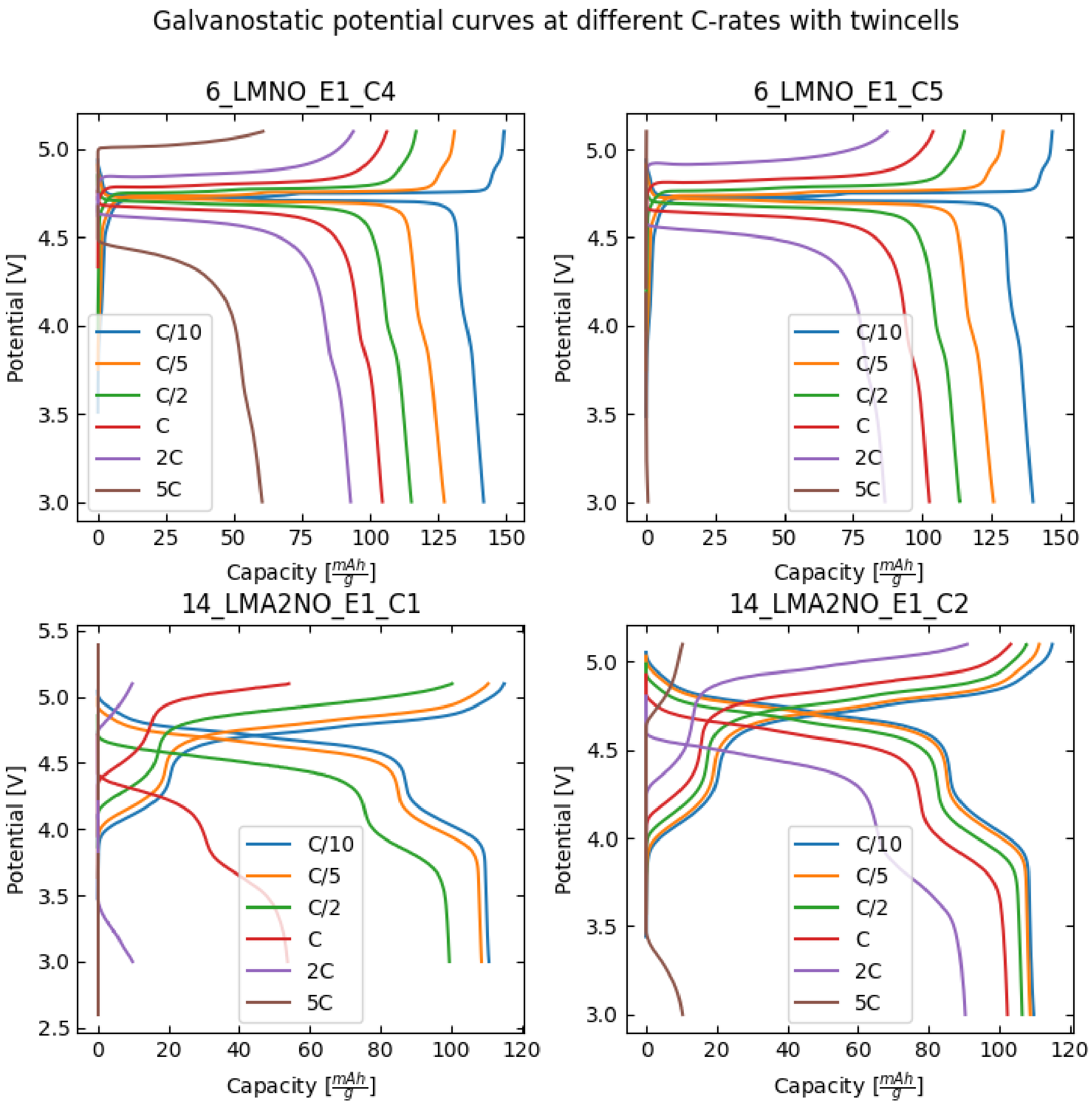

Figure B.12: Galvanostatic cycling curves at different C-rates with twin cell data

### B.5.2 Rate capability data

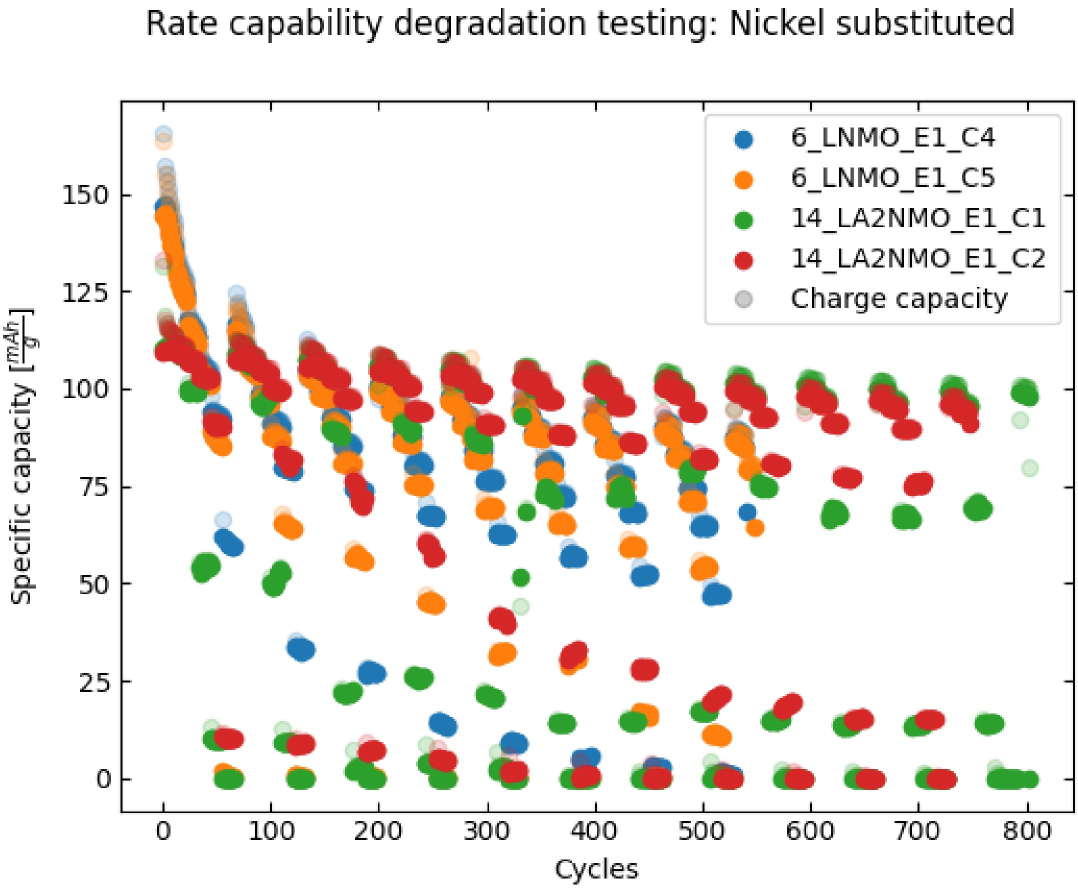

Figure B.13: Ratecapability degradation testing with both parallels of sample 14_LA2NMO included

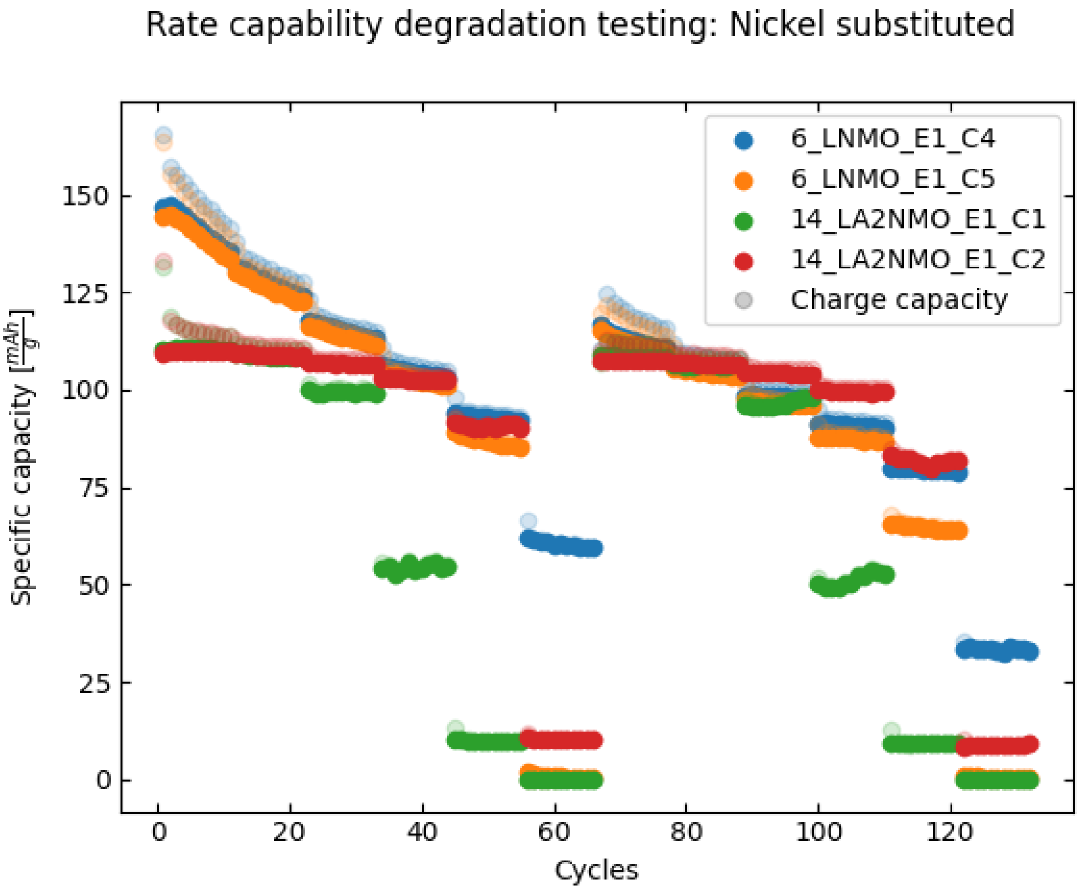

Figure B.14: Ratecapability testing with both parallels of sample 14_LA2NMO included

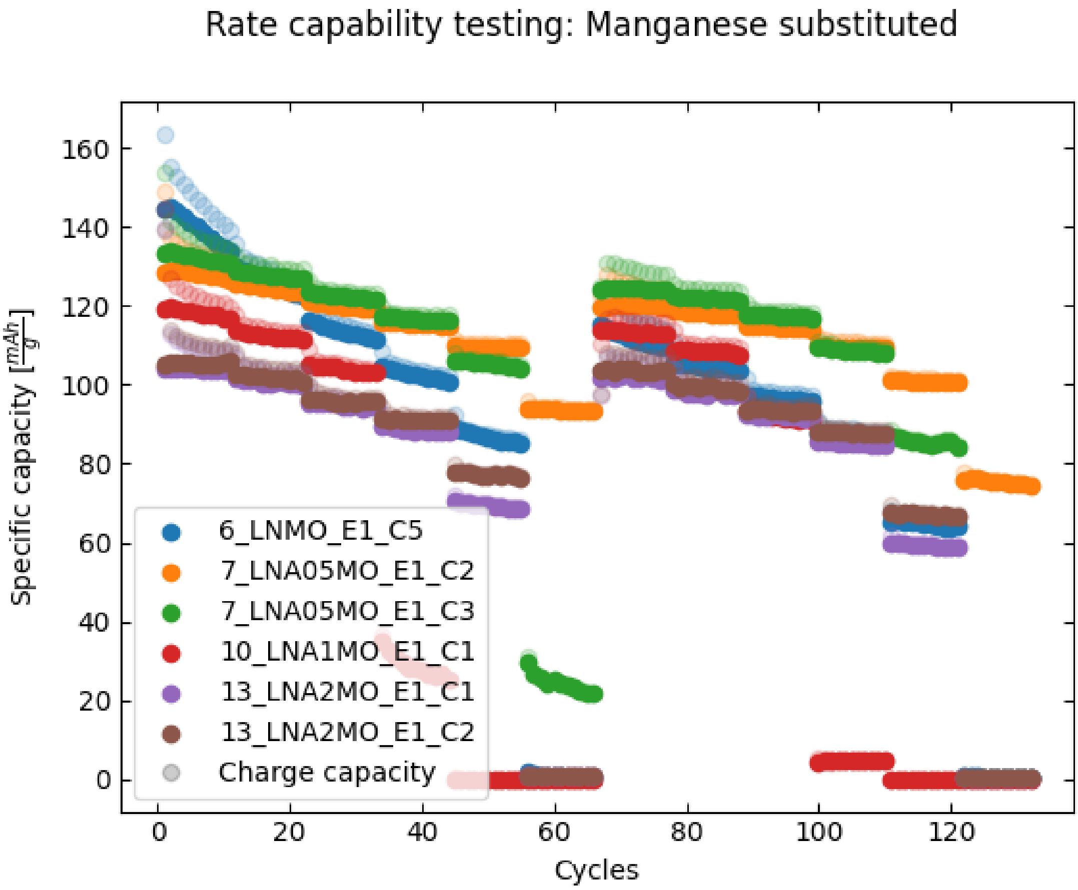

Figure B.15: Ratecapability testing with all parallels of all Mn substitution amounts.

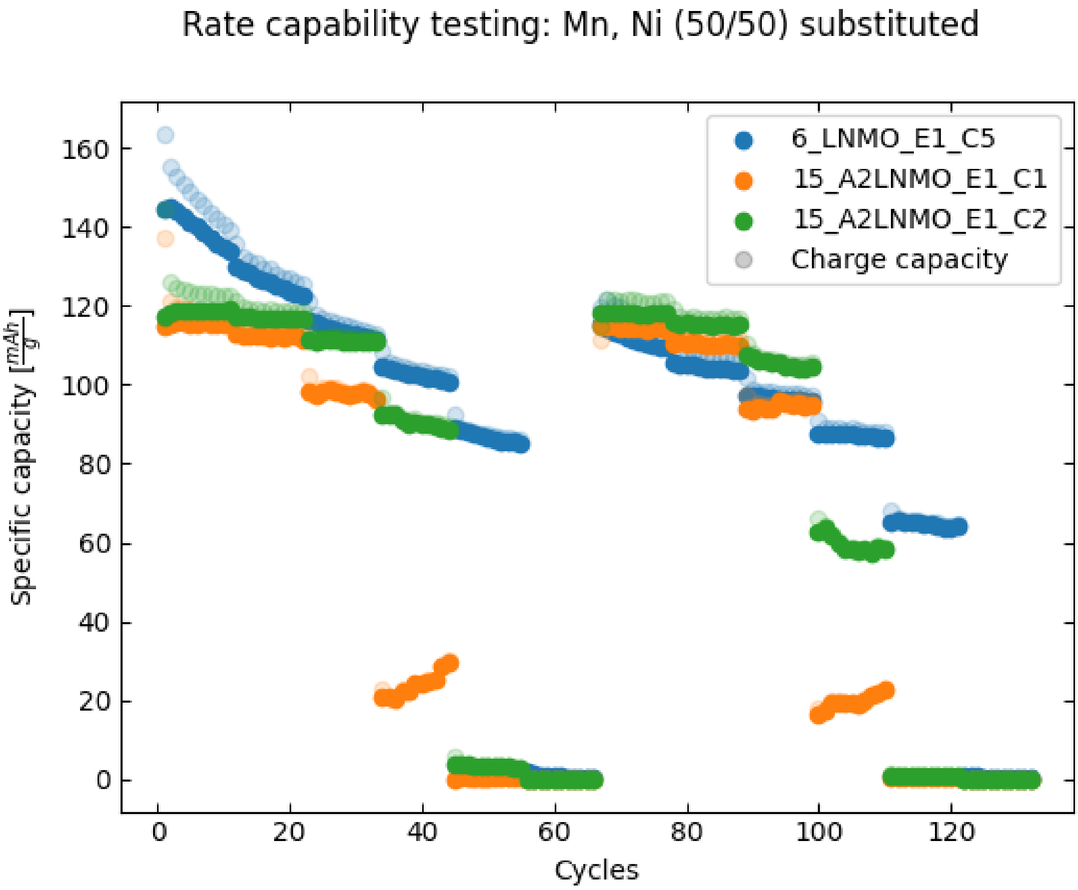

Figure B.16: Ratecapability testing with all parallels of sample 15_A2LNMO.

### B.5.3 Overview of cells used for electrochemical data viewing

Figure 4.13:

| **Cell name** | **Sample name used in figure** |
|---|---|
| 6_LMNO_E1_C4 | LMNO |
| 6_LMNO_E1_C5 | LMNO twin |
| 15_A2LMNO_E1_C1 | $Al_{0.2}$-Mn/Ni |
| 15_A2LMNO_E1_C2 | $Al_{0.2}$-Mn/Ni twin |

Figure 4.15:

| **Cell name** | **Sample name used in figure** |
|---|---|
| 6_LMNO_E1_C5 | LMNO |
| 13_LA2MNO_E1_C1 | $Al_{0.2}$-Mn |
| 14_LMA2NO_E1_C2 | $Al_{0.2}$-Ni |
| 15_A2LMNO_E1_C2 | $Al_{0.2}$-Mn/Ni |

Table 4.5:

| **Cell name** | **Sample name used in table** |
|---|---|
| 6_LMNO calc | LMNO calc |
| 6_LMNO_E1_C4 | LMNO |
| 6_LMNO_E1_C5 | LMNO twin |
| 13_LA2MNO calc | $Al_{0.2}$-Mn calc |
| 13_LA2MNO_E1_C1 | $Al_{0.2}$-Mn |
| 13_LA2MNO_E1_C2 | $Al_{0.2}$-Mn twin |
| 14_LMA2NO calc | $Al_{0.2}$-Ni calc |
| 14_LMA2NO_E1_C1 | $Al_{0.2}$-Ni |
| 14_LMA2NO_E1_C2 | $Al_{0.2}$-Ni twin |
| 15_A2LMNO calc | $Al_{0.2}$-Mn/Ni calc |
| 15_A2LMNO_E1_C1 | $Al_{0.2}$-Mn/Ni |
| 15_A2LMNO_E1_C2 | $Al_{0.2}$-Mn/Ni twin |

Figure 4.16:

| **Cell name** | **Sample name used in table** |
|---|---|
| 6_LMNO_E1_C5 | LMNO |
| 8_LMA05NO_E1_C2 | $Al_{0.05}$-Ni |
| 14_LMA2NO_E1_C2 | $Al_{0.2}$-Ni |

Figure 4.17, 4.18, 4.19 and 4.21:

| Cell name | Sample name used in table |
|---|---|
| 6_LMNO_E1_C5 | a) LMNO |
| 14_LMA2NO_E1_C2 | b) $Al_{0.2}$-Ni |

Figure 4.20:

| Cell name | Sample name used in table |
|---|---|
| 6_LMNO_E1_C5 | LMNO |
| 7_LA05MNO_E1_C3 | $Al_{0.05}$-Mn |
| 10_LA1MNO_E1_C1 | $Al_{0.1}$-Mn |
| 13_LA2MNO_E1_C1 | $Al_{0.2}$-Mn |

Figure **??**:

| Cell name | Sample name used in table |
|---|---|
| 6_LMNO_E1_C5 | LMNO twin |
| 15_A2LMNO_E1_C2 | $Al_{0.2}$-Mn/Ni twin |

### B.5.4 Accelerated degradation testing

Below in figure B.17 and B.18, the twin data for the accelerated degradation testing experiment can be found.

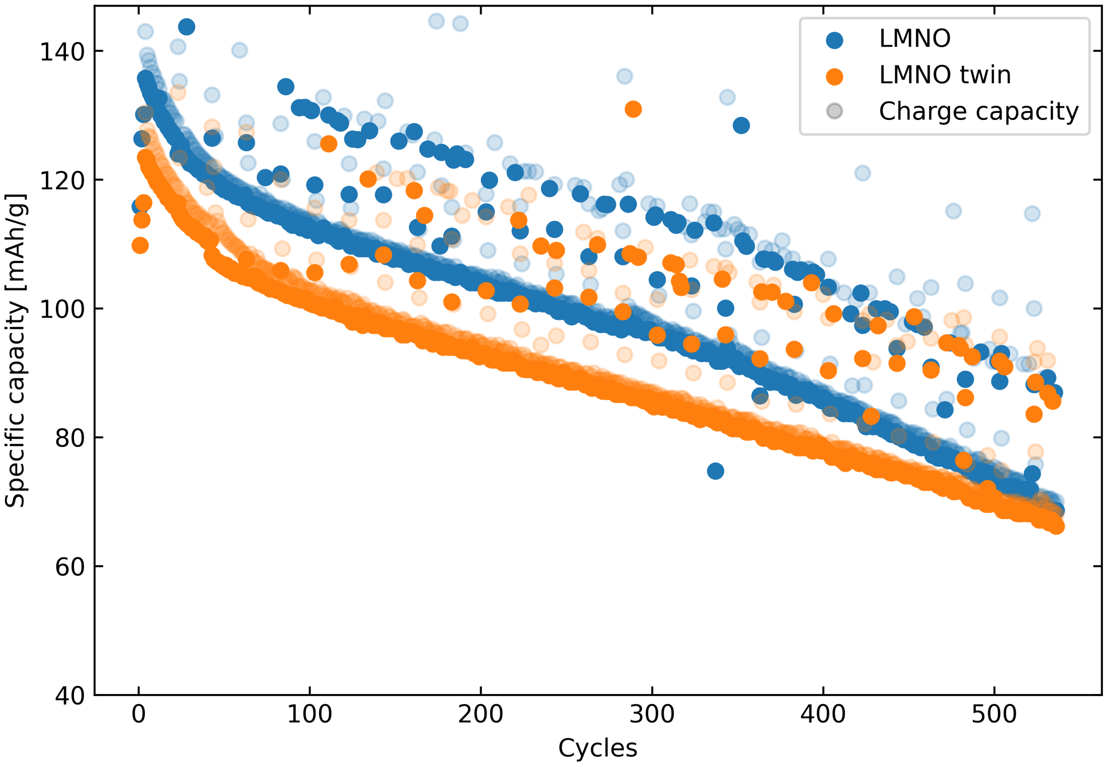

Figure B.17: Accelerated degradation testing twin data for LMNO

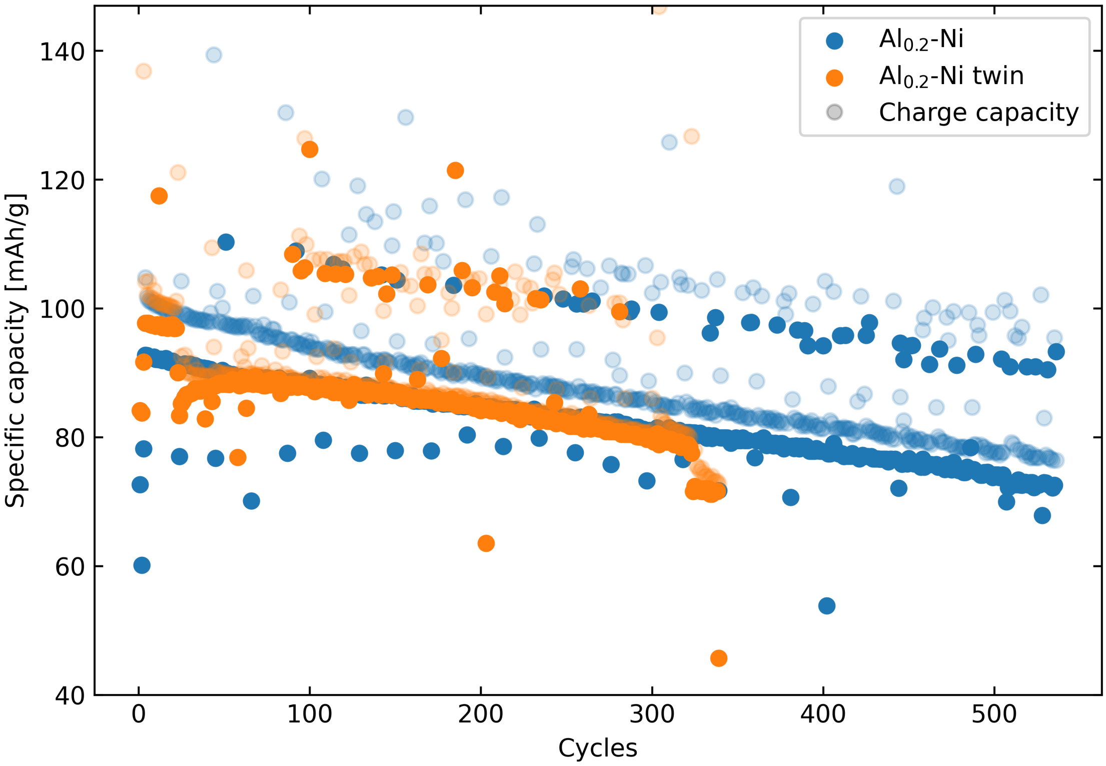

Figure B.18: Accelerated degradation testing twin data for $Al_{0.2}$-Ni

The cell names used for this datapresentation can be found in the table below.

| **Cell name** | **Sample name used in table** |
|---|---|
| 6_LNMO_E2_C2 | LMNO |
| 6_LNMO_E2_C1 | LMNO twin |
| 11_LA1NMO_E2_C1 | $Al_{0.1}$-Ni |
| 14_LA2NMO_E3_C1 | $Al_{0.2}$-Ni |
| 14_LA2NMO_E3_C4 | $Al_{0.2}$-Ni twin |

### B.5.5 Calculated theoretical capacities for the differently substituted compounds

Table B.10: Theoretical capacities of all samples calculated as explained in experimental section 3.7 from the measured weigh-in of precursors to the synthesis. All units are $\frac{mAh}{g}$

| **Sample** | **Ni**$^{2+\rightarrow 4+}$ | **Mn**$^{3+\rightarrow 4+}$ | **Mn**$^{4+\rightarrow 5+}$ | **Total (excl. Mn5+)** |
|---|---|---|---|---|
| 6_LMNO | 146.9 | -0.1 | 0.0 | 146.9 |
| 7_LA05MNO | 137.5 | 1.0 | 7.3 | 138.5 |
| 8_LMA05NO | 129.9 | 8.3 | 7.4 | 138.1 |
| 9_A05LMNO | 133.4 | 4.6 | 7.4 | 138.0 |
| 10_LA1MNO | 130.7 | 0.9 | 14.8 | 131.6 |
| 11_LMA1NO | 116.1 | 15.8 | 14.9 | 131.9 |
| 12_A1LMNO | 123.4 | 8.3 | 14.8 | 131.8 |
| 13_LA2MNO | 117.7 | 0.9 | 30.1 | 118.7 |
| 14_LMA2NO | 87.9 | 31.2 | 30.3 | 119.1 |
| 15_A2LMNO | 102.9 | 16.0 | 30.2 | 118.9 |

## B.6 Accelerated rate calorimetry

Table B.11: Names of the pouch cells and the names used in the figures in this thesis.

| **Pouch name** | **Sample name used in table** |
|---|---|
| P6_6_LMNO | LMNO test |
| P17_6_LMNO | LMNO |
| P12_6_LMNO | LMNO twin |
| P16_14_LMA2NO | $Al_{0.2}$-Ni |
| P14_14_LMA2NO | $Al_{0.2}$-Ni twin |
| P7_NMC | NMC 1 |
| P9_NMC | NMC 2 |

| Pouch name | Sample name used in table |
|---|---|
| P10_NMC | NMC 3 |
| P5_SecretLMNO | Commercial LMNO |

Di-tert-butyl peroxide (DTBP) in toulene calibration test and drift tests conducted for the ARC experiments are shown in figure B.19 below. The two parallels of sample 14_LMA2NO is found in figure B.20 below.

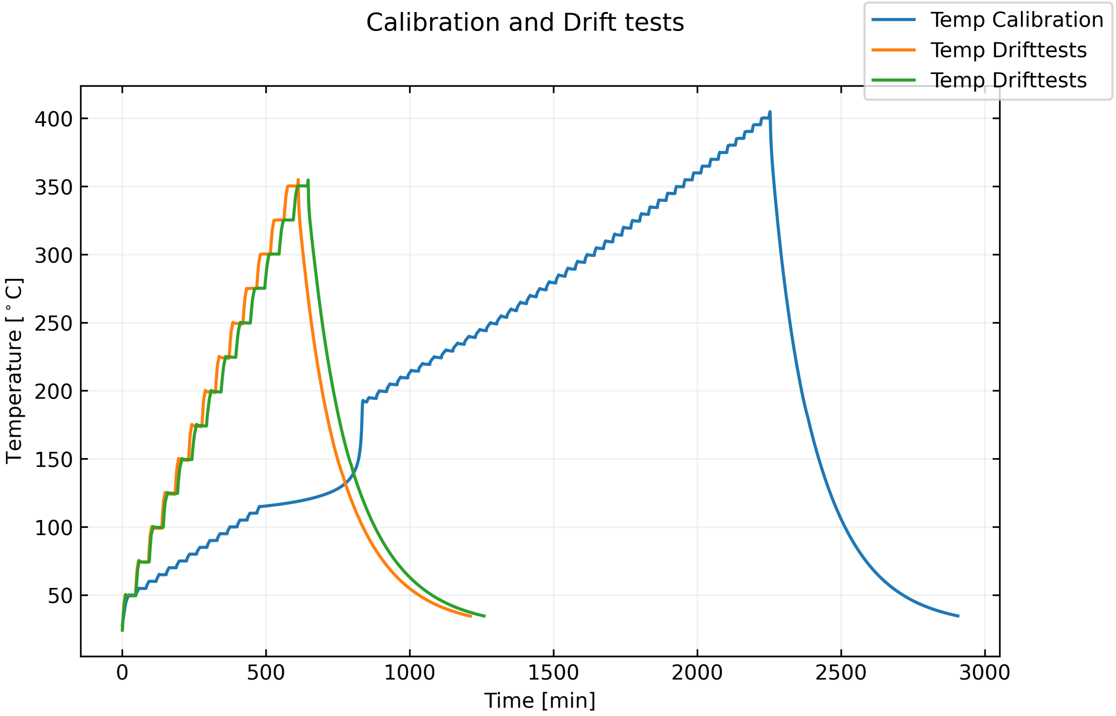

Figure B.19: Di-tert-butyl peroxide (DTBP) in toulene calibration test and drift tests conducted for the ARC experiments.

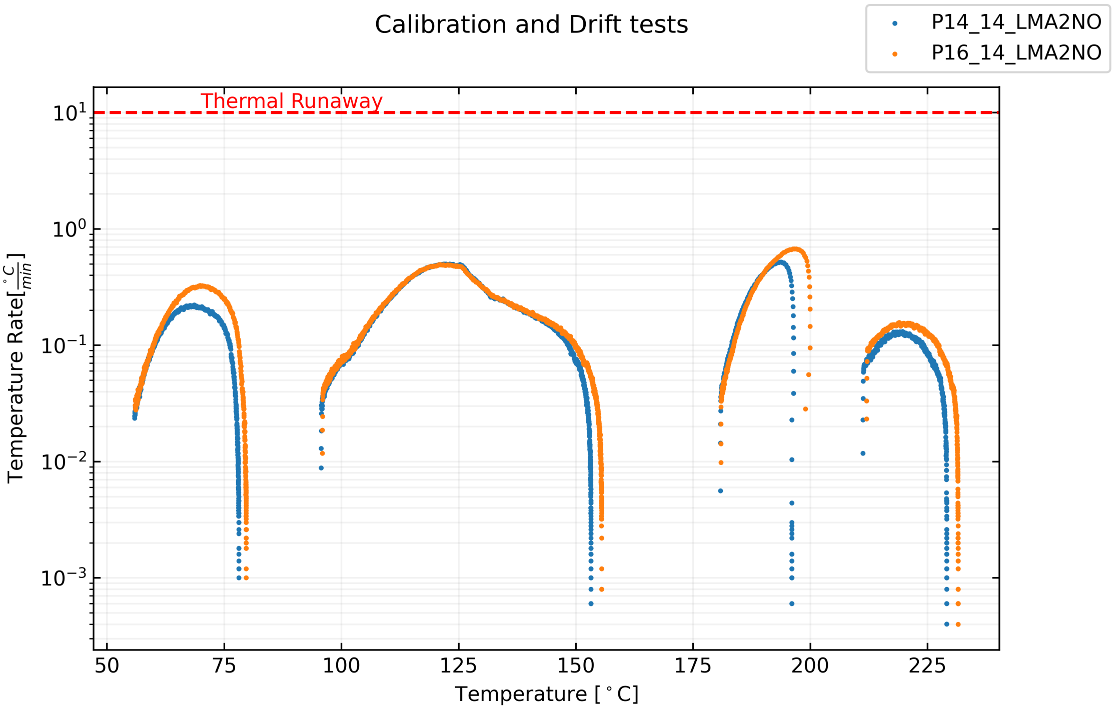

Figure B.20: The two parallels of ARC experiments for sample 14_LMA2NO.

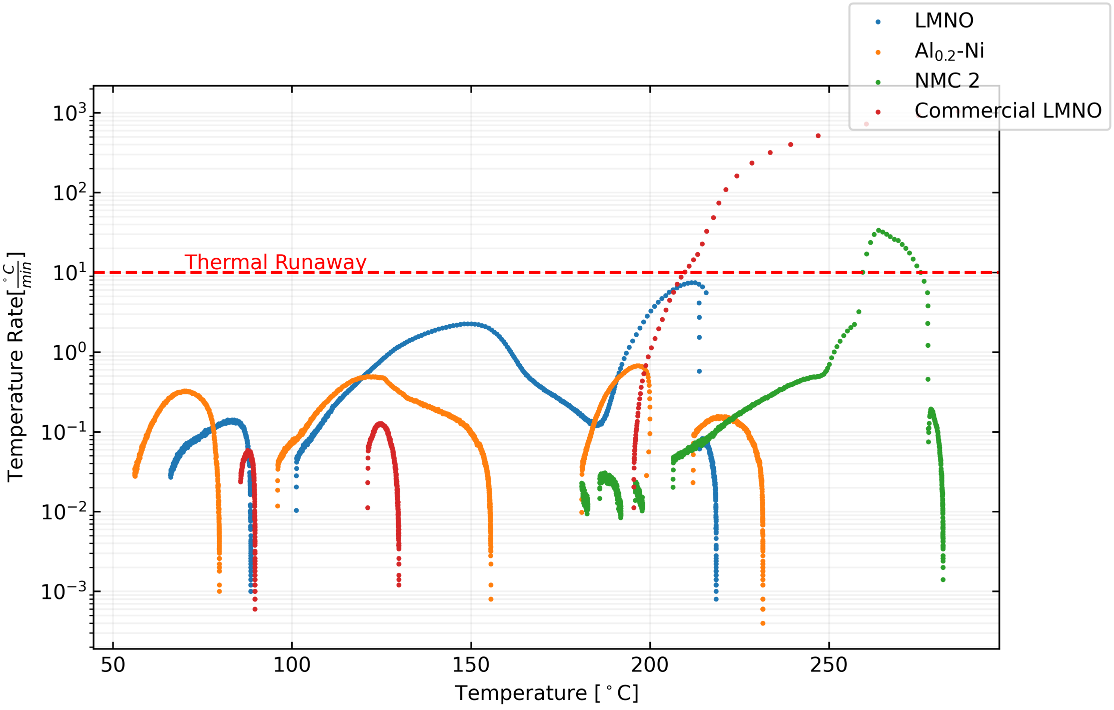

Figure B.21: Comparison of ARC data from delithiated Al-substituted LMNO, pure LMNO, commercial LMNO and CustomCells NMC622.

# Appendix C

# Code

## C.1 Electrochemical

Published on GitHub: https://github.com/amundmr/ecdh [114]

## C.2 X-Ray Diffraction

Data plotting software published on GitHub: https://github.com/amundmr/fdat

Data analysis with TOPAS v6 was done by extensive use of the INP files. These were created by first setting parameters like *iters* and *do_errors* which limit the maximum amount of iterations for a refinement and turns on error calculations respectively. After this, the diffraction data is loaded using the following snippet:

```
xdd filename
    x_calculation_step = Yobs_dx_at(Xo); convolution_step 4
    bkg @  378.541975`_1.54058121 -315.190147`_2.64321778  212.945635`_2.13253843 -52.9735087`_2.3

    lam ymin_on_ymax 0.0001 la 1.0 lo 0.68925 lh 0.1
    LP_Factor( 90) 'change the LP correction  or lh value if required

    Zero_Error(zero, 0.03373`_0.00023)

    start_X 2
    'exclude 16.4 17

    finish_X 63

    #include LaB6.txt                   ' Parameters for LaB6 for DC peakshape
    gauss_fwhm = Sqrt(ad_SR_pos1 Cos(2 * Th)^4 + bd_SR_pos1 Cos(2 * Th)^2 + cd_SR_pos1);

    capillary_diameter_mm  0.3
        capillary_u_cm_inv @  111.00036`_0.94028
        capillary_parallel_beam
```

Which essentially loads the filename (a macro defined earlier in the INP file), sets an x-step to optimize refinements, defines the background with *bkg* through a 10th order Chebyshev polynomial and sets instrumental parameters like the wavelength (*lo*). Two corrections are done, the lorentz polarisation factor is set to 90 to comply with the synchrotron radiation and the zero error is set to be refined. After this, *start_X* and *finish_X* defines the angular range to do the refinement on, while the *exclude* keyword can be used to exclude specific areas which interferes with the refinement. The *#include LaB6.txt* statement imports peakshape parameters generated from a refinement of a $LaB_6$ sample tested right before my materials were tested. This is then inserted as an instrumental peakshape for TOPAS through the *gauss_fwhm* parameter. Lastly, the capillary diameter is set, with a sample absorption coefficient ($\mu$) in order for TOPAS to do the angular absorption correction.

Below this, all the different phases are inserted. The ordered LMNO phase is used as an example in the code snippet below.

```
'======== Ordered ========   '{{{
#ifdef ordered
    str
        prm ordered_a  8.17066_0.00015 min 8.1 max 8.3
        r_bragg  2.35462815
        phase_MAC  24.7152517
        phase_name "LNMO_Ordered"
        MVW( 2099.699, 545.471_0.030, 14.294_0.954)
        space_group P4332
        scale @  1.60181367e-006_1.236e-007
        Phase_LAC_1_on_cm( 157.97910_0.00880)
        Phase_Density_g_on_cm3( 6.39197_0.00036)

        a = ordered_a;
        b = Get(a);
        c = Get(a);

        site Ni1 num_posns  4 x  0.625 y  0.625 z  0.625 occ Ni+2  1 beq  0
        site O1 num_posns  8 x  0.3856 y  0.3856 z  0.3856 occ O-2  1 beq  0
        site Li1 num_posns  8 x  0.0051 y  0.0051 z  0.0051 occ Li+1  1 beq  0
        site O2 num_posns  24 x  0.1028 y  0.1249 z  0.3925 occ O-2  1 beq  0
        site Mn1 num_posns  24 x  0.125 y  0.3766 z  0.8736 occ Mn+4  0.984 beq  0

        LVol_FWHM_CS_G_L(1, 4489.02820_5209511.70326, 0.89, 5424.32462_8164246.37016, csgc_ordere
        e0_from_Strain( 0.00005_0.00016, sgc_ord, 0.02350_0.07276_LIMIT_MIN_0.0001, slc_ord, 0.000
        prm lvol_calc_ordered = 1 / Voigt_Integral_Breadth_GL(1/csgc_ordered, 1/cslc_ordered);:  4
#endif
        '}}}
```

From this, it is visible that parameters with limits can be set through the *prm* keyword and defined as e.g. lattice parameters or measure of crystallite size. Paramaters like this can be used for virtually all values in a refinement, and can be put into equations to lay constraints on the refinement. For my doped materials for instance, a constraint was often set so that all the transition metals would add up to the stoichiometry of 2 in the formula $LiM_2O_4$. The use of parameters is also useful when it comes to printing values to file.

Printing refinement results to file is normally done with the *out* command where first an output file has to be set before the commands *Out(prm, formatting, formatting)* can be used to output the parameter and the formatting of the value and its error. An example of this is showed in the code below.

```
out "results.txt" append

Out_String(##samplename##)
Out(Get (r_wp), " %11.5f")

#ifdef disordered
Out(unordered_a, " %11.5f", " %11.5f")
Out(lvol_calc_unordered, " %11.5f", " %11.5f")
#else
Out_String(" 0.0     0.0     0.0     0.0 ")
#endif
```

The two following commands are also used to output valuable data from a refinement. *Create_hklm_d_Th2_Ip_file(file)* writes a list of planes with hkl, d-spacing and calculated intensity. *Out_Yobs_Ycalc_and_Difference(file)* writes the x-y values for the raw data, refinement and their difference to the file which can then be used for plotting.

## C.3 Accelerating rate calorimetry

The following code was used for plotting the ARC data.

```
import pandas as pd
import numpy as np
import matplotlib.pyplot as plt


files = [
        #"Calibrations/DTBP 250122.DAT",
        #"P7_NMC/CustomCell NMC622 100%SoC P7 SSTUBE side branch 500ml 140222.DAT",
        #"P9_NMC/CustomCell NMC622 100%SoC P9 SSTUBE side branch 500ml 210222.DAT",
        #"P10_NMC/CustomCell NMC622 100%SoC P10 SSTUBE side branch 500ml 010322.DAT",
        "P5_SecretLNMO/P5_SecretLNMO 100%SoC SSTUBE side branch 500ml 250222.DAT",
        #"P6_6_LNMO/P6_6_LNMO 100%SoC SSTUBE side branch 500ml 170222.DAT",
        #"P12_6_LNMO/P12_6_LNMO 100%SoC SSTUBE side branch 500ml 030322.DAT",
        "P17_6_LNMO/P17_6_LNMO 100%SoC SSTUBE side branch 500ml 140322.DAT",
        #"P14_14_LA2NMO/P14_14_LA2NMO 100%SoC SSTUBE side branch 500ml 070322.DAT",
        "P16_14_LA2NMO/P16_14_LA2NMO 100%SoC SSTUBE side branch 500ml 100322.DAT",

]

fig, ax = plt.subplots(figsize=(10,6))
fig.suptitle("Comparing Al-subtituted and pure LNMO with commercial LNMO")

pressure = False
if pressure:
    ax2 = ax.twinx()
    ax2.set_ylim(1,1.6)

ax.set_axisbelow(True)
ax.grid(True, color='gray', which="both", alpha = 0.1)
```

```
ax.axhline(10, color = "r", linestyle = 'dashed')
ax.text(70, 11, "Thermal Runaway", color = "r")
#ax.set_ylim(0.005, 500)
#ax.set_xlim(50,355)


for file in files:
    print(f"Plotting file: {file}")
    colnames = ['Time/min', 'Temp/C', 'TempRate_Cmin', 'Pressure/bar', 'PressureRate/bar/min', 'To
    """
    Modes:
        0: ??
        1: Seeking
        2: Heating (as a step in the heat-wait-seek)
        3: ??
        4: Exothermic
    """

    with open(file, 'r') as f:
        f.readline()
        f.readline()
        lines = f.readlines()

    data = []
    for line in lines:
        x = [float(i) for i in line.split()]
        data.append(x)
    print(x)
    df = pd.DataFrame(data, columns = colnames)
    #df = pd.read_csv(file, header = None, delim_whitespace=True, encoding = "ANSI", names = colna

    import os
    label = os.path.basename(os.path.dirname(file))



    def _plot_rate(df):


        #Removing all data where the instrument isnt in exothermic mode
        df = df[df.Mode == 4]
        #Removing all data with negative heatrate
        df = df[df.TempRate_Cmin >= 0]

        #ax.scatter(df['Temp/C'], df['TempRate_Cmin'], label = "P16 raw", s = 2)

        # Smoothing:
        df['Pressure/bar'] = df['Pressure/bar'].rolling(5).sum() / 5
        df['TempRate_Cmin'] = df['TempRate_Cmin'].rolling(5).sum() / 5
```

```
        rate_label = f"{label}"
        if pressure:
            ax2.plot(df['Temp/C'], df['Pressure/bar'], label = f"Pressure {label}", alpha = 0.5)
            ax2.set_ylabel(r"Pressure [bar]")
            rate_label = f"Temp Rate {label}"

        ax.scatter(df['Temp/C'], df['TempRate_Cmin'], label = rate_label, s = 2)

        #different smoothings
        """df['TempRate_Cmin5'] = df['TempRate_Cmin'].rolling(5).sum() / 5
        ax.scatter(df['Temp/C'], df['TempRate_Cmin5'], label = "Rolling (5)", s = 2)
        df['TempRate_Cmin10'] = df['TempRate_Cmin'].rolling(10).sum() / 10
        ax.scatter(df['Temp/C'], df['TempRate_Cmin10'], label = "Rolling (10)", s = 2)
        df['TempRate_Cmin20'] = df['TempRate_Cmin'].rolling(20).sum() / 20
        ax.scatter(df['Temp/C'], df['TempRate_Cmin20'], label = "Rolling (20)", s = 2)"""

        ax.set_xlabel(r"Temperature [$^\circ$C]")
        ax.set_ylabel(r"Temperature Rate[$\frac{^\circ C}{min}$]")
        ax.set_yscale('log')


    def _plot_temp():
        ax.plot(df['Time/min'], df['Temp/C'], label = f"Temp {label}")
        if pressure:
            # Smoothing:
            df['Pressure/bar'] = df['Pressure/bar'].rolling(20).sum() / 20
            ax2.plot(df['Time/min'], df['Pressure/bar'], label = f"Pressure {label}")
            ax2.set_ylabel(r"Pressure [bar]")

        ax.set_xlabel("Time [min]")
        ax.set_ylabel(r"Temperature [$^\circ$C]")


    _plot_rate(df)
    #_plot_temp()

ax.tick_params(direction='in', top = 'true', right = 'true')

fig.legend()
plt.savefig("./ARCComparison_commLNMO.png", bbox_inches="tight", dpi=300)
plt.show()
```

# Appendix D

# Safety documentation

This appendix contains details of chemicals and their associated HSE risk (table D.1), specific work/methods and their associated HSE risk (table D.2, D.3, D.4, D.5) and HSE measures taken to reduce severity of an eventual scenario (table D.6).

Table D.1: Chemicals and associated HSE risk.

| **Chemical** | **Manufacturer, MW (g/mol), Purity (%)** | **HSE risk** |
|---|---|---|
| $LiMn_{1.5}Ni_{0.5}O_4$ (LMNO) | Self-made, 182.69, N/A | May cause an allergic skin reaction. Suspected to cause cancer. Causes damage to organs through prolonged or repeated exposure. Harmful to aquatic life with long lasting effects. |
| Carbon (Super P) | TimCal, 12.01, N/A | May cause eye, skin and respiratory tract irritation. Possible carcinogen. Avoid open flames. |
| Polyvinylidene fluoride (PVDF) | Sigma-Aldrich, 534000, N/A | May cause eye irritation. |
| N-Methyd-2-Pyrrolidone (NMP) | Sigma-Aldrich, 99.13, 99 | Causes skin, respiratory and serious eye irritation. Has reproductive toxicity and is a carcinogen. |
| Lithium metal | Sigma Aldrich, 6.94, N/A | Corrosive through contact with skin, eyes, ingestion, inhalation. Reacts violently with water forming flammable gases and corrosive dust. |
| $MnN_2O_6$ | Alfa Aesar, 251.01, 98 | May intensify fire; oxidizer. May damage fertility or the unborn child. Causes damage to organs through prolonged or repeated exposure. |
| $LiNO_3$ | Alfa Aesar, 68.95, 99.999 | Causes skin, respiratory and eye irritation. Can be toxic by ingestion, targeting the central nervous system, thyroids, kidneys and the cardio-vascular system. |
| $NiN_2O_6$ | Sigma-Aldrich, 290.79, 98.5 | May intensify fire; oxidizer. Causes skin, respiratory and eye irritation. Is a carcinogen. Toxic to aquatic organisms. |
| Citric acid | Sigma-Aldrich, 192.12, 99.5 | Exposure of concentrated solutions to skin and eyes can cause redness and pain. |
| Ethylene glycol | Sigma-Aldrich, 62.07, 99.8 | Damages internal organs upon ingestion of large amounts. |

Table D.2: HSE risks of synthesis.

| **Step** | **HSE risk and mitigation** |
|---|---|
| Weighing nitrate solutions | Risk of spilling. If spilt, avoid contact with skin, eyes and inhalation. |
| Mixing and heating | Fumes, spilling. If spilt, avoid contact with skin, eyes and inhalation. Work in fume hood, and be careful with the stirring speed. |
| Combustion | Fumes, fire, explosion. Max 20cm opening on fume hood, use glasses and lab coat. Stay below $200^{\circ}C$ on the heater. |
| Citric acid oven | Hot equipment. Finger burn. Evaporation of volatile components. Oven in fume hood. |

Table D.3: HSE risk of electrode fabrication and cell assembly.

| **Step** | **HSE risk and mitigation** |
|---|---|
| Mixing powders | Risk of spilling and airborne particles. If spilt, avoid contact with skin, eyes and inhalation. Use mask to cover mouth at all times. |
| Mixing in NMP | Spilling. If spilt, avoid contact with skin, eyes and inhalation. Work in fume hood. |
| Vacuum oven | Hot equipment. Finger burn. Evaporation of volatile components. |
| Cell assembly | Risk of puncturing glove in glovebox and bad cell assembly exposing metallic lithium to air upon extraction from the glovebox. |

Table D.4: HSE risk of pouch-cell post mortem.

| **Step** | **HSE risk and mitigation** |
|---|---|
| Handling DEC | Risk of contaminating gloves and surroundings. Work in glove box. |
| Packing capillaries | Risk of cutting. Handle with care. |

Table D.5: HSE risk of material handling.

| **Step** | **HSE risk and mitigation** |
|---|---|
| Waste handling | Possible reactions with other compounds. Pack in glove or zip-lock and use yellow waste buckets. |
| Washing of equipment | LMNO powder into the sink. Use paper and throw in waste bucket. Let NMP containing residues stay in fume hood until dried. |
| Powder transport | Transport all nitrates, citric acid and LMNO sample powders in a box to avoid spilling during transport. |

Table D.6: HSE measured: Dangers and precations.

| **Danger** | **Precaution** |
|---|---|
| Skin irritation | Lab coat, Gloves - Nitrile, Glove box |
| Eye irritation | Lab glasses / goggles, glove box, fume hood |

| **Danger** | **Precaution** |
|---|---|
| Powder inhalation | Fume hood, mask |
| Side reactions | Deposit waste in designated containers. No significant or dangerous side reactions expected. |